INTERNATIONAL JOURNAL OF
IJCOE
COASTAL, OFFSHORE AND
ENVIRONMENTAL ENGINEERING

Volume 11 | Isssue 1| JAN 2026

www.ijcoe.org

International Journal of Coastal, Offshore and Environmental Engineering (IJCOE) Vol.11/Issue 1/ JAN 2026

International Journal of
Coastal, Offshore
& Environmental
Engineering
Since 2015
ISSN: 2345-6728 (Online)

IJCOE
Editor-in-Chief: Prof. Hamid S.Bahai

International Journal of Coastal, Offshore & Environmental Engineering
Since 2015
ISSN: 2980-8721 (online)

In The Name of God

Message from the Editor-in-Chief

The IJCOE journal office was established in 2015,and its first issue was published in 2016. TheIJCOE covers a wide range of research in thefields of oceanography & ocean technology, aswell as marine industries & marine engineering.The editorial board of IJCOE consists of nearly130 of the greatest scientists and researchersfrom over 30 countries worldwide, and thejournal's review board comprises 1,000 membersfrom all five continents. The membership andapplication process for joining the editorial andreview boards of this journal is ongoing. IJCOE isa research-academic quarterly journal that haspublication and distribution permissions fromthe Press Organization and permission topublish scientific-research articles from theMinistry of Science, Research, and Technology(MSRT) with an "A" rating. It also holds a "Q1"rating from the ISC institute with an impactfactor (IF) of approximately 0.43 and isconsidered a "core journal" (prestigious andoutstanding journal). IJCOE is an open-accessjournal and allows the download and receipt ofaccepted articles in full text for free. It respectsand adheres to copyright and COPE regulations.The journal's office operates 24/7, providingservices to researchers. In addition to publishinga regular quarterly journal, IJCOE has 16 specialissues on specific topics in preparation. It alsoprovides conditions for publishing specializedbooks, references, and handbooks. Moreover, itis ready to cooperate with the secretariats ofreputable international conferences to publishtheir selected and outstanding articles. IJCOEevaluates, appraises, and publishes books,articles, and the scientific achievements andfindings of esteemed researchers and scientistsworldwide who are innovating and conductingin-depth research in the "important and strategicfield of the maritime technology & Oceanengineering." It welcomes any form of jointcooperation with universities, research institutes,and related research centers at the national,regional, and international levels, and extends ahand for collaboration.

Classification of Editorial Board in IJCOE

Editor-in-Chief

Director-in-Chief

Deputy Editor

Executive Managers

English Text Editor

Technical Editor

International Editorial Board

National Editorial Board

Editorial Board Associate

Editorial Board Assistant

Guest Editorial Board

Advisory Board

Administrative Coordinator

Honorary Board Member

Methodology Advisor

Author Benefits

- Open Access
- Rapid Publication
- Thorough Peer-Review
- No Copyright Constraints
- Coverage by Leading Indexing Services
- Discounts On Article Processing Charges (APC)
- No Space Constraints, No restriction on the maximum length of the papers, number of figures or colors

INTERNATIONAL JOURNAL OF IJCOE COASTAL, OFFSHORE & ENVIRONMENTAL ENGINEERING

Aims of IJCOE

Hydrodynamics

Marine equipment

Structural mechanics

Ocean environmental predictions

Stochastic calculations Experimental

Automatic Control of Marine Systems

Scope of IJCOE

Marine Hazards

Ocean Acoustics

Naval Architecture

Ocean Engineering

Coastal Engineering

Marine Meteorology

Marine Earth Sciences

Underwater Technology

Marine Renewable Energy

Polar & Arctic Engineering

Marine Renewable Energy

Marine Geography & Geodesy

Marine Environmental Engineering

Automatic Control of Marine Systems

Hydro Physics & Physical Oceanography

Type of papers

- Case Studies
- Book Reviews
- Review Article
- Letters to the Editor
- Methodology Papers
- Editorials and Commentaries
- Response or Rejoinder Papers
- Perspective or Opinion Papers
- Conceptual or Theoretical Papers
- Meta-Analysis and Systematic Reviews
- Short Communications or Brief Reports
- Research Articles (Original Research Papers)

Scientific Research Journal

Ministry of Science, Research And Technology (MSRT)

Jurnal Ranking 2023: A

Ministry Of Science, Research And Technology (ISC)

Citation Impact 2022: 0.429

Quartile 2022 : Q1

Core Collection

IJCOE is a Member of

Cantact Us

Office 1 | Research Institute of Meteorology and Atmospheric Science

Address | Tehran, Shahid Kharrazi Highway, Pajoohesh Blvd, Research Institute of Meteorology and Atmospheric Science, Sand and Dust Storm International Research Center (SDS-IRC), No. 13, 1st floor.

Phone | +982144787652

Postal code | 13611-14977

website | www.rimac.ac.ir

Office 2 | Iranian National Institute for Oceanography and Atmospheric Science

Address | Tehran, Dr. Fatemi Gharbi St., Shahid Etemadzade St., No. 3, third floor.

Phone | +982166944873

Postal code | 13389 – 14118

website | www.inio.ac.ir

Email | Info@ijcoe.org

Website | www.ijcoe.org

Follow Us

Volume & Issue:

Volume 11, Issue 1, JAN 2026

Number of Articles: 8

Content

IJCOE
COASTAL, OFFSHORE & ENVIRONMENTAL ENGINEERING

INTERNATIONAL JOURNAL OF
COASTAL, OFFSHORE & ENVIRONMENTAL ENGINEERING IJCOE Vol.11/No. 1/Winter 2026 (1-33)

Available online at: www. Ijcoe.org

A model of human capital in the law of Marine Agile Project-Oriented Organizations

Saeed Karami[1] , Mohammadreza Zahedi[* 2]
[1] *Assistant Professor of Payame Nour University, Tehran, Tran, karami.t54@pnu.ac.ir*
[2*] *Associate Professor of Malek Ashtar University of Technology, zahedy182@gmail.com*

ARTICLE INFO

Article History:
Receive: 26 Jun 2025
Accepted : 23 Dec 2025

Keywords:
***Human Capital, Project-Based Organization, Agile Organization, law,* Marine Organizations**

ABSTRACT

High-tech industries technology industries that have superior technology and technical knowledge, innovation and creativity, attention to its definition and development, need to create a knowledge management system in such a way that the flow of knowledge required by the organization and individuals is effective and timely. By examining the main dimensions of human capital of Marine Agile Project-Oriented Organizations, law, indicators related to these dimensions and their relationship with each other; Relationship between human capital components in the human capital model of Marine Agile Project-Oriented Organizations We prioritized the dimensions and components presented. Considering that extensive research in such organizations has not been done so far; Therefore, the results of this research can be very useful for completing the circle of knowledge management and achieving the goals of knowledge flow in high-tech industries organizations, as well as making available and transferring the experiences of people working in this field, as well as saving time and reducing costs

1. Introduction

Research shows that human capital is the highest, most valuable and largest asset of any organization or country. Today, organizations are well aware that they need the best talent to succeed in a complex global economy and staying competitive in the business environment. In this environment, organizations need to work together to strengthen their human capital. The results show that by choosing the best human capital for organizations, success can be achieved and an effective step can be taken to advance the goals of the organization. On the other hand, given that the world is changing, organizations need to change to progress and compete, and in a word, to be "agile." Agility means the ability to respond quickly and successfully to environmental changes(Armstrong & Taylor, 2020). An organization will be agile when it is able to coordinate and support all the required resources quickly and efficiently by leveraging knowledge and cooperation (internally and with other organizations), sharing sensitive information with suppliers, partners and Share customers, anticipate market changes and changes in customer value. Numerous studies show that countries have higher economic growth with educated, skilled and adequate labor. Continuing the research process suggests that proper human capital management is one of the biggest challenges facing projects. The goal of all project-oriented organizations is the successful implementation of projects(Ekambaram, Sørensen, Bull-Berg, & Olsson, 2018). One of the important dimensions in project implementation is the discussion of human capital management and related processes. So far, various models have been proposed to explain the different dimensions as well as measuring the human capital of organizations; general models that have measured this capital in general and do not consider the differences in the structure and texture of different areas(Wright, 2014). It is also worthwhile to consider competence, speed, flexibility, accountability, and cultivate them within oneself as much as possible (Kerzner, 2017). It is essential that organizations develop. Accordingly, the main goal of the present study is to provide a model for the:

1) What are the main dimensions of human capital of Marine Agile Project-Oriented Organizations?

2) What are the indicators related to the key dimensions of human capital of Marine Agile Project-Oriented Organizations?

3) What is the relationship between the key dimensions of human capital in the human capital model of Marine Agile Project-Oriented Organizations?

4) how is the relationship between the components of human capital in the human capital model of agile project-based organizations?

5) What is the priority of the dimensions and components of human capital in the model of Marine Agile Project-Oriented Organizations?

2. Theoretical foundations and background of research

Leslie and Zerley (2003). Human capital is the result of a combination of professional knowledge of employees, leadership skills, risk-taking, and problem-solving ability. According to Bonites, human capital represents the knowledge of individuals in an organization that lies within its employees. Human capital is a combination of knowledge, the power of innovation, and the ability of individuals to perform their duties, values, culture, and philosophy(Birasnav, Rangnekar, & Dalpati, 2011). Human capital refers to knowledge, education, job competencies, and psychometric assessments. Human capital is very important because of its scarcity, value, irreplaceability and imitation. Human capital is an important factor in determining the growth of countries or explains

the difference in productivity between countries(Premalatha, 2016).

"Maritime law, sometimes referred to as admiralty law, is the branch of law that governs all aspects of the sea. Maritime law encompasses various issues, including: The regulation of shipping and insurance. The navigation and passage of ships through different jurisdictions and in the open seas. The rights of seafarers"

2.1 Project-based organization

It is an organization that is ultimately a priority with the project and does most of its work in the form of a project (Kerzner, 2017). An organization that organizes its work in the form of separate projects in such a way that it organizes skilled and capable people to perform innovative and complex tasks for different purposes and customers (Gemünden, Lehner, & Kock, 2018). It is an organization in which employees have a permanent employment relationship with the organization, but have a temporary employment relationship with the project (Sparrow & Cooper, 2012).According to Pakandorf, the initial dependence of project staff on the organization and the project is routine. In general, it can be said that the project-based organization is an organization that has six characteristics: 1- Objectivism 2- Central and knowledge-based team 3- Temporality 4- Multi-task and inter-unit structure 5- Stress generation 6- Multi-employment.

Project-based organizations are organizations whose operations consist mainly of projects. These organizations are divided into two categories. Organizations whose main income comes from project implementation in the form of a contract for others, and organizations that have accepted project-based management. Project-oriented organizations are a type of matrix organization that has flexible, smooth, fast structures and is based on teams and projects. Project-based organizations are usually in areas of industry, especially construction, information technology, communication, Cars, media and professional services are active. Their strategy is to create results to meet the demand of specific customers by organizing projects to temporarily employ internal specialized employees and run the business in a limited time frame(Cattani, Ferriani, Frederiksen, & Täube, 2011). Project-based organizations are also referred to as knowledge-based and learning organizations. These organizations have dynamic boundaries because the number and type of projects are constantly changing(Pemsel, Müller, & Söderlund, 2016).

2.2 Agile organization

Today, rapid and unexpected changes due to technological innovations, changing customer needs, and a lack of confidence in competitive environments have hampered the flexibility and responsiveness of organizations; Thus, the formation of this critical situation has left no choice but to make major reforms in the strategic perspective, reviewing traditional models and business priorities for organizations; therefore, organizations are well aware that to overcome these challenges. The environment and the preservation of competitiveness, approaches and solutions have lost their capability and the current strategic and modern weapon environment requires new paradigms and perspectives; therefore, agility to take advantage of potential opportunities and The opposite is true of environmental threats(Hamalainen, Kosonen, & Doz, 2012) .Agile organizations are more integrated than traditional organizations. In these organizations, goals can change weekly or even daily. Agile organizations think beyond adaptation to change and tend to use potential opportunities in a turbulent environment and gain a steady position They remember their innovations and merits. Agile organizations think differently about meeting customer needs. Not only do they sell their products, but they also offer solutions to meet the real needs of their customers, believing that their products are not perfect and enriching their customers' values and creating added value by enriching their product.

This makes the position of agile organizations inaccessible to competitors (Andzulis, Panagopoulos, & Rapp, 2012).

In fact, agility refers to an organization's ability to anticipate, respond effectively and efficiently, think quickly and intelligently, and use appropriate selection strategies to deal with factors affecting organizational performance(Triaa, Gzara, & Verjus, 2016). Since the beginning of the third millennium, intense competition over technology development, increasing customer expectations, increasing cost pressures, instability and market instability, etc., have been among the factors that necessitate the use of new patterns, procedures and tools for organizations to succeed and survive. Impose. The intensification of global competition has prompted organizations to choose agility in human capital as the dominant paradigm in the face of these challenges, among the various solutions offered to deal with the turbulent environment. Ability to streamline human capital can bring a wide range of benefits to the organization, such as speeding up the learning curve, improving quality, better customer service, and saving in scope and depth(Tolf, Nyström, Tishelman, Brommels, & Hansson, 2015). so, agility can be considered as active responses to change, the use of change as inherent opportunities in a turbulent environment, and the ability to survive and thrive in a changing and unpredictable environment(Nafei, 2016).

In fact, agile human capital has the potential to conquer new markets with the flag of innovation, to develop, to ensure the excellence of the organization, and to paint a bright future for it (Rodina, Simpkis and Foxx, 2003).

3. General models of human capital

Table 1 presents the general models of human capital of organizations and the main dimensions proposed for each of these models.

Table 1: Different models of human capital of organizations

researcher	Components and indicators of human capital
(Dhir, 2019)	Rational capital, social capital, emotional capital
(Gendron, Kouremenou, & Rusu, 2016)	Human intellectual capital, Human social capital, Human emotional capital
(Shastry, 2012)	Education,Wages,Communication,Human capital
(Trivellas, Akrivouli, Tsifora, & Tsoutsa, 2015)	Organizational competencies and , Learning Motivation , Culture ، Leadership and management satisfaction
(Bailey, Albassami, & Al-Meshal, 2016)	Employee satisfaction, job satisfaction and employee commitment
(Dobson, Rose, Parton, & Hart, 2020)	Leadership, employee participation, access to knowledge, labor optimization and learning capacity
(Ulvenblad, Berggren, & Winborg, 2013)	Ability, Skills, Competence, Education, Experience, Number of Company People Related to Previous Field, Accurate Distribution of Customer Liability Responsibilities

(Aldrich & Meyer, 2015)	Rational capital, social capital, and emotional capital
(Karamustafaoğlu, 2011)	Knowledge, skills, ability
(Tan, 2016)	Knowledge: Higher education, knowledge-based staff, periodic training, organizational leadership knowledge Skills and Abilities: Knowledgeable Staff, Expert Advisors, Information Technology, Ability to Upgrade to Management Levels - Using Knowledge-Based Team Structure Attitude: Loyalty and commitment of Daneshvar staff, Daneshvar staff satisfaction, evaluation of Daneshvar's attitude and opinions, organization's ability to motivate Daneshvar.
(Kashi, 2017)	Competence: experience and expertise, competencies, skills and training Attitude: employee motivation and satisfaction, teamwork spirit, valuable adaptability of the organization and leadership Intellectual agility: creativity and innovation, problem-solving ability, mental flexibility
(Schuler, Jackson, & Tarique, 2011)	Leadership, cultural communication, strategic integration, intelligence and talent, knowledge management
(Subramanian, Abdulrahman, Wu, & Nath, 2016)	General knowledge, employee competence
(Hong, Hao, Kumar, Ramendran, & Kadiresan, 2012)	Employee competence, which includes strategic management leadership; employee traits; employee learning ability; employee training efficiency; employee ability to participate in decision-making and management; technical and management staff training; Employee attitudes that include the acquisition of identity from organizational values; Satisfaction rate; Employee dropout rate; Moderate useful life of employees and employee creativity that includes employee creativity ability; Income from employees' creative thoughts
Quintana, Mora,) Pérez, & Vila, (2016	Technical knowledge, education, work-related knowledge, work-related competence, entrepreneurial spirit, skills related to innovation and the effectiveness of change or flexibility, professional competence

Human capital in project-oriented organizations

Table 2: presents the dimensions and components of human capital in project-based organizations.

Reference	Dimensions and components
(Kleitman, Stankov, Allwood, Young, & Mak, 2012)	Education level, verbal and communication skills, self-confidence, leadership power
(Hislop, Bosua, & Helms, 2018)	Motivation, general and specialized knowledge, work experience, knowledge sharing and application, high flexibility and quick response
(Yan, 2020)	Riskability
(Lin & Chen, 2017)	Knowledge sharing and application, specialized knowledge

(Lin & Chen, 2017)	Creating alignment structures, implementing strategies and producing knowledge
(Sabeeh, Mustapha, & Mohamad, 2018)	Goal-based management as an organizational strategy
(Decker, 2018)	Expert knowledge, skills and resources, flexible response to changing customer needs, risks and uncertainty
(Azeez, 2015)	Experience, training, creativity, skill and health
(Turner & Pennington, 2015)	Knowledge, ability, motivation

Human capital in agile organizations

Table 3: presents the dimensions and components of human capital in agile organizations.

)Liu, Zhang, Liao, Hao, & Mao, 2016(	Strengthen employee creativity, integrate employee ideas
(Afsar & Badir, 2017)	Flexibility in providing services, nurturing employees with skills, worthy and compatible with technologies, creating motivation, knowledge, skills
(Chang, Gong, Way, & Jia, 2013)	Trained and flexible human resources, responsiveness and rapid adaptability
(Ghajargar, Zenezini, & Montanaro, 2016)	Flexibility in service delivery, speed and quality of meeting customer needs, managing and motivating employees, capability, skill, technology compatibility
(Laureiro-Martínez & Brusoni, 2018)	Ability, flexibility, decision-making ability and problem solving
(Charan, 2017)	Accept new responsibilities, be willing to develop and train yourself, be able to solve problems, adapt to changes, new ideas and technologies, and accept new responsibilities
(Casey & Sieber, 2016)	Involve employees, train and motivate employees
(Sotsh, 2014)	Efficiency: Reading the market, having a broad vision, customer orientation, foresight, having knowledge about the market, the environment and direction of the organization and being result-oriented, spontaneous cooperation, constructive behavior, education and learning Focus: Ability to prioritize, find solutions and solutions, patience and speed of action Being productive: Skillful in organizational matters, quick learning, welcoming experience, willingness to use new knowledge and teamwork spirit
(Sousa & Rocha, 2019)	Competency: Acceleration of essential skills, changes in business processes, speed of innovation of management skills, speed of acquisition of software skills, new information technology and speed of development of new skills and competencies Intelligence: Responding to changing market conditions, the business environment, and changing customer needs

(Enalls-Fenner, 2015)	Flexibility and positive attitude towards change, tolerance in uncertain situations, constructive interaction with stress, intelligence, competence, cooperation, culture, information system, active behavior
(Harden, Laidlaw, & Mmed, 2020)	Responding to external changes, benchmarks for assessing skills and speed in skills development, speed of adaptation to the new work environment, speed of access to information, use of fluid technology, independence in the workplace, participatory technologies, knowledge sharing and employee empowerment
(Nayak, 2016)	IT skills, teamwork and negotiation knowledge, technology and production strategies knowledge, capable, multi-tasking staff and self-governing teams
(Cetin, Demirciftci, & Bilgihan, 2016)	Ability to change ability and capacity, training, knowledge, skills

By examining the type of expression of the subject, the dimensions and components of human capital in agile project-based organizations were identified and the initial research model was presented.

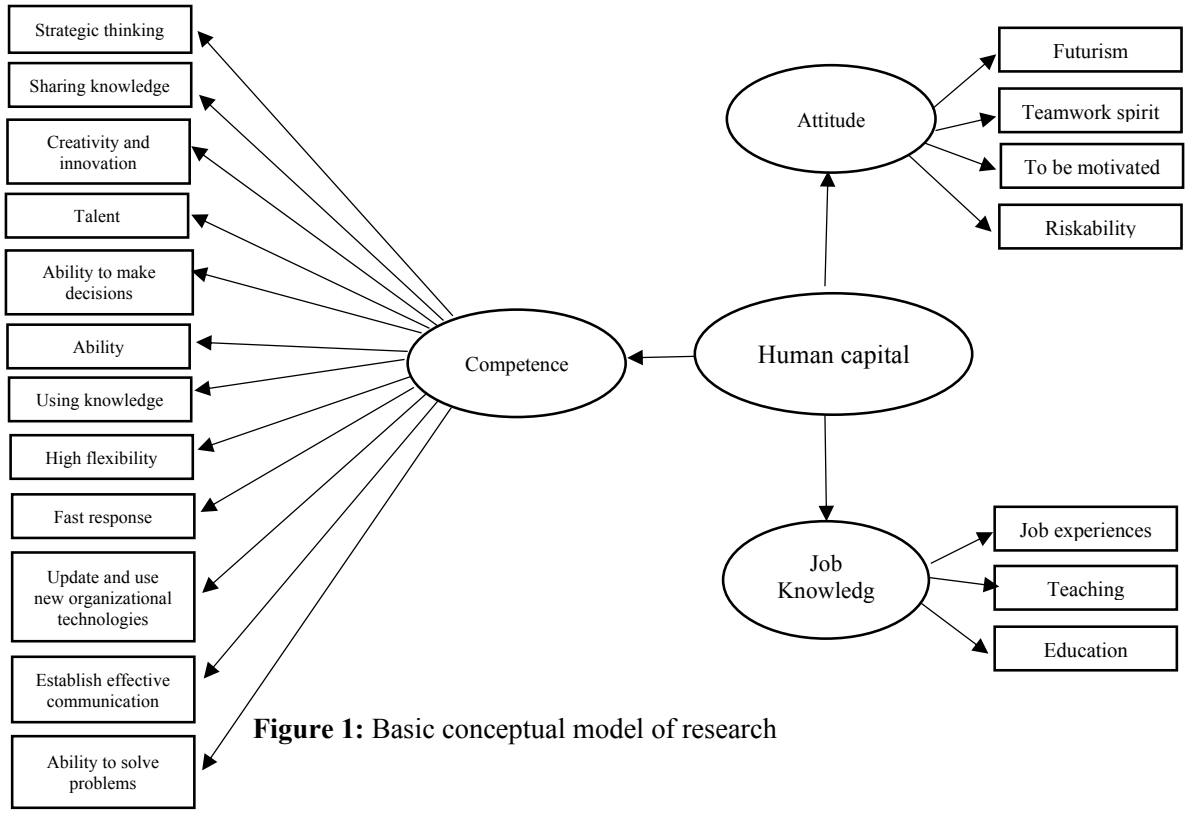

Figure 1: Basic conceptual model of research

4. Research methodology

This research is applied from the perspective of the research goal because it tries to put the results of this research into practical use and with the help of its results, to solve the problems of the organization. But this research is from the perspective of collecting descriptive-survey research information. When research is attempted to rely on library studies of the early model of human capital, research is descriptive, but when it is attempted with the help of an expert questionnaire, the opinion of experts on the model is survey research. The statistical population of this study consists of experts who are familiar with the subject and also familiar with project-based organizations and agile organizations. On the other hand, due to the specialization of the subject, determining the sampling method and also determining the sample size has not been very effective and efforts have been made to emphasize more on the qualification of individuals and their familiarity with relevant issues. In total, in this research, the opinions of 8 experts who have been informed about snowballs have been used. In this research, to collect the necessary data for designing the conceptual model of the research, the method of reviewing library documents has been used. For this purpose, the necessary searches were carried out in databases and libraries, and after reviewing and reading numerous articles, three dimensions and nineteen components were identified. In addition, expert interviews were conducted, and finally a questionnaire was used to test the model's expertise.

4.1 Expert interview

After reviewing articles and resources related to human capital in project-based and agile organizations, expert interviews were conducted with relevant experts. These interviews were conducted with the aim of presenting the dimensions and components extracted from library studies to experts and consulting relevant experts. Also, for variables that may have been neglected in library studies, a better understanding of the variables for their operational definition, appropriate classification, was also surveyed.

4.2 Formation of the proposed framework (dimensions and components) of the proposed research model

According to experts, the components of ethics, legalism, tolerance, secrecy, and attention to the benefits of the organization were added to the attitude. Also, according to experts, the components mentioned in the attitude dimension are among the dimensions of personality traits because human personality is a constant and stable trait that characterizes the commonalities and differences between a person and others, but the attitude of any kind of expression of opinion. It is about an object or a person or an event in which judgment and evaluation lie (regardless of whether it is positive or negative).

Feeling +
Interpretation⇨Perception⇨Attitude⇨
behavior⇨ personality

So then the attitude towards personality traits changed.

In terms of job knowledge, the components of education and training were eliminated, and the components of general knowledge and specialized knowledge were proposed. General knowledge includes university education, and specialized knowledge includes job-related education and on-the-job training. They also confirmed the component of job experiences that were considered as research findings.

In the competency dimension, the skill component was eliminated due to competency overlap. It was suggested that the component of knowledge application be integrated with the component of knowledge sharing and be considered as knowledge sharing and application of knowledge. It was also suggested that the component of decision-making ability and problem-solving ability be integrated with each other, so it was considered as decision-making and problem-solving ability. After interviewing

various experts, the components: interaction with the external environment (customers, competitors), systemic thinking were added to the model.

Table 2 shows the variables calculated from the literature and the expert interview.

Table 4: Human Capability Variables in Project-Based Organizations

Extract from		Variable	Extract from		Variable
interview	Dialect		interview	Dialect	
*	*	Knowledge Sharing and Knowledge Application	*	*	Futurism
*	-	Interact With The External environment (customers, competitors)	*	*	Riskability
*	*	Ability to Make Decisions and Solve Problems	*	*	To be motivated
*	-	Systematic Thinking	*	*	Team Work Sprint
*	*	Update and Use New Organizational Technologies	*	*	obligation
*	*	Establish Effective Communication and Interaction	*	*	General Knowledge
*	*	Creativity and Innovation	*	*	Dedicated Knowledge
*	*	Strategic Thinking	*	*	Job experiences
*	*	Work Talent	*	*	High Flexibility
-	*	Skill	*	*	Fast Response
*	-	Secrecy	*	-	Ethical
*	-	Pay Attention to The Interests of The Organization	*	-	Legitimacy
*	-	Honesty	*	-	Tolerance

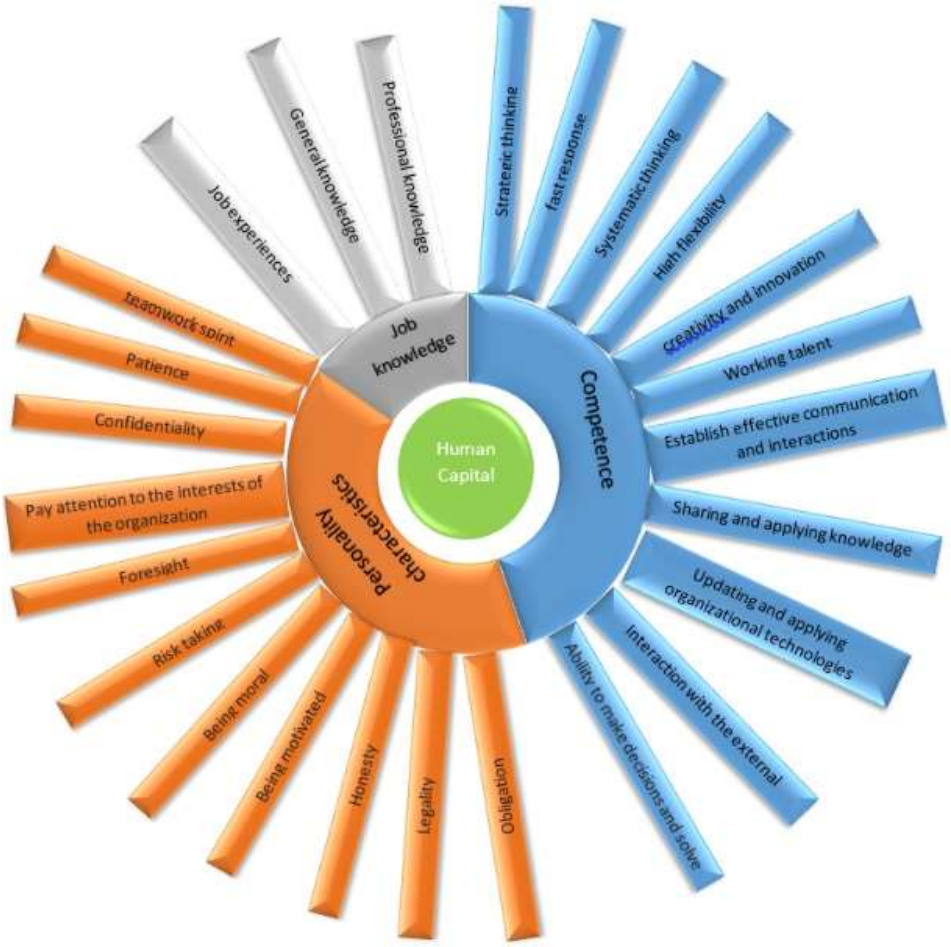

Figure 2: The final model of human capital in Marine Agile Project-Oriented Organizations

4.3 Expert testing of the dimensions and components of the proposed model

After designing the proposed research model, this model was tested on a large scale and using the opinions of 8 experts. To this end, the DANP Expert Questionnaire was designed, in which experts assessed the importance and appropriateness of the proposed components according to the DANP method.

4.4 Expert Questionnaire

DANP questionnaire was used in this study. The measurement tool must have the necessary validity and reliability so that the researcher can collect data appropriate to the research and through these data and their analysis, test the desired hypotheses and answer the research questions. Given that all the components and indicators that make up the questions were derived from the literature and related theories, and in this questionnaire the couple comparison, all the two-to-two factors are compared. This eliminates all chances of ignoring a criterion or question. Also, before duplicating the questionnaire, it was examined with several experts, and the validity of the questionnaire was confirmed from the very beginning of the research with the opinion of experts and experts.

The following relation is used in the DANP method to calculate the measurement of data reliability.

$$g = \frac{1}{n(n-1)} \sum_{i=1}^{n} \sum_{j=1}^{n} \frac{\left| t_{ij}^{p} - t_{ij}^{p-1} \right|}{t_{ij}^{p}} \times 100$$

That g is the discrepancy rate and $\mathbf{t_{ij}^{p}}$, indicating the matrix values and $\mathbf{t_{ij}^{p-1}}$ Indicates the matrix values of the mean of the experts' opinions by deleting the experts No. **i** and **n** , the number of criteria.

5. Data analyzing method

DANP method steps

5.1 calculate the direct communication matrix

The evaluation of the relationships between the criteria (the effect of one criterion on another criterion) is based on the opinions of research experts using a rating range of 0 to 4, in which 0 means no effect, 1 means little effect, 2 means moderate effect, 3 means high impact and 4 means very high impact. Experts are asked to determine the effect of one criterion on another.

$$D = \begin{bmatrix} d_c^{11} & \dots & d_c^{1j} & \dots & d_c^{1n} \\ \vdots & & \vdots & & \vdots \\ d_c^{i1} & \dots & d_c^{ij} & \dots & d_c^{in} \\ \vdots & & \vdots & & \vdots \\ d_c^{n1} & \dots & d_c^{nj} & \dots & d_c^{nn} \end{bmatrix}$$

The D-direct communication matrix is normalized using the following equation and the N-matrix is obtained.

$$N = VD;\ V = \min\left\{1/\max_i \sum_{j=1}^{n} d_c^{ij},\ 1/\max_j \sum_{i=1}^{n} d_c^{ij}\right\}.\ i.j \in \{1,2,\dots,n\}$$

$$T = N + N^2 + \cdots + N^h = N(I - N)^{-1},\ \text{when} \lim Nh \to \infty$$

Reliability is also obtained from the following equation:

Reliability = 1-g

If the g value is less than 5% (reliability above 95%), the reliability of the data (validity) is confirmed.

Here the value of the discrepancy rate was calculated to be 0.48493546, and since it is less than 0.05, the compatibility of the comparisons is accepted and shows that it is reliable.

That is, if they believe that the criterion i affects the criterion j, they must show it as d_c ^ ij. Therefore, the matrix D = [d_c ^ ij] will be obtained from the direct relation. In the DANP method, when we have criteria and sub-criteria, we only form the sub-criteria. In fact, we form the DANP method for the sub-criteria and draw conclusions from it for the criteria. Therefore, considering that the research model has 25 components, it is a matrix with dimensions of 25 * 25. Combine the opinions of the 8 experts by means of an arithmetic mean to form the initial matrix.

5.2 Normalize the direct communication matrix

Step 3 - Calculate the total communication matrix

Once the D matrix is normalized and the N matrix is obtained, the complete communication matrix will be obtained through the following equation. In this regard, I represents the unit matrix.

The total communication matrix can be calculated by the criteria shown in T_C :

$$T_c = \begin{array}{c} \\ D_1 \\ \vdots \\ D_i \\ \vdots \\ D_n \end{array} \begin{array}{c} \begin{array}{cccccc} D_1 & & D_j & & D_n \\ c_{11}\ldots c_{1m_1} & \cdots & c_{j1}\ldots c_{jm_j} & \cdots & c_{n1}\ldots c_{nm_n} \end{array} \\ \begin{bmatrix} T_c^{11} & \cdots & T_c^{1j} & \cdots & T_c^{1n} \\ \vdots & & \vdots & & \vdots \\ T_c^{i1} & \cdots & T_c^{ij} & \cdots & T_c^{in} \\ \vdots & & \vdots & & \vdots \\ T_c^{n1} & \cdots & T_c^{nj} & \cdots & T_c^{nn} \end{bmatrix} \end{array}$$

The r_i index represents the sum of the i-th row and the c_j represents the sum of the j-column. The r_i + c_j index is obtained from the sum of the row i and the column j (i = j). This index indicates the importance of the i-th criterion. Similarly, the r_i-c_j index is the result of the difference between the sum of the i-row and the j-column and indicates the influence or effectiveness of the i-criterion. In general, if r_i-c_j is positive (i = j), the i-th criterion is one of the causal or influential criteria. If r_i-c_j is negative (i = j), criterion i-th is part of the group of influential criteria. The scientific diagram can be drawn based on the two mentioned indicators, which is known as the network relations map. According to this map, it is possible to decide how the dimensions and criteria can be improved.

$$T_D = \begin{bmatrix} t_{11}^{D_{11}} & \cdots & t_{1j}^{D_{1j}} & \cdots & t_{1m}^{D_{1m}} \\ \vdots & \vdots & \vdots & \vdots & \vdots \\ t_{i1}^{D_{i1}} & \cdots & t_{ij}^{D_{ij}} & \cdots & t_{im}^{D_{im}} \\ \vdots & \vdots & & \vdots & \vdots \\ t_{m1}^{D_{m1}} & \cdots & t_{mj}^{D_{mj}} & \cdots & t_{mm}^{D_{mm}} \end{bmatrix} \begin{array}{l} \longrightarrow d_1 = \sum_{j=1}^{m} t_{1j}^{D_{1j}} \\ \\ \longrightarrow d_i = \sum_{j=1}^{m} t_{ij}^{D_{ij}} \\ \\ \longrightarrow d_m = \sum_{j=1}^{m} t_{mj}^{D_{mj}} \end{array} \quad , d_i = \sum_{j=1}^{m} t_{ij}^{D_{ij}}, i = 1,\ldots,m$$

Normalize the relationship matrix of the whole criteria ($T_C^{\propto}$)

Normalization of T_C with the sum of the degrees of impact and effectiveness of the criteria and dimensions for obtaining $T_C^{\propto}$ as follows:

Step 4 - Analyze the results

In this step, the sum of the rows and columns of the total connection matrix is calculated separately according to the following equation.

$$T = [t_{ij}], \quad i, j \in \{1, 2, \ldots, n\}$$

$$r = [r_i]_{n\times 1} = \left[\sum_{j=1}^{n} t_{ij}\right]_{n\times 1} \qquad c = [c_j]_{1\times n} = \left[\sum_{i=1}^{n} t_{ij}\right]_{1\times n}$$

5.3 DANP technique for finding effective weights in any criterion

Normalize the communication matrix of all dimensions($T_D^{\propto}$)

The T_D matrix is obtained from the average T_C^{ij}. Ij. This matrix will be normalized according to the following method, so that the sum of each row is calculated and each element is divided by the sum of the elements of the corresponding row. The normalized $T_D$total communication matrix is shown as $T_D^{\propto}$.

$$T_C^{\alpha} = \begin{array}{c} \\ D_1 \\ \vdots \\ D_i \\ \vdots \\ D_n \end{array} \begin{array}{c} \begin{array}{cccccc} D_1 & & D_j & & D_n \\ c_{11}\ldots c_{1m_1} & \cdots & c_{j1}\ldots c_{jm_j} & \cdots & c_{n1}\ldots c_{nm_n} \end{array} \\ \begin{bmatrix} T_c^{\alpha 11} & \cdots & T_c^{\alpha 1j} & \cdots & T_c^{\alpha 1n} \\ \vdots & & \vdots & & \vdots \\ T_c^{\alpha i1} & \cdots & T_c^{\alpha ij} & \cdots & T_c^{\alpha in} \\ \vdots & & \vdots & & \vdots \\ T_c^{\alpha n1} & \cdots & T_c^{\alpha nj} & \cdots & T_c^{\alpha nn} \end{bmatrix} \end{array}$$

$$T_D^{\alpha} = \begin{bmatrix} t_{11}^{D_{11}}/d_1 & \cdots & t_{1j}^{D_{1j}}/d_1 & \cdots & t_{1m}^{D_{1m}}/d_1 \\ \vdots & \vdots & \vdots & \vdots & \vdots \\ t_{i1}^{D_{i1}}/d_i & \cdots & t_{ij}^{D_{ij}}/d_i & \cdots & t_{im}^{D_{im}}/d_i \\ \vdots & \vdots & & \vdots & \vdots \\ t_{m1}^{D_{m1}}/d_m & \cdots & t_{mj}^{D_{mj}}/d_m & \cdots & t_{mm}^{D_{mm}}/d_m \end{bmatrix} = \begin{bmatrix} t_D^{\alpha 11} & \cdots & t_D^{\alpha 1j} & \cdots & t_D^{\alpha 1n} \\ \vdots & & \vdots & & \vdots \\ t_D^{\alpha i1} & \cdots & t_D^{\alpha ij} & \cdots & t_D^{\alpha in} \\ \vdots & & \vdots & & \vdots \\ t_D^{\alpha n1} & \cdots & t_D^{\alpha nj} & \cdots & t_D^{\alpha nn} \end{bmatrix}$$

An example of how to normalize $T_C^{\propto 11}$ is described below, as are other $T_c^{\propto nm}$ calculations.

$$\mathbf{d_{ci}^{11}} = \sum_{\mathbf{j=1}}^{\mathbf{m_1}} \mathbf{t_{cij}^{11}} \ , \mathbf{i = 1, 2, \ldots, m_1}$$

$$\mathbf{T_C^{\propto 11}} = \begin{bmatrix} t_{c11}^{11}/d_{c1}^{11} & \cdots & t_{c1j}^{11}/d_{c1}^{11} & \cdots & t_{c1m1}^{11}/d_{c1}^{11} \\ \vdots & & \vdots & & \vdots \\ t_{ci1}^{11}/d_{ci}^{11} & \cdots & t_{cij}^{11}/d_{ci}^{11} & \cdots & t_{cim1}^{11}/d_{ci}^{11} \\ \vdots & & \vdots & & \vdots \\ t_{cm11}^{11}/d_{cm1}^{11} & \cdots & t_{cm1j}^{11}/d_{cm1}^{11} & \cdots & t_{cm1m1}^{11}/d_{cm1}^{11} \end{bmatrix} =$$

$$\begin{bmatrix} t_{c11}^{\propto 11} & \cdots & t_{c1j}^{\propto 11} & \cdots & t_{c1m1}^{\propto 11} \\ \vdots & & \vdots & & \vdots \\ t_{ci1}^{\propto 11} & \cdots & t_{cij}^{\propto 11} & \cdots & t_{cim1}^{\propto 11} \\ \vdots & & \vdots & & \vdots \\ t_{cm1\,1}^{\propto 11} & \cdots & t_{cm1j}^{\propto 11} & \cdots & t_{cm1m1}^{\propto 11} \end{bmatrix}$$

Form an unbalanced super matrix W

In this step, the full matrix song matrix is normalized, $T_C^{\propto}$ Is calculated, and the W matrix is obtained. For example, if a matrix such as the W^{11} matrix is empty or zero, it means that the corresponding matrices are independent.

Form a balanced super matrix

$$\mathbf{W} = (\mathbf{T_C^{\propto}})' = \begin{bmatrix} W^{11} & \cdots & W^{i1} & \cdots & W^{n1} \\ \vdots & & \vdots & & \vdots \\ W^{1j} & \cdots & W^{ij} & \cdots & W^{nj} \\ \vdots & & \vdots & & \vdots \\ W^{1n} & \cdots & W^{in} & \cdots & W^{nn} \end{bmatrix}$$

In order to form a harmonic super matrix, the normal $T_D^{\propto}$ complete communication matrix is transposed and multiplied by the unbalanced super matrix.

$$\mathbf{W^{\propto}} = \mathbf{T_D^{\propto} W} = \begin{bmatrix} t_D^{\propto 11} \times W^{11} & \cdots & t_D^{1i1} \times W^{i1} & \cdots & t_D^{\propto n1} \times W^{n1} \\ \vdots & & \vdots & & \vdots \\ t_D^{\propto 1j} \times W^{1j} & \cdots & t_D^{\propto ij} \times W^{ij} & \cdots & t_D^{\propto nj} \times W^{nj} \\ \vdots & & \vdots & & \vdots \\ t_D^{\propto 1n} \times W^{1n} & \cdots & t_D^{\propto in} \times W^{in} & \cdots & t_D^{\propto nn} \times W^{nn} \end{bmatrix}$$

Limit rhythmic super matrix

We limit the balanced super matrix by reaching a large number like Z, until the super matrix converges and stabilizes. The output of this step will be the effective DANP weights.

$$\lim_{Z \to \infty} (W^{\propto})^{Z}$$

Findings using DANP method

Table 1: Decision matrix

T(norm)	a1	a2	a3	a4	a5	a6	a7	a8	a9	a10	a11	b1	b2	b3	b4	b5	b6	b7	b8	b9	b10	b11	c1	c2	c3
a1	0	0.039	0.039	0.022	0.022	0.051	0.017	0.051	0.041	0.039	0.017	0.029	0.012	0.002	0.036	0.038	0.038	0.039	0.031	0.022	0.038	0.024	0.005	0.005	0.019
a2	0.038	0	0.010	0.026	0.007	0.019	0.031	0.041	0.027	0.039	0.031	0.033	0.041	0.009	0.034	0.034	0.034	0.039	0.031	0.038	0.041	0.019	0.026	0.024	0.024
a3	0.045	0.017	0	0.017	0.046	0.050	0.017	0.043	0.039	0.039	0.033	0.022	0.015	0	0.031	0.026	0.045	0.024	0.022	0.015	0.043	0.014	0.015	0.015	0.019
a4	0.015	0.033	0.021	0	0.015	0.021	0.033	0.050	0.024	0.019	0.017	0.045	0.034	0.017	0.038	0.038	0.050	0.043	0.043	0.041	0.046	0.024	0.022	0.021	0.026
a5	0.031	0.021	0.051	0	0	0.048	0	0.039	0.043	0.019	0.024	0.019	0	0	0.019	0.015	0.019	0.015	0.014	0.015	0.022	0.015	0.015	0.015	0.019
a6	0.055	0.019	0.050	0.019	0.045	0	0.009	0.050	0.039	0.033	0.019	0.019	0.015	0	0.017	0.017	0.039	0.036	0.036	0.024	0.043	0.015	0.015	0.015	0.024
a7	0.017	0.022	0.015	0.034	0	0.015	0	0.026	0.022	0.033	0.043	0.027	0.024	0	0.034	0.027	0.034	0.024	0.050	0.028	0.034	0.019	0	0.022	
a8	0.048	0.034	0.026	0.050	0.019	0.050	0.027	0	0.043	0.029	0.041	0.029	0.027	0.026	0.038	0.038	0.046	0.046	0.045	0.046	0.048	0.026	0.024	0.027	0.033
a9	0.048	0.019	0.036	0.009	0.019	0.031	0.017	0.050	0	0.022	0.015	0.022	0.015	0	0.026	0.031	0.029	0.024	0.033	0.021	0.039	0.019	0.017	0.017	0.024
a10	0.034	0.038	0.031	0.017	0.012	0.041	0.031	0.029	0.029	0	0.024	0.038	0.034	0.019	0.050	0.046	0.046	0.050	0.046	0.029	0.053	0.034	0.027	0.026	0.038
a11	0.021	0.024	0.033	0.007	0.019	0.015	0.050	0.027	0.007	0.010	0	0.019	0.021	0.002	0.024	0.021	0.045	0.021	0.029	0.033	0.041	0.009	0.010	0.009	0.024
b1	0.019	0.027	0.021	0.046	0.017	0.027	0.027	0.046	0.029	0.036	0.021	0	0.031	0.012	0.043	0.043	0.046	0.041	0.048	0.039	0.046	0.039	0.027	0.027	0.038
b2	0.017	0.033	0.017	0.027	0.017	0.017	0.026	0.031	0.017	0.038	0.021	0.036	0	0.034	0.043	0.041	0.033	0.031	0.055	0.043	0.043	0.027	0.031	0.045	0.038
b3	0	0.015	0	0.026	0	0.002	0.017	0.024	0	0.021	0.022	0.027	0.039	0	0.015	0.024	0.021	0.038	0.039	0.036	0.015	0.017	0.043	0.046	0.041
b4	0.022	0.027	0.021	0.034	0.015	0.015	0.027	0.043	0.027	0.051	0.024	0.043	0.034	0.019	0	0.015	0.045	0.048	0.048	0.046	0.050	0.024	0.026	0.026	0.033
b5	0.041	0.034	0.022	0.039	0.015	0.015	0.022	0.041	0.021	0.050	0.022	0.043	0.036	0.017	0.050	0	0.050	0.050	0.050	0.048	0.048	0.027	0.031	0.031	0.038
b6	0.026	0.029	0.048	0.022	0.022	0.036	0.029	0.046	0.026	0.045	0.031	0.045	0.034	0.022	0.048	0.055	0	0.031	0.034	0.045	0.053	0.027	0.038	0.033	0.045
b7	0.034	0.033	0.024	0.038	0.015	0.022	0.036	0.046	0.024	0.046	0.024	0.045	0.033	0.033	0.046	0.046	0.043	0	0.046	0.050	0.043	0.029	0.055	0.055	0.055
b8	0.031	0.038	0.029	0.026	0.021	0.019	0.046	0.041	0.038	0.034	0.039	0.015	0.041	0.036	0.046	0.045	0.050	0.038	0	0.041	0.050	0.039	0.039	0.041	0.048
b9	0.012	0.036	0.019	0.051	0.019	0.021	0.036	0.048	0.026	0.026	0.027	0.043	0.041	0.033	0.048	0.048	0.041	0.043	0.043	0	0.039	0.026	0.043	0.045	0.046
b10	0.024	0.031	0.045	0.041	0.022	0.029	0.026	0.050	0.022	0.050	0.029	0.043	0.027	0.010	0.050	0.048	0.053	0.039	0.050	0.036	0	0.027	0.026	0.022	0.039
b11	0.022	0.010	0.010	0.033	0.007	0.010	0.026	0.029	0.012	0.031	0.034	0.039	0.021	0.009	0.031	0.034	0.034	0.031	0.038	0.024	0.029	0	0.024	0.019	0.027
c1	0.005	0.015	0.005	0.038	0.003	0.007	0.027	0.017	0.010	0.031	0.034	0.045	0.039	0.039	0.043	0.048	0.048	0.050	0.051	0.048	0.039	0.031	0	0.050	0.050
c2	0.015	0.019	0	0.041	0	0.015	0.027	0.033	0.015	0.027	0.034	0.048	0.043	0.043	0.043	0.050	0.048	0.050	0.053	0.050	0.038	0.033	0.053	0	0.050
c3	0.019	0.021	0.034	0.048	0.021	0.017	0.036	0.033	0.010	0.036	0.027	0.048	0.043	0.034	0.043	0.050	0.048	0.046	0.051	0.039	0.043	0.031	0.051	0.050	0

Table 2: Normalized matrix

Criteria	a1	a2	a3	a4	a5	a6	a7	a8	a9	a10	a11	b1	b2	b3	b4	b5	b6	b7	b8	b9	b10	b11	c1	c2	c3
a1	0	2.75	2.75	1.625	1.625	3.75	1.25	3.75	3	2.875	1.25	2.125	0.875	0.125	2.625	2.75	2.75	2.875	2.25	1.625	2.75	1.75	0.375	0.375	1.375
a2	2.75	0	0.75	1.875	0.5	1.375	2.25	3	2	2.875	2.25	2.375	3	0.625	2.5	2.5	2.75	2.875	2.25	2.75	3	1.375	1.875	1.75	1.75
a3	3	1.25	0	1.25	3.375	3.625	1.25	3.125	2.875	2.875	2.375	1.625	1.125	0	2.25	1.875	3.25	1.75	1.625	1.125	3.125	1	1.125	1.125	1.375
a4	1.125	2.375	1.5	0	1.125	1.5	2.375	3.625	1.75	1.375	1.25	3.25	2.5	1.25	2.75	2.75	3.625	3.125	3.125	3	3.375	1.75	1.625	1.5	1.875
a5	2.25	1.5	3.75	0	0	3.5	0	2.875	3.125	1.375	2	1.375	0	0	1.375	1.125	1.375	1.125	1	1.125	1.625	1.125	1.125	1.125	1.375
a6	4	1.375	3.625	1.375	3.25	0	0.625	3.625	2.875	2.375	1.375	1.375	1.125	0	1.25	1.25	2.875	2.625	2.625	1.75	3.125	1.125	1.125	1.125	1.75
a7	1.25	1.625	1.125	2.5	0	1.125	0	1.875	1.625	2.375	3.125	2	1.75	0	2.5	2	2.5	1.75	3.625	2.75	2.5	1.375	0	0	1.625
a8	3.5	2.5	1.875	3.625	1.375	3.625	2	0	3.125	2.125	3	3.125	2	1.875	2.75	2.75	3.375	3.375	3.25	3.375	3.5	1.875	1.75	2	2.375
a9	3.5	1.375	2.625	0.625	1.375	2.25	1.25	3.625	0	1.625	1.125	1.625	1.125	0	1.875	2.25	2.125	1.75	2.375	0.875	2.875	1.375	1.25	1.25	1.75
a10	2.5	2.75	2.25	1.25	0.875	3	2.25	2.125	2.125	0	1.75	2.75	2.5	1.375	3.625	3.375	3.375	3.625	3.375	2.125	3.875	2.5	2	1.875	2.75
a11	1.5	1.75	2.375	0.5	1.375	1.125	3.625	2	0.5	0.75	0	1.375	1.5	0.125	1.75	1.5	3.25	1.75	3.125	2.375	3	0.625	0.75	0.625	1.75
b1	1.375	2	1.5	3.375	1.25	2	2	3.375	2.125	2.625	1.5	0	2.25	0.875	3.125	3.125	3.375	3	3.5	2.875	3.375	2.875	2	2	2.75
b2	1.25	2.375	1.25	2	1.25	1.25	1.875	2.25	1.25	2.75	1.5	2.625	0	2.5	3.125	2.5	2.375	2.25	4	3.125	3.125	2	2.25	2.5	2.75
b3	0	1.125	0	1.875	0	0.125	1.25	1.75	0	1.5	1.625	2	2.875	0	1.25	1.75	1.5	2.75	2.875	2.625	1.125	1.25	3.125	3.375	3
b4	1.625	2	1.5	2.5	1.125	1.125	2	3.125	2	3.75	1.75	3.125	2.5	1.375	0	3.625	3.75	3.25	3.5	3.375	3.625	1.75	1.875	1.875	2.375
b5	3	2.5	1.625	2.875	1.125	1.125	1.625	3	1.5	3.625	1.625	3.125	2.625	1.25	3.625	0	3.625	3.625	3.625	3.5	3.5	2	2.25	2.25	2.75
b6	1.875	2.125	3.5	3.125	1.625	2.625	2.125	3.375	1.875	3.25	2.25	3.25	2.5	1.625	3.5	4	0	2.25	2.5	3.25	3.875	2	2.75	2.75	3.25
b7	2.5	2.375	1.75	2.75	1.125	1.625	2.625	3.375	1.75	3.375	1.75	3.25	2.375	2.375	3.375	3.125	3.125	0	3.375	0.375	3.125	2.125	4	4	4
b8	2.25	2.75	2.125	1.875	1.5	1.375	3.375	3	2.75	2.5	2.875	3.75	3	2.625	3.375	3.25	3.625	2.75	0	3	3.625	2.875	4	3	3.5
b9	0.875	2.625	1.375	3.75	1.375	1.5	2.625	3.5	1.875	1.875	2	3.125	3	2.375	3.5	3.5	3	3.125	3.125	0	2.875	1.875	3.125	3.25	3.375
b10	1.75	2.25	3.25	3	1.625	2.125	1.875	3.625	1.625	3.625	2.125	3.125	2	0.75	3.625	3.5	3.875	2.875	3.625	2.625	0	2	1.875	1.625	2.875
b11	1.625	0.75	0.75	2.375	0.5	0.75	1.875	2.125	0.875	2.25	0.25	2.875	1.5	0.625	2.25	2.5	2.5	2.25	2.75	1.75	2.125	0	1.75	1.375	2
c1	0.375	1.125	0.375	2.75	0.25	0.5	2	1.25	0.75	2.25	0.25	3.25	2.875	2.875	3.125	3.5	3.5	3.625	3.75	3.5	2.875	2.25	0	3.625	3.625
c2	1.125	1.375	0	3	0	1.125	2	2.375	1.125	2	0.25	3.5	3.125	3.125	3.125	3.625	3.5	3.625	3.875	3.625	2.75	2.375	3.875	0	3.625
c3	1.375	1.5	2.5	3.5	1.5	1.25	2.625	2.375	0.75	2.625	2	3.5	3.125	2.5	3.125	3.625	3.5	3.375	3.75	2.875	3.125	2.25	3.75	3.625	0

Table 3: TC matrix

TC	a1	a2	a3	a4	a5	a6	a7	a8	a9	a10	a11	b1	b2	b3	b4	b5	b6	b7	b8	b9	b10	b11	c1	c2	c3
a1	0.71	0.22	0.11	0.13	0.07	0.12	0.05	0.15	0.22	0.15	0.05	0.13	0.05	0.05	0.14	0.14	0.15	0.14	0.05	0.12	0.15	0.06	0.05	0.18	0.11
a2	0.11	0.05	0.05	0.11	0.05	0.12	0.05	0.15	0.08	0.14	0.03	0.14	0.22	0.09	0.15	0.15	0.16	0.14	0.01	0.14	0.16	0.09	0.01	0.11	0.13
a3	0.12	0.06	0.07	0.10	0.09	0.12	0.01	0.15	0.11	0.13	0.06	0.12	0.09	0.05	0.13	0.13	0.15	0.02	0.13	0.11	0.15	0.08	0.09	0.09	0.11
a4	0.06	0.12	0.09	0.10	0.07	0.07	0.17	0.17	0.10	0.13	0.01	0.14	0.22	0.01	0.16	0.16	0.18	0.06	0.17	0.15	0.17	0.04	0.17	0.11	0.13
a5	0.09	0.07	0.11	0.06	0.04	0.07	0.15	0.12	0.09	0.09	0.07	0.09	0.06	0.04	0.08	0.09	0.00	0.09	0.09	0.08	0.10	0.05	0.09	0.07	0.09
a6	0.13	0.05	0.12	0.10	0.09	0.07	0.05	0.15	0.11	0.12	0.08	0.12	0.09	0.05	0.12	0.12	0.17	0.05	0.14	0.12	0.15	0.08	0.09	0.09	0.12
a7	0.08	0.07	0.08	0.10	0.04	0.08	0.06	0.12	0.08	0.11	0.02	0.12	0.10	0.05	0.13	0.11	0.13	0.01	0.17	0.12	0.13	0.08	0.07	0.07	0.04
a8	0.14	0.03	0.12	0.16	0.08	0.13	0.03	0.19	0.12	0.15	0.02	0.17	0.13	0.08	0.17	0.18	0.19	0.08	0.20	0.17	0.20	0.12	0.13	0.13	0.13
a9	0.13	0.05	0.10	0.10	0.06	0.09	0.08	0.14	0.06	0.10	0.07	0.11	0.09	0.08	0.17	0.12	0.13	0.01	0.14	0.08	0.15	0.08	0.07	0.09	0.07
a10	0.13	0.03	0.12	0.13	0.07	0.12	0.02	0.16	0.11	0.12	0.05	0.16	0.13	0.08	0.18	0.17	0.19	0.02	0.19	0.15	0.19	0.12	0.12	0.12	0.16
a11	0.08	0.06	0.09	0.08	0.06	0.07	0.02	0.11	0.06	0.11	0.06	0.10	0.09	0.04	0.09	0.11	0.14	0.02	0.14	0.11	0.13	0.05	0.07	0.07	0.10
b1	0.11	0.12	0.12	0.15	0.07	0.11	0.13	0.17	0.11	0.15	0.01	0.13	0.13	0.08	0.17	0.17	0.18	0.07	0.19	0.17	0.20	0.12	0.12	0.15	
b2	0.10	0.12	0.09	0.13	0.08	0.09	0.11	0.15	0.09	0.15	0.06	0.15	0.10	0.10	0.16	0.15	0.16	0.06	0.19	0.16	0.17	0.12	0.13	0.14	0.15
b3	0.06	0.08	0.06	0.10	0.07	0.06	0.08	0.11	0.06	0.10	0.04	0.11	0.11	0.05	0.10	0.11	0.12	0.12	0.16	0.12	0.10	0.08	0.11	0.12	0.12
b4	0.11	0.12	0.02	0.14	0.07	0.09	0.02	0.12	0.10	0.11	0.05	0.17	0.14	0.08	0.11	0.11	0.19	0.07	0.08	0.17	0.19	0.11	0.13	0.12	0.15
b5	0.13	0.03	0.11	0.15	0.07	0.10	0.03	0.18	0.11	0.17	0.01	0.17	0.14	0.09	0.18	0.14	0.20	0.02	0.20	0.18	0.20	0.12	0.12	0.13	0.16
b6	0.12	0.04	0.14	0.15	0.08	0.13	0.01	0.19	0.12	0.16	0.01	0.18	0.14	0.09	0.19	0.14	0.15	0.09	0.19	0.18	0.20	0.12	0.14	0.14	0.17
b7	0.14	0.04	0.12	0.16	0.08	0.12	0.04	0.19	0.14	0.18	0.02	0.19	0.15	0.11	0.19	0.20	0.20	0.15	0.21	0.19	0.20	0.13	0.17	0.16	0.19
b8	0.13	0.03	0.13	0.15	0.08	0.11	0.05	0.16	0.13	0.17	0.01	0.13	0.16	0.10	0.19	0.19	0.21	0.08	0.19	0.19	0.21	0.13	0.17	0.16	0.19
b9	0.11	0.02	0.08	0.08	0.07	0.11	0.03	0.19	0.13	0.15	0.01	0.18	0.15	0.10	0.18	0.19	0.19	0.02	0.19	0.19	0.19	0.12	0.14	0.15	0.18
b10	0.12	0.03	0.13	0.15	0.08	0.12	0.01	0.16	0.11	0.17	0.01	0.17	0.14	0.08	0.18	0.18	0.20	0.09	0.19	0.16	0.15	0.12	0.15	0.12	0.16
b11	0.11	0.08	0.07	0.12	0.05	0.07	0.09	0.01	0.01	0.11	0.05	0.13	0.09	0.06	0.12	0.13	0.13	0.01	0.14	0.11	0.13	0.06	0.02	0.11	0.11
c1	0.09	0.10	0.08	0.15	0.06	0.09	0.02	0.14	0.09	0.14	0.06	0.16	0.14	0.02	0.17	0.17	0.18	0.07	0.18	0.17	0.17	0.12	0.10	0.14	0.16
c2	0.10	0.11	0.05	0.15	0.06	0.06	0.01	0.17	0.09	0.14	0.07	0.18	0.15	0.01	0.17	0.18	0.19	0.02	0.19	0.17	0.18	0.12	0.11	0.10	0.17
c3	0.11	0.10	0.08	0.15	0.08	0.11	0.04	0.17	0.10	0.16	0.01	0.18	0.16	0.10	0.18	0.19	0.20	0.05	0.20	0.17	0.19	0.13	0.16	0.15	0.13

Table 4: TD matrix

Criteria	a	b	c
a	0/101795	0/124025	0/101532
b	0/117689	0/151299	0/138173
c	0/112881	0/164711	0/139849

Table 5:

T(norm)	a1	a2	a3	a4	a5	a6	a7	a8	a9	a10	a11	b1	b2	b3	b4	b5	b6	b7	b8	b9	b10	b11	c1	c2	c3
a1	0.00	0.04	0.04	0.02	0.02	0.05	0.02	0.05	0.04	0.04	0.02	0.03	0.01	0.00	0.04	0.04	0.04	0.04	0.03	0.02	0.04	0.02	0.01	0.01	0.02
a2	0.04	0.00	0.01	0.03	0.01	0.02	0.03	0.04	0.03	0.04	0.03	0.03	0.04	0.01	0.03	0.03	0.03	0.04	0.03	0.04	0.04	0.02	0.03	0.02	0.02
a3	0.04	0.02	0.00	0.02	0.05	0.05	0.02	0.04	0.04	0.04	0.03	0.02	0.02	0.00	0.03	0.03	0.04	0.02	0.02	0.02	0.04	0.01	0.02	0.02	0.02
a4	0.02	0.03	0.02	0.00	0.02	0.02	0.03	0.05	0.02	0.02	0.02	0.04	0.03	0.02	0.04	0.04	0.05	0.04	0.04	0.04	0.05	0.02	0.02	0.02	0.03
a5	0.03	0.02	0.05	0.00	0.00	0.05	0.00	0.04	0.04	0.02	0.02	0.02	0.00	0.00	0.02	0.02	0.02	0.02	0.01	0.02	0.02	0.02	0.02	0.02	0.02
a6	0.05	0.02	0.05	0.02	0.04	0.00	0.01	0.05	0.04	0.03	0.02	0.02	0.02	0.00	0.02	0.02	0.04	0.04	0.04	0.02	0.04	0.02	0.02	0.02	0.02
a7	0.02	0.02	0.02	0.03	0.00	0.02	0.00	0.03	0.02	0.03	0.04	0.03	0.02	0.00	0.03	0.03	0.03	0.02	0.05	0.03	0.03	0.02	0.00	0.02	
a8	0.05	0.03	0.03	0.05	0.02	0.05	0.03	0.00	0.04	0.03	0.04	0.03	0.03	0.03	0.04	0.04	0.05	0.05	0.04	0.05	0.05	0.03	0.02	0.03	0.03
a9	0.05	0.02	0.04	0.01	0.02	0.03	0.02	0.05	0.00	0.02	0.02	0.02	0.02	0.00	0.03	0.03	0.03	0.02	0.03	0.02	0.04	0.02	0.02	0.02	0.02
a10	0.03	0.04	0.03	0.02	0.01	0.04	0.03	0.03	0.03	0.00	0.02	0.04	0.03	0.02	0.05	0.05	0.05	0.05	0.05	0.03	0.05	0.03	0.03	0.03	0.04
a11	0.02	0.02	0.03	0.01	0.02	0.02	0.05	0.03	0.01	0.01	0.00	0.02	0.02	0.00	0.02	0.02	0.04	0.02	0.03	0.03	0.04	0.01	0.01	0.01	0.02
b1	0.02	0.03	0.02	0.05	0.02	0.03	0.03	0.05	0.03	0.04	0.02	0.00	0.03	0.01	0.04	0.04	0.05	0.04	0.05	0.04	0.05	0.04	0.03	0.03	0.04
b2	0.02	0.03	0.02	0.03	0.02	0.02	0.03	0.03	0.02	0.04	0.02	0.04	0.00	0.03	0.04	0.04	0.03	0.03	0.05	0.04	0.04	0.03	0.03	0.04	0.04
b3	0.00	0.02	0.00	0.03	0.00	0.00	0.02	0.02	0.00	0.02	0.02	0.03	0.04	0.00	0.02	0.02	0.02	0.04	0.04	0.04	0.02	0.02	0.04	0.05	0.04
b4	0.02	0.03	0.02	0.03	0.02	0.02	0.03	0.04	0.03	0.05	0.02	0.04	0.03	0.02	0.00	0.02	0.04	0.05	0.05	0.05	0.05	0.02	0.03	0.03	0.03
b5	0.04	0.03	0.02	0.04	0.02	0.02	0.02	0.04	0.02	0.05	0.02	0.04	0.04	0.02	0.05	0.00	0.05	0.05	0.05	0.05	0.05	0.03	0.03	0.03	0.04
b6	0.03	0.03	0.05	0.02	0.02	0.04	0.03	0.05	0.03	0.04	0.03	0.04	0.03	0.02	0.05	0.05	0.00	0.03	0.03	0.04	0.05	0.03	0.04	0.03	0.04
b7	0.03	0.03	0.02	0.04	0.02	0.02	0.04	0.05	0.02	0.05	0.02	0.04	0.03	0.03	0.05	0.05	0.04	0.00	0.05	0.05	0.04	0.03	0.05	0.05	0.05

b8	0.03	0.04	0.03	0.03	0.02	0.02	0.05	0.04	0.04	0.03	0.04	0.02	0.04	0.04	0.05	0.04	0.05	0.04	0.00	0.04	0.05	0.04	0.04	0.04	0.05
b9	0.01	0.04	0.02	0.05	0.02	0.02	0.04	0.05	0.03	0.03	0.03	0.04	0.04	0.03	0.05	0.05	0.04	0.04	0.04	0.00	0.04	0.03	0.04	0.04	0.05
b10	0.02	0.03	0.04	0.04	0.02	0.03	0.03	0.05	0.02	0.05	0.03	0.04	0.03	0.01	0.05	0.05	0.05	0.04	0.05	0.04	0.00	0.03	0.03	0.02	0.04
b11	0.02	0.01	0.01	0.03	0.01	0.01	0.03	0.03	0.01	0.03	0.03	0.04	0.02	0.01	0.03	0.03	0.03	0.03	0.04	0.02	0.03	0.00	0.02	0.02	0.03
c1	0.01	0.02	0.01	0.04	0.00	0.01	0.03	0.02	0.01	0.03	0.03	0.04	0.04	0.04	0.04	0.05	0.05	0.05	0.05	0.05	0.04	0.03	0.00	0.05	0.05
c2	0.02	0.02	0.00	0.04	0.00	0.02	0.03	0.03	0.02	0.03	0.03	0.05	0.04	0.04	0.04	0.05	0.05	0.05	0.05	0.05	0.04	0.03	0.05	0.00	0.05
c3	0.02	0.02	0.03	0.05	0.02	0.02	0.04	0.03	0.01	0.04	0.03	0.05	0.04	0.03	0.04	0.05	0.05	0.05	0.05	0.04	0.04	0.03	0.05	0.05	0.00

Table 6: D + R and D-R values for all components

TC	a1	a2	a3	a4	a5	a6	a7	a8	a9	a10	a11	b1	b2	b3	b4	b5	b6	b7	b8	b9	b10	b11	c1	c2	c3		D
a1	0.08	0.12	0.11	0.11	0.07	0.12	0.09	0.16	0.11	0.14	0.09	0.13	0.10	0.05	0.14	0.14	0.15	0.14	0.15	0.12	0.15	0.10	0.08	0.08	0.11		1.20
a2	0.11	0.08	0.08	0.12	0.06	0.09	0.11	0.15	0.10	0.14	0.10	0.14	0.13	0.06	0.15	0.15	0.16	0.15	0.15	0.14	0.16	0.09	0.11	0.11	0.13		1.15
a3	0.12	0.09	0.07	0.10	0.09	0.12	0.09	0.15	0.11	0.13	0.10	0.12	0.09	0.05	0.13	0.13	0.15	0.12	0.13	0.11	0.15	0.08	0.09	0.09	0.11		1.15
a4	0.10	0.12	0.10	0.10	0.07	0.10	0.12	0.17	0.10	0.13	0.09	0.16	0.13	0.08	0.16	0.16	0.18	0.16	0.17	0.15	0.17	0.10	0.11	0.11	0.13		1.18
a5	0.09	0.07	0.10	0.06	0.04	0.10	0.05	0.12	0.09	0.09	0.07	0.09	0.06	0.03	0.09	0.09	0.10	0.09	0.09	0.08	0.10	0.06	0.07	0.07	0.08		0.88
a6	0.13	0.09	0.12	0.10	0.09	0.07	0.08	0.15	0.11	0.12	0.08	0.12	0.09	0.05	0.12	0.12	0.15	0.13	0.14	0.12	0.15	0.08	0.09	0.09	0.12		1.16
a7	0.08	0.09	0.08	0.11	0.04	0.07	0.07	0.12	0.08	0.11	0.10	0.12	0.10	0.04	0.13	0.12	0.13	0.11	0.15	0.12	0.13	0.08	0.07	0.07	0.10		0.95
a8	0.14	0.13	0.12	0.16	0.08	0.14	0.13	0.14	0.13	0.15	0.13	0.17	0.13	0.09	0.17	0.18	0.19	0.18	0.19	0.18	0.20	0.12	0.13	0.13	0.16		1.45
a9	0.11	0.08	0.10	0.09	0.06	0.09	0.08	0.14	0.06	0.10	0.07	0.11	0.09	0.04	0.12	0.12	0.13	0.11	0.13	0.10	0.14	0.08	0.08	0.08	0.11		1.00
a10	0.13	0.13	0.12	0.13	0.07	0.12	0.12	0.16	0.11	0.12	0.11	0.16	0.14	0.08	0.18	0.18	0.19	0.18	0.19	0.15	0.19	0.12	0.12	0.12	0.16		1.32
a11	0.08	0.08	0.09	0.08	0.06	0.07	0.11	0.11	0.06	0.09	0.06	0.10	0.09	0.04	0.11	0.11	0.14	0.10	0.13	0.11	0.13	0.07	0.07	0.07	0.10		0.89
b1	0.11	0.12	0.11	0.15	0.07	0.11	0.12	0.17	0.11	0.15	0.10	0.13	0.13	0.08	0.17	0.17	0.18	0.17	0.19	0.16	0.18	0.12	0.12	0.12	0.15		1.68
b2	0.10	0.12	0.10	0.13	0.07	0.09	0.11	0.15	0.10	0.15	0.10	0.15	0.10	0.09	0.16	0.16	0.16	0.15	0.19	0.16	0.17	0.11	0.12	0.14	0.15		1.62
b3	0.06	0.08	0.06	0.10	0.04	0.06	0.08	0.11	0.06	0.10	0.08	0.11	0.11	0.05	0.10	0.11	0.12	0.12	0.14	0.12	0.11	0.08	0.11	0.11	0.12		1.18
b4	0.11	0.12	0.11	0.14	0.07	0.10	0.12	0.17	0.11	0.17	0.11	0.17	0.14	0.08	0.13	0.18	0.19	0.17	0.19	0.17	0.19	0.11	0.12	0.12	0.15		1.72
b5	0.13	0.13	0.11	0.15	0.07	0.10	0.12	0.18	0.11	0.17	0.11	0.17	0.14	0.08	0.18	0.14	0.20	0.18	0.20	0.18	0.19	0.12	0.13	0.13	0.16		1.79
b6	0.12	0.13	0.14	0.16	0.08	0.13	0.13	0.19	0.12	0.17	0.12	0.18	0.14	0.09	0.19	0.20	0.15	0.17	0.19	0.18	0.20	0.12	0.14	0.14	0.17		1.81
b7	0.13	0.14	0.12	0.16	0.08	0.12	0.14	0.19	0.12	0.18	0.12	0.19	0.15	0.11	0.19	0.20	0.20	0.15	0.21	0.19	0.20	0.13	0.16	0.16	0.19		1.90
b8	0.13	0.14	0.12	0.15	0.08	0.11	0.15	0.19	0.13	0.16	0.13	0.19	0.15	0.11	0.19	0.19	0.21	0.18	0.16	0.18	0.20	0.14	0.15	0.15	0.18		1.89
b9	0.11	0.13	0.11	0.17	0.08	0.11	0.13	0.18	0.11	0.15	0.11	0.18	0.15	0.10	0.18	0.19	0.19	0.18	0.19	0.13	0.19	0.12	0.14	0.15	0.17		1.79
b10	0.12	0.13	0.13	0.15	0.08	0.12	0.12	0.18	0.11	0.17	0.11	0.17	0.13	0.08	0.18	0.18	0.20	0.17	0.19	0.16	0.15	0.12	0.13	0.12	0.16		1.73
b11	0.08	0.08	0.07	0.11	0.05	0.07	0.09	0.12	0.07	0.11	0.06	0.13	0.09	0.05	0.12	0.13	0.13	0.12	0.14	0.11	0.13	0.06	0.09	0.09	0.11		1.21
c1	0.09	0.10	0.08	0.14	0.06	0.08	0.12	0.14	0.09	0.14	0.08	0.16	0.14	0.10	0.17	0.17	0.18	0.17	0.18	0.17	0.17	0.11	0.10	0.14	0.16		0.40
c2	0.10	0.11	0.08	0.15	0.06	0.10	0.12	0.16	0.10	0.14	0.09	0.18	0.15	0.11	0.17	0.18	0.19	0.18	0.19	0.17	0.18	0.12	0.15	0.10	0.17		0.42
c3	0.11	0.12	0.12	0.16	0.08	0.11	0.14	0.17	0.10	0.16	0.11	0.18	0.15	0.10	0.18	0.19	0.20	0.18	0.20	0.17	0.19	0.13	0.16	0.15	0.13		0.44

R	1.16	1.09	1.09	1.16	0.72	1.09	1.05	1.57	1.07	1.14	1.00	1.77	1.44	0.92	1.81	1.85	1.93	1.75	1.96	1.74	1.92	1.22	0.40	0.40	0.46		
D+R	2.36	2.23	2.24	2.34	1.60	2.25	2.01	3.02	2.07	2.63	1.89	3.45	3.06	2.09	3.53	3.64	3.74	3.65	3.86	3.52	3.65	2.44	0.80	0.82	0.90		
D-R	0.04	0.06	0.06	0.02	0.15	0.06	0.10	0.12	0.75	0.00	0.10	0.88	0.18	0.26	0.97	0.62	0.13	0.15	0.69	0.05	0.18	0.90	0.32	0.02	0.21		

Table 7: D + R and D-R values for model components

Ceriteria	C1	C2	C3	D
C1	0.101795	0.124025	0.101532	0.327352
C2	0.117689	0.151299	0.138173	0.407162
C3	0.112881	0.164711	0.139849	0.41744
R	0.332365	0.440035	0.379554	
D+R	0.659717	0.847197	0.796995	
D-R	-0.00501	-0.03287	0.037886	

Figure 2: Impact and impact of the dimensions and components of the research model

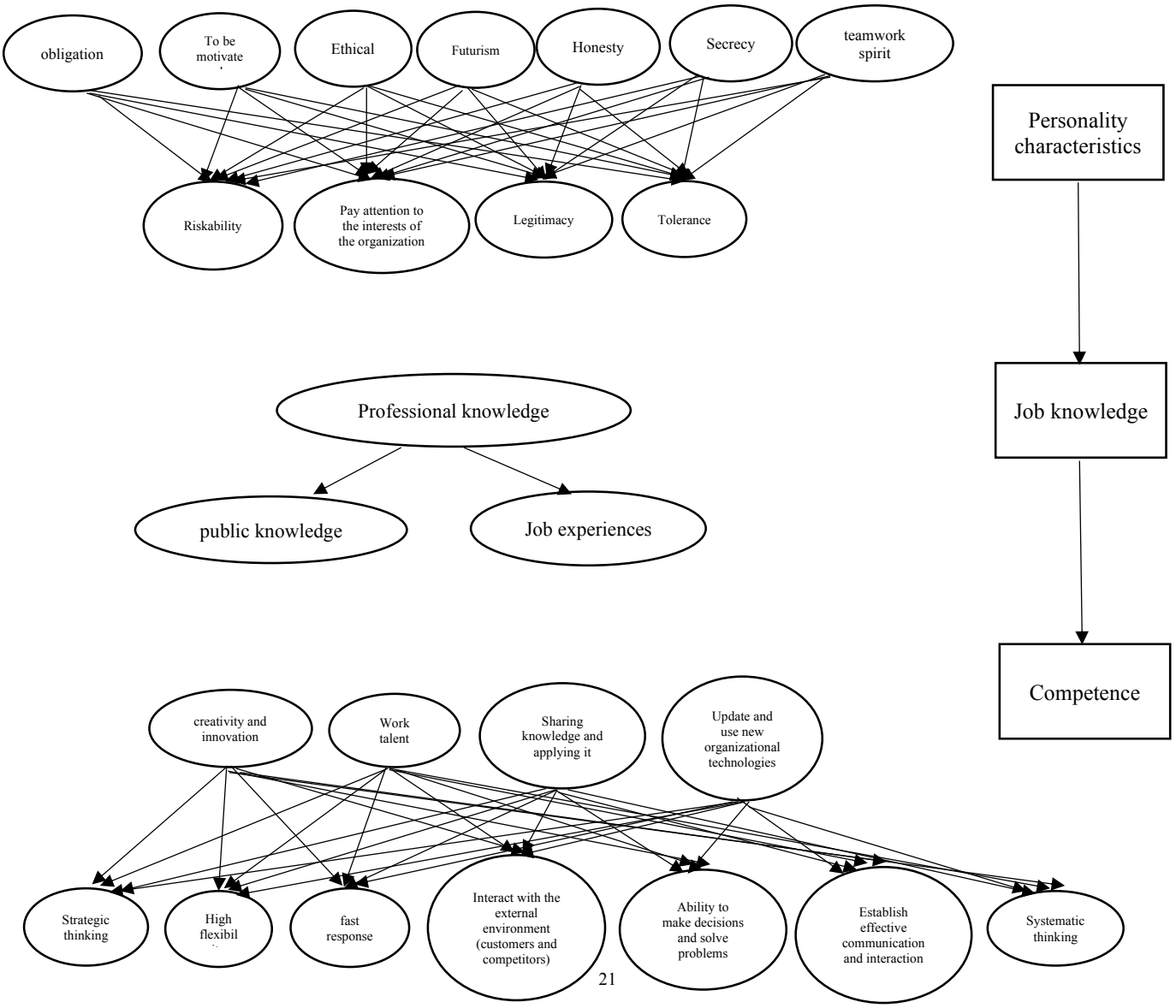

Table 8: Normalized total communication matrix

Ceriteria	C1	C2	C3
C1	0.310965	0.378875	0.31016
C2	0.289048	0.371594	0.339358
C3	0.270411	0.394573	0.335016

Table 9: Transposed normal total communication matrix

Ceriteria	C1	C2	C3
C1	0.310965	0.289048	0.270411
C2	0.378875	0.371594	0.394573
C3	0.31016	0.339358	0.335016

Table 10: Normalized communication matrix of all indicators

	a1	a2	a3	a4	a5	a6	a7	a8	a9	a10	a11	b1	b2	b3	b4	b5	b6	b7	b8	b9	b10	b11	c1	c2	c3
a1	0.08	0.12	0.11	0.11	0.07	0.12	0.09	0.16	0.11	0.14	0.09	0.13	0.10	0.05	0.14	0.14	0.15	0.14	0.15	0.12	0.15	0.10	0.08	0.08	0.11
a2	0.11	0.08	0.08	0.12	0.06	0.09	0.11	0.15	0.10	0.14	0.10	0.14	0.13	0.06	0.15	0.15	0.16	0.15	0.15	0.14	0.16	0.09	0.11	0.11	0.13
a3	0.12	0.09	0.07	0.10	0.09	0.12	0.09	0.15	0.11	0.13	0.10	0.12	0.09	0.05	0.13	0.13	0.15	0.12	0.13	0.11	0.15	0.08	0.09	0.09	0.11
a4	0.10	0.12	0.10	0.10	0.07	0.10	0.12	0.17	0.10	0.13	0.09	0.16	0.13	0.08	0.16	0.16	0.18	0.16	0.17	0.15	0.17	0.10	0.11	0.11	0.13
a5	0.09	0.07	0.10	0.06	0.04	0.10	0.05	0.12	0.09	0.09	0.07	0.09	0.06	0.03	0.09	0.09	0.10	0.09	0.09	0.08	0.10	0.06	0.07	0.07	0.08
a6	0.13	0.09	0.12	0.10	0.09	0.07	0.08	0.15	0.11	0.12	0.08	0.12	0.09	0.05	0.12	0.12	0.15	0.13	0.14	0.12	0.15	0.08	0.09	0.09	0.12
a7	0.08	0.09	0.08	0.11	0.04	0.07	0.07	0.12	0.08	0.11	0.10	0.12	0.10	0.04	0.13	0.12	0.13	0.11	0.15	0.12	0.13	0.08	0.07	0.07	0.10
a8	0.14	0.13	0.12	0.16	0.08	0.14	0.13	0.14	0.13	0.15	0.13	0.17	0.13	0.09	0.17	0.18	0.19	0.18	0.19	0.18	0.20	0.12	0.13	0.13	0.16
a9	0.11	0.08	0.10	0.09	0.06	0.09	0.08	0.14	0.06	0.10	0.07	0.11	0.09	0.04	0.12	0.12	0.13	0.11	0.13	0.10	0.14	0.08	0.08	0.08	0.11
a10	0.13	0.13	0.12	0.13	0.07	0.12	0.12	0.16	0.11	0.12	0.11	0.16	0.14	0.08	0.18	0.18	0.19	0.18	0.19	0.15	0.19	0.12	0.12	0.12	0.16
a11	0.08	0.08	0.09	0.08	0.06	0.07	0.01	0.11	0.06	0.09	0.06	0.10	0.09	0.04	0.11	0.11	0.14	0.10	0.13	0.11	0.13	0.07	0.07	0.07	0.10
b1	0.11	0.12	0.11	0.15	0.07	0.11	0.12	0.17	0.11	0.15	0.10	0.13	0.13	0.08	0.17	0.17	0.18	0.17	0.19	0.16	0.18	0.12	0.12	0.12	0.15
b2	0.10	0.12	0.10	0.13	0.07	0.09	0.11	0.15	0.10	0.15	0.10	0.15	0.10	0.09	0.16	0.16	0.16	0.15	0.19	0.16	0.17	0.11	0.12	0.14	0.15
b3	0.06	0.08	0.06	0.10	0.04	0.06	0.08	0.11	0.06	0.10	0.08	0.11	0.11	0.05	0.10	0.11	0.12	0.12	0.14	0.12	0.11	0.08	0.11	0.11	0.12
b4	0.11	0.12	0.11	0.14	0.07	0.10	0.12	0.17	0.11	0.17	0.11	0.17	0.14	0.08	0.13	0.18	0.19	0.17	0.19	0.17	0.19	0.11	0.12	0.12	0.15
b5	0.13	0.13	0.11	0.15	0.07	0.10	0.12	0.18	0.11	0.17	0.11	0.17	0.14	0.08	0.18	0.14	0.20	0.18	0.20	0.18	0.19	0.12	0.13	0.13	0.16
b6	0.12	0.13	0.14	0.16	0.08	0.13	0.13	0.19	0.12	0.17	0.12	0.18	0.14	0.09	0.19	0.20	0.15	0.17	0.19	0.18	0.20	0.12	0.14	0.14	0.17
b7	0.13	0.14	0.12	0.16	0.08	0.12	0.14	0.19	0.12	0.18	0.12	0.19	0.15	0.11	0.19	0.20	0.20	0.15	0.21	0.19	0.20	0.13	0.16	0.16	0.19
b8	0.13	0.14	0.12	0.15	0.08	0.11	0.15	0.19	0.13	0.16	0.13	0.19	0.15	0.11	0.19	0.19	0.21	0.18	0.16	0.18	0.20	0.14	0.15	0.15	0.18
b9	0.11	0.13	0.11	0.17	0.08	0.11	0.13	0.18	0.11	0.15	0.11	0.18	0.15	0.10	0.18	0.19	0.19	0.18	0.19	0.13	0.19	0.12	0.14	0.15	0.17

b10	0.12	0.13	0.13	0.15	0.08	0.12	0.12	0.18	0.11	0.17	0.11	0.17	0.13	0.08	0.18	0.18	0.20	0.17	0.19	0.16	0.15	0.12	0.13	0.12	0.16
b11	0.08	0.08	0.07	0.11	0.05	0.07	0.09	0.12	0.07	0.11	0.06	0.13	0.09	0.05	0.12	0.13	0.13	0.12	0.14	0.11	0.13	0.06	0.09	0.09	0.11
c1	0.09	0.10	0.08	0.14	0.06	0.08	0.12	0.14	0.09	0.14	0.08	0.16	0.14	0.10	0.17	0.17	0.18	0.17	0.18	0.17	0.17	0.11	0.10	0.14	0.16
c2	0.10	0.11	0.08	0.15	0.06	0.10	0.12	0.16	0.10	0.14	0.09	0.18	0.15	0.11	0.17	0.18	0.19	0.18	0.19	0.17	0.18	0.12	0.15	0.10	0.17
c3	0.11	0.12	0.12	0.16	0.08	0.11	0.14	0.17	0.10	0.16	0.11	0.18	0.15	0.10	0.18	0.19	0.20	0.18	0.20	0.17	0.19	0.13	0.16	0.15	0.13

Table 11: Uneven Super Matrix

TC	a1	a2	a3	a4	a5	a6	a7	a8	a9	a10	a11	b1	b2	b3	b4	b5	b6	b7	b8	b9	b10	b11	c1	c2	c3
0.08	0.08	0.12	0.11	0.11	0.07	0.12	0.09	0.16	0.11	0.14	0.09	0.13	0.10	0.05	0.14	0.14	0.15	0.14	0.15	0.12	0.15	0.10	0.08	0.08	0.11
0.11	0.11	0.08	0.08	0.12	0.06	0.09	0.11	0.15	0.10	0.14	0.10	0.14	0.13	0.06	0.15	0.15	0.16	0.15	0.15	0.14	0.16	0.09	0.11	0.11	0.13
0.12	0.12	0.09	0.07	0.10	0.09	0.12	0.09	0.15	0.11	0.13	0.10	0.12	0.09	0.05	0.13	0.13	0.15	0.12	0.13	0.11	0.15	0.08	0.09	0.09	0.11
0.10	0.10	0.12	0.10	0.10	0.07	0.10	0.12	0.17	0.10	0.13	0.09	0.16	0.13	0.08	0.16	0.16	0.18	0.16	0.17	0.15	0.17	0.10	0.11	0.11	0.13
0.09	0.09	0.07	0.10	0.06	0.04	0.10	0.05	0.12	0.09	0.09	0.07	0.09	0.06	0.03	0.09	0.09	0.10	0.09	0.09	0.08	0.10	0.06	0.07	0.07	0.08
0.13	0.13	0.09	0.12	0.10	0.09	0.07	0.08	0.15	0.11	0.12	0.08	0.12	0.09	0.05	0.12	0.12	0.15	0.13	0.14	0.12	0.15	0.08	0.09	0.09	0.12
0.08	0.08	0.09	0.08	0.11	0.04	0.07	0.07	0.12	0.08	0.11	0.10	0.12	0.10	0.04	0.13	0.12	0.13	0.11	0.15	0.12	0.13	0.08	0.07	0.07	0.10
0.14	0.14	0.13	0.12	0.16	0.08	0.14	0.13	0.14	0.13	0.15	0.13	0.17	0.13	0.09	0.17	0.18	0.19	0.18	0.19	0.18	0.20	0.12	0.13	0.13	0.16
0.11	0.11	0.08	0.10	0.09	0.06	0.09	0.08	0.14	0.06	0.10	0.07	0.11	0.09	0.04	0.12	0.12	0.13	0.11	0.13	0.10	0.14	0.08	0.08	0.08	0.11
0.13	0.13	0.13	0.12	0.13	0.07	0.12	0.12	0.16	0.11	0.12	0.11	0.16	0.14	0.08	0.18	0.18	0.19	0.18	0.19	0.15	0.19	0.12	0.12	0.12	0.16
0.08	0.08	0.08	0.09	0.08	0.06	0.07	0.01	0.11	0.06	0.09	0.06	0.10	0.09	0.04	0.11	0.11	0.14	0.10	0.13	0.11	0.13	0.07	0.07	0.07	0.10
0.11	0.11	0.12	0.11	0.15	0.07	0.11	0.12	0.17	0.11	0.15	0.10	0.13	0.13	0.08	0.17	0.17	0.18	0.17	0.19	0.16	0.18	0.12	0.12	0.12	0.15
0.10	0.10	0.12	0.10	0.13	0.07	0.09	0.11	0.15	0.10	0.15	0.10	0.15	0.10	0.09	0.16	0.16	0.16	0.15	0.19	0.16	0.17	0.11	0.12	0.14	0.15
0.06	0.06	0.08	0.06	0.10	0.04	0.06	0.08	0.11	0.06	0.10	0.08	0.11	0.11	0.05	0.10	0.11	0.12	0.12	0.14	0.12	0.11	0.08	0.11	0.11	0.12
0.11	0.11	0.12	0.11	0.14	0.07	0.10	0.12	0.17	0.11	0.17	0.11	0.17	0.14	0.08	0.13	0.18	0.19	0.17	0.19	0.17	0.19	0.11	0.12	0.12	0.15
0.13	0.13	0.13	0.11	0.15	0.07	0.10	0.12	0.18	0.11	0.17	0.11	0.17	0.14	0.08	0.18	0.14	0.20	0.18	0.20	0.18	0.19	0.12	0.13	0.13	0.16
0.12	0.12	0.13	0.14	0.16	0.08	0.13	0.13	0.19	0.12	0.17	0.12	0.18	0.14	0.09	0.19	0.20	0.15	0.17	0.19	0.18	0.20	0.12	0.14	0.14	0.17
0.13	0.13	0.14	0.12	0.16	0.08	0.12	0.14	0.19	0.12	0.18	0.12	0.19	0.15	0.11	0.19	0.20	0.20	0.15	0.21	0.19	0.20	0.13	0.16	0.16	0.19
0.13	0.13	0.14	0.12	0.15	0.08	0.11	0.15	0.19	0.13	0.16	0.13	0.19	0.15	0.11	0.19	0.19	0.21	0.18	0.16	0.18	0.20	0.14	0.15	0.15	0.18
0.11	0.11	0.13	0.11	0.17	0.08	0.11	0.13	0.18	0.11	0.15	0.11	0.18	0.15	0.10	0.18	0.19	0.19	0.18	0.19	0.13	0.19	0.12	0.14	0.15	0.17

0.12	0.12	0.13	0.13	0.15	0.08	0.12	0.12	0.18	0.11	0.17	0.11	0.17	0.13	0.08	0.18	0.18	0.20	0.17	0.19	0.16	0.15	0.12	0.13	0.12	0.16
0.08	0.08	0.08	0.07	0.11	0.05	0.07	0.09	0.12	0.07	0.11	0.06	0.13	0.09	0.05	0.12	0.13	0.13	0.12	0.14	0.11	0.13	0.06	0.09	0.09	0.11
0.09	0.09	0.10	0.08	0.14	0.06	0.08	0.12	0.14	0.09	0.14	0.08	0.16	0.14	0.10	0.17	0.17	0.18	0.17	0.18	0.17	0.17	0.11	0.10	0.14	0.16
0.10	0.10	0.11	0.08	0.15	0.06	0.10	0.12	0.16	0.10	0.14	0.09	0.18	0.15	0.11	0.17	0.18	0.19	0.18	0.19	0.17	0.18	0.12	0.15	0.10	0.17
0.11	0.11	0.12	0.12	0.16	0.08	0.11	0.14	0.17	0.10	0.16	0.11	0.18	0.15	0.10	0.18	0.19	0.20	0.18	0.20	0.17	0.19	0.13	0.16	0.15	0.13

Table 12: Weighted Super Matrix

Criteria	a1	a2	a3	a4	a5	a6	a7	a8	a9	a10	a11	b1	b2	b3	b4	b5	b6	b7	b8	b9	b10	b11	c1	c2	c3
TC	0.08	0.12	0.11	0.11	0.07	0.12	0.09	0.16	0.11	0.14	0.09	0.13	0.10	0.05	0.14	0.14	0.15	0.14	0.15	0.12	0.15	0.10	0.08	0.08	0.11
a1	0.08	0.12	0.11	0.11	0.07	0.12	0.09	0.16	0.11	0.14	0.09	0.13	0.10	0.05	0.14	0.14	0.15	0.14	0.15	0.12	0.15	0.10	0.08	0.08	0.11
a2	0.11	0.08	0.08	0.12	0.06	0.09	0.11	0.15	0.10	0.14	0.10	0.14	0.13	0.06	0.15	0.15	0.16	0.15	0.15	0.14	0.16	0.09	0.11	0.11	0.13
a3	0.12	0.09	0.07	0.10	0.09	0.12	0.09	0.15	0.11	0.13	0.10	0.12	0.09	0.05	0.13	0.13	0.15	0.12	0.13	0.11	0.15	0.08	0.09	0.09	0.11
a4	0.10	0.12	0.10	0.10	0.07	0.10	0.12	0.17	0.10	0.13	0.09	0.16	0.13	0.08	0.16	0.16	0.18	0.16	0.17	0.15	0.17	0.10	0.11	0.11	0.13
a5	0.09	0.07	0.10	0.06	0.04	0.10	0.05	0.12	0.09	0.09	0.07	0.09	0.06	0.03	0.09	0.09	0.10	0.09	0.09	0.08	0.10	0.06	0.07	0.07	0.08
a6	0.13	0.09	0.12	0.10	0.09	0.07	0.08	0.15	0.11	0.12	0.08	0.12	0.09	0.05	0.12	0.12	0.15	0.13	0.14	0.12	0.15	0.08	0.09	0.09	0.12
a7	0.08	0.09	0.08	0.11	0.04	0.07	0.07	0.12	0.08	0.11	0.10	0.12	0.10	0.04	0.13	0.12	0.13	0.11	0.15	0.12	0.13	0.08	0.07	0.07	0.10
a8	0.14	0.13	0.12	0.16	0.08	0.14	0.13	0.14	0.13	0.15	0.13	0.17	0.13	0.09	0.17	0.18	0.19	0.18	0.19	0.18	0.20	0.12	0.13	0.13	0.16
a9	0.11	0.08	0.10	0.09	0.06	0.09	0.08	0.14	0.06	0.10	0.07	0.11	0.09	0.04	0.12	0.12	0.13	0.11	0.13	0.10	0.14	0.08	0.08	0.08	0.11
a10	0.13	0.13	0.12	0.13	0.07	0.12	0.12	0.16	0.11	0.12	0.11	0.16	0.14	0.08	0.18	0.18	0.19	0.18	0.19	0.15	0.19	0.12	0.12	0.12	0.16
a11	0.08	0.08	0.09	0.08	0.06	0.07	0.01	0.11	0.06	0.09	0.06	0.10	0.09	0.04	0.11	0.11	0.14	0.10	0.13	0.11	0.13	0.07	0.07	0.07	0.10
b1	0.11	0.12	0.11	0.15	0.07	0.11	0.12	0.17	0.11	0.15	0.10	0.13	0.13	0.08	0.17	0.17	0.18	0.17	0.19	0.16	0.18	0.12	0.12	0.12	0.15
b2	0.10	0.12	0.10	0.13	0.07	0.09	0.11	0.15	0.10	0.15	0.10	0.15	0.10	0.09	0.16	0.16	0.16	0.15	0.19	0.16	0.17	0.11	0.12	0.14	0.15
b3	0.06	0.08	0.06	0.10	0.04	0.06	0.08	0.11	0.06	0.10	0.08	0.11	0.11	0.05	0.10	0.11	0.12	0.12	0.14	0.12	0.11	0.08	0.11	0.11	0.12
b4	0.11	0.12	0.11	0.14	0.07	0.10	0.12	0.17	0.11	0.17	0.11	0.17	0.14	0.08	0.13	0.18	0.19	0.17	0.19	0.17	0.19	0.11	0.12	0.12	0.15
b5	0.13	0.13	0.11	0.15	0.07	0.10	0.12	0.18	0.11	0.17	0.11	0.17	0.14	0.08	0.18	0.14	0.20	0.18	0.20	0.18	0.19	0.12	0.13	0.13	0.16
b6	0.12	0.13	0.14	0.16	0.08	0.13	0.13	0.19	0.12	0.17	0.12	0.18	0.14	0.09	0.19	0.20	0.15	0.17	0.19	0.18	0.20	0.12	0.14	0.14	0.17
b7	0.13	0.14	0.12	0.16	0.08	0.12	0.14	0.19	0.12	0.18	0.12	0.19	0.15	0.11	0.19	0.20	0.20	0.15	0.21	0.19	0.20	0.13	0.16	0.16	0.19
b8	0.13	0.14	0.12	0.15	0.08	0.11	0.15	0.19	0.13	0.16	0.13	0.19	0.15	0.11	0.19	0.19	0.21	0.18	0.16	0.18	0.20	0.14	0.15	0.15	0.18
b9	0.11	0.13	0.11	0.17	0.08	0.11	0.13	0.18	0.11	0.15	0.11	0.18	0.15	0.10	0.18	0.19	0.19	0.18	0.19	0.13	0.19	0.12	0.14	0.15	0.17
b10	0.12	0.13	0.13	0.15	0.08	0.12	0.12	0.18	0.11	0.17	0.11	0.17	0.13	0.08	0.18	0.18	0.20	0.17	0.19	0.16	0.15	0.12	0.13	0.12	0.16
b11	0.08	0.08	0.07	0.11	0.05	0.07	0.09	0.12	0.07	0.11	0.06	0.13	0.09	0.05	0.12	0.13	0.13	0.12	0.14	0.11	0.13	0.06	0.09	0.09	0.11
c1	0.09	0.10	0.08	0.14	0.06	0.08	0.12	0.14	0.09	0.14	0.08	0.16	0.14	0.10	0.17	0.17	0.18	0.17	0.18	0.17	0.17	0.11	0.10	0.14	0.16
c2	0.10	0.11	0.08	0.15	0.06	0.10	0.12	0.16	0.10	0.14	0.09	0.18	0.15	0.11	0.17	0.18	0.19	0.18	0.19	0.17	0.18	0.12	0.15	0.10	0.17
c3	0.11	0.12	0.12	0.16	0.08	0.11	0.14	0.17	0.10	0.16	0.11	0.18	0.15	0.10	0.18	0.19	0.20	0.18	0.20	0.17	0.19	0.13	0.16	0.15	0.13

Table 13: Weight and dimensions of human capital using DANP method

Component level	**Component size**	**Component**		**Dimensions level**	**Dimensions size**	**Dimensions**	
19	0.02506	obligation	a1	3	0/289247	Personality characteristics	A
17	0.026035	To be motivated	a2				
20	0.024	Ethical	a3				
14	0.03163	Futurism	a4				
25	0.015875	Honesty	a5				
22	0.023298	Secrecy	a6				
16	0.026992	Riskability	a7				
9	0.037028	Pay attention to the interests of the organization	a8				
21	0.023422	Legitimacy	a9				
13	0.033121	teamwork spirit	a10				
23	0.022786	Tolerance	a11				
11	0.03657	Strategic thinking	b1	1	0/381271	Competence	B
15	0.029872	creativity and innovation	b2				
24	0.01915	Work talent	b3				

8	0.037397	High flexibility	b4				
7	0.038304	fast response	b5				
5	0.040722	Interact with the external environment (customers and competitors)	b6				
10	0.03696	Knowledge sharing and knowledge application	b7				
4	0.040998	Ability to make decisions and solve problems	b8				
12	0.035914	Update and use new organizational technologies	b9				
6	0.04011	Establish effective communication and interaction	b10				
18	0.025273	Systematic thinking	b11				
2	0.103184	public knowledge	C1	2	0.329482	Job knowledge	C
3	0.102666	Professional knowledge	C2				
1	0.123632	Job experiences	C3				

6. Conclusion

The main purpose of the research is to present the model of intellectual capital in law of Marine Agile Project-Oriented Organizations and prioritize factors using the dump method. The study consists of three components and twenty-five indicators that can be used as a basis for human capital in agile project-based organizations. The results showed that the dimension of job knowledge is influential and the dimensions of competence and personality traits are influential. In terms of personality traits, the components (commitment, motivation, morality, foresight, honesty, confidentiality, teamwork spirit) are influential and the components (risk-taking, attention to the interests of the organization, tolerance, legalism) are influential. In terms of competence, the components (updating and using new organizational technologies, knowledge sharing and application, work talent, creativity and innovation) are effective and the components (strategic thinking, high flexibility, fast response, interaction with the external environment (Customers and competitors), decision-making and problem-solving ability, systemic thinking, effective communication and interaction) are effective. In terms of job knowledge, the component of specialized knowledge is influential and the components (general knowledge, job experience) are influential. According to the final weight of the dimensions and components, their ranking was done. Competence is the most important dimension, followed by job knowledge and personality traits. Also, in the components of the research model, the components of job experience, general knowledge and specialized knowledge have the first, second and third ranks, respectively. The components of decision-making and problem-solving ability, interaction with the external environment (customers and competitors), communication and effective interactions have the fourth, fifth and sixth ranks, respectively. The components of rapid response, high flexibility and attention to the interests of the organization are ranked seventh, eighth and ninth, respectively. Components of knowledge sharing and its application, strategic thinking, updating and using new organizational technologies, teamwork spirit, foresight, creativity and innovation, risk-taking, motivation, systemic thinking, commitment, core ethics, legalism, Secrecy, tolerance, talent, honesty are ranked tenth to twenty-fifth, respectively.

Challenges and solutions of human capital in agile project-based organizations

It takes a lot of time and money to get the right human capital with the goals of an organization, so you need to have a special and strategic view of human capital. The most important challenge is the lack of proper understanding of human capital in Marine Agile Project-Oriented Organizations, because thought has been underestimated. According to the results of this study, as the next components of competence such as work talent, creativity and innovation, decision-making ability and problem solving, etc., people are valued. The next components of personality traits such as secrecy and legality, etc. are also very important. Therefore, in order to change the attitude of the senior management of the organization, it is necessary to train the managers and plan to hold training courses for the managers.

One of the organizational is to know the performance status of employees, and to achieve this, it is necessary to establish a performance appraisal system. Therefore, due to the low component of motivation in human capital, it is necessary to pay more attention to employee motivation in this system.

Some experts are reluctant to join the organization or are motivated to stay or people who have just entered the organization and need special expertise, after being trained in that particular course, if they are not motivated enough to continue working together, they are no longer willing to cooperate and go out of the

organization. Therefore, the weakness of the necessary attractions and motivational systems and mechanisms for the use of specialized personnel and the maintenance of specialized human capital is one of the problems of human capital. By designing motivational systems and mechanisms such as increasing salaries and benefits, rewards, rewards, providing ideas and opportunities, the possibility of career advancement based on people's abilities and competencies, the possibility of participating in organizational decisions that can cause It creates a sense of belonging to the organization, maintains a high level of human capital satisfaction, and strives to maintain it. Considering that the component of job knowledge has a favorable situation in the organization, solutions have been proposed for the survival and growth of the expertise and expertise of the employees. One of the factors influencing the survival and growth of the company is the expertise and expertise of employees, and to achieve this, a history of service in the current job is essential, so it is necessary to use employees with a high service record in related jobs. Another factor affecting the growth and survival of the company is in-service training of employees, and to meet this issue, training needs assessment is essential. Therefore, in order to increase the level of learning, it is necessary to use a new and more effective needs assessment method. Employee in-service training is also an important factor, and the use of reputable suppliers and training centers is essential to achieve this. It is necessary to periodically evaluate suppliers and use educational technology and modern equipment and technologies in the field of education.

The development of information systems is another change and for this development, the necessary hardware and software platform must be provided and the functional processes must be provided. Also, due to the importance and necessity of communication in recent years, this will increase organizational interactions.

If effective communication and interaction in the organization increases, outsourcing projects can be done by defeating smaller projects. It is also important for the organization and interaction of individuals and organizations in the organization, both on and off the Internet.

Refrences

Afsar, B., & Badir, Y. (2017). Workplace spirituality, perceived organizational support and innovative work behavior. *Journal of workplace Learning*.

Aldrich, D. P., & Meyer, M. A. (2015). Social capital and community resilience. *American behavioral scientist, 59*(2), 254-269.

Andzulis, J. M., Panagopoulos, N. G., & Rapp, A. (2012). A review of social media and implications for the sales process. *Journal of Personal Selling & Sales Management, 32*(3), 305-316.

Armstrong, M., & Taylor, S. (2020). *Armstrong's handbook of human resource management practice*: Kogan Page Publishers.

Azeez, R. O. (2015). The Mediating Impact of Emotional Intelligence and Brainwriting Creativity Skill Training Programmes in Enhancing Peacebugilding Skills among Secondary School Students. *Editorial Board*, 11.

Bailey, A. A., Albassami, F., & Al-Meshal, S. (2016). The roles of employee job satisfaction and organizational commitment in the internal marketing-employee bank identification relationship. *International Journal of Bank Marketing*.

Birasnav, M., Rangnekar, S., & Dalpati, A. (2011). Transformational leadership and human capital benefits: The role of knowledge management. *Leadership & Organization Development Journal*.

Casey, D., & Sieber, S. (2016). Employees, sustainability and motivation: Increasing employee engagement by addressing sustainability and corporate social responsibility.

Research in Hospitality Management, 6(1), 69-76.

Cattani, G., Ferriani, S., Frederiksen, L., & Täube, F. (2011). Project-based organizing and strategic management: A long-term research agenda on temporary organizational forms. *Advances in Strategic Management, 28*(3-26).

Cetin, G., Demirciftci, T., & Bilgihan, A. (2016). Meeting revenue management challenges: Knowledge, skills and abilities. *International Journal of Hospitality Management, 57*, 132-142.

Chang, S., Gong, Y., Way, S. A., & Jia, L. (2013). Flexibility-oriented HRM systems, absorptive capacity, and market responsiveness and firm innovativeness. *Journal of Management, 39*(7), 1924-1951.

Charan, R. (2017). *The High-potential Leader: How to Grow Fast, Take on New Responsibilities, and Make an Impact*: John Wiley & Sons.

Decker, C. (2018). Utility and regulatory decision-making under conditions of uncertainty: Balancing resilience and affordability. *Utilities Policy, 51*, 51-60.

Dhir, K. S. (2019). Contribution of language to the creation of corporate social capital. *Revista Internacional de Organizaciones*(23), 243-263.

Dobson, T., Rose, A., Parton, G., & Hart, M. (2020). Boundary crossing in school governing bodies: Perspectives from the business community. *Educational Management Administration & Leadership, 48*(3), 532-548.

Ekambaram, A., Sørensen, A. Ø., Bull-Berg, H., & Olsson, N. O. (2018). The role of big data and knowledge management in improving projects and project-based organizations. *Procedia computer science, 138*, 851-858.

Enalls-Fenner, T. (2015). *Exploring appreciative intelligence competencies for small business leadership during stressful situations.* Colorado Technical University,

Gemünden, H. G., Lehner, P., & Kock, A. (2018). The project-oriented organization and its contribution to innovation. *International Journal of Project Management, 36*(1), 147-160.

Gendron, B., Kouremenou, E.-S., & Rusu, C. (2016). Emotional Capital Development, Positive Psychology and Mindful Teaching: Which Links? *International Journal of emotional education, 8*(1), 63-74.

Ghajargar, M., Zenezini, G., & Montanaro, T. (2016). Home delivery services: innovations and emerging needs. *IFAC-PapersOnLine, 49*(12), 1371-1376.

Hamalainen, T., Kosonen, M., & Doz, Y. L. (2012). Strategic agility in public management.

Harden, R. M., Laidlaw, J. M., & Mmed, D. (2020). *Essential skills for a medical teacher: an introduction to teaching and learning in medicine*: Elsevier.

Hislop, D., Bosua, R., & Helms, R. (2018). *Knowledge management in organizations: A critical introduction*: Oxford university press.

Hong, E. N. C., Hao, L. Z., Kumar, R., Ramendran, C., & Kadiresan, V. (2012). An effectiveness of human resource management practices on employee retention in institute of higher learning: A regression analysis. *International journal of business research and management, 3*(2), 60-79.

Karamustafaoğlu, S. (2011). Improving the science process skills ability of science student teachers using I diagrams. *International Journal of Physics & Chemistry Education, 3*(1), 26-38.

Kashi, K. (2017). Proposal of Employee Training and Development System in a Middle Size Automotive Company by Utilizing Competency Model and Multiple Criteria Decision Making Methods.

Kerzner, H. (2017). *Project management: a systems approach to planning, scheduling, and controlling*: John Wiley & Sons.

Kleitman, S., Stankov, L., Allwood, C. M., Young, S., & Mak, K. K. L. (2012). Metacognitive self-confidence in school-aged children. In *Self-directed learning oriented assessments in the Asia-Pacific* (pp. 139-153): Springer.

Laureiro-Martínez, D., & Brusoni, S. (2018). Cognitive flexibility and adaptive decision-making: Evidence from a laboratory study of expert decision makers. *Strategic Management Journal, 39*(4), 1031-1058.

Lin, Y.-H., & Chen, Y.-S. (2017). Determinants of green competitive advantage: the roles of

green knowledge sharing, green dynamic capabilities, and green service innovation. *Quality & Quantity, 51*(4), 1663-1685.

Liu, W., Zhang, P., Liao, J., Hao, P., & Mao, J. (2016). Abusive supervision and employee creativity. *Management Decision*.

Nafei, W. A. (2016). The role of organizational agility in enhancing organizational excellence: A study on telecommunications sector in Egypt. *International Journal of Business and Management, 11*(4), 121-135.

Nayak, T. (2016). *Impact of Quality of Work Life on Turnover Intention: A Study on Private Health Care Units in Odisha.*

Pemsel, S., Müller, R., & Söderlund, J. (2016). Knowledge governance strategies in project-based organizations. *Long Range Planning, 49*(6), 648-660.

Premalatha, P. (2016). Return on retention (RoR): A grounded theory study of knowledge workers in Indian IT services industry. *Management and Labour Studies, 41*(4), 267-293.

Quintana, C. D. D., Mora, J. G., Pérez, P. J., & Vila, L. E. (2016). Enhancing the development of competencies: The role of UBC. *European Journal of Education, 51*(1), 10-24.

Sabeeh, Z., Mustapha, S. S., & Mohamad, R. (2018). Healthcare knowledge sharing among a community of specialized physicians. *Cognition, Technology & Work, 20*(1), 105-124.

Schuler, R. S., Jackson, S. E., & Tarique, I. (2011). Global talent management and global talent challenges: Strategic opportunities for IHRM. *Journal of World Business, 46*(4), 506-516.

Shastry, G. K. (2012). Human capital response to globalization education and information technology in india. *Journal of Human Resources, 47*(2), 287-330.

Sousa, M. J., & Rocha, Á. (2019). Skills for disruptive digital business. *Journal of Business Research, 94*, 257-263.

SOUTH-SOUTH, M. S. I. (2014). URANTA, ROSELINE AGBOYEFORI APAWARI PG/M. ED/11/58795.

Sparrow, P., & Cooper, C. L. (2012). *The employment relationship: Key challenges for HR*: Routledge.

Subramanian, N., Abdulrahman, M. D., Wu, L., & Nath, P. (2016). Green competence framework: evidence from China. *The International Journal of Human Resource Management, 27*(2), 151-172.

Tan, C. N.-L. (2016). Enhancing knowledge sharing and research collaboration among academics: the role of knowledge management. *Higher education, 71*(4), 525-556.

Tolf, S., Nyström, M. E., Tishelman, C., Brommels, M., & Hansson, J. (2015). Agile, a guiding principle for health care improvement? *International journal of health care quality assurance*.

Triaa, W., Gzara, L., & Verjus, H. (2016). *Organizational agility key factors for dynamic business process management.* Paper presented at the 2016 IEEE 18th Conference on Business Informatics (CBI).

Trivellas, P., Akrivouli, Z., Tsifora, E., & Tsoutsa, P. (2015). The impact of knowledge sharing culture on job satisfaction in accounting firms. The mediating effect of general competencies. *Procedia Economics and Finance, 19*, 238-247.

Turner, T., & Pennington, W. W. (2015). Organizational networks and the process of corporate entrepreneurship: how the motivation, opportunity, and ability to act affect firm knowledge, learning, and innovation. *Small Business Economics, 45*(2), 447-463.

Ulvenblad, P., Berggren, E., & Winborg, J. (2013). The role of entrepreneurship education and start-up experience for handling communication and liability of newness. *International Journal of Entrepreneurial Behavior & Research*.

Yan, Y. (2020). Application of Data Mining Method Based on Integrated Learning in Early Warning Research of SMEs' Financial Crisis. *MS&E, 740*(1), 012200.

INTERNATIONAL JOURNAL OF
COASTAL, OFFSHORE & ENVIRONMENTAL ENGINEERING IJCOE Vol.11 /No.1 /Winter 2026 (34-45)

Available online at: www. ijcoe.org

Numerical Modeling and Hydrodynamic Sensitivity Analysis of Storm Surge in the Southern Caspian Sea: The Role of Bathymetry and Wind Stress

Mahmood Reza Akbarpour Jannat[1*]; Abbas Hamidi Najafabadi[2]

[1]Iranian National Institute for Oceanography and Atmospheric Science, No.3, Etemad Zadeh St., Fatemi Ave, P.C: 1411813389, Tehran, Iran, E-mail: akbarpour@inio.ac.ir*
[2]M.Sc. Graduate, Department of Marine Engineering, Science and Research Branch, Islamic Azad University, Tehran, Iran. E-mail: abbass_hamidi@yahoo.com

ARTICLE INFO

Article History:
Received: 17 Aug 2025
Accepted: 17 Dec 2025

Keywords:
Storm Surge
ADCIRC
Southern Caspian Sea
Wind Shear Stress
Coastal Hydrodynamics

ABSTRACT

The precise estimation of extreme water level fluctuations induced by storm surges constitutes a fundamental prerequisite for the reliable design of marine structures and effective coastal risk management. In this study, the hydrodynamic response of the Southern Caspian Sea coast to atmospheric forcing mechanisms is investigated using the advanced ADCIRC numerical model, employing the solution of Shallow Water Equations (SWE) over an unstructured finite element mesh. To conduct a rigorous spatial and parametric sensitivity analysis, simulations were executed under various wind field and atmospheric pressure scenarios across six strategic stations characterized by distinct morphological features, ranging from the shallow waters of Gomishan to the steep bathymetry of Astara. Quantitative results substantiate a distinct non-linear inverse correlation between the seabed depth gradient and surge amplitude; specifically, the southeastern coasts experience surge magnitudes of a higher order compared to the steep western coasts, attributed to the continental shelf geometry and the momentum trapping phenomenon. Furthermore, the decoupling of driving forces reveals that water level variations within the Caspian basin are predominantly governed by the wind shear stress vector and effective fetch, with the inverse barometric effect playing a secondary role. By elucidating the spatial heterogeneity of coastal risks—inundation hazards in the east versus wave impact loads in the west—the findings provide a novel framework for determining the Design Water Level (DWL) and calculating hydrodynamic loads on offshore piles and protective seawalls.

1. Introduction

The sustainable development of coastal zones and the assurance of the structural integrity of critical infrastructure including ports, power plants, and offshore platforms are intrinsically linked to a precise understanding of the complex interactions between the atmosphere and the ocean. One of the most challenging parameters in the design of hydraulic structures is the determination of the "Design Water Level" (DWL).

While the water level is typically conceptualized as the superposition of Mean Sea Level (MSL), astronomical tides, and surge, in the context of extreme events, the "Storm Surge" phenomenon emerges as the dominant governing factor in short-term water level fluctuations. Neglecting the nonlinear and dynamic nature of this phenomenon can lead to gross errors in estimating the crest elevation of breakwaters and hydrodynamic loads on platform piles, ultimately resulting in catastrophic structural failure or severe inundation of the hinterland (Mahdizadeh, 2004).

From a hydrodynamic perspective, storm surge represents the response of the water body to meteorological forcing mechanisms, primarily comprising Wind Stress and atmospheric pressure gradients. When high-velocity wind fields blow over the sea surface with sufficient duration, the induced

shear stress facilitates momentum transfer to the surface layers, resulting in water pile-up in the direction of the wind (Wind Setup). Concurrently, the pressure deficit at the center of low-pressure systems leads to a rise in the sea surface via the Inverse Barometric Effect. The magnitude and amplitude of this phenomenon are complex functions of the wind field characteristics, the Coriolis effect due to latitude, coastal geometry, and, critically, the seabed morphology (Bathymetry) (Williams, 1986). Classical principles of coastal hydraulics dictate that in shallow waters, the potential for surge generation amplifies significantly due to the reduced return flow area and increased bottom friction a fact that underscores the absolute necessity of site-specific studies.

The Caspian Sea, as the world's largest enclosed body of water, serves as a unique natural laboratory for studying hydrodynamic phenomena. Lacking connection to the open oceans, its astronomical tidal range is negligible (micro-tidal). Consequently, short-term water level fluctuations within this basin are almost exclusively governed by atmospheric forces and storm surges. Historical records and observational data indicate that the Caspian Sea is prone to severe storms with long return periods. The severe heterogeneity in seabed topography ranging from the extremely shallow northern sector to the deep southern basin dictates a dual behavior for storm surges. While extensive studies have focused on massive 4–5 meter surges in the Northern Caspian (Mahdizadeh, 2004), the hydrodynamics of the Southern Caspian Basin (bordering Iran), characterized by a narrower continental shelf and greater depths, have been less rigorously scrutinized. However, the historical record of the November 1910 storm, which generated a surge of approximately 2 meters under easterly winds of 20–26 m/s, corroborates the high hazard potential in this region (Wu, 1982).

In recent decades, with the rapid expansion of strategic infrastructure along the southern coastline (including the ports of Anzali, Nowshahr, and Amirabad, as well as oil facilities), reliance on traditional methods and one-dimensional empirical formulas for surge estimation is no longer sufficient for modern engineering requirements. These conventional approaches fail to resolve current refraction, spatial variability of wind fields, and the complexities of the coastline. Therefore, the deployment of advanced numerical hydrodynamic models that solve the Shallow Water Equations (SWE) over refined computational grids is inevitable (Yan, 1987).

The present research is formulated to bridge the existing knowledge gap regarding the hydrodynamics of the Southern Caspian coast. In this study, the ADCIRC (Advanced Circulation) model, based on the Finite Element Method (FEM), is utilized for the two-dimensional simulation of flow and water levels (Luettich and Westerink, 2004). The distinctive approach of this study extends beyond mere simulation; we conduct a rigorous sensitivity analysis of the basin's response to parameters including "Wind Direction," "Atmospheric Pressure," and "Bathymetry" across six key stations with distinct morphological characteristics (ranging from the shallow waters of Gomishan to the deeper coast of Astara). Furthermore, a novel aspect of this research lies in coupling the model's hydrodynamic outputs with structural design equations, where the effects of wave-current interaction and surge-induced water level rise on the forces exerted on marine piles and seawalls are quantitatively evaluated (Karami Khaniki, 2006). The findings of this investigation provide profound insights for optimizing structural design and enhancing risk management strategies in the Southern Caspian Sea.

2. Theoretical Framework, Mathematical Formulation, and Numerical Solution Method

Developing a reliable numerical model for storm surge prediction necessitates a profound understanding of the physical mechanisms governing long-wave generation and propagation. This section first examines the system's behavior under limit states using analytical solutions to provide necessary physical insight. Subsequently, the numerical solution algorithm for the Shallow Water Equations (SWE) is elucidated, and finally, the mathematical framework for calculating hydrodynamic loading on marine structures is presented.

2.1 Asymptotic Behavior Analysis: Steady State and Wind Stress

To isolate the effect of **Wind Stress** as the dominant forcing agent in the Caspian Sea, an idealized channel with uniform depth d and finite length is initially considered. Assuming the system has reached a steady state and the net flow within the channel is zero ($M=0$), the linearized momentum balance equation, neglecting Coriolis effects and advective accelerations, can be expressed as (Williams, 1986):

$$\rho_w g(d+\zeta)\frac{d}{dx}(\zeta-\zeta_\circ)=\tau_s-\tau_b \qquad (1)$$

In this relationship, the water surface gradient ($d\zeta/dx$) directly counteracts the surface wind shear stress (τ_s) and the bottom friction stress (τ_b). Adopting the conventional assumption of a linear relationship between bottom and surface stresses ($\tau_b = -k\tau_s$), where k is the bottom calibration coefficient, Eq. (1) is rewritten as:

$$\tau_b=-5\gamma_b\tau_s=-k\tau_s \qquad (2)$$

By substituting and integrating over the spatial domain, and assuming that water level variations are negligible

compared to the total depth ($d \gg \zeta$), the analytical expression for the surge profile is obtained:

$$\frac{d}{dx}(\zeta - \zeta_{\circ}) = \frac{(1+k)\tau_s}{\rho_w g d} = \frac{(1+k)\rho_a \gamma_s^2}{\rho_w g d} U^2 \tag{3}$$

$$\zeta = \zeta_{\circ} + k \int_{xo}^{x} U^2 dx, k = (1+k)\frac{\rho_a \gamma_s^2}{\rho_w g d} \tag{4}$$

Equation (4), a generalized form of Colding's Formula, demonstrates that surge height is inversely proportional to water depth (d). This physical reality justifies the extreme vulnerability of the shallow southeastern Caspian coasts (e.g., Gomishan) compared to the deep western coasts.

2.2. Wave Dynamics and Proudman Resonance

The second factor driving storm surge is atmospheric pressure variation. The sea surface response to a moving low-pressure center with velocity V can lead to resonance phenomena. By modeling the pressure function as a traveling disturbance $\zeta_0 = -F(t-x/V)$ and solving the unsteady continuity and momentum equations (Wu, 1982):

$$\begin{aligned} \frac{\partial M}{\partial t} &= -gd\frac{\partial}{\partial x}(\zeta - \zeta_{\circ}) \\ \frac{\partial \zeta}{\partial t} &= -\frac{\partial M}{\partial x} \end{aligned} \tag{5}$$

The governing wave equation for the system is derived:

$$\frac{\partial^2 M}{\partial t^2} - gd\frac{\partial^2 M}{\partial x^2} = gd\frac{\partial^2 \zeta_{\circ}}{\partial x \partial t} \tag{6}$$

The analytical solution to this partial differential equation reveals the system's strong dependence on the wave Froude number ($F_r = V/c$), where $c = \sqrt{gd}$ is the shallow-water wave celerity:

$$\begin{aligned} M &= \frac{Vc^2}{C^2 - V^2}\left[F(t - \frac{x}{V}) - F(t + \frac{x}{c})\right] \\ \zeta &= \frac{c}{c^2 - V^2}\left[cF(t - \frac{x}{V}) + VF(t + \frac{x}{c})\right] \\ C &\equiv \sqrt{gd} \end{aligned} \tag{7}$$

Analysis of this relationship reveals three distinct behavioral regimes:

1. Sub-critical Regime ($V < c$): The system response is stable.
2. Resonance Regime ($V = c$): Continuous energy transfer occurs from the atmosphere to the ocean, and the wave amplitude approaches infinity (mathematical singularity). This phenomenon, known as Proudman Resonance, can lead to destructive rogue surges in regions of the Caspian Sea where the storm propagation speed matches the shallow water wave speed.
3. Super-critical Regime ($V > c$): The system undergoes a phase shift, resulting in a negative response (set-down).

2.3. Numerical Solution Strategy: Spatio-Temporal Discretization

To accurately simulate non-linear interactions within the complex geometry of the Caspian Sea, numerical methods are indispensable. The solution algorithm is based on discretizing the governing equations ($\partial f/\partial t = F$) using a central difference (Leap-Frog) scheme, which provides second-order temporal accuracy (Yan, 1987; Luettich and Westerink, 2004:

$$f_{n+1} = f_{n-1} + 2F_n \Delta t \tag{8}$$

Applying this scheme to the full momentum and continuity equations (incorporating Coriolis and surface stress terms), the discrete form on the computational grid (i ,j)is derived:

$$\begin{aligned} \frac{\partial M}{\partial t} &= -gd\frac{\partial}{\partial x}(\zeta - \zeta_{\circ}) + \tau_S{}^{(x)} \\ \frac{\partial N}{\partial t} &= -gd\frac{\partial}{\partial y}(\zeta - \zeta_{\circ}) + \tau_S{}^{(y)} \\ \frac{\partial \zeta}{\partial t} &= \frac{\partial M}{\partial x} - \frac{\partial N}{\partial y} \end{aligned} \tag{9}$$

This method allows for the step-by-step simulation of the temporal evolution of the water surface (ζ) and flow fields (M, N) under various storm scenarios.

2.4. Implications for Marine Structural Design and Integrity Assessment

Although the primary objective of this research is centered on hydrodynamic simulation, the derived model outputs—specifically the spatiotemporal evolution of water surface elevation (ζ) and the associated current velocity fields constitute the fundamental "Hydrodynamic Boundary Conditions" for the design and reliability assessment of coastal infrastructure. The storm-induced rise in the mean water level is not merely a static addition; it effectively augments the total water depth at the toe of coastal structures ($d_{total}=d_{MSL}+\zeta_{surge}+\zeta_{wave\_setup}$). This depth modulation fundamentally alters the wave-

structure interaction regime, shifting the design parameters from standard operational conditions to critical Ultimate Limit States (ULS).

2.4.1. Effects on Slender, Pile-Supported Structures

For pile-supported structures such as offshore platforms, jetties, and dolphins, the surge-induced increase in water depth has a cascading effect on hydrodynamic loading. According to the principles of the Morison Equation, the total force is a summation of drag and inertia components. The surge elevation extends the wetted length of the pile, thereby exposing a larger surface area to hydrodynamic stress. More critically, the increase in depth modifies the wave kinematics; it reduces the attenuation of orbital particle velocities near the surface. Consequently, the structure is subjected to higher velocities at higher elevations. This upward shift of the force center significantly increases the "overturning moment" at the mudline (seabed), which is often the governing failure mode for pile foundations. Therefore, neglecting the surge component can lead to a severe underestimation of the lever arm and the resulting bending moments.

2.4.2. Impact on Gravity Structures (Seawalls and Breakwaters)

In the context of gravity-based coastal defense structures like vertical seawalls and rubble-mound breakwaters, the implications of storm surge are even more decisive. The stability of these structures is governed by the dynamic pressure distribution, typically calculated using methods such as Goda's Theory. The depth-limited wave breaking criterion ($H_{max} \approx 0.78 d_{total}$) dictates that the maximum wave height capable of reaching a structure is a function of the local depth.

During a surge event, the deepened water column mitigates or delays wave breaking on the foreshore. This phenomenon allows larger, high-energy waves which would otherwise break and dissipate energy offshore to propagate closer to the coast and impact the structure directly. This shift can transition the loading regime from a "pulsating" (non-breaking) load to a catastrophic "impulsive" (breaking/shock) load, exerting extreme instantaneous pressures on the wall. Furthermore, the elevated water level significantly increases the risk of "Wave Overtopping," threatening the structural integrity of the crest and the safety of the hinterland. Thus, integrating the computed surge values into the "Design Water Level" (DWL) is indispensable for ensuring structural resilience and preventing functional failure during extreme events.

3. Study Area and Environmental Characterization

3.1. Physiography and Hydrodynamic Characteristics of the Southern Caspian Basin

The Caspian Sea, distinguished as the world's largest endorheic (landlocked) body of water, constitutes a unique hydrodynamic laboratory where the conventional drivers of oceanic variability are fundamentally altered. Unlike open oceans where astronomical tides often dictate coastal water levels, the Caspian Sea functions as a non-tidal system (micro-tidal range < 10 cm). Consequently, short-term water level fluctuations are predominantly governed by stochastic atmospheric forcing, making "storm surges" the critical hazard for coastal management. This research specifically targets the Southern Caspian Basin, which encompasses the entire northern coastline of Iran. Physiographically, this basin represents the deepest sector of the sea, characterized by an oceanic-type crust and abyssal depths reaching approximately 1025 meters.

However, from the perspective of long-wave hydrodynamics and surge generation, the governing parameter is not the maximum abyssal depth, but rather the stark asymmetry in the continental shelf geometry and the variable width of the shallow coastal zone (nearshore hypsometry). The basin exhibits a pronounced morphological anisotropy; the western shelf is narrow and steep, rapidly dropping to deep water, whereas the eastern shelf is extensive and gently sloping. This morphological configuration interacts critically with the region's meteorology. The sea's significant meridional elongation (stretching over 1200 km from north to south) aligns perfectly with the dominant synoptic wind patterns.

During storm events, particularly in the cold season, high-velocity Northerly and North-Westerly winds sweep across the entire length of the sea. This alignment generates an exceptionally long "Effective Fetch" exceeding 800 km for the southern coast. This immense fetch facilitates the maximum transfer of momentum flux from the atmosphere to the sea surface, allowing wind-driven currents to accelerate over vast distances without topographic interruption. This process significantly enhances the potential for the generation of high-energy long waves and the mass transport of water towards the Iranian coast. Furthermore, the coastal topography in the southeastern sector (Gomishan and Gorgan Bay) functions as a "geometric funnel." In this region, the converging coastlines and the dissipative shallow bottom act to trap the incoming wind-driven currents. This "hydrodynamic confinement" prevents the lateral escape of the water mass, leading to a localized, non-linear amplification of surge heights that is significantly more severe than in the deep western sectors.

3.2. Morphological Classification and Hydrodynamic Characterization of Selected Stations

To ensure a rigorous hydrodynamic analysis that is spatially generalizable across the entire ~860 km southern coastline, six strategic monitoring stations

were selected based on distinct bathymetric gradients and socio-economic vulnerability profiles. The spatial configuration of these stations is visualized in Figure 1(a), while a comparative analysis of their cross-shore depth profiles is presented in Figure 1(b), revealing a pronounced east-west morphological asymmetry.

At the eastern extremity of the study domain, the Gomishan station serves as the archetype for the "Shallow Coastal Plain Regime." As delineated by the solid blue profile in Figure 1(b), this sector is characterized by an exceptionally gentle seabed gradient (slope S_0<1:1000), where shallow waters persist for significant distances offshore. From a theoretical fluid dynamics standpoint, this bathymetric configuration creates a friction-dominated environment. The governing momentum balance in this zone is heavily influenced by the bottom shear stress term (τ_b), which, combined with the inverse dependence of wind setup on water depth ($\partial\zeta/\partial x \propto \tau_s/h$), renders this region uniquely susceptible to extreme water level accumulation. Consequently, Gomishan serves as a critical indicator for "worst-case" inundation scenarios, where the synergy of low-lying topography and sustained storm winds creates a high-risk zone for extensive coastal flooding.

Moving westward, the central coastal sector-encompassing Amirabad Port, Neka, and Nowshahr exhibits a "Transitional Morphological Regime." This zone, which hosts vital energy and commercial infrastructure, features a bathymetric slope that represents an intermediate state between the dissipative east and the reflective west (Figure 1b). In this sector, the hydrodynamic focus shifts towards the interaction between the sea state and coastal structures; specifically, the determination of safe crest elevations for breakwaters against combined surge and wave run-up becomes paramount. Furthermore, the Nowshahr station presents a unique meteorological complexity; the immediate proximity of the Alborz Mountain range to the coastline induces localized orographic effects that modify the wind field structure, thereby increasing the complexity of the nearshore current generation.

Conversely, the western littoral zone, represented by Anzali Port and Astara, typifies the "Narrow Shelf Regime." In this region, bathymetric contours (isobaths) run parallel and in close proximity to the shoreline, indicating a steep seabed gradient as evidenced by the rapid depth descent in Figure 1(b) (dashed orange and solid purple lines). The fundamental nature of marine hazards in this sector is distinct from the east; while the amplitude of wind-induced surge is hydrodynamically constrained by the greater water depths, the steep slope allows high-energy, deep-water waves to propagate to the nearshore zone with minimal energy dissipation due to friction. Consequently, the primary engineering concern transitions from inundation to structural integrity, as coastal defenses are subjected to severe dynamic pressures and impulsive wave impact loads. Additionally, the hydrodynamics at Anzali are further complicated by the hydraulic exchange with the Anzali Lagoon and the interaction of inflow/outflow currents with port breakwaters. This strategic stratification of stations ensures a holistic coverage of the diverse hydrodynamic boundary conditions characterizing the Southern Caspian Sea.

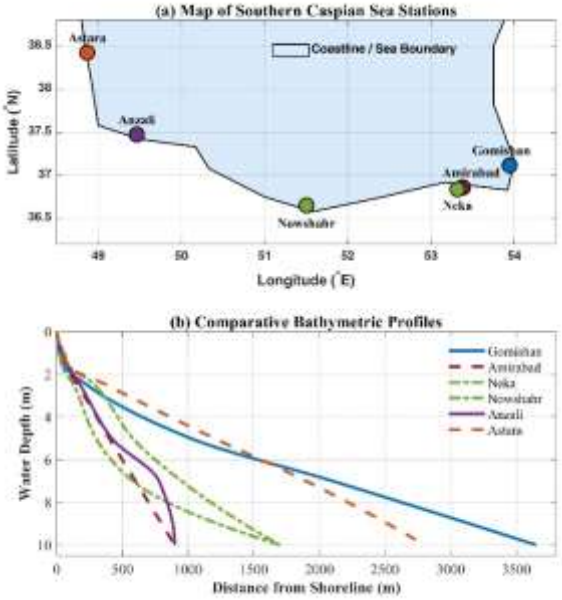

Figure 1: (a) Geographical map of the Southern Caspian Sea indicating the locations of the six selected study stations. The sea domain is highlighted in light blue, bounded by the coastline (solid black line). (b) Comparative cross-shore bathymetric profiles for the selected stations. The plots illustrate the significant morphological heterogeneity across the basin, contrasting the extremely gentle slope at Gomishan (solid blue line) with the steep gradients observed at Astara (dashed orange line) and Amirabad (dashed red line).

4. Results and Discussion

In this section, the complex hydrodynamic response of the Southern Caspian Basin to a spectrum of atmospheric forcing scenarios is critically examined through a rigorous quantitative analysis of the ADCIRC numerical model outputs. The discussion is structured to systematically unravel the physical mechanisms governing surge generation and propagation within this semi-enclosed water body. The analytical framework is founded on three primary axes designed to provide a holistic understanding of the basin's behavior. First, the study evaluates the non-linear damping and amplification effects induced by the basin's heterogeneous seabed morphology, specifically contrasting the dissipative, friction-dominated regime of the shallow southeastern shelf with the reflective nature of the deep western coast. Second, a decomposition analysis is performed to rigorously decouple the static, hydrostatic contribution of barometric pressure anomalies (Inverse Barometric

Effect) from the dynamic, momentum-driven wind shear stress, thereby isolating the dominant energy source responsible for extreme water levels. Finally, the investigation extends to the temporal dynamics of surge evolution relative to the wind field orientation, meticulously assessing how the effective fetch length and the angle of wave incidence interact with the basin's geometry to determine the magnitude, timing, and phase of the resulting storm surges.

4.1. The Role of Bathymetric Morphology in Non-linear Surge Amplification

A fundamental finding of this research is the elucidation of a distinct, non-linear inverse correlation between the nearshore water depth (h) and the amplitude of surge oscillations (ζ). The quantitative results, summarized in Table 1, reveal a severe spatial heterogeneity in the hydrodynamic response of the sea along the southern coastline. By isolating the critical "North-West Wind" scenario, the disparity in surge magnitudes becomes starkly evident. The Gomishan station, situated in the shallow southeastern coastal plain, recorded the highest surge level among all stations (5.88×10^{-2} m). In sharp contrast, at stations characterized by steep continental slopes and deep waters, such as Nowshahr and Anzali, this value diminishes significantly to 4.6×10^{-3} m and 4.7×10^{-3} m, respectively. This represents an order-of-magnitude difference—approximately a factor of 12—between the eastern and western sectors, despite both regions being subjected to identical wind forcing vectors.

The physical interpretation of this amplification phenomenon is rooted in the balance of momentum within the Shallow Water Equations (SWE), where the wind setup slope ($\partial\zeta/\partial x$) is inversely proportional to the total water depth. In the deep western regions like Astara, the large water depth results in a negligible surface gradient. Furthermore, in these deep waters, a vertical circulation cell is typically established where the wind-driven surface transport is effectively balanced by a deep "return flow" (undertow) driven by the pressure gradient, thereby preventing excessive water accumulation at the boundary. However, in the extensive shallow shelf of Gomishan, where depths remain below a few meters for significant offshore distances, the limited cross-sectional area restricts this return flow mechanism. Consequently, the turbulent bottom boundary layer expands to occupy the entire water column, drastically increasing the bottom friction stress (τ_b) and creating a "hydrodynamic impedance" that traps the water mass against the coast. With the return flow effectively choked, the kinetic energy of the wind-driven current cannot be dissipated through circulation and is almost entirely converted into potential energy, manifesting as a severe rise in the water surface. Thus, the seabed depth gradient serves as the primary controlling parameter determining the hydrodynamic regime, shifting the system from a diffusive, circulatory state in the west to a dissipative, accumulative state in the east.

4.2. Decoupling the Hydrostatic Atmospheric Pressure Contribution from Wind Shear Stress

In the complex hydrodynamics of enclosed basins, distinguishing the specific contribution of atmospheric pressure anomalies from the dominant wind shear stress is fundamental for accurate surge prediction. To rigorously quantify these relative contributions, the water level response to atmospheric pressure variations is meticulously analyzed in Figure 2. This comparative analysis examines the temporal evolution of the water surface under two distinct synoptic scenarios: a reference condition characterized by a standard pressure of 1025 hPa, and a storm condition defined by a cyclonic depression to 1020 hPa.

A detailed examination of the resultant time-series reveals that the imposed 5 hPa pressure deficit induces a nearly constant, vertical translation of the surge hydrograph across the entire simulation period. This uniform vertical shift is physically attributable to the sea's isostatic adjustment to the reduced weight of the atmospheric column, a phenomenon classically defined as the "Inverse Barometric Effect" (IBE). In accordance with the hydrostatic equilibrium principle, the sea surface rises approximately 1 centimeter for every 1 hPa drop in atmospheric pressure to balance the total pressure at the seabed. Consequently, the observed difference represents a static, scalar addition to the datum level rather than a dynamic generation of new wave energy.

Crucially, a closer inspection of Figure 2 demonstrates a high degree of "temporal phase synchronization" between the two scenarios. The onset time of the surge, the rate of rise, the exact moment of the peak, and the subsequent relaxation curve remain virtually invariant despite the pressure difference. This phase congruency provides compelling evidence that the system's dynamic characteristics—including flow inertia, wave celerity, and resonance frequencies—are dictated almost exclusively by the "Wind Stress Field." While the pressure anomaly modifies the potential energy of the system by elevating the mean water level, it does not significantly alter the kinetic energy transfer or the momentum balance within the basin. Therefore, in the context of coastal engineering for the Caspian Sea, atmospheric pressure functions primarily as a linear additive component, whereas the wind field acts as the vector driver determining the severity and temporal dynamics of the storm surge. This distinction is vital for design purposes, suggesting that while pressure drops must be accounted for in Total Water Level (TWL) calculations, the structural resilience against hydrodynamic impact loads must be designed based on wind-generated kinematics.

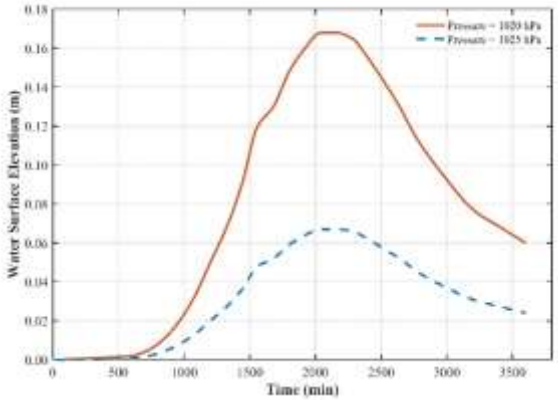

Figure 2: Time-series comparison of storm surge elevation under normal (1025 hPa) and storm (1020 hPa) atmospheric pressure scenarios.

4.3 Hydrodynamic Sensitivity to Wind Vector Orientation and Temporal Dynamics

The orientation of the wind stress vector relative to the basin's geometry serves as the governing determinant for the "Effective Fetch" length and the angle of wave incidence, which in turn dictates the magnitude of momentum transfer from the atmosphere to the sea surface. The sea surface response to Northerly winds, as plotted in Figure 3(a), illustrates a basin-wide setup phenomenon where the wind vector aligns perfectly with the longitudinal axis of the Caspian Sea. This alignment maximizes the effective fetch to over 800 km, facilitating a sustained transfer of momentum and allowing wind shear stress to act over a vast distance. Consequently, significant kinetic energy is converted into potential energy in the form of surge setup. A critical observation in this scenario is the spatial disparity in growth rates; the curve for the Gomishan station ascends with a significantly steeper gradient compared to deep-water stations. This behavior is attributed to the "shoaling effect," where long-period surge waves encounter the shallow continental shelf, decreasing in celerity but increasing in amplitude to conserve energy flux. Furthermore, the post-storm relaxation phase at Gomishan exhibits a noticeable hydrodynamic hysteresis; this delayed subsidence is attributable to the high bottom friction in the shallow, semi-enclosed region, which impedes the rapid drainage of the accumulated water mass back into the deep basin.

Conversely, the basin's response to lateral zonal forcing specifically Easterly Figure 3(e) and Westerly Figure 3(d) winds exhibits a fundamentally different, damped behavior. Due to the severe limitation of fetch length in the transverse direction, which is approximately 200 to 300 km, the wind lacks sufficient distance to generate a large hydraulic gradient or significant cross-shore setup. Instead, the hydrodynamics in these scenarios are governed by Ekman Transport. For instance, under Easterly winds, surface water is deflected to the right (Northward) due to the Coriolis effect, moving away from the Southern coast. Consequently, western stations like Anzali do not experience a rise and may even record a distinct "set-down" or negative surge. In these zonal scenarios, the generated currents acquire a predominantly "longshore" nature, dissipating storm energy by transporting water masses parallel to the coast rather than piling them up against the shoreline.

Table 1: Maximum storm surge elevation (*m*) calculated for selected stations under various wind direction scenarios.

Station	North (N)	North-West (NW)	North-East (NE)	West (W)	East (E)
Gomishan	0.0225	0.0588	0.0388	0.0670	0.0713
Amirabad	0.0108	0.0127	0.0071	0.0028	0.0028
Nowshahr	0.0107	0.0046	0.0041	0.0021	0.0022
Anzali	0.0116	0.0047	0.0075	0.0020	0.0020
Astara	0.0185	0.0150	0.0106	0.0190	0.0190

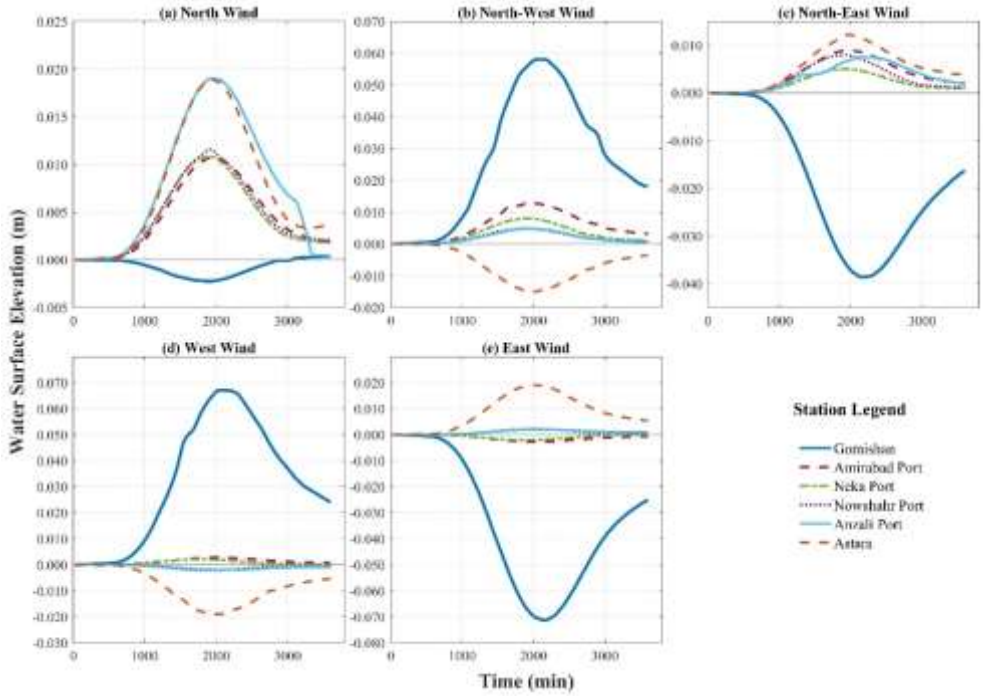

Figure 3: Multi-panel time series analysis of water surface elevation fluctuations across selected stations under five distinct wind direction scenarios (Wind Speed *U*=12 m/s). The subplots represent the hydrodynamic response to: (a) North, (b) North-West, (c) North-East, (d) West, and (e) East wind forcing. Panel (f) provides the unified legend for all stations. Note the scenario-specific vertical scales used to visualize the varying magnitudes of surge setup and set-down.

The interaction becomes more complex under oblique wind forcing. Examination of the North-East wind in Figure 3(c) reveals a nuanced mechanism involving both wind stress and the Coriolis force. The broad peak width observed in this graph indicates a sustained high-water stand. While the wind vector drives water toward the southwest, the Coriolis force deflects the flow to the right, effectively compressing the water mass against the Southern shoreline. This results in a "flow convergence" zone in the central parts of Mazandaran, which is evident in the overlapping curves of Amirabad and Nowshahr, creating a unique hazard profile for central ports. Finally, the most critical "Limit State" scenario is depicted in Figure 3(b) under North-West wind conditions. This graph represents the worst-case hydrodynamic loading for the southeastern sector, where the water level at Gomishan and Amirabad grows exponentially. The physical interpretation of this catastrophic event stems from the synergy of three destructive factors: the maximization of fetch along the sea's longest diagonal, the nearly orthogonal incidence of the wind relative to the bathymetric contours, and the "Momentum Trapping" caused by the funnel-shaped geometry of Gorgan Bay. In this state, the driven water mass encounters a closed boundary with no escape route, forcing a direct conversion of kinetic energy into a drastic vertical rise and posing an extreme risk of coastal flooding.

To synthesize the directional sensitivity results into a holistic framework, Figure 4 integrates the maximum surge responses from all simulated scenarios into a unified Polar Diagram. This synoptic visualization highlights a profound morphological disparity in hydrodynamic behavior across the study area. The Gomishan station, delineated by the expansive outer polygon, exhibits acute sensitivity to a broad spectrum of wind vectors, a phenomenon that can be termed the "Gomishan Anomaly." This empirically corroborates that in shallow hydrodynamic regimes, surge amplification is less constrained by the precise angle of wind incidence and is driven primarily by the sheer magnitude of bottom friction and shallow-water terms. In contrast, deep-water stations such as Nowshahr and Anzali form a constricted, compact core near the origin of the plot. Their response is highly anisotropic, reacting predominantly to direct Northerly forcing while remaining largely unresponsive to lateral winds. This behavior validates the energy-damping capacity of steep bathymetric slopes, which function as reflective boundaries. Collectively, the elongation of all station polygons towards the North and North-West sectors visually underscores these vectors as the determinant "Design Wind Directions" for the basin.

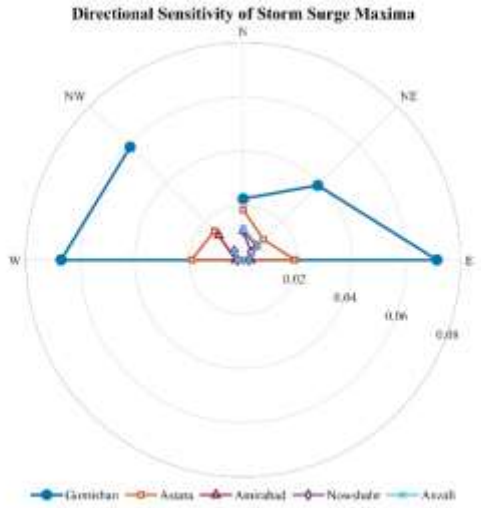

Figure 4: Polar diagram illustrating the directional sensitivity of maximum storm surge elevation across selected stations in the Southern Caspian Sea.

Finally, to quantify the "hydrodynamic stability" of different coastal sectors for reliability-based design, a statistical analysis of surge variability is presented in the Box-and-Whisker plot in Figure 5. This visualization reveals a critical distinction in risk profiles. The Gomishan station exhibits a significantly larger Interquartile Range (IQR) combined with a high median value, indicating that the region is not only subject to high water levels but is also highly volatile; the surge magnitude fluctuates wildly depending on slight shifts in the storm track. Conversely, stations in the central and western sectors show compact distributions with low medians, suggesting a stable hydrodynamic response where extreme surges are rare anomalies rather than frequent occurrences. This statistical evidence supports the engineering recommendation for implementing higher Safety Factors and more conservative freeboard allowances in the design of coastal structures in the southeastern Caspian basin compared to the western coast.

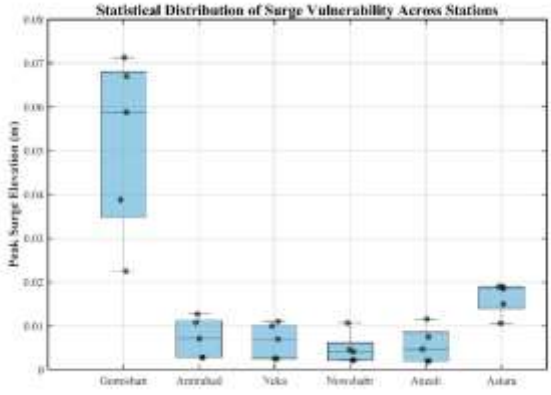

Figure 5: Statistical box-and-whisker plot illustrating the variability and distribution of peak surge elevations for each station across all simulated wind directions. The solid boxes represent the interquartile range (IQR), the red lines indicate the median surge, and the scattered points denote specific scenario outcomes.

4.4 Critical Scenario Analysis and Limit State Assessment

While historical records and long-term field observations suggest that the frequency of extreme storm surge events in the deep Southern Caspian Basin is lower compared to the shallow Northern sector, relying solely on average or moderate storm conditions ($U \approx 12$ m/s) is insufficient from the perspective of rigorous risk management and critical infrastructure design. In resilience engineering, defining a "Limit State" is essential to understand the structural behavior under "worst-case" scenarios that may occur within a 50 or 100-year return period. It is posited that analyzing a hypothetical "Critical Scenario" is indispensable to fully elucidate the basin's latent hydrodynamic potential, reveal hidden vulnerabilities in seemingly safe zones, and determine the upper bounds of Design Water Levels (DWL).

To this end, a comprehensive limit state scenario was constructed and simulated. This scenario is characterized by a sustained, high-velocity wind field of 25 m/s (classified as a severe storm in the Caspian region) combined with a barometric pressure depression to 1019 hPa. A "Westerly" wind vector was strategically selected as the critical forcing direction. This orientation is particularly hazardous because it aligns with the major East-West axis of the southern basin, maximizing the "effective fetch" for the southeastern coastline and driving strong Ekman transport currents directly toward the shallow Gomishan region.

4.4.1. Divergent Hydrodynamic Response

The simulation results under this extreme forcing, presented in Figure 6, reveal a drastic and highly non-linear bifurcation in the basin's hydrodynamic response. As illustrated, the water level at the Gomishan station undergoes a catastrophic escalation, experiencing a massive surge that reaches a peak of approximately +1.00 m. This phenomenon is not merely a linear increase but a result of "momentum trapping" within the funnel-shaped, shallow bathymetry of the southeastern corner, where bottom friction prevents the return flow of the piled-up water mass.

Conversely, the western sector exhibits a significant inverse response. The Astara station records a severe set-down (water level depression) of -0.59 m. Intermediate stations display a transitional behavior; Amirabad and Neka record moderate positive surges (~0.20–0.25 m), while centrally located stations like Nowshahr and Anzali experience water level drops of approximately 0.20 m. This profound divergence representing a nearly 1.6-meter hydraulic

gradient between the eastern and western coasts in a single event underscores the necessity for distinct, site-specific design strategies across the Southern Caspian littoral zone.

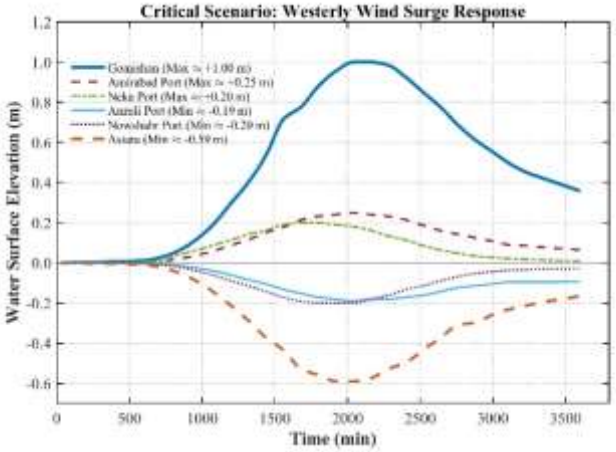

Figure 6: Hydrodynamic response simulation under the "Critical Limit State" scenario (Westerly wind, U=25 m/s, P_{atm}=1019 hPa). The graph highlights the extreme spatial heterogeneity, contrasting the massive surge setup at Gomishan (+1.0 m) with the significant set-down at Astara (−0.59 m).

4.4.2. Sensitivity and Amplification Analysis

To quantitatively assess the basin's sensitivity to wind stress intensification, Figure 7 presents a comparative "Dumbbell Plot." This advanced visualization illustrates the hydrodynamic shift from "Normal Conditions" (baseline, 12 m/s) to the "Critical Limit State" (25 m/s). In this chart, the vertical connector lines represent the magnitude of the surge shift, while the annotated values indicate the specific "Amplification Factor" calculated for each station. The analysis of these amplification factors yields critical engineering insights that challenge linear assumptions:

1. Severe Non-linearity: The approximate doubling of wind velocity (from 12 to 25 m/s) results in a disproportionate, non-linear surge response. At the critical Gomishan station, the surge elevation is amplified by a factor of approximately 15, escalating from negligible levels to a hazardous 1.00 m. This empirically validates the power-law dependence of wind stress ($\tau \propto U^2$) and its complex interaction with shallow water physics ($d \to 0$).
2. Unveiling Latent Vulnerability: A significant finding is the exceedingly high amplification factors observed in central and western deep-water stations (e.g., Anzali, Nowshahr, and Amirabad). Although these locations exhibit negligible fluctuations under normal forcing (indicated by blue markers near zero), the limit state simulation reveals their latent hydrodynamic potential. Under extreme stress, they experience significant hydraulic shifts (up to ±0.25 m). This underscores that the apparent "safety" of these deep-water zones under moderate winds must not lead to underestimating risks during high-return-period storms.
3. **Symmetry in Negative Response:** The Astara station exhibits a massive amplification factor (approx. 31x) for water level depression. This indicates that the physical mechanism driving water evacuation from the steep western coast operates with even greater intensity than the accumulation mechanism under extreme forcing, posing risks for navigation safety and water intake structures.

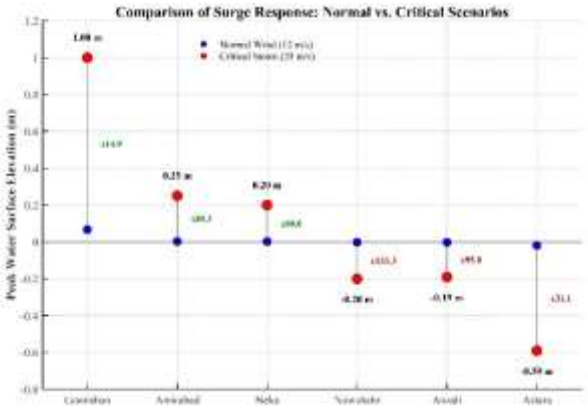

Figure 7: Comparative analysis of surge response sensitivity to wind velocity intensification. The chart illustrates the transition from the baseline scenario (12 m/s, blue markers) to the critical limit state (25 m/s, red markers). The calculated "Amplification Factors" (e.g., x14.9, x31.0) highlight the non-linear hydrodynamic response across all stations.

4.4.3. Basin-Scale Hydraulic Gradient

To visualize the holistic, basin-wide hydrodynamic response, the spatial distribution of the peak surge is plotted along the coastline in Figure 8. This profile reveals a coherent and continuous "Longitudinal Hydraulic Gradient" spanning approximately 850 km. The interplay between the sustained wind stress and the variable bathymetry creates a distinct "tilting" of the entire water surface in the Southern Caspian basin. The western sector (from Astara to Nowshahr) acts as a "source region" characterized by negative water levels (set-down zone), while the eastern sector functions as a "sink region," accumulating the displaced water mass. The pivotal point (hydrodynamic node or zero-crossing) is located in the central region between Nowshahr and Neka. This sharp gradient rising from -0.59 m in the west to +1.00 m in the east confirms that the storm surge in the Southern Caspian is not a localized event but a coupled, basin-scale oscillation (seiche-like behavior). This finding is crucial for integrated coastal zone management, as it implies that extreme events affect the entire coastline simultaneously but with opposing signs and magnitudes.

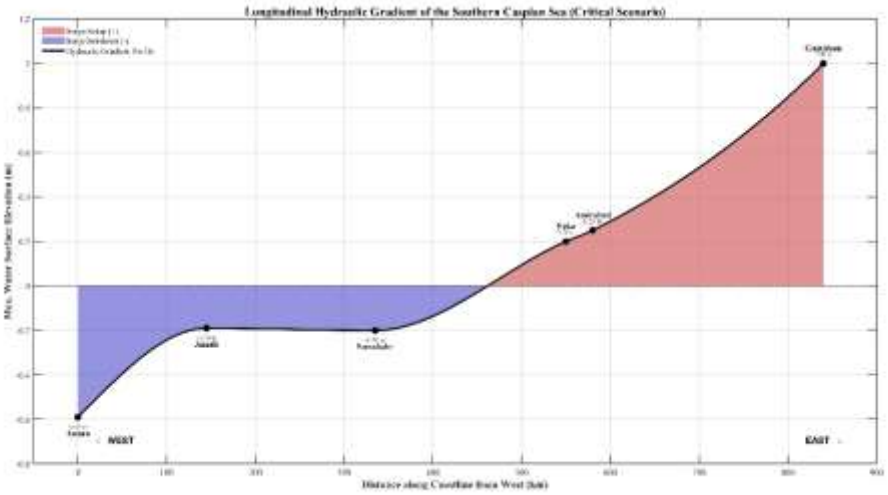

Figure 8: Longitudinal spatial profile of the maximum water surface elevation along the Southern Caspian coastline (from West to East) under the critical Westerly storm scenario (U=25 m/s). The plot visualizes the basin-scale "Hydraulic Gradient," illustrating the transition from significant set-down in the West (Astara) to extreme setup in the East (Gomishan).

5. Conclusion and Future Perspectives

This research constitutes a systematic effort to characterize the hydrodynamic response of the Southern Caspian Sea basin to extreme atmospheric forcing. By deploying the advanced, finite-element-based ADCIRC numerical model, this study successfully decoupled the complex, non-linear interactions governing storm surge generation, offering critical insights into the interplay between meteorological inputs and bathymetric controls. The comprehensive analysis of various synoptic scenarios yields the following pivotal conclusions and strategic recommendations:

5.1. Dominance of Wind Stress and Hydrodynamic Forcing

The simulation results provide conclusive evidence that within the semi-enclosed basin of the Caspian Sea, water level fluctuations during storm events are predominantly driven by the vector and magnitude of "wind shear stress" combined with the "effective fetch length." Unlike open oceanic environments where tidal constituents or barometric pressure drops often dictate peak water levels, in the Caspian Sea, the Inverse Barometric Effect plays a secondary, linear role, contributing only incrementally to the surge datum. Specifically, during the unstable transition seasons of autumn and winter, the alignment of high-velocity Northerly and North-Westerly wind fields with the sea's longitudinal axis facilitates a maximized momentum transfer from the atmosphere to the water column. This sustained energy input fosters the development of long-period surge waves that propagate southward, accumulating significant energy before impacting the Iranian coastline.

5.2. Bathymetric Control and Spatial Heterogeneity

A fundamental scientific contribution of this study is the quantitative elucidation of the critical role played by the "seabed gradient" in dictating the coastal hydrodynamic regime. The spatial analysis reveals a stark dichotomy in surge behavior:

- The "Hydrodynamic Trap" of the Southeast: The southeastern coastal zones, encompassing Gomishan and the Miankaleh peninsula, are characterized by a wide continental shelf, extremely shallow bathymetry, and a funnel-shaped coastal geometry. This configuration acts as a dissipative domain that effectively traps flow momentum. The high bottom friction in these shallow waters impedes the return flow, converting kinetic wind energy directly into potential energy, thereby generating severe surge setup and prolonged high-water stands.
- The Reflective Regime of the West: In sharp contrast, the western coasts (e.g., Anzali and Astara) feature steep bathymetric slopes and narrow shelves. These areas exhibit a reflective hydrodynamic behavior where deep-water waves reach the shoreline with minimal energy dissipation but limited potential for water pile-up. This severe spatial heterogeneity invalidates the use of a uniform "Design Water Level" (DWL) across the basin, necessitating a site-specific hazard zoning approach.

5.3. Implications for Marine Structural Design and Coastal Management

From an engineering perspective, the identified hydrodynamic distinctiveness mandates tailored design philosophies for the eastern and western sectors:

- Eastern Sector (Inundation Risk): In regions like the Amirabad Port and Gomishan, the primary threat is "coastal inundation and overtopping." Consequently, the design priority must focus on optimizing the crest elevation

(freeboard) of breakwaters and coastal dikes. Calculations must account for the superposition of the maximum storm surge, wave setup, and potential sea-level rise to ensure structural safety over a 50-year return period.

- Western/Central Sector (Structural Integrity): In areas like Nowshahr and Anzali, although the surge elevation is comparatively lower, the significant water depth at the toe of structures allows for the penetration of high-energy, non-breaking waves. Here, the primary hazards shift to "impulsive impact loads" and "toe scour." Design strategies must therefore prioritize the stability of armor units, the robustness of vertical seawalls against dynamic pressures, and the implementation of extensive scour protection measures.

5.4. Future Roadmap: Monitoring and Integrated Management

Finally, this study highlights an often-overlooked risk: the potential for resonance phenomena arising from the interaction between storm surges and infragravity waves (long waves) within harbor basins. It is strongly recommended that future research initiatives prioritize the establishment of a high-frequency field monitoring network. Synchronizing real-time water level registration with wave characteristics in identified critical zones (particularly the Gomishan anomaly) is essential for model calibration and early warning systems.

Furthermore, given the Caspian Sea's unique susceptibility to long-term sea-level fluctuations driven by climate change, the insights derived from this research should serve as a robust baseline for formulating Integrated Coastal Zone Management (ICZM) guidelines. These guidelines must establish conservative construction setbacks and define dynamic hazard lines to protect critical infrastructure and coastal communities against the compounding effects of extreme storms and sea-level variability.

References

Karami Khaniki, A. (2006). *Coasts of Iran*. Soil Conservation and Watershed Management Research Institute, Tehran, Iran (in Persian).

Luettich, R.A., & Westerink, J.J. (2004). *Formulation and numerical implementation of the 2D/3D ADCIRC finite element model version 44.xx*. Theory Report. Available at: <www.adcirc.org>.

Mahdizadeh, M. (2004). Numerical modeling of storm and wind-driven currents in the Caspian Sea. *Journal of Marine Sciences*, (in Persian).

Williams, A.E. (1986). *Engineering and design: Storm surge analysis and design water level determinations* (EM 1110-2-1412). Washington, D.C.: U.S. Army Corps of Engineers.

Wu, J. (1982). Wind-stress coefficients over sea surface from breeze to hurricane. *Journal of Geophysical Research: Oceans*, 87(C12), 9704–9706.

Yan, Y. (1987). *Numerical modeling of current and wave interactions of an inlet-beach system* (Doctoral dissertation). University of Florida, Gainesville, FL.

INTERNATIONAL JOURNAL OF
COASTAL, OFFSHORE & ENVIRONMENTAL ENGINEERING IJCOE Vol.11/No. 1/Winter 2026 (46-56)

Available online at: www. ijcoe.org

Effects of bridge curvature radius on results of nonlinear dynamic analysis in coastal curved bridges

Shahrouz Arabestani[1], Mohammad Reza Mansoori[2*], Fereshteh Emami[3], Panam Zarfam[4]
Department of Civil Engineering, SR.C., Islamic Azad University, Tehran, Iran.
1- *0057059551@iau.ir*
2- *m.mansoori@iau.ac.ir (Corresponding Author).*
3- *femami@iau.ac.ir*
4- *zarfam@iau.ac.ir*

ARTICLE INFO

Article History:
Received: 07 Sep 2025
Accepted : 4 Jan 2026

Keywords:
seismic vulnerability, curved bridges, Curvature radius, BEP analysis, IDA

ABSTRACT

One of the methods that has appropriate accuracy, applicability and reliability and will be discussed in this study is the Bidirectional Energy Based Pushover (BEP) method. Because the capacity curve obtained from BEP is unique and the main parameters of the pusher (load pattern, control point and monitor point) cannot question the accuracy of this approach; because there is no need to select a point monitor to obtain the capacity curve and instead, all the monitor points must be displaced to calculate the energy absorbed in the pusher stage. This method has been evaluated in terms of accuracy and applicability in building structures. This is while the aim of this study is to extend this method to assess the seismic vulnerability of bridges with curvature in plan.
After identifying and selecting the methods and models considered for each element, and considering the defined uncertainties, the proposed models are modeled in OpenSeesPy software to perform IDA analysis. In order of material behavior, concrete, steel, geometry and modeling details, boundary conditions are selected based on previous studies, and modeling is performed accordingly. In this paper evaluated the effects of radius of curvature on the seismic response of curved bridges. For 4-span bridges, the weak and strong earthquake errors increase with increasing radius of curvature. However, for 2-span and 3-span bridges, the curved bridge with a radius of 420 m in two spans and the curved bridge with a radius of 1000 m in three spans experienced lower average errors in very strong motions (84th percentile) than the other curves. This indicates that the effect of curvature on accuracy depends on the bridge configuration. The errors between the BEP curve and the accurate IDA vary depending on the earthquake magnitude (percentiles). Weaker and stronger earthquakes (84th and 16th percentiles) generally showed higher errors compared to moderate intensity (50th percentile).

1. Introduction

A systematic investigation into the impact of the design parameters of bridges (e.g. the radius of curvature and the longitudinal slope) on their seismic pounding response is necessary. However, there have only a few studies on these kinds of parameters of curved bridges. Naseri et al. (2020) [1] investigated effects of curvature radius on vulnerability of curved bridges subjected to near and far-field strong ground motions. Analytical seismic fragility curves have been derived thru considering uncertainties in the earthquake records, material and geometric properties of bridges. The findings indicate that near-field effects reasonably increase the seismic vulnerability in this bridge sub-class. The results pave the way for future regional risk assessments regarding the importance of either including or excluding near-field effects on the seismic performance of horizontally curved bridges.

Jiao et al. (2021) [2] evaluated experimental and numerical investigations on the effects of radius of curvature and longitudinal slope on the responses of curved bridges subject to seismic pounding.
Because of the irregular geometries, earthquake-induced adjacent curved bridge pounding may lead to more complex local damage or even collapse. A series of parametric studies were then conducted to examine the impacts of the radius of curvature and longitudinal slope of the superstructure of the curved bridge on its seismic pounding response. The results show that the maximum pounding force first increases and then decreases as the radius of curvature increases, but that it decreases monotonically with the growth of the longitudinal slope. These results suggest that controlling the radius of curvature and the longitudinal slope of the superstructure of the bridge can reduce the localized high stress that is induced by seismic pounding. Also, the unevenly distributed pounding forces can significantly increase the relative radial displacement of the bridge's deck corners, although the relative tangential displacement may decrease. It is thus necessary to adopt effective anti-pounding measures to prevent the superstructure of the bridge from being unseated.
Wilson et al. (2014) [3] performed a comprehensive performance analysis on eight bridge configurations of various degrees of skew and curvature. Nonlinear time-history analysis is carried out on each bridge configuration using detailed finite element models. The results show the curved bridge models induced higher moment demand in the weak axis of the substructure and overall lower shear demand in comparison to the other configurations. Curvature also introduced higher moment demand on the interior pier-columns, which increased with lower radii. However, when the pounding effect is considered, these laws may not be applicable. Results stated the relationship between the radius of curvature and the displacement and force demands on the curved bridge. Result showed that the curvature radius of the bridge has a relatively small influence on the tangential displacement at the four corners. The induced difference was within 33%. In general, as the radius of curvature decreases, the tangential displacement at the corners slightly decreases, indicating that the pounding between adjacent girders has a constraining effect on the tangential movement of the bridges' deck. Such an effect always increases as the radius of curvature decreases. Compared with the tangential displacement, the curvature radius has more impacts on the radial displacement. Results showed that the radial displacement changed abruptly when the radius of curvature was larger than 100 m. When the radius of curvature is 100 m, the maximum radial displacement at the corners has reached approximately 4.5 times that of the straight bridge. As the results, the torsional response of the main girder changed significantly with the radius of curvature. Compared with the straight one, the horizontal and vertical rotation of the model with the radius of curvature of 30 m are up 22.4 times and 18.3 times, respectively. Overall, as the radius of curvature decreases, the horizontal and vertical torsional responses significantly increases, which could be detrimental to the structure.
Mirza Goltabar Roshan et al. (2021) investigated effect of curvature radius on probabilistic evaluation of seismic horizontally Curves RC Box girder bridges using Monte Carlo simulation under three-dimensional excitations under Near-Field Earthquakes [4].
Agrawal and Kumar Gupta (2024) evaluated effect of radius of curvature on the seismic response of curved bridges [5].

Figure 1: A coastal curved bridge (Laguna Garzon bridge in Uruguay).

2. Methods

IDA is one of the most reliable methods, especially in the case of irregular structures, to estimate the seismic response of structures. In addition to the complexity associated with the formulation of the mathematical model, other major issues arise with respect to the definition of the seismic load, which can lead to different levels of uncertainty in terms of the global and local responses of the structure. Therefore, pushover analysis (nonlinear static analysis), with less time and simple initial principles and while ensuring results with appropriate accuracy, can be a suitable alternative method.

One of the methods that has appropriate accuracy, applicability and reliability and will be discussed in this study is the Bidirectional Energy Based Pushover (BEP) method. Because the capacity curve obtained from BEP is unique and the main parameters of the pusher (load pattern, control point and monitor point) cannot question the accuracy of this approach; because there is no need to select a point monitor to obtain the capacity curve and instead, all the monitor points must be displaced to calculate the energy absorbed in the pusher stage. This method has been evaluated in terms of accuracy and applicability in building structures. This is while the aim of this study is to extend this method to assess the seismic vulnerability of bridges with curvature in plan.

After identifying and selecting the methods and models considered for each element, and considering the defined uncertainties, the proposed models are modeled in OpenSeesPy software to perform IDA analysis. In order of material behavior, concrete, steel, geometry and modeling details, boundary conditions are selected based on previous studies, and modeling is performed accordingly.

However, since this approach relies on the assumption that the seismic response of any structure can be considered as the sum of the responses to individual modal forces (Soleimani et al. (2018)) [6], the effective and at the same time sufficient number of modes for the structure must be investigated. To do this, BEP is performed on the leading curve bridge for different numbers of modes.

In this section, we first introduced the class of bridges under study, and then discuss the details of modeling the substructure (columns and foundation), abutments, and deck.

The class of bridges studied in this study, based on the studies of Arajo et al. (2014) [7], Pinto et al. (1996) [8], Akbari (2012) [9] and Tehrani and Michel (2021) [10], has the following characteristics:

- Number of piers one, two and three respectively for two, three and four span bridges
- Height of piers 7, 14 and 21 meters
- Variable span length (100, 150 and 200 meters respectively for two, three and four spans and the length of each span is fixed and equal to 50 meters)
- Continuous deck (two, three and four spans)
- Deck width 14 meters
- Angles of curvature in the horizontal plane for two, three and four span bridges are equal to 130, 240, 420, 700 and 1000 meters respectively

Direction Modeling The reference bridge model tested in the Elsa laboratory by Pinto et al. (1996) [8] was used (Figure 2). This model was a straight bridge and all its geometric characteristics were used for modeling this research.

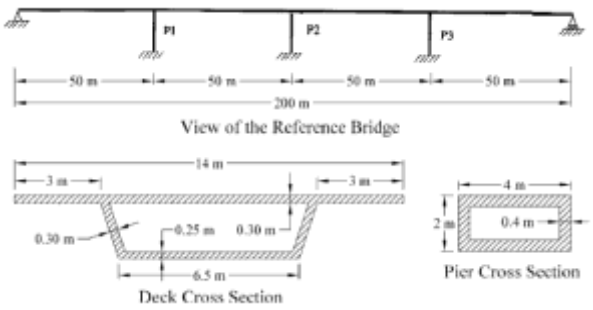

Figure 2: Configuration and details of the bridge studied by Pinto et al. (1996) at the Elsa Laboratory [8].

Reinforced concrete columns with a rectangular hollow section in the OpenSeesPy software must be modeled as Nonlinear Beam Column. Therefore, fiber has been used to consider the nonlinear behavior of the columns. On the other hand, the element used to model the columns is displacement-based beam-column elements. The cross-section of the columns in OpenSeesPy is defined as fiber elements to allow for the formation of a plastic hinge widely across the cross-section of the member.

Element: Displacement-based beam-column elements are used to model the columns, which allow the formation of plastic hinges in each part of the element. The upper and lower parts of the column, in other words, the connection between the top of the column and the deck and the base of the column and the

foundation, are modeled using rigid elements to enable the transfer of moment and force between these members. To create the rigid element in OpenSeesPy, elastic beam-column elements with very high stiffness are used (because we expect the deck to remain elastic during an earthquake).

In the modeling, the columns are divided into 10 parts (mesh). It is worth noting that due to the symmetry of the columns, the consideration of rotational mass has been omitted (because the columns do not have eccentricity). Figure 3 shows the discrete finite element model of the single columns that has been studied.

Mass: Since the columns are fiberized and divided into 10 parts, half the mass is allocated to the first and last nodes (nodes 1 and 10) and the full mass is allocated to the remaining nodes (nodes 2 to 8).

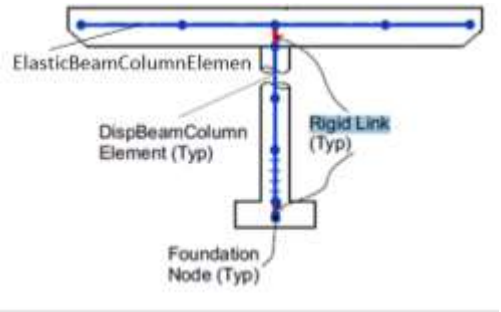

Figure 3: Single column discrete finite element model (schematic).

Bridge foundation modeling in OpenSeesPy: According to studies and information collected from the bridge maps studied by Ramanathan [11], a significant percentage of bridges, both in the middle frames and in the abutments, have extensive foundations supported by cast-in-place reinforced concrete piles. The structural system of the foundation consists of several vertical piles with a cap (the cap is modeled with a rigid element).

Materials: In this study, Uniaxialmaterials were used for the rotational and translational springs. For the rotational springs of two-span bridges, a value of 6.5 × 107 kip.in in radians has been assigned, and for three- and four-span bridges, no value has been assigned due to the articulated construction of the column footings (this information is based on the data and research of Ramanathan et al. in 2012 [12]). For the translational spring of two-span bridges, a value of 1400 kip/in has been used, and for three- and four-span bridges, a value of 1200 kip/in has been used (Ramanathan (2012)) [12].

Element: In OpenSeesPy, two coincident nodes are connected using the zeroLength element. In the present study, this element has been used to build the foundation model.

Mass: In this study, the calculation of the mass of the foundation has been omitted (based on technical literature).

Deck modeling: The height of the reinforced concrete box of the bridge decks under study is considered to be 2.3 m, based on the research of Pinto et al. [8] in 1996, which was carried out at the Elsa Laboratory. The width of the deck is also considered to be 14 m, and the geometric characteristics of the deck are modeled according to the reference model in the SAP2000 software. According to Figure 4, the box and single-cell decks are modeled. As can be seen in Figure 5, the box deck of the bridge class under study is modeled with one cell.

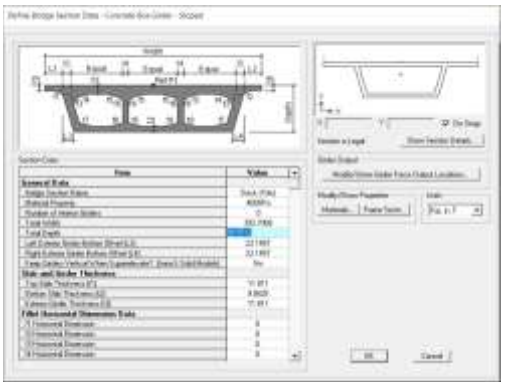

Figure 4: Deck specifications of the studied bridge class.

Based on these details, the cross-sectional area parameters and moment of inertia of the box-shaped deck of the bridges in two different directions (strong axis, Y and weak axis Z) were calculated and assigned to the elastic beam-column element of the deck in the OpenSeesPy software. Figure 7 shows the analytical deck model of one of the bridge models under study (a two-span bridge with a radius of 130 m) in the OpenSeesPy software, displaying the nodes in the longitudinal direction (20 nodes) and in the transverse direction (7 nodes for each section).

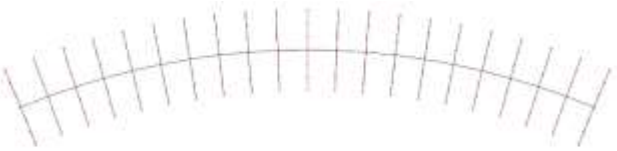

Figure 5: Analytical model of a box deck of a two-span bridge with a radius of 130 meters in OpenSeesPy software

The mechanical specifications of the deck are the same as the reference model and are considered as follows for deck modeling (unit kN, m):

fc=42.0e6

Ec= 2.5e10

Gc= 1.0e10

IzDeck=88.4

IyDeck=5.36

JDeck=11.7

ADeck=6.96

A three-line model based on the model proposed by Choi (2002) was used to model the behavior of piles [13]. It is worth noting that in this study, the bridge class with integral keel was used for modeling and according to the reference model, there is no gap between the deck and the keel and the effect of the side walls was ignored in this study. In the modeling, the keel was divided into seven equal parts on each side and a tangential and a radial spring were assigned perpendicular to each node. The ZeroLength element was used for the springs.

Figure 6 shows a representation of the 70PC class pile model. It is worth noting that only the pile stiffness, K, which is a constant value and is obtained from the derivative of the slope of the line in Figure 8, is considered in the modeling (the pile stiffness is modeled with a spring).

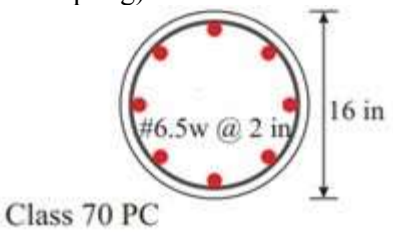

Figure 6: 70PC class pile model where only the pile stiffness, K, is used in the modeling with a constant value (Ramanathan 2012) [12]

It is worth noting that in the X direction (degree of freedom 1) the piles and the backfill soil are considered parallel, and in the Y direction (degree of freedom 2) we have only the piles.

Figure 7 shows the finite element model of a four-span curved bridge. In this figure, the deck, along with the longitudinal and transverse elements, abutments, columns, and bridge foundation, are defined with materials, and the details are shown along with the behavior of the relevant materials.

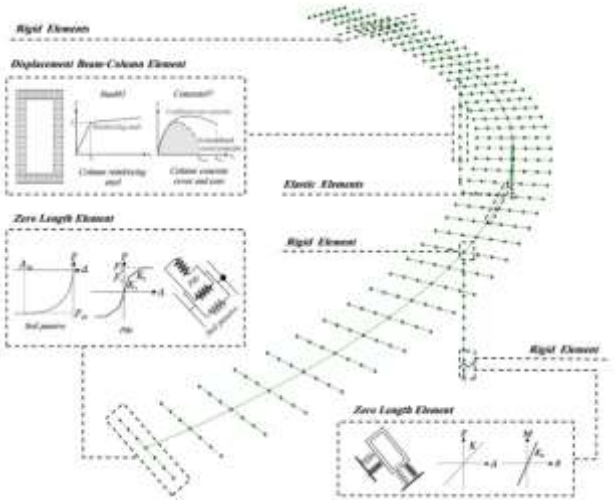

Figure 7: Finite element model of a four-span curved bridge

Study Bridges

Three-dimensional analytical modeling of the study bridges was performed in the OpenSeesPy software based on the analytical models presented by Pinto et al. (1996) [8], Araujo et al. (2014) [7] and Ramanathan (2012) [12]. It was performed by considering 5 radii of curvature (130, 240, 420, 700, and 1000 m) in the horizon line for the plan of the study bridges [11], different numbers of spans (two, three, and four spans), earthquake impact angles (0, 45, and 90 degrees), and 22 different FEMA-P690 earthquake records from g0.1 to g3.7. Two main reasons can be given for choosing these different curvatures, the first reason is the significant difference in their dynamic response (due to the change in the structural structure of these models) and the second reason is the difference in the correspondence between nonlinear static analysis (push-pull analysis) and nonlinear dynamic analysis (nonlinear time history analysis). The reason for choosing different numbers of spans is that by changing the model, the angle of curvature, θ, (θ = L/R, L is the length of the deck and R is the radius of curvature) changes, which causes a change in the dynamic response of the structure. On the other hand, the reason for choosing different angles of impact of earthquakes is the angle of the bridge structural members such as the girders, columns and deck, relative to the general axis. For example, by changing the local axes or the strong axis of the columns or girders relative to the general axis, a change in the dynamic response of the structure may be obtained, which should be investigated. The nomenclature and geometric specifications of the 15 bridge classes studied are described in Table 1 for radii of 130, 240, 420, 700 and 1000 m in the two-, three- and four-span bridge classes, respectively.

First step: First, all the mechanical parameters of the members (including the cross-sectional area of the reinforcement, compressive strength, elastic modulus of concrete and steel materials, yield strength of steel, etc.) and uncertainties of the applied seismic force (including earthquake characteristics and properties) are identified and modeled to build a model for fragility assessment. In addition, the capacity functions and limit state functions of the types of bridge elements that are necessary for fragility assessment are also studied and extracted from technical references. In this step, methods for selecting appropriate earthquake records are also discussed, and accordingly, appropriate earthquakes are selected from the existing earthquake collection based on scientific and appropriate methods to perform probabilistic seismic vulnerability assessment of bridge models. For this purpose, a set of 22 pairs of far-field earthquake records (FEMA P-695) is used.

As shown in Figure 1, the record set covers a diverse spectrum of earthquakes with significant effects, including variations in duration and frequency content (16th, 50th,

and 84th percentiles). This diversity helps to create a more general dataset for the training algorithm in the following chapters.

Step 2: Based on the objectives of this research, in this step, curved bridges in plan are carefully and thoroughly studied in the technical literature and the effects of irregularities on the seismic behavior of various bridge members are identified. In this section, an attempt is made to identify the factors that have a greater impact on the results of fragility analysis so that these factors can be used in the subsequent sections where rapid methods are to be developed. In addition, definitions and values of bridge curvature available in the technical literature are identified and, based on this, curvature angles are selected and used to model curved bridges in the plan.

Step Three: Performing fragility analysis on all probabilistic models constructed in the first step and based on the selected irregularity levels, regular and irregular models are produced in the second step. All these regular and irregular models produced are subjected to IDA by the set of earthquakes selected in the first step and then its results, along with the capacity functions determined in the first step, are used for fragility analysis. In this step, first, the factors affecting the behavior of irregular bridges will be investigated and their fragility values will be compared with the aim of identifying the factors affecting the seismic behavior of irregular bridges. On the other hand, the results of this step will be used to validate the rapid method discussed in this study. Step Four: In this step, fragility analysis is performed for probabilistic models built based on selected irregularity levels using the probabilistic capacity spectrum method and considering record-to-record changes. In this step, using the IDA results in the third step, the validity and accuracy of this method are evaluated and then, in accordance with the factors identified in the first and second steps, this method will be improved and modified based on the reliability capabilities of this method for the model of bridges with curvature in plan.

One of these simple and practical methods is the Bidirectional Energy Pushover (BEP) method. This method uses the work done by lateral loads and moments, through Pushover analysis, as an index to determine the characteristics of modal single-degree-of-freedom systems. The proposed formulation of this method allows for the simultaneous effect of both components of ground motion in each mode. To combine the modal responses of this method, a modified perfect quadratic combination (CQC) method is also presented, which is specifically developed for two-component excitations. The accuracy of this proposed method is investigated on a two-way asymmetric three-story building. The findings show that BEP is able to estimate the two-component IDA results with sufficient accuracy. A bilinear energy-based pushover analysis has been developed to approximate the two-component IDA curves for buildings that are asymmetrical in plan. BEP applies both components of a ground motion simultaneously to each mode and uses a modified CQC combination rule to combine the modal responses. In addition, the energy-based approach used in BEP eliminates the possibility of changes in the pushover curve in the capacity curves. These features minimize the impact of the complexities associated with asymmetry in buildings and the two-component nature of the ground motion on the accuracy of BEP. In this study, the intention is to use this method to estimate the response of irregular bridges in plan and to evaluate its performance.

Step 5: In this step, the results of the rapid fragility analysis method are evaluated and compared, and its solutions, limitations, and advantages are stated. On the other hand, the parameters and factors affecting the results of the fragility analysis of curved bridges in plan are discussed and suggestions are made to improve the performance and also increase the accuracy of the rapid method.

In summary, the set of necessary measures to reach the fragility curves in this study is as follows:

• Collecting a set of earthquakes that indicate the risk of areas with high seismicity and include a wide range of severity criteria

• Building three-dimensional nonlinear analytical models using analytical models of various bridge members

• Determining critical members by performing a deterministic analysis on the model

• Building probabilistic models of seismic demand for each member at each angle of curvature of the bridge

• Using a combination of descriptive and prescriptive approaches in building limit state models

• Drawing system fragility curves for different angles of curvature of the bridge for different angles of impact.

In this study, considering the variety of structural analysis methods for estimating seismic demand, in addition to a complete description of how to model the nonlinear behavior of elements and configure the hollow section bridge system, nonlinear analysis methods such as nonlinear statics and IDA on bridge structures are investigated and evaluated. In addition, the IDA method under two-component ground motions has received less attention as a requirement for evaluating curved bridges in plan. Therefore, to fill this study gap, this study has presented a method for approximating two-component IDA in bidirectional energy-based Pushover analysis (BEP).

Table 1: 22 different FEMA-P695 earthquake records used in this study from 0.1 g to 3.7 g.

	Ground Motion X Dir		
	GMPath	dt	NPTS
1	YER360.AT2.txt	0.02	2200
2	TCU045-E.AT2.txt	0.005	18000
3	SHI000.AT2.txt	0.01	4096
4	RIO360.AT2.txt	0.02	1800
5	PEL180.AT2.txt	0.01	2800
6	NIS000.AT2.txt	0.01	4096
7	MUL009.AT2.txt	0.01	2999
8	LOS000.AT2.txt	0.01	1999
9	HEC000.AT2.txt	0.01	4531
10	H-E11140.AT2.txt	0.005	7807
11	H-DLT352.AT2.txt	0.01	9992
12	G03000.AT2.txt	0.005	7989
13	DZC180.AT2.txt	0.005	5437
14	CLW-LN.AT2.txt	0.0025	11186
15	CHY101-E.AT2.txt	0.005	18000
16	CAP000.AT2.txt	0.005	7991
17	BOL000.AT2.txt	0.01	5590
18	B-POE360.AT2.txt	0.01	2230
19	B-ICC000.AT2.txt	0.005	8000
20	ARC000.AT2.txt	0.005	6000
21	ABBAR--L.AT2.txt	0.02	2676
22	A-TMZ000.AT2.txt	0.005	7269

Table 2: Nomenclature and geometric specifications of the 15 bridge classes studied

Row	Class of bridge	Number of spans	Number of columns per frame	Angle of curvature in line with the horizon (degrees)	Span length (m)	Deck width (m)	Column height (m)
١	2 Span-130	٢	١	١٣٠	١٠٠	١٤	٧
٢	2 Span-240	٢	١	٢٤٠	١٠٠	١٤	٧
٣	2 Span-420	٢	١	٤٢٠	١٠٠	١٤	٧
٤	2 Span-700	٢	١	٧٠٠	١٠٠	١٤	٧
٥	2 Span-1000	٢	١	١٠٠٠	١٠٠	١٤	٧
٦	3 Span-130	٣	١	١٣٠	١٥٠	١٤	١٤ ، ٧
٧	3 Span-240	٣	١	٢٤٠	١٥٠	١٤	١٤ ، ٧
٨	3 Span-420	٣	١	٤٢٠	١٥٠	١٤	١٤ ، ٧
٩	3 Span-700	٣	١	٧٠٠	١٥٠	١٤	١٤ ، ٧
١٠	3 Span-1000	٣	١	١٠٠٠	١٥٠	١٤	١٤ ، ٧
١١	4 Span-130	٤	١	١٣٠	٢٠٠	١٤	٢١ ، ١٤ ، ٧
١٢	4 Span-240	٤	١	٢٤٠	٢٠٠	١٤	٢١ ، ١٤ ، ٧
١٣	4 Span-420	٤	١	٤٢٠	٢٠٠	١٤	٢١ ، ١٤ ، ٧
١٤	4 Span-700	٤	١	٧٠٠	٢٠٠	١٤	٢١ ، ١٤ ، ٧

١٥	4 Span-1000	٤	١	١٠٠٠	٢٠٠	١٤	٢١ ،١٤ ،٧

The column arrangement for the two-span bridge class is 7 meters, for the three-span bridge class, 7 and 14 meters respectively from left to right, and for the four-span bridge class, 14, 7 and 21 meters respectively from left to right (known as the P213 bridge in previous studies).

In the OpenSeesPy software, the fiber model has a unique feature that allows the definition of materials with different characteristics at different points of the cross-section. For example, the characteristics of unconfined concrete can be assigned to the concrete cover and confined concrete to the concrete core. In addition, the location of the reinforcements along with their diameters on the fiber cross-section are specified and the characteristics of the steel used in the longitudinal reinforcements are assigned to them. In the present study, the fiber model has been used to model the nonlinear behavior in columns.

In this study, the behavior of the concrete of the bridge components was modeled using the Concrete07 material, which is the newest material type available in the OpenSeesPy software. This material uses the Cheng and Mander (1994) model [14] to define the stress-strain curves for confined and unconfined concrete. This model is based on statistical analysis of laboratory Concrete07 material was used to model concrete in the OpenSeesPy software, which uses the Cheng and Mander model [14]. The method for obtaining its parameters for unconfined and confined concrete is given below [17].

Table 3: Specifications of the concrete used [17].

Parameters	values
(E) Modulus of elasticity (GPa)	30.5
Concrete Compressive (f'_c) Strength (MPa)	42
Tensile Strength (MPa) (F_t)	Waste
Strain at Maximum Compressive Stress	0.002
Confinement Factor	1.2
Specific weight (kN/m^3)	24

data obtained from cyclic compression tests conducted by a number of researchers.

Figure 8 shows the stress-strain curves of concrete in different unconfined and confined states with different stirrup spacings. The reinforcement of the bridge components was also modeled using the Steel02 material available in the OpenSeesPy software. This type of material uses the model of Mangoto and Pinto (1973) [15], modified by Filippo et al. (1983) [16], and is also capable of modeling isotropic strain hardening in steel.

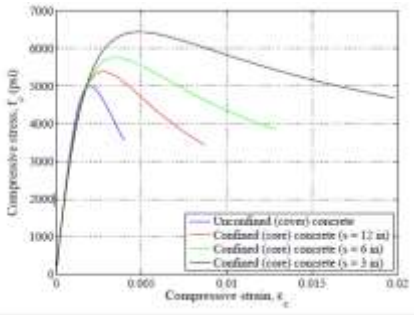

Figure 8: Comparison of concrete behavior curves at different levels of confinement

Table 4: Characteristics of steel used [17].

Parameters	values
(E) Modulus of elasticity (GPa)	200
(Fy) Yield stress of steel (MPa)	500
Strain hardening parameter (b)	0.005
Primary parameter of the shape of the transfer curve (a1, a2)	20
Transition curve calibration shape coefficients (a3, a4)	18.5 , 0.15
Isotropic hardening calibration coefficients	0 , 1
Specific weight (kN/m^3)	77

The constants Xn and Xp for confined concrete are taken to be 30 and 2 [18] according to figure 9.

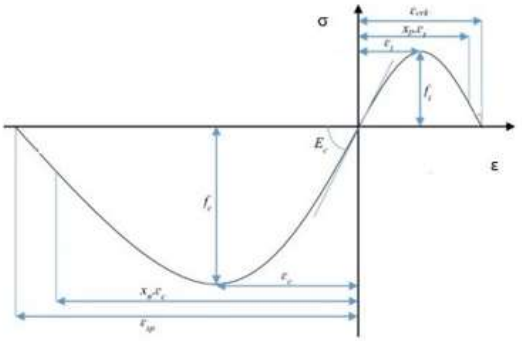

Figure 9: General stress-strain diagram used in Concrete07 materials (not to scale) [18].

3. Results and Discussions

In this study, the results discussed are used to complete the proposed framework, which leads to a fragility curve with low computational cost and high accuracy. For this purpose, the estimated EDP in the BEP and IDA results is converted into damage levels. In addition, 7 earthquake parameters are defined to determine stronger, milder or weaker earthquakes, as the results show that the accuracy of BEP varies between these classifications. Two structural features (radius and length) are used in the training process to predict the IDA damage levels along with 8 other features as figure 10.

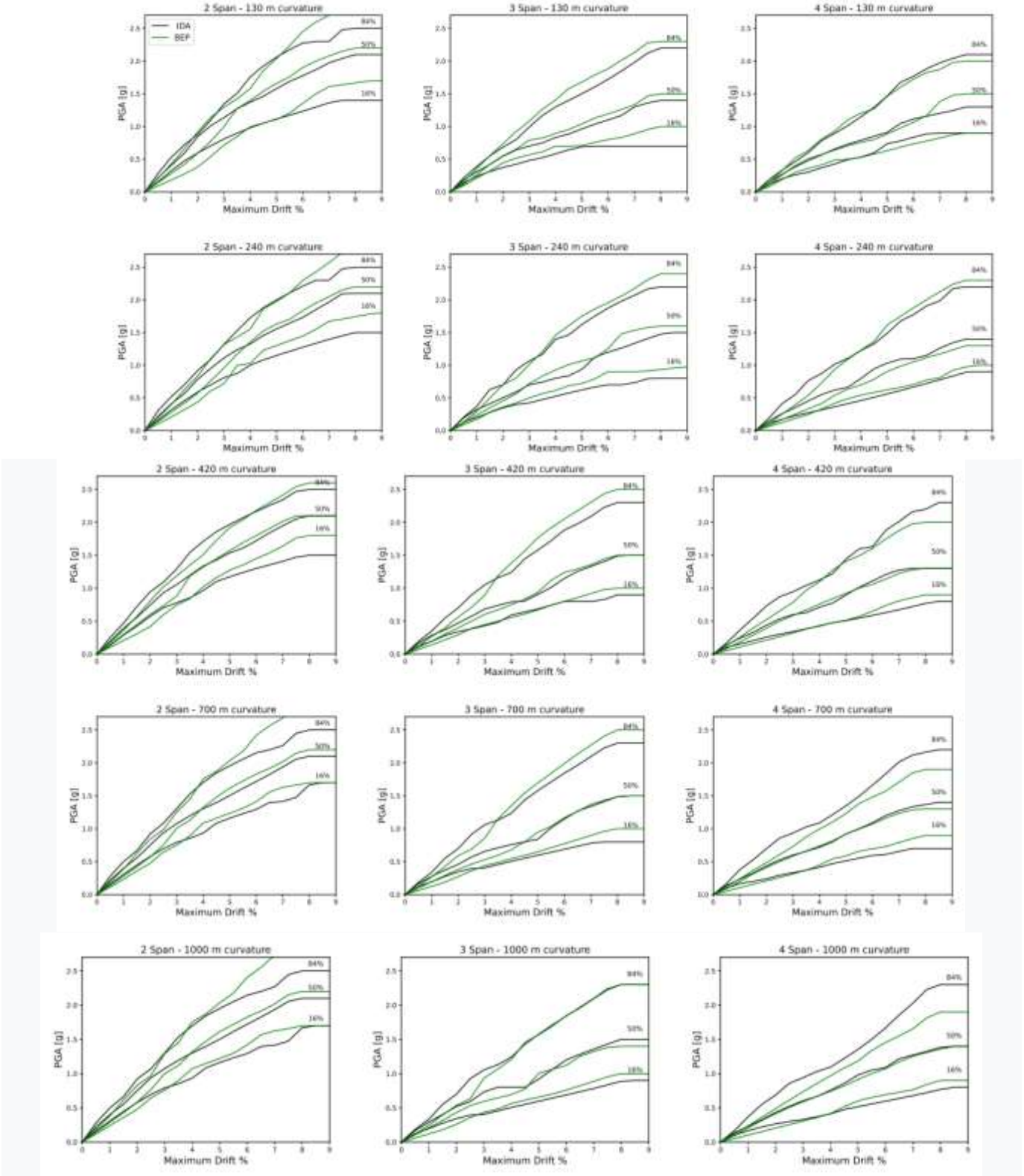

Figure 10: Results of BEP with two modes in a set of curved bridges

4. Conclusions

This research introduces a new framework for seismic performance assessment of complex structures. The framework achieves high accuracy and significantly reduces the computational burden associated with detailed finite element models. This study uses a set of distinct RC curved bridges to validate the accuracy of the framework through comparison with incremental dynamic analysis (IDA), which serve as examples of complex structures. To generalize the approach, the set includes curved bridges with important differences, including different curvatures, number of spans, and column height configurations. In addition, earthquakes with variations in amplitude, duration, and frequency content are selected to consider the effects of different earthquake strengths. First, the framework uses a bidirectional energy-based pushover (BEP) analysis to approximate the behavior of the structure. In this study, BEP is specifically extended for curved bridges to represent the nonlinear behavior of curved bridges with low computational costs. The accuracy of this method was observed by evaluating the following results:

• The relationship between bridge curvature and BEP accuracy appears to be complex, and other factors such as the number of spans and column height also play an important role. For 4-span bridges, the weak and strong earthquake errors increase with increasing radius of curvature. However, for 2-span and 3-span bridges, the bridge with moderate curvature (420 m) showed the lowest error. This indicates that the effect of curvature on accuracy depends on the bridge configuration.
• The errors between the BEP curve and the accurate IDA vary depending on the earthquake magnitude (percentiles). Weaker and stronger earthquakes (84th and 16th percentiles) generally showed higher errors compared to moderate intensity (50th percentile).
At radii of curvature of 130 and 240 meters, the values of the 84% damage level with the IDA and BEP methods are closer to each other, and with increasing the radius of curvature to 420 meters, 700 meters, and 1000 meters, the results of the maximum relative displacement at the 84% damage level differ more from each other, and the results in the four-span case at the 84% damage level with the BEP method are lower than with the IDA method.
Results by Wilson et al. (2014) [3] showed that the radial displacement changed abruptly when the radius of curvature was larger than 100 m. When the radius of curvature is 100 m, the maximum radial displacement at the corners has reached approximately 4.5 times that of the straight bridge. As the results, the torsional response of the main girder changed significantly with the radius of curvature. Compared with the straight one, the horizontal and vertical rotation of the model with the radius of curvature of 30 m are up 22.4 times and 18.3 times, respectively. Overall, as the radius of curvature decreases, the horizontal and vertical torsional responses significantly increase, which could be detrimental to the structure.
In this paper, by increasing the radius of curvature from 130 meters and above, we achieve the highest relative displacement for smaller values of PGA. By increasing the number of spans at a fixed radius of curvature, we achieve the highest relative displacement for smaller values of PGA. These results confirm the results by Wilson et al. (2014) [3]. The most irregular curved bridge with the highest length-to-radius ratio experiences the lowest average error between the exact and approximate IDA. However, a relatively large error in the 16th percentile of the three-span curved bridge with a curvature of 130 m indicates that the consistency of this approach is not simply related to the length-to-radius ratio and that the difference between the column heights plays an important role. As a result, the validity of this approach is different for each category in this study. In the four-span curved bridge category, the errors related to very weak or very strong ground motions (16th and 84th percentiles) increase from 5% to 17% with an increase in the radius of curvature to 1000 m, while the 50th percentile acts in the opposite way. The results are relatively different for two-span and three-span bridges; For these two categories with less irregularity than the other, the curved bridge with a radius of 420 m in two spans and the curved bridge with a radius of 1000 m in three spans experienced lower average errors in very strong motions (84th percentile) than the other curves. Furthermore, this approach led to perfectly consistent results for weaker earthquakes (84th and 50th percentiles) in the two-span curved bridge with the mentioned

curvature, while stronger earthquakes (16th and 50th percentiles) were better predicted in the three-span curved bridge, indicating that the radius can affect the accuracy of the approach differently depending on the number of spans (length and irregularity). Therefore, both radius (R) and length (L) are used as important features in the following chapter.

5. References

1. Ali Naseri, A.R. M.Goltabar.R, Hossein Pahlavan and Gholamreza Ghodrati Amiri .2020. Effects of curvature radius on vulnerability of curved bridges subjected to near and far-field strong ground motions. Structural Monitoring and Maintenance 7(4):367-392.
2. Chiyu Jiao, Junrui Lu, Chuang Wang, Peiheng Long, Zhe Sun. 2021. Experimental and numerical investigations on the effects of radius of curvature and longitudinal slope on the responses of curved bridges subject to seismic pounding. Measurement and Control. Volume 54, Issue 3-4.
3. Wilson T, Mahmoud H, Chen S. 2014. Seismic performance of skewed and curved reinforced concrete bridges in mountainous states. *Eng Struct*: 70: 158–167.
4. Alireza Mirza Goltabar Roshan., Hossein Pahlavan., Gholamreza Ghodrati Amiri. Effect of curvature radius on probabilistic evaluation of seismic horizontally Curves RC Box girder bridges using Monte Carlo simulation under three-dimensional excitations under Near-Field Earthquakes. *Journal of Structural and Construction Engineering (JSCE)*, 2021. Volume 8, Issue 7. Pages 5-30.
5. Suyesha Agrawal and Praveen Kumar Gupta. 2024. Effect of radius of curvature on the seismic response of curved bridges. *IOP Conf. Ser.: Earth Environ. Sci*. 1326 012017.
6. Soleimani, S., Aziminejad, A., & Moghadam, A. S. (2017). Extending the concept of energy-based pushover analysis to assess seismic demands of asymmetric-plan buildings. Soil Dynamics and Earthquake Engineering, 93, 29-41.
7. Araújo, Miguel, Mário Marques, and Raimundo Delgado. (2014) "Multidirectional pushover analysis for seismic assessment of irregular-in-plan bridges." Engineering Structures 79: 375-389.
8. Pinto, A. V., Verzeletti, G., Magonette, G., Pegon, P., Negro, P., & Guedes, J. (1996). Pseudo-dynamic testing of large-scale R/C bridges in ELSA. In 11th world conference on earthquake engineering (pp. 23-28).
9. Akbari, R. (2012). Seismic fragility analysis of reinforced concrete continuous span bridges with irregular configuration. Structure and Infrastructure Engineering, 8(9), 873-889.
10. Tehrani, P., & Mitchell, D. (2021). Prediction of mean responses of RC bridges considering the incident angle of ground motions and displacement directions. Applied Sciences, 11(6), 2462.
11. Ramanathan, K., DesRoches, R., & Padgett, J. E. (2010). Analytical fragility curves for multispan continuous steel girder bridges in moderate seismic zones. Transportation Research Record, 2202(1), 173-182.
12. Ramanathan, K. N. (2012). Next generation seismic fragility curves for California bridges incorporating the evolution in seismic design philosophy. Georgia Institute of Technology.
13. Choi, E. (2002). Seismic analysis and retrofit of mid-America bridges. Georgia Institute of Technology.
14. Chang, G. A., & Mander, J. B. (1994). Seismic energy based fatigue damage analysis of bridge columns: Part I-Evaluation of seismic capacity (p. 222). Buffalo, NY: National Center for Earthquake Engineering Research.
15. Menegotto, M., Pinto, P. E. (1973). Method of Analysis for Cyclically Loaded Reinforced Concrete Plane Frames Including Changes in Geometry and Non-Elastic Behavior of Elements Under Combined Normal Force and Bending, Proceedings of the IABSE Symposium on Resistance and Ultimate Deformability of Structures Acted on by Well-Defined Repeated Loads, Lisbon, Portugal, pp: 15-22.
16. Filippou, F. C., Popov, E. P. Bertero, V. V. (1983). Effects of Bond Deterioration on Hysteretic Behavior of Reinforced Concrete Joints, Report No. EERC 83-19, Earthquake Engineering Research Center, University of California, Berkeley, CA.
17. Monteiro, Ricardo Nuno Carvalho. (2011) "Probabilistic seismic assessment of bridges." PhD diss., Universidade do Porto, Portugal.
18. Pahlavan, H., Zakeri, B., Amiri, G. G., & Shaianfar, M. (2015). Probabilistic vulnerability assessment of horizontally curved multiframe RC box-girder highway bridges. Journal of Performance of Constructed Facilities, 30(3), 04015038.

INTERNATIONAL JOURNAL OF
COASTAL, OFFSHORE & ENVIRONMENTAL ENGINEERING IJCOE Vol.11 /No.1 /Winter 2026 (57-69)

Available online at: www. ijcoe.org

Deterministic Tsunami Hazard Assessment for a Nearshore–Onshore Domain close to the Strait of Hormuz: The Overlooked Threat of the Western Makran Segment and Tidal Sensitivity

Mohammad Hossein Kazeminezhad [1*]; Mahmood Reza Akbarpour Jannat [2]; Ehsan Rastgoftar[3]

[1*]*Iranian National Institute for Oceanography and Atmospheric Science, No.3, Etemad Zadeh St., Fatemi Ave, P.C: 1411813389, Tehran, Iran, E-mail: mkazeminezhad@inio.ac.ir*
[2]*Iranian National Institute for Oceanography and Atmospheric Science, No.3, Etemad Zadeh St., Fatemi Ave, P.C: 1411813389, Tehran, Iran, E-mail: akbarpour@inio.ac.ir*
[3]*Iranian National Institute for Oceanography and Atmospheric Science, No.3, Etemad Zadeh St., Fatemi Ave, P.C: 1411813389, Tehran, Iran, E-mail: e.rastgoftar@inio.ac.ir*

ARTICLE INFO

Article History:
Received:31 Aug 2025
Accepted:14 Jan 2026

Keywords:
Makran Subduction Zone
Tsunami Modeling
Strait of Hormuz
Tidal Sensitivity
Hydrodynamic Loads

ABSTRACT

The Makran Subduction Zone (MSZ) represents a critical tsunamigenic structure in the northwestern Indian Ocean. While the historical seismicity of the eastern segment has been extensively studied following the 1945 earthquake, the hazard potential of the western segment, specifically its threat to strategic energy infrastructure near the Strait of Hormuz, remains poorly constrained. This study presents a high-resolution deterministic tsunami hazard assessment for the Kooh Mobarak coastal onshore developments and its associated marine facilities. Utilizing the ComMIT/MOST numerical model within a nested grid framework, twelve fault rupture scenarios ranging from M_w 8.0 to 9.0 were simulated across the western, central, and eastern Makran segments. The results challenge conventional hazard zonations, demonstrating that a rupture in the Western segment (M_w 8.9) generates wave heights (~2.8 m) and current velocities (>2.0 m/s) at the Kooh Mobarak area that are comparable to those of a worst-case Central Makran scenario (M_w 9.0). Furthermore, a sensitivity analysis regarding the initial tidal level reveals a critical hydrodynamic dichotomy: while increasing the water level to Mean High Water Springs (MHWS) slightly attenuates the pure tsunami amplitude due to reduced non-linear shoaling, it significantly elevates the Total Water Level, thereby expanding the inundation extent into backshore tidal creeks. These findings underscore the imperative of adopting a dual-criterion design approach that incorporates near-field western ruptures and compound tidal interactions to ensure the resilience of critical coastal structures.

1. Introduction

The Makran Subduction Zone (MSZ), an extensive geological feature stretching approximately 900 km along the northern Arabian Sea, represents one of the most enigmatic and potentially hazardous tsunamigenic structures in the Indian Ocean basin. Formed by the northward subduction of the Arabian Plate beneath the Eurasian Plate at a rate of approximately 4 cm/year, the MSZ is characterized by an exceptionally thick accretionary wedge, sediments scraped off the subducting plate, which exceeds 7 km in thickness. This unique geological configuration distinguishes it from other well-studied subduction zones, such as the Japan Trench or the Sumatra-Andaman zone. While the seismic recurrence intervals in the Makran region are historically longer than those of the Pacific Ring of Fire, the geomorphological evidence suggests a capacity for generating mega-thrust earthquakes with magnitudes exceeding M_w 8.5 (Heidarzadeh et al., 2008; Smith et al., 2013). The catastrophic potential of this region was vividly demonstrated on November 28, 1945, when an M_w 8.1

earthquake occurred in the eastern segment of the MSZ. This event generated a trans-oceanic tsunami that devastated the coasts of Pakistan, Iran, Oman, and western India, claiming over 4,000 lives. Reports of run-up heights exceeding 12 meters in some localities, combined with the delayed arrival of the largest waves, have led researchers to hypothesize that the 1945 event was likely amplified by secondary submarine landslides triggered by the seismic shock (Okal and Synolakis, 2008; Rajendran et al., 2008). This historical precedent underscores a critical reality: despite the paucity of instrumental records compared to other subduction zones, the Makran coast is highly vulnerable to extreme hydrodynamic events.

From a tectonic perspective (Fig. 1), the MSZ is complex and heterogeneous. It is widely accepted in the scientific community that the zone is segmented into eastern and western blocks, separated roughly by the Sonne Fault or the Pol-Abneh interpretation structure (Kukowski et al., 2001). The eastern segment, located primarily offshore Pakistan, has been seismically active in recent history and is relatively well-documented in earthquake catalogs. Conversely, the western segment, extending offshore from the Iranian coast towards the Strait of Hormuz, has exhibited a distinct lack of large instrumental earthquakes over the past few centuries. This prolonged period of quiescence has created a prominent "seismic gap" (Byrne et al., 1992). This has led to significant debate regarding the frictional properties of the plate interface. Early hypotheses suggested that the western Makran might be behaving a seismically, releasing stress through stable sliding or "creep" due to the high-water content within the soft sediments. However, recent advancements in geodetic monitoring and thermal modeling have challenged this view. GPS measurements of coastal uplift and plate motion vectors strongly suggest that the plate interface in the western Makran is structurally coupled (locked) to a significant depth (Frohling and Szeliga, 2016; Penney and Copley, 2019). If this locking hypothesis holds true, the accumulated elastic strain over centuries could be released in a future mega-thrust earthquake with a magnitude comparable to, or exceeding, the 1945 event. Consequently, hazard assessments that focus solely on the historically active eastern segment, or assume the western segment is benign, may drastically underestimate the risk to the rapidly developing Iranian coast.

In the aftermath of the devastating 2004 Indian Ocean Tsunami, the scientific community intensified efforts to quantify the hazard in the northwestern Indian Ocean. Pioneering numerical studies by Heidarzadeh et al. (2008, 2009) provided the first systematic evaluation of historical and hypothetical tsunamis in the region. Their work was instrumental in establishing regional propagation patterns and verifying the source mechanisms of the 1945 event. Concurrently, field surveys and theoretical analyses by Okal and Synolakis (2008) highlighted the complexity of tsunami generation in the Makran, emphasizing the role of sedimentary features. More recently, El-Hussain et al. (2016) presented a comprehensive Probabilistic Tsunami Hazard Assessment (PTHA) for the coast of Oman, providing valuable return period estimates for various wave heights. Regarding the Iranian coastline, however, site-specific engineering studies have been geographically skewed. The majority of research has concentrated on the port of Chabahar and the eastern sectors, driven by the proximity to the 1945 rupture zone (Mokhtari, 2011; Rashidi et al., 2020). Furthermore, many of these regional studies utilized relatively coarse bathymetric grids, which are insufficient for resolving the complex wave-structure interactions in nearshore environments. As a result, the specific hydrodynamic risks to the westernmost extremity of the Makran zone, specifically the Kooh Mobarak region, remain poorly understood. This lack of detailed data is particularly concerning given the complex coastal morphology of the area, which includes tidal creeks (Khors) and shallow shelves that can significantly alter tsunami amplification factors.

In this study, Kooh Mobarak is selected as the case-study area due to ongoing marine-oriented development and the presence of diverse coastal and offshore infrastructure, including ports, breakwaters, jetties, energy-related facilities, and offshore loading and mooring systems. Unlike static coastal structures, offshore facilities are particularly sensitive not only to wave height (run-up) but also to current velocities. Strong tsunami-induced currents can exert substantial drag forces on moored vessels and subsea pipelines, potentially triggering operational failures or environmental impacts even when coastal inundation is moderate. Therefore, generic regional hazard maps may be insufficient for the design and safety assessment of such high-value assets, and high-resolution local modeling is warranted.

Another critical limitation in many existing deterministic assessments is the simplification of the background sea level. Most studies simulate tsunami run-up assuming Mean Sea Level (MSL) as a static datum. However, the Persian Gulf and the Gulf of Oman are characterized by a mixed semi-diurnal tidal regime with significant tidal ranges, often exceeding 2 meters. The interaction between a tsunami wave train and the astronomical tide is non-linear; the water depth modulation caused by tides affects the wave celerity, shoaling coefficients, and bottom friction dissipation (Kowalik and Proshutinsky, 2010). Neglecting the High-Water Spring (MHWS) condition, effectively the "worst-case" hydraulic scenario, can lead to a dangerous underestimation of the maximum inundation limit and the total water level required for determining the crest elevation of coastal defense structures. Conversely, ignoring low-tide conditions might

underestimate the current velocities induced by the receding drawdown.

To address these knowledge gaps and provide a robust basis for engineering design, this study presents a comprehensive, high-resolution deterministic tsunami hazard assessment for the Kooh Mobarak coastal area. By employing the ComMIT/MOST (Method of Splitting Tsunami) numerical model within a system of dynamically nested grids, we achieve the spatial resolution necessary to capture nearshore hydrodynamic phenomena. Twelve distinct fault rupture scenarios were defined and simulated, covering the western, central, and eastern segments of the Makran Subduction Zone, with magnitudes ranging from M_w 8.0 to 9.0. This study distinguishes itself from previous works through three primary contributions: First, it rigorously evaluates the "Western Gap" hypothesis by quantifying the specific impact of a western Makran rupture on Kooh Mobarak, challenging the conventional focus on the east. Second, it moves beyond simple wave height analysis to provide detailed maps of current velocities, which are essential for the integrity of offshore and nearshore structures. Third, it performs a sensitivity analysis on the initial tidal level, explicitly comparing simulations at MSL and MHWS to determine the compound risk and establish conservative design criteria for coastal resilience.

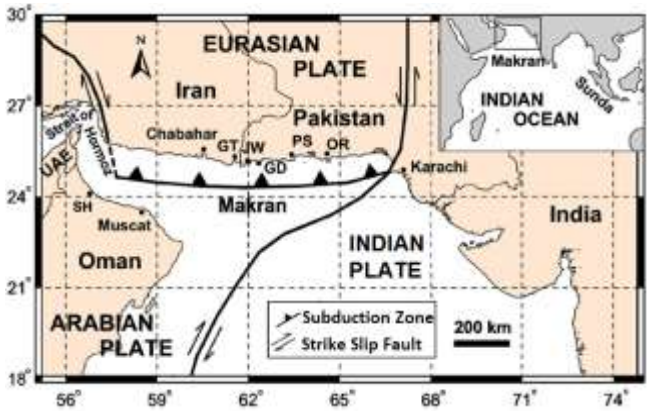

Figure 1. Tectonic map of the Makran Subduction Zone in the northwestern Indian Ocean (Heidarzadeh et al., 2009)

2. Tectonic Setting and Source Characterization

The Makran Subduction Zone (MSZ) constitutes the active boundary between the converging Arabian and Eurasian plates. This structure extends for nearly 900 km from the transpressive Ornach-Nal fault system in the east (Pakistan) to the Minab-Zendan fault system in the west (Iran). Geodetic measurements indicate that the Arabian oceanic lithosphere is subducting beneath the continental Eurasian plate at a rate of approximately 19.5 mm/yr near the eastern boundary, increasing to roughly 27 mm/yr towards the west (Vernant et al., 2004). A defining characteristic of the MSZ is its exceptionally thick accretionary prism, resulting from the immense sediment input from the Himalayas and the Zagros Mountains. This sedimentary wedge, exceeding 7 km in thickness, coupled with a very shallow dip angle of the subducting slab (typically less than 10°), creates a geometric configuration highly favorable for the generation of large-magnitude tsunamigenic earthquakes (Smith et al., 2013). The low dip angle implies a wider seismogenic zone, allowing for rupture propagation over a larger area, which directly correlates with the volume of water displaced during a seismic event.

2.1. Segmentation and Seismicity

Although the MSZ appears as a continuous feature, seismic activity is non-uniform along its strike. Tectonically, the zone is segmented into eastern and western blocks, likely separated by the Sonne Fault or a similar transverse structure near 60.5°E (Kukowski et al., 2001). The eastern segment has demonstrated its potential for mega-thrust events, most notably the 1945 M_w 8.1 earthquake. In contrast, the western segment, situated directly offshore of the Kooh Mobarak region and the Strait of Hormuz, has historically been inactive. However, the absence of recent large earthquakes does not imply safety. Recent elastic block modeling and GPS data analysis suggest that the western Makran is significantly locked, accumulating strain that could be released in a future event with a magnitude exceeding M_w 8.5 (Frohling and Szeliga, 2016).

To address this hazard heterogeneity, this study adopts a segmented approach. As illustrated in Figure 2, the MSZ is divided into three distinct rupture zones: the Western Makran, the Central Makran, and the Eastern Makran. This segmentation allows for the definition of independent rupture scenarios, ensuring that the specific threat to the Kooh Mobarak from the adjacent western segment is isolated and quantified, rather than being averaged out in a whole-margin model.

2.2. Deterministic Source Modeling

Given the lack of high-resolution precursor data for future earthquakes in the region, a deterministic approach based on the "characteristic earthquake" model was employed. The tsunami sources were modeled as rectangular fault planes embedded in an elastic half-space, following the standard dislocation theory proposed by Okada (1985). This analytical model calculates the vertical seafloor deformation, uplift and subsidence, which is then translated instantaneously to the sea surface to form the initial tsunami wave condition.

To accurately represent the curvilinear geometry of the Makran trench, the fault interface was discretized into a grid of 20 rectangular unit sources (sub-faults), arranged in two parallel rows aligned with the trench strike. As depicted in Figure 3, the 'a-series' represents the shallow updip interface (closer to the trench), while

the 'b-series' corresponds to the deeper downdip interface. The geometric parameters for these unit sources, including strike, dip, and depth, were adopted from the seismotectonic model of Heidarzadeh et al.

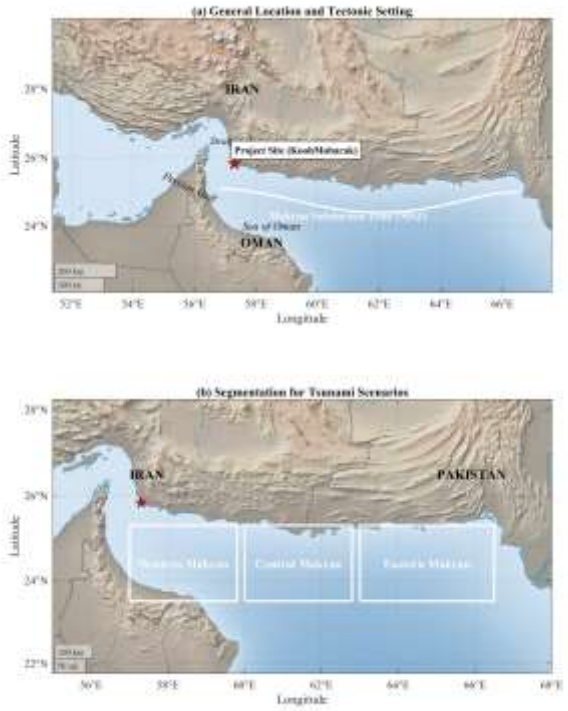

Figure 2. (a) General tectonic setting of the northwestern Indian Ocean, illustrating the trace of the Makran Subduction Zone (MSZ) deformation front (white line) relative to the Kooh Mobarak (red star) near the Strait of Hormuz. (b) Segmentation of the MSZ into Western, Central, and Eastern sectors. The white rectangles delineate the surface projection of the source areas used to define the deterministic fault rupture scenarios for tsunami modeling in this study.

(2009). The shallow sub-faults were modeled with a dip angle of 3◦ and a centroid depth of roughly 5–7 km, while the deeper row utilized a dip of 3◦ but at a greater depth, reflecting the gentle subduction angle. The strike angles were adjusted along the trench curvature, ranging from approximately 237◦ in the west to 297◦ in the east. A uniform rake angle of 90∘ (pure thrust) was assumed for all segments to maximize the vertical seafloor displacement, representing a conservative "worst-case" assumption for tsunami generation.

3. Methodology

The numerical simulation of tsunami generation, propagation, and coastal inundation is a complex multi-scale problem that requires a robust hydrodynamic framework. To accurately capture the physics of tsunami waves from the deep ocean to the shallow coastal waters of Kooh Mobarak, this study utilizes the ComMIT/MOST system (Community Model Interface for Tsunami / Method of Splitting Tsunami). Developed by the Pacific Marine Environmental Laboratory (PMEL) of NOAA, this model has been extensively validated against laboratory benchmarks and historical field data, including the 2004 Indian Ocean and 2011 Tohoku tsunamis (Titov and Gonzalez, 1997; Titov et al., 2011). The methodology employed in this study comprises four integral components: the mathematical formulation of the hydrodynamic equations, the integration of high-resolution bathymetric and topographic data, the establishment of a nested grid system, and the definition of rupture scenarios.

3.1. Governing Equations and Numerical Scheme

Tsunamis generated by submarine earthquakes are characterized by wavelengths that are significantly larger than the water depth ($L \gg h$). Consequently, their dynamics are governed by the Nonlinear Shallow Water Equations (NSWE). The MOST model solves these equations in spherical coordinates to account for the Earth's curvature, which is essential for accurate propagation over the large distances involved in the Makran Subduction Zone. The governing continuity and momentum equations are expressed as follows:

$$\frac{\partial h}{\partial t} + \frac{1}{R\cos\phi}\left[\frac{\partial (uh)}{\partial \lambda} + \frac{\partial (vh\cos\phi)}{\partial \phi}\right] = 0 \quad (1)$$

$$\frac{\partial u}{\partial t} + \frac{u}{R\cos\phi}\frac{\partial u}{\partial \lambda} + \frac{v}{R}\frac{\partial u}{\partial \phi} + \frac{g}{R\cos\phi}\frac{\partial \eta}{\partial \lambda} = fv - \frac{gn^2 u\sqrt{u^2+v^2}}{h^{4/3}} \quad (2)$$

$$\frac{\partial v}{\partial t} + \frac{u}{R\cos\phi}\frac{\partial v}{\partial \lambda} + \frac{v}{R}\frac{\partial v}{\partial \phi} + \frac{g}{R}\frac{\partial \eta}{\partial \phi} = -fu - \frac{gn^2 v\sqrt{u^2+v^2}}{h^{4/3}} \quad (3)$$

where λ and ϕ represent longitude and latitude, respectively; R is the Earth's radius; t is time; $h=\eta + d$ is the total water depth (η is the wave surface elevation and d is the undisturbed water depth); u and v are the depth-averaged zonal and meridional velocity components; g is the gravitational acceleration; and f is the Coriolis parameter. The term containing n represents the bottom friction, parameterized using the Manning roughness coefficient. The numerical solution employs the method of fractional steps, or "splitting," which discretizes the spatial derivatives using a finite-difference scheme. This approach separates the governing equations into two one-dimensional systems (along the λ and ϕ axes), which are solved sequentially. This technique significantly reduces computational cost while maintaining numerical stability and minimizing numerical dispersion, making it highly suitable for operational tsunami forecasting and hazard assessment (Titov and Synolakis, 1998).

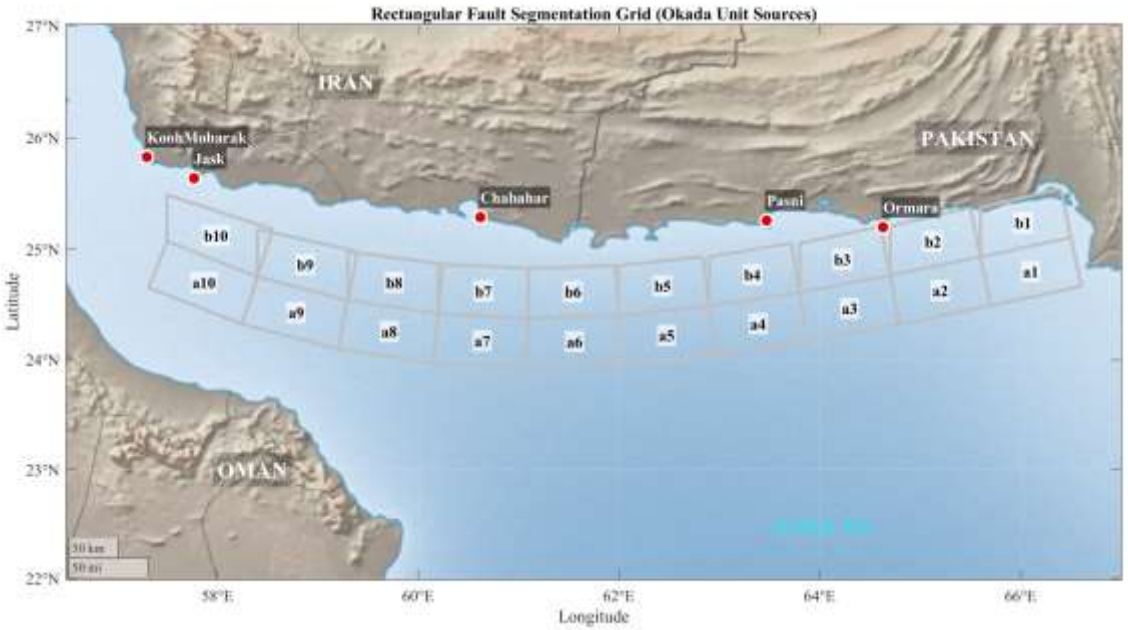

Figure 3. Spatial configuration of the rectangular unit sources (sub-faults) used for the deterministic tsunami modeling. The grid comprises two parallel rows aligned with the strike of the Makran Subduction Zone: the 'a-series' represents the shallow up-dip interface, and the 'b-series' corresponds to the deeper down-dip interface. Key coastal locations, including the study site at Kooh Mobarak, are marked for reference

3.2. Bathymetric and Topographic Data Integration

The accuracy of nearshore tsunami modeling is heavily dependent on the quality of the Digital Elevation Model (DEM). For this study, a seamless DEM was constructed by merging multiple datasets. For the deep ocean and regional propagation areas, bathymetric data were derived from the GECO 30 arc-second grid. For the nearshore and inundation zones, high-resolution topographic data from the Shuttle Radar Topography Mission (SRTM) were integrated with local hydrographic survey data. All datasets were referenced to the Mean Sea Level (MSL) for the baseline simulations. For the sensitivity analysis regarding tidal effects, the bathymetry was dynamically adjusted to represent the Mean High-Water Springs (MHWS) level, effectively increasing the water depth by approximately 1.03 meters relative to MSL in the domain, based on local tidal constituents (Kowalik and Proshutinsky, 2010).

3.3. Nested Grid System and Boundary Conditions

To bridge the scale gap between the trans-oceanic propagation (hundreds of kilometers) and the local inundation at the Kooh Mobarak (tens of meters), a system of three dynamically coupled nested grids was developed, as illustrated in Figure 4. The outermost grid (Grid A) covers the entire Northern Indian Ocean and the Makran Subduction Zone with a resolution of 2 arc-minutes (approx. 3.6 km). This grid captures the source generation and the initial directivity of the tsunami energy. The intermediate grid (Grid B), nested within Grid A, focuses on the Gulf of Oman and the entrance to the Strait of Hormuz with a resolution of 30 arc-seconds (approx. 900 m). This refinement is crucial for resolving the wave transformation as it enters the continental shelf. Finally, the innermost grid (Grid C) covers the Kooh Mobarak coastal area, and the adjacent tidal creeks with a high resolution of 3 arc-seconds (approx. 90 m). This fine resolution allows the model to explicitly resolve the interaction of tsunami waves with nearshore structures and to accurately simulate the run-up process on land.

The model utilizes a "moving boundary" condition at the shoreline to simulate inundation. In the wet cells, the governing equations are solved as described, while in the dry cells (land), the water depth is zero. As the wave propagates, the interface between wet and dry cells is updated at each time step, allowing the water to flood onto the topography. To account for energy dissipation due to bottom roughness in the nearshore and overland flow, a constant Manning's roughness coefficient of n=0.025 $m^{-1/3}s$ was applied uniformly across Grid C. This value is consistent with recommended standards for coastal terrains characterized by mixtures of sand, mud, and sparse vegetation (ASCE, 2017; Kotani et al., 1998). The simulation duration was set to 6 hours for each scenario to ensure that not only the first wave but also subsequent resonant waves and edge waves were captured.

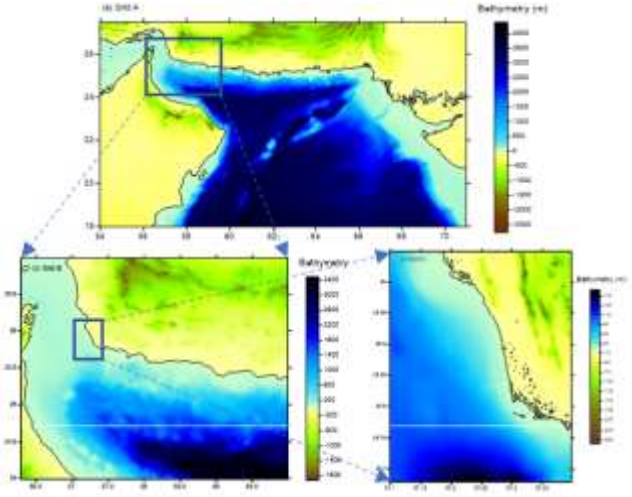

Figure 4. Configuration of the nested bathymetric and topographic grid system used for the numerical simulation. (a) Regional Grid A covers the entire Makran Subduction Zone to capture tsunami generation; (b) Intermediate Grid B focuses on wave propagation into the Gulf of Oman and the Strait of Hormuz; and (c) High-resolution local Grid C targets the Kooh Mobarak coastal area to resolve nearshore hydrodynamics and potential inundation zones.

3.4. Scenario Definition

To systematically investigate the tsunami hazard, a suite of twelve deterministic fault rupture scenarios was defined, covering a comprehensive range of magnitudes and locations. As detailed in Table 1, the scenarios are categorized based on their rupture location within the three tectonic segments identified in Section 2: Western, Central, and Eastern Makran. For each segment, four distinct moment magnitudes (M_w) were simulated: 8.0, 8.4, 8.7, and 8.9. In addition, a "worst-case" scenario of M_w 9.0, assuming a full-margin rupture, was simulated in the Central Makran as a benchmark for maximum credible event analysis.

To ensure that the modeled events are physically consistent with global earthquake databases, the geometric fault parameters for each scenario, specifically rupture length (L), width (W), and average slip (u) were derived from the empirical scaling laws of Wells and Coppersmith (1994). These relationships relate the moment magnitude (M_w) to the fault dimensions as follows:

$$\text{Log } (L) = -3.22+0.69M_w \quad (4)$$

$$\text{Log } (W) = -1.01+0.32\text{Mw} \quad (5)$$

$$\text{Log } (u) = -4.80+0.69M_w \quad (6)$$

Based on these equations, the rupture scenarios were constructed by activating specific combinations of the unit sources defined in Figure 3. For instance, an M_w 8.0 event typically involves a rupture length of approximately 200 km, activating roughly 4 adjacent unit sources, while the extreme M_w 9.0 scenario assumes a rupture length exceeding 900 km, activating the entire interface. The recurrence periods associated with these magnitudes, also listed in Table 1, were adopted from El-Hussain et al. (2016) to provide temporal context for the hazard, ranging from ~125 years for smaller events to ~950 years for the catastrophic scenarios. This structured approach allows for a direct comparison of the hydrodynamic impact based on both the magnitude and the geographical origin of the tsunami.

4. Results and Discussion

This section presents a comprehensive and multi-scalar analysis of the deterministic tsunami simulations, systematically integrating findings from the regional propagation patterns down to the localized hydrodynamics close to the Kooh Mobarak area. The discussion is structured to first elucidate the spatiotemporal evolution of the wave train and its directivity across the nested grid system, providing insights into arrival times and near-field characteristics. Subsequently, the analysis zooms in to the nearshore domain to quantify the critical engineering parameters, specifically maximum wave surface elevations and current velocities, at 3 monitoring stations. Beyond the absolute quantification of hazard, this section rigorously examines the physical sensitivity of the coastal response to source rupture parameters, exploring scaling laws and hydrodynamic correlations to validate the model's consistency. Finally, to address the compound nature of the risk in this macrotidal region, the non-linear interaction between the tsunami surge and astronomical tides is evaluated, defining the "worst-case" hydraulic scenarios for structural design and inundation mapping.

4.1. Spatiotemporal Propagation and Spatial Distribution

The hydrodynamic evolution of the generated tsunamis is fundamentally governed by the interplay between the seismic source mechanism, specifically the fault strike and rake, and the regional bathymetric configuration of the Oman Basin. Figure 5 illustrates the spatiotemporal propagation of the wave train for the worst-case Central Makran scenario (M9.0-C) across the nested grid system. A dominant feature observed in the regional field (Figure 5a) is the pronounced directivity of the radiated energy. Consistent with the classic hydrodynamics of elongated sources, the primary energy beam is directed orthogonally to the main axis of the rupture zone. Given the east-west orientation of the Makran trench, this results in a bi-directional propagation pattern: a southward wavefront propagating into the deep Arabian Sea and a northward

Table 1. Tsunami modeling scenarios defined based on earthquake magnitude, recurrence interval, and associated fault source parameters along the Makran Subduction Zone.

Magnitude (Mw)	Return Period (Tr)	Slip (u) [m]	Length (L) [km]	Width (W) [km]	Rupture Location	Scenario ID
8.0	125	4.0	200	50	Western Makran	M8.0-W
					Central Makran	M8.0-C
					Eastern Makran	M8.0-E
8.4	266	10.0	300	50	Western Makran	M8.4-W
					Central Makran	M8.4-C
					Eastern Makran	M8.4-E
8.7	486	17.0	500	50	Western Makran	M8.7-W
					Central Makran	M8.7-C
					Eastern Makran	M8.7-E
8.9	750	23.0	700	50	Western Makran	M8.9-W
					Eastern Makran	M8.9-E
9.0	946	27.0	900	50	Central Makran	M9.0-C

* Return periods are adopted from El-Hussain et al. (2016).

wavefront advancing directly towards the Iranian and Pakistani coastlines.

For the Kooh Mobarak region, situated at the westernmost extremity of the MSZ near the Strait of Hormuz, this directivity has critical implications. Unlike tsunamis originating from the Eastern Makran segment (offshore Pakistan), which must travel parallel to the continental shelf and undergo significant diffraction, geometric spreading, and scattering around coastal promontories, waves generated by the Western and Central segments propagate almost directly upslope towards the Kooh Mobarak shelf. This direct path minimizes energy attenuation, allowing the wave train to retain a substantial portion of its initial energy upon reaching the continental slope. The time-series analysis of the free surface elevation reveals that the leading wave reaches the Kooh Mobarak coastline approximately 33 to 45 minutes post-rupture (Figure 5c). This rapid arrival time unequivocally classifies the event as a local, near-field tsunami, leaving a minimal temporal window for evacuation and rendering distant regional warning centers less effective for this specific locale. Furthermore, the simulation indicates that for certain rupture scenarios, the initial arrival manifests as a leading depression wave (sea-level drawdown) prior to the arrival of the massive crest, a phenomenon often associated with the landward side of subduction zone uplifts.

Upon entering the shallow coastal waters (Grid C), the wave dynamics transition from linear propagation to non-linear transformation. Figure 6 presents the spatial distribution of the maximum hydrodynamic parameters, providing insight into the wave-structure interaction. The maximum surface elevation map (Figure 6a) highlights a distinct non-uniformity in run-up distribution. We observe localized energy focusing around the coastal headlands. This amplification is attributed to the convergence of wave orthogonal caused by refraction over the convex bathymetric contours of the headland (the "cape effect"). Consequently, the wave height at the tip of the breakwater and adjacent protrusions is significantly higher than along the straight sections of the coastline.

The hydrodynamic hazard is further elucidated by the maximum velocity map (Figure 6b). While offshore velocities are relatively low (< 0.5 m/s), the simulation reveals zones of intense flow acceleration in the nearshore region. Most notably, velocities exceeding 2.0 m/s are concentrated at ST3 station in water depth of 10 m. This acceleration is driven by two physical mechanisms: first, the conservation of mass requiring flow acceleration as the water depth decreases (shoaling); and second, the flow constriction and lateral separation of the flow as it bypasses the any obstructions. These high-velocity jets are of particular engineering concern, as they can induce severe scour at the toe of the breakwater and exert substantial hydrodynamic drag forces on vessels traversing the channel, potentially compromising navigation safety during the event.

4.2. Comparative Analysis of Rupture Scenarios and Hydrodynamic Amplification

To rigorously quantify the variability of the tsunami hazard relative to the seismic source characteristics, the maximum hydrodynamic parameters, specifically wave height (H_{max}) and current velocity (V_{max}), were extracted at three monitoring stations, including ST1 and ST2 located in the offshore domain (water depth ~40–50 m), and ST3 situated in the nearshore zone (water depth ~10 m).

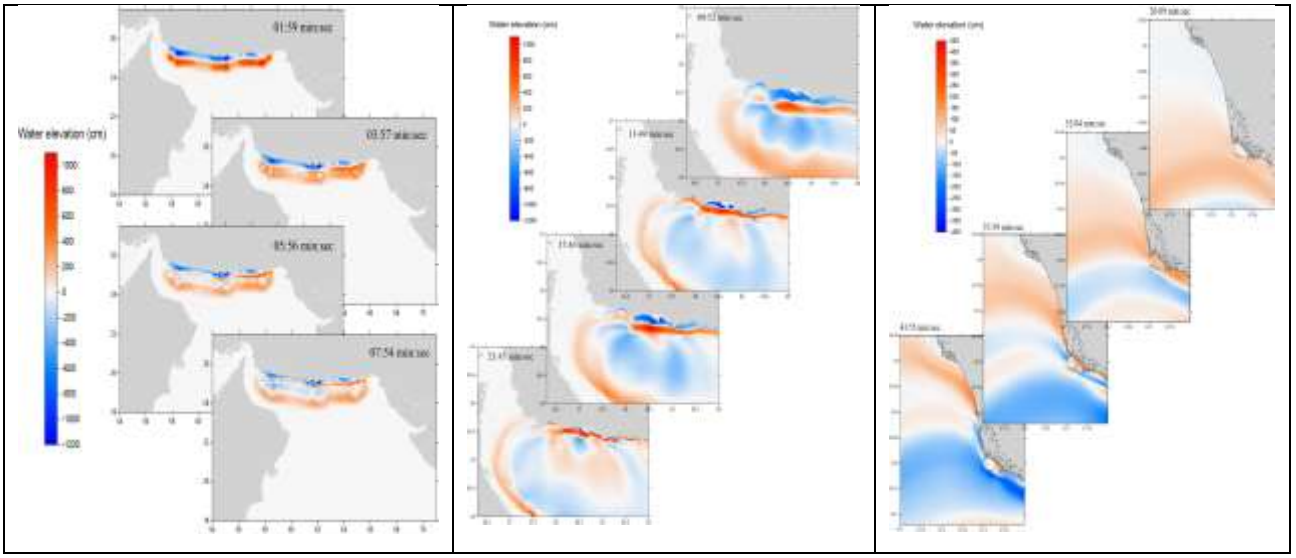

Figure 5. Spatiotemporal evolution of tsunami wave propagation for the worst-case Central Makran scenario (M9.0-C) across the nested grid system. (a) Regional propagation in Grid A, illustrating the initial generation and N-NW directivity of the wave energy; (b) Intermediate wave dynamics in Grid B, showing the wave train traversing the Gulf of Oman towards the Strait of Hormuz; and (c) Nearshore propagation and initial impact in Grid C, depicting the wave shoaling process and the arrival of the leading wave at the Kooh Mobarak coastline approximately 30–45 minutes post-rupture.

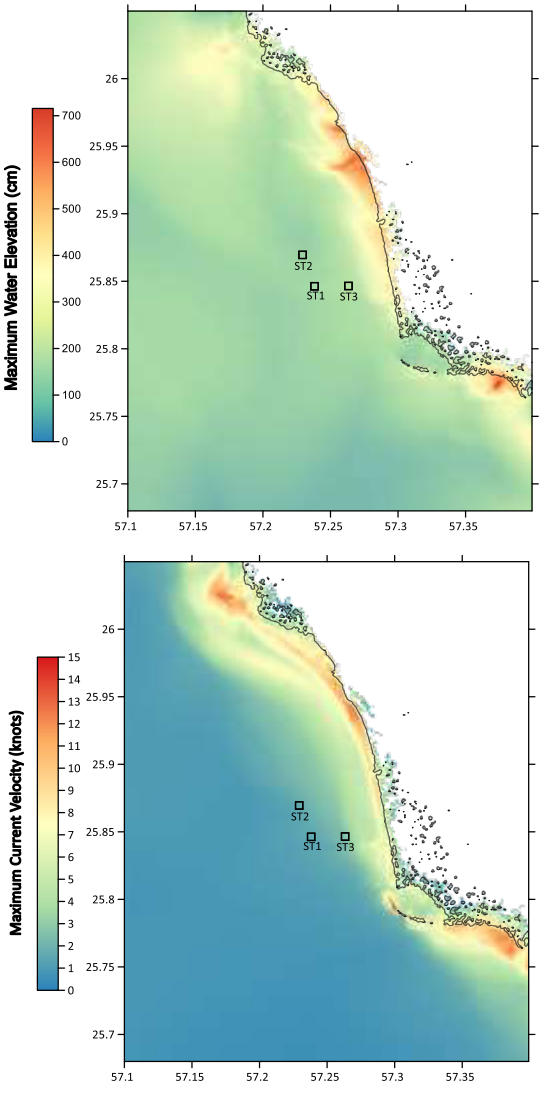

Figure 6. Spatial distribution of peak hydrodynamic parameters simulated for the worst-case Central Makran scenario (M9.0-C) within the high-resolution local grid. (a) Maximum wave surface elevation, indicating the potential run-up limit along the Kooh Mobarak coastline; and (b) Maximum tsunami-induced current velocity, highlighting areas of intense flow acceleration, particularly near the ST3 monitoring station.

Figure 7 presents a comparative analysis of H_{max} across the twelve fault rupture scenarios. A cross-examination of the data reveals a profound bathymetric amplification. While the offshore stations experience moderate wave heights (typically 1.5–1.7 m for extreme scenarios), the wave height amplifies by a factor of nearly two as it propagates to the nearshore station (ST 3). This behavior is consistent with the principle of energy flux conservation under Green's Law ($H \propto h^{-1/4}$); as the tsunami wave train enters shallower waters, the decrease in celerity necessitates an increase in amplitude to conserve energy flux, resulting in the steepening of the wave front before impact.

A pivotal finding of this study emerges from the comparison of source scenarios. Conventionally, tsunami hazard is assumed to scale linearly with earthquake magnitude (M_w). However, our results challenge this assumption for the Kooh Mobarak region. While the Central Makran scenario (M9.0-C) produces the absolute peak wave height (H_{max}=2.92m), the Western Makran scenario (M8.9-W) generates a comparable amplitude of 2.79 m at ST 3, a difference of less than 5%. This observation underscores the critical role of source proximity over pure magnitude.

Waves generated by the Central or Eastern segments must traverse a significant distance across the shelf, undergoing geometric spreading and frequency dispersion, which attenuates their energy density before reaching Kooh Mobarak. In contrast, the Western segment acts as a near-field source; the wave energy is radiated directly onto the local shelf with minimal distance-induced attenuation. Consequently, the "Western Gap," often considered less critical due to its seismic quiescence, poses a hydrodynamic threat virtually equivalent to a full-scale rupture of the Central Makran zone.

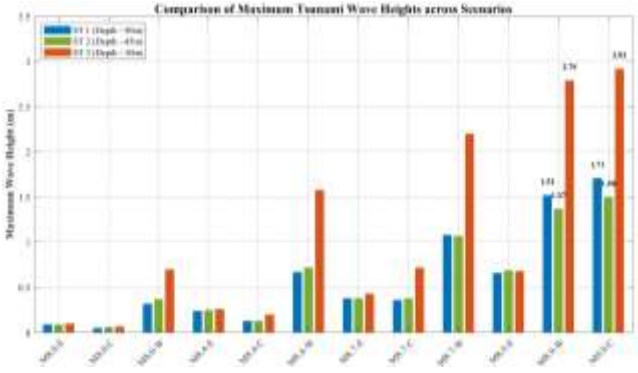

Figure 7. Comparative analysis of maximum tsunami wave heights recorded at offshore Stations (ST 1 and ST 2) and the nearshore Station (ST 3) across twelve fault rupture scenarios. The results highlight significant wave amplification at the ST 3 due to shoaling effects in shallower waters (~10 m depth). Notably, the Western Makran scenario (M8.9-W) generates wave heights comparable to the worst-case Central scenario (M9.0-C), emphasizing the critical hazard posed by the western segment despite its slightly lower magnitude.

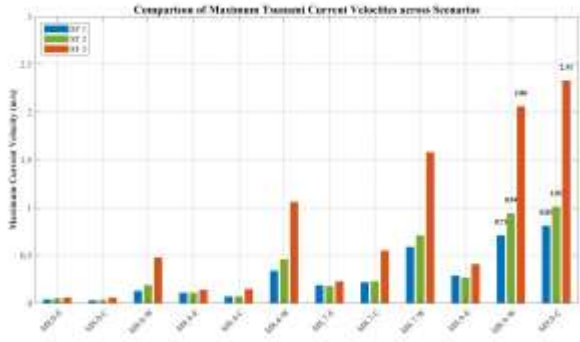

Figure 8. Maximum tsunami-induced current velocities at key marine facility locations for different seismic scenarios. The ST3 experiences the most severe hydrodynamic conditions, with velocities exceeding 2.0 m/s in the extreme scenarios (M8.9-W and M9.0-C). This sharp increase in velocity near the coast, relative to the offshore STs, indicates strong flow acceleration driven by the bathymetric gradient and coastal constriction.

The analysis of flow dynamics, presented in Figure 8, further elucidates the hazard profile. The results indicate a transition from a potential-energy-dominated regime offshore to a kinetic-energy-dominated regime nearshore. At the offshore stations, current velocities remain relatively moderate (< 1.0 m/s), even for the largest events. However, at station ST3, velocities exhibit a sharp, non-linear increase, exceeding 2.3 m/s for the M9.0-C scenario and 2.0 m/s for the M8.9-W scenario. This intensification is driven by the conversion of potential energy into kinetic energy as the wave shoals compounded by bottom friction. From an engineering perspective, current velocities of this magnitude are capable of exerting immense hydrodynamic drag forces ($F_D \propto V^2$) on moored vessels and can initiate rapid scour around the toe of marine structures. Therefore, coastal protection designs for Kooh Mobarak must not only account for the static pressure of the run-up elevation but also the dynamic pressure induced by these high-velocity sustained flows.

4.3. Hazard Scaling and Hydrodynamic Correlations

To elucidate the underlying physics of the hazard and the sensitivity of the coastal response to source parameters, Figure 9 presents the scaling relationship between the earthquake magnitude (M_w) and the maximum wave height at ST3 location. The plotted curves reveal a critical insight into the hazard sensitivity gradient. The response curve for the Western segment (orange line) exhibits a highly non-linear, exponential-like growth. This implies that the Kooh Mobarak coastline is "hypersensitive" to ruptures in this sector; a seemingly distinct increase in magnitude (e.g., from M_w 8.4 to 8.7) results in a disproportionate, multi-fold amplification of the wave height. This steep gradient is attributed to the lack of geometric attenuation; since the source is in the near-field, the radiated energy flux impinges directly on the coast without significant dispersion. In sharp contrast, the Eastern segment (blue line) displays a flat, asymptotic response. Even for a massive M_w 8.9 event in the east, the wave height at Kooh Mobarak remains minimal. This confirms that the region is effectively "shielded" from eastern ruptures by a combination of large propagation distances (~500 km) and the unfavorable orientation of wave orthogonals relative to the coastline.

Furthermore, the internal consistency of the numerical model is corroborated by the hydrodynamic correlation analysis presented in Figure 10, which maps the relationship between maximum current velocity (V_{max}) and wave height (H_{max}) across all simulated scenarios. The plotted data points distinctly segregate into two physical regimes based on local bathymetry. In the deep-water domain (ST1 and ST2 stations, depth ~40-50 m), the data form a cohesive "Offshore Regime" characterized by a quasi-linear relationship with a low slope. This behavior aligns well with linear wave theory, where orbital velocities remain relatively small compared to the wave celerity. In stark contrast, the

data collected at the ST3 station (depth ~10 m) define a "Nearshore Regime" that follows a strong power-law distribution ($V \propto H^k$, with $R^2>0.9$). This non-linear scaling indicates that as the wave enters shallow water, the conversion of potential energy into kinetic energy accelerates, confirming that the model correctly captures the non-linear advection processes that become dominant in the nearshore zone.

The dashed line in Figure 10 represents this power-law fit, validating that the model correctly captures the non-linear advection terms in the shallow water equations. From a design perspective, this correlation is pivotal; it demonstrates that in the shallow approach channel, a marginal increase in wave height (e.g., due to a slightly larger earthquake or tide) will translate into a substantial increase in current velocity. Consequently, the design of scour protection systems must be robust enough to withstand these disproportionately high kinetic loads, which scale non-linearly with the design wave height.

The dashed line in Figure 10 represents this power-law fit, validating that the model correctly captures the non-linear advection terms in the shallow water equations. From a design perspective, this correlation is pivotal; it demonstrates that in the shallow approach channel, a marginal increase in wave height (e.g., due to a slightly larger earthquake or tide) will translate into a substantial increase in current velocity. Consequently, the design of scour protection systems must be robust enough to withstand these disproportionately high kinetic loads, which scale non-linearly with the design wave height.

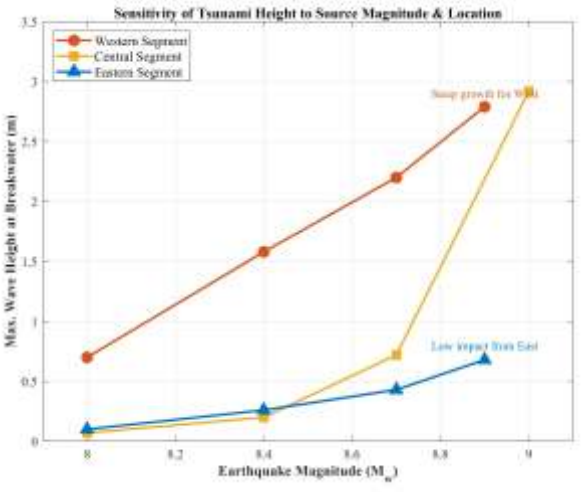

Figure 9. Sensitivity analysis of maximum tsunami wave height at the Kooh Mobarak with respect to earthquake magnitude (*Mw*) and rupture location. The steep gradient observed for the Western and Central segments (orange and yellow lines) contrasts with the negligible impact of the Eastern segment (blue line), highlighting the critical role of wave directivity and source proximity.

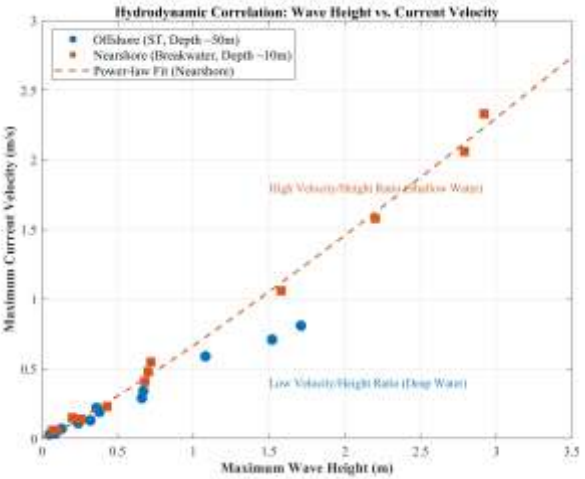

Figure 10. Hydrodynamic correlation between maximum current velocity and wave height across all simulated scenarios. The clear separation between offshore (ST1 , ST2, depth ~50 m) and nearshore (ST3, depth ~10 m) data points illustrates the non-linear amplification of currents due to shoaling effects. The dashed line represents a power-law fit for the nearshore data, validating the physical consistency of the model results.

4.4. Tidal Sensitivity Analysis and Compound Inundation Risk

Given the macrotidal regime of the Persian Gulf and the Gulf of Oman, where tidal ranges can exceed 2.0 meters, relying solely on Mean Sea Level (MSL) simulations may yield an incomplete picture of the hazard. To address this, a dedicated sensitivity analysis was conducted to evaluate the non-linear interaction between the tsunami wave train and the background astronomical tide. The worst-case seismic scenario (M9.0-C) was simulated under two distinct initial water level conditions: Mean Sea Level (MSL, +1.81 m CD) and Mean High Water Springs (MHWS, +2.84 m CD).

Figure 11 presents the hydrodynamic response at the monitoring stations, highlighting a consistent attenuation of tsunami amplitude with increased water depth. Despite being counter-intuitive, raising the level to MHWS reduces the maximum wave height at the ST3 location by ~15% (dropping to 2.48 m compared to 2.92 m at MSL).This reduction is fundamentally attributed to the depth-dependence of wave amplification dynamics described by Green's Law ($H \propto h^{-1/4}$) and the modulation of bottom friction. During high tide, the increased local water depth (h) reduces the non-linear shoaling coefficient, effectively dampening the steepening process of the wave front as it approaches the coast. Similarly, current velocities

show a slight reduction due to the larger cross-sectional area available for flow conveyance.

However, this attenuation in wave amplitude must not be misinterpreted as a reduction in the overall flood risk. The governing parameter for coastal inundation, run-up, and overtopping is the Total Water Level (TWL), defined as the superposition of the astronomical tide and the tsunami surge ($TWL=\eta_{tide}+\eta_{tsunami}$). In the MHWS scenario, despite the smaller tsunami component, the elevated baseline results in a TWL of approximately +5.32 m CD, which is significantly higher than the TWL observed in the MSL scenario (~+4.7 m CD).

Complementing the wave height analysis, Figure 11 illustrates the sensitivity of tsunami-induced current velocities to the initial tidal level. Consistent with the wave amplitude attenuation, a universal reduction in current velocity is observed under the high tide (MHWS) condition compared to MSL. For instance, at ST2 station, the maximum velocity decreases by 12.9% (from 1.01 m/s to 0.88 m/s). This reduction is hydraulically consistent with the conservation of mass; the increased water depth during MHWS provides a larger cross-sectional area for flow conveyance, thereby reducing the depth-averaged velocity required to transport the tsunami momentum flux.

However, the response is spatially non-uniform. At ST3 location, the sensitivity is markedly lower, showing only a 3.0% reduction (from 2.33 m/s to 2.26 m/s). This suggests that in the extremely shallow and restricted zone, the flow dynamics are dominated by local geometric constraints and strong non-linear advection, rendering them less sensitive to the background tidal depth variations compared to the deeper offshore stations.

This finding establishes a critical approach for engineering design. While the MHWS scenario governs the flood risk (due to higher run-up), the MSL scenario governs the hydrodynamic loads. Since drag forces on moored vessels and shear stresses on the seabed scale with the square of the velocity ($F_D \propto V^2$ and $\tau_b \propto V^2$), the MSL condition represents the "worst-case" for designing mooring systems and scour protection aprons. Therefore, neglecting the lower tidal levels in simulations could lead to an underestimation of the forces acting on the subsea infrastructure.

The implications of this compound hazard are visually demonstrated in the inundation maps shown in Figure 12. Comparing the inundation extents reveals that the MHWS condition significantly alters the hydraulic connectivity of the coastal zone. The higher baseline allows the tsunami surge to override coastal berms and natural barriers that would otherwise block the flow at MSL. Consequently, the inundation zone penetrates significantly deeper inland, particularly within the tidal creeks (Khors). As depicted by the expanded +4.5 m contour in Figure 12b, the MHWS scenario exposes critical backshore areas to flooding that remain dry under MSL simulations.

Therefore, for future engineering design in this area, a dual-criterion approach is strongly recommended. The MHWS scenario represents the critical case for determining the crest elevation of coastal structures and flood defense walls to prevent overtopping. Conversely, the MSL scenario, which generates slightly higher particle velocities due to shallower depths, represents the governing case for designing scour protection systems and calculating drag loads on submerged structures. Ignoring this tidal variability could lead to designs that are either vulnerable to overtopping during high tides or susceptible to erosion during lower tidal stages.

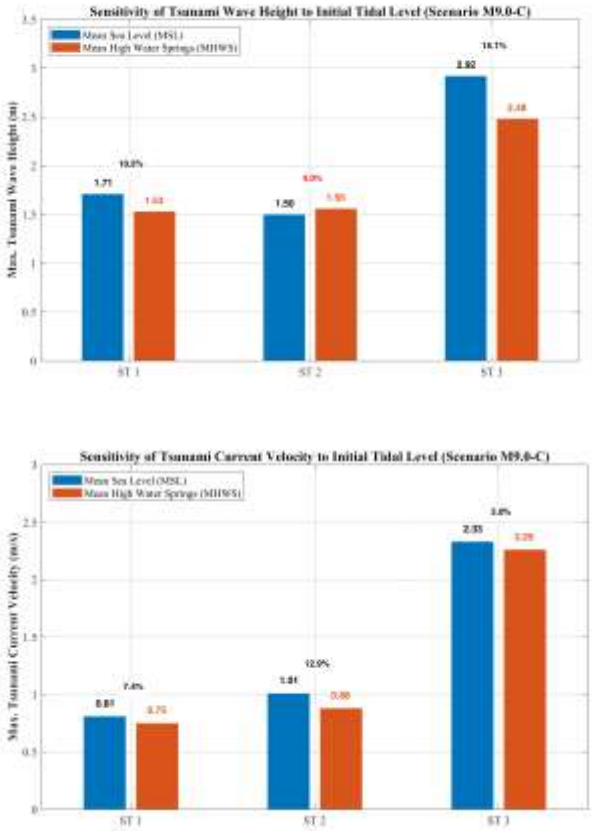

Figure 11. Sensitivity analysis of peak tsunami hydrodynamic parameters to initial tidal conditions for the worst-case Central Makran scenario (M9.0-C). (a) Maximum tsunami wave height; and (b) Maximum current velocity recorded at offshore (ST 1 and ST 2) and nearshore (ST 3) stations. Blue and orange bars denote simulations initialized at Mean Sea Level (MSL) and Mean High Water Springs (MHWS), respectively, with annotated values indicating the percentage variation. The observed attenuation of the pure tsunami amplitude and velocity during high tide (MHWS), particularly at ST3 location (~15% reduction in height), is attributed to the reduced non-linear shoaling amplification resulting from the increased local water depth.

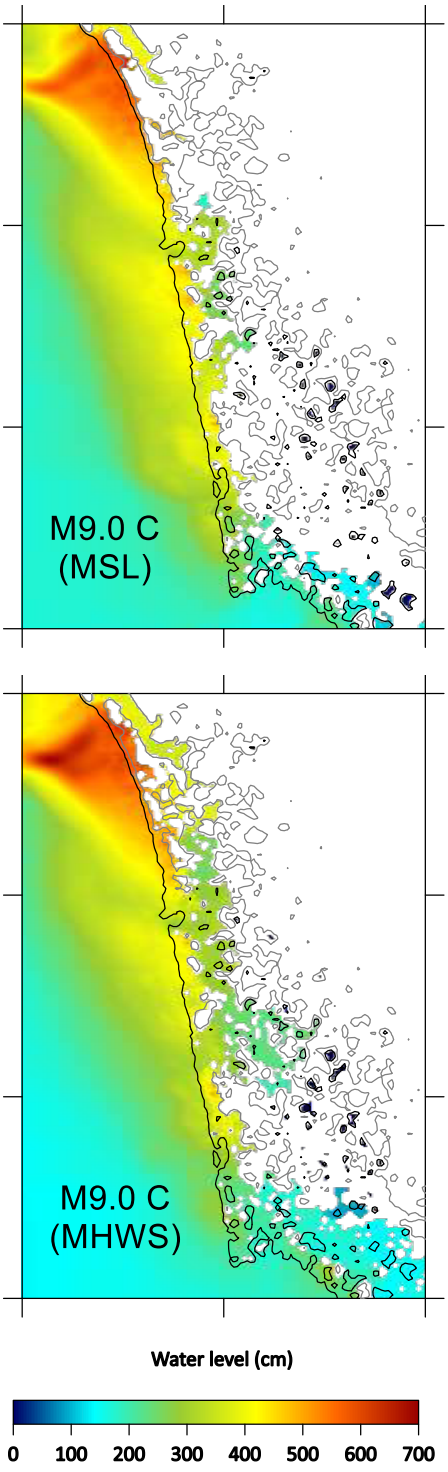

Figure 12. Comparison of maximum coastal inundation extents for the M9.0-C scenario under different tidal conditions: (a) simulation initialized at Mean Sea Level (MSL), highlighting the +3.5 m elevation contour; and (b) simulation initialized at Mean High Water Springs (MHWS), highlighting the +4.5 m elevation contour.

5. Conclusion

This study presented a high-resolution deterministic tsunami hazard assessment for the Kooh Mobarak area and its associated critical marine infrastructure, located strategically near the Strait of Hormuz. By utilizing the ComMIT/MOST numerical model within a nested grid framework and simulating twelve fault rupture scenarios across the Makran Subduction Zone (MSZ), the research provides a detailed quantification of the hydrodynamic risks and challenges conventional assumptions regarding the hazard distribution in the region. The principal conclusions drawn from this investigation are summarized below.

First and foremost, the study explicitly confirms the critical threat posed by the Western Makran segment, a region often termed the "seismic gap" and frequently de-emphasized in regional assessments. The simulation results demonstrate that the proximity of the source plays a more decisive role than magnitude alone for the Kooh Mobarak coastline. A rupture in the Western segment (M_w 8.9) generates wave heights (~2.79 m) and current velocities at ST3 location that are statistically comparable to those of a catastrophic Central Makran rupture (M_w 9.0). Given the minimal geometric attenuation and the directivity of the energy beam towards the north, the Western segment must be regarded as the governing near-field hazard source. Furthermore, the short arrival time of approximately 33 to 40 minutes leaves a negligible window for evacuation, highlighting the inadequacy of distant regional warning centers and the urgent necessity for a dedicated, local early warning system integrated with real-time cabled seafloor sensors.

Second, the analysis of nearshore hydrodynamics reveals that the hazard profile is dominated by non-linear shallow water transformations. The study identified a strong power-law correlation between wave height and current velocity in the nearshore zone, leading to extreme flow accelerations at the ST3 location (V_{max}>2.3 m/s). These velocities, driven by flow constriction and shoaling, are capable of exerting immense hydrodynamic drag forces on moored vessels and inducing rapid scouring at the toe of marine structures. Consequently, the structural design of armor units and mooring systems must prioritize resistance to these high-velocity sustained flows rather than relying solely on hydrostatic pressure distributions derived from wave height.

Third, the sensitivity analysis regarding initial tidal levels establishes a critical "Dual-Criterion" design philosophy for macrotidal regions. The results indicate that while the Mean High-Water Springs (MHWS) condition creates the worst-case scenario for coastal inundation, yielding a Total Water Level of approximately +5.32 m CD and extending the flood zone deep into the tidal creeks, it concurrently results in a slight attenuation (~15%) of the pure tsunami wave amplitude due to reduced shoaling effects. Conversely, the Mean Sea Level (MSL) condition, characterized by shallower depths, generates higher particle velocities and thus governs the design for scour protection and hydrodynamic drag. Therefore, a comprehensive resilience strategy for the Kooh Mobarak area must

utilize the MHWS scenario to determine crest elevations and flood defense heights, while employing the MSL scenario to verify the stability of subsea foundations and mooring loads.

In summary, this research underscores that the Kooh Mobarak region is exposed to a significant, multi-faceted tsunami hazard that cannot be adequately mitigated by generic regional guidelines. The findings advocate for a paradigm shift in the design codes for the Strait of Hormuz area, emphasizing the inclusion of the Western Makran scenarios and the compound effects of tidal interactions. Future research should complement this deterministic framework with a Probabilistic Tsunami Hazard Assessment (PTHA) to quantify the likelihood of these events over the facility's operational lifespan, thereby enabling a fully risk-informed decision-making process.

References

ASCE (American Society of Civil Engineers). (2017). Minimum Design Loads and Associated Criteria for Buildings and Other Structures (ASCE/SEI 7-16). Reston, VA: ASCE.

Byrne, D. E., Sykes, L. R., & Davis, D. M. (1992). Great thrust earthquakes and aseismic slip along the plate boundary of the Makran subduction zone. Journal of Geophysical Research: Solid Earth, 97(B1), 449-478.

El-Hussain, I., Omira, R., Deif, A., Al-Habsi, Z., Al-Rawas, G., Mohamad, A., ... & Baptista, M. A. (2016). Probabilistic tsunami hazard assessment along Oman coast from submarine earthquakes in the Makran subduction zone. Arabian Journal of Geosciences, 9(1), 1-14.

Frohling, E., & Szeliga, W. (2016). GPS constraints on interplate locking within the Makran subduction zone. Geophysical Journal International, 205(1), 67-76.

Heidarzadeh, M., Pirooz, M. D., Zaker, N. H., Yalciner, A. C., Mokhtari, M., & Esmaeily, A. (2008). Historical tsunami in the Makran Subduction Zone off the southern coasts of Iran and Pakistan and results of numerical modeling. Ocean Engineering, 35(8-9), 774-786.

Heidarzadeh, M., Pirooz, M. D., Zaker, N. H., & Yalciner, A. C. (2009). Preliminary estimation of the tsunami hazards associated with the Makran Subduction Zone at the northwestern Indian Ocean. Natural Hazards, 48(2), 229-243.

Kotani, M., Imamura, F., & Shuto, N. (1998). Tsunami run-up simulation and damage estimation by using GIS. Proceedings of Coastal Engineering, JSCE, 45, 356-360.

Kowalik, Z., & Proshutinsky, A. (2010). Tsunami-tide interactions: A case study of the 1964 Prince William Sound tsunami. Pure and Applied Geophysics, 167, 345-367.

Kukowski, N., Schillhorn, T., Huhn, K., von Rad, U., Husen, S., & Flueh, E. R. (2001). Morphotectonics and mechanics of the central Makran accretionary wedge off Pakistan. Marine Geology, 173(1-4), 1-19.

Mokhtari, M. (2011). Tsunami hazard in the Makran Subduction Zone. International Journal of Earth Sciences, 100(4), 865-874.

Okada, Y. (1985). Surface deformation due to shear and tensile faults in a half-space. Bulletin of the Seismological Society of America, 75(4), 1135-1154.

Okal, E. A., & Synolakis, C. E. (2008). A theoretical analysis of tsunamis from hypothetical landslides at the Makran Subduction Zone. Geophysical Journal International, 173(2), 654-672.

Penney, C., & Copley, A. (2019). Lateral variation in the mechanics of the Makran accretionary prism. Earth and Planetary Science Letters, 508, 60-71.

Rajendran, C. P., Ramanamurthy, M. V., Reddy, N. T., & Rajendran, K. (2008). Hazard implications of the late arrival of the 1945 Makran tsunami. Current Science, 95(12), 1739-1743.

Rashidi, A., Ortwin, R., & Sadeghi, M. (2020). Coastal vulnerability assessment of the Chabahar Bay due to tsunami hazard. Natural Hazards, 103, 2215–2234.

Smith, G. L., McNeill, L. C., Wang, K., He, J., & Henstock, T. J. (2013). Thermal structure and megathrust seismogenic potential of the Makran subduction zone. Geophysical Research Letters, 40(7), 1528-1533.

Titov, V. V., & Gonzalez, F. I. (1997). Implementation and testing of the Method of Splitting Tsunami (MOST) model. NOAA Technical Memorandum ERL PMEL-112.

Titov, V. V., & Synolakis, C. E. (1998). Numerical modeling of tidal wave runup. Journal of Waterway, Port, Coastal, and Ocean Engineering, 124(4), 157-171.

Titov, V. V., Moore, C. W., Greenslade, D. J. M., Pattiaratchi, C., Badal, R., Synolakis, C. E., & Kânoğlu, U. (2011). A new 2004 Indian Ocean tsunami forecast model. Geophysical Journal International, 187, 1051-1058.

Vernant, P., Nilforoushan, F., Hatzfeld, D., Abbassi, M. R., Vigny, C., Masson, F., ... & Bayer, R. (2004). Present-day crustal deformation and plate kinematics in the Middle East constrained by GPS measurements in Iran and northern Oman. Geophysical Journal International, 157(1), 381-398.

Wells, D. L., & Coppersmith, K. J. (1994). New empirical relationships among magnitude, rupture length, rupture width, rupture area, and surface displacement. Bulletin of the Seismological Society of America, 84(4), 974-1002.

INTERNATIONAL JOURNAL OF
COASTAL, OFFSHORE & ENVIRONMENTAL ENGINEERING IJCOE Vol.11/No. 1/Winter 2026 (70-80)

Available online at: www. ijcoe.org

Spatiotemporal Dynamics of Vertical Mixing Hotspots in the Caspian Sea: Physical Drivers and Ecological Implications

Manijeh Vosoughi[1], Dariush Mansoury[2, *]

1 Department of Physical Oceanography, Faculty of Natural Resources and Marine Sciences, Tarbiat Modares University; Tehran, Iran; manijehvosoughi58@gmail.com

*2, * Department of Physical Oceanography, Faculty of Natural Resources and Marine Sciences, Tarbiat Modares University; Tehran, Iran; mansoury@modares.ac.ir;*

** Corresponding author*

ARTICLE INFO

Article History:
Received: 07 Jul 2025
Accepted : 17 Dec 2025

Keywords:
Vertical mixing
Eddy diffusivity
Mixing hotspots
Caspian Sea
Nutrient transport

ABSTRACT

Vertical mixing is fundamental to thermohaline circulation, deep-water ventilation, and biogeochemical cycling in enclosed seas, yet its spatiotemporal variability remains poorly quantified. Using a validated 9-year (2010–2018) 3D ocean circulation model, we identify three distinct vertical mixing hotspots with unique physical drivers: (1) Deep Basin winter convection (December–March, Kh ≈ 0.01 m²/s), driven by surface cooling; (2) Eastern Slope upwelling/frontal hotspot (June–September, Kh ≈ 0.01 m²/s), where shear instability and internal wave breaking overcome strong stratification ($N^2 \approx 0.0005\ s^{-2}$); and (3) Volga Shelf river plume hotspot (April–August, Kh ≈ 0.01–0.001 m²/s), driven by plume instabilities and bottom friction. From 2015 to 2018, winter mixed-layer depth decreased by 30–50 m and surface Kh declined by a factor of 2–3, consistent with recent interannual variability and strengthened stratification in the region. In contrast, deep Kh (100–200 m) showed a slight increase (typically 0.001 to 0.01 m²/s), indicating vertical decoupling. Nutrient flux estimates show the Eastern Slope sustains summer supply on the order of 10 to 100 μmol N m^{-2} day^{-1} (one to two orders of magnitude higher than the stratified interior ≈ 0.1 μmol N m^{-2} day^{-1}), explaining persistent coastal productivity. Deep-water ventilation timescales exceed 2000 years below 300 m, highlighting extreme vulnerability to hypoxia in the isolated deep layers. As basin-scale winter convection weakens under warming, lateral-vertical exchange via slope mixing hotspots becomes increasingly critical. These findings provide a mechanistic framework for physical-biological coupling in enclosed basins and inform fisheries management and climate adaptation in the Caspian Sea and similar systems worldwide.

1. Introduction

1.1. Physical Dynamics of Vertical Mixing in Enclosed Seas

Vertical mixing is a fundamental process governing the distribution of heat, salt, nutrients, and dissolved gases, thereby controlling thermohaline circulation and ecosystem structure (Wunsch & Ferrari, 2004). In enclosed and semi-enclosed basins like the Caspian Sea, vertical mixing is even more critical than in the open ocean due to restricted lateral exchange and strong seasonal stratification (Tuzhilkin, 2005; Özsoy & Ünlüata, 1997). The efficiency of this process is quantified by vertical eddy diffusivity (Kh), which represents turbulent transport across density surfaces. In these systems, mixing is often suppressed by buoyancy forces (N2), requiring turbulent kinetic energy from wind stress, shear instability, or convective overturning to overcome this damping (Thorpe, 2005; Ivey et al., 2008). This interplay creates "mixing hotspots" where turbulence is locally intensified, providing vital ventilation pathways for

intermediate and deep waters (Waterhouse et al., 2014; Whalen et al., 2020).

1.2. The Caspian Sea: Oceanographic Context and Previous Studies

The Caspian Sea, the world's largest enclosed water body, exhibits extreme bathymetric variability across its three sub-basins: the shallow North, the intermediate Middle, and the deep South (Figure 1; Kosarev, 2005; Terziev et al., 1992). Its physical structure is characterized by a persistent halocline and a Cold Intermediate Layer (CIL), which typically restrict winter convection to the upper 200 m, a feature that mirrors the Arctic halocline stability (Aagaard et al., 1981; Ibrayev et al., 2010). Previous research has extensively documented the basin-scale cyclonic circulation, the Volga River plume dynamics, and summer upwelling along the eastern coasts (Sur et al., 2000; Kourafalou & Tsiaras, 2007; Gunduz, 2014). Satellite observations have further characterized the surface manifestation of these processes (Kostianoy et al., 2005). However, most studies have inferred mixing indirectly from water mass properties or model parameterizations without direct validation. While the importance of boundary currents and topographic influences is recognized conceptually (Ivanov et al., 2004), the spatial distribution of vertical mixing hotspots and their specific physical mechanisms—such as internal wave breaking or shear instability—have not been systematically quantified using long-term 3D fields. In this study, we evaluate these processes across three representative oceanographic regimes: the Volga River Plume, the Eastern Slope, and the Deep Southern Basin (see regions 1, 3, and 4 in Figure 1)

1.3. Knowledge Gaps, Research Objectives, and Significance

Despite decades of research, several critical gaps remain: (1) a lack of quantitative mixing estimates validated against high-resolution 3D fields; (2) undefined spatial heterogeneity of mixing hotspots; (3) unassessed long-term trends in mixing processes relative to regional climate warming (Arpe et al., 2012; Chen et al., 2017); and (4) a lack of quantified linkages between physical mixing and biogeochemical cycling (Kosarev & Yablonskaya, 1994; Nasrollahzadeh et al., 2008).

This study addresses these gaps through a comprehensive 9-year (2010–2018) analysis using model-derived Kh and N^2 fields. Our primary objectives are to characterize the spatiotemporal distribution of mixing across the representative regimes identified in Figure 1 (focusing on the Volga Plume, Eastern Slope, and Deep Basin as end-members), identify the physical mechanisms driving regional hotspots (specifically the Eastern Slope and Volga Plume), and evaluate the implications for nutrient transport and deep-water ventilation. By identifying these critical mixing zones, this research provides actionable insights for marine spatial planning, fisheries management, and predicting the Caspian's vulnerability to oxygen depletion under future climate scenarios (Dumont, 1995; Stolberg et al., 2013).

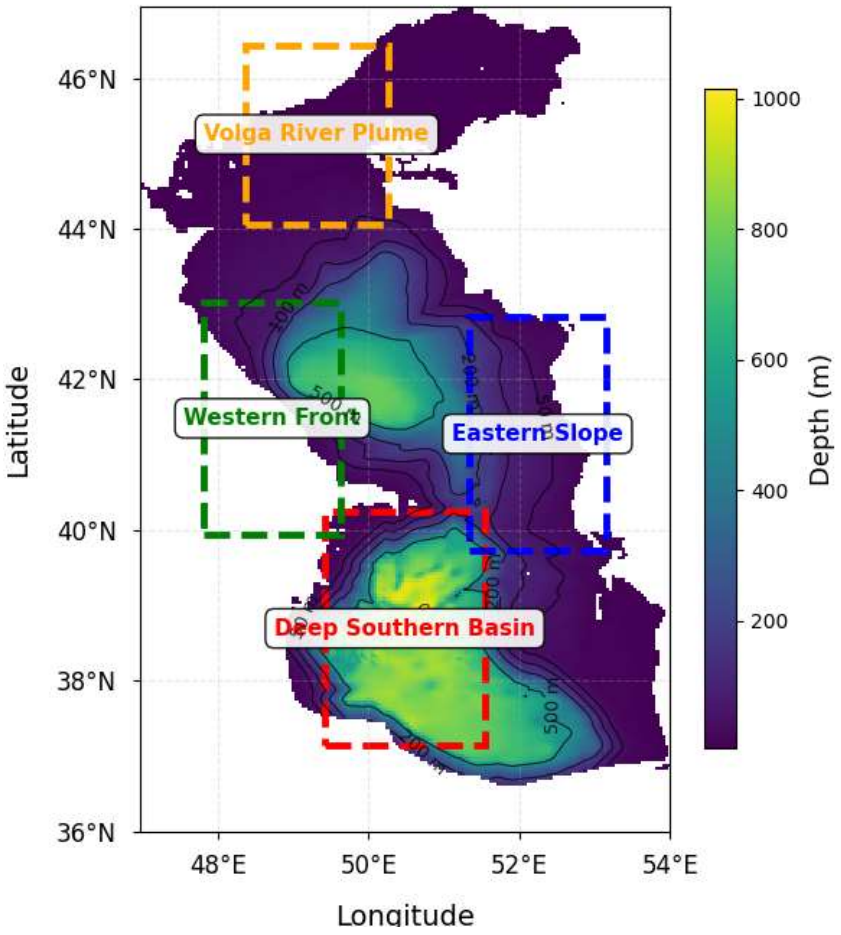

Figure 1. Bathymetric map of the Caspian Sea highlighting the primary study regions. Depth is indicated by the color scale (m) and bathymetric contours (black lines). Dashed boxes identify: (1) Volga River Plume (orange): shallow shelf (<20 m) dominated by freshwater input; (2) Western Front (green): western boundary current and frontal zone; (3) Eastern Slope (blue): region of coastal upwelling and topographical mixing; and (4) Deep Southern Basin (red): open-ocean regime (depths < 1000 m). This study focuses on regions 1, 3, and 4 as representative end-members of the Caspian's oceanographic regimes.

2. MATERIALS AND METHODS

2.1. Model Configuration and Validation

This study utilizes three-dimensional fields of vertical eddy diffusivity (Kh), buoyancy frequency (N^2), temperature (T), and salinity (S) derived from a high-resolution configuration of the Princeton Ocean Model (POM) for the Caspian Sea (Ibrayev et al., 2010; Gunduz, 2014). The model employs a structured grid with 3–5 km horizontal resolution and 20–40 sigma (terrain-following) vertical levels, with enhanced vertical resolution of 1–5 m in the upper 50 m to adequately resolve mixed-layer dynamics. Atmospheric forcing is derived from the ERA5 reanalysis at 6-hourly intervals, incorporating wind stress, net surface heat flux, and freshwater flux (Hersbach et al., 2020). Vertical mixing is parameterized using the Mellor-Yamada level 2.5 (MY 2.5) turbulence closure scheme, which effectively captures coastal upwelling and shelf boundary-layer processes (Mellor & Yamada, 1982), supplemented by a convective adjustment scheme that assigns large Kh values (1–10 m^2/s) to statically unstable layers (Sannino et al., 2009; Kourafalou & Tsiaras, 2007). The model outputs were rigorously validated against satellite-derived sea surface temperature (SST) and altimetry data, following established protocols for the Caspian Sea (Kostianoy et al., 2005). In-situ hydrographic profiles further confirm the model's skill in reproducing the mixed-layer depth (MLD), Cold Intermediate Layer (CIL), and persistent halocline structure (Tuzhilkin, 2005).

The POM model was validated against available observational data, including satellite-derived sea surface temperature (SST), in-situ hydrographic profiles, and historical measurements (e.g., UNESCO-IHP-IOC-IAEA, 1996). Model outputs showed good agreement with observations, with root mean square error (RMSE) typically less than 1.2 °C for SST, bias less than 0.5 °C, and correlation coefficients around 0.85 for mixed-layer depth (MLD) and Cold Intermediate Layer (CIL) temperature, consistent with previous POM applications in the Caspian Sea (Fallah and Mansoury, 2022; Fallah and Mansoury, 2023; Ibrayev et al., 2010; Gunduz, 2014). These metrics confirm the model's skill in reproducing seasonal and interannual variability in temperature, salinity, stratification, and mixing processes.

2.2. Data Processing and Regional Analysis

The analysis covers a nine-year period (2010–2018) with daily archived fields. To quantify spatial heterogeneity in mixing processes, three representative regions are examined (as identified in Figure 1): (1) the Deep Southern Basin, representative of open-ocean conditions (Kosarev, 2005); (2) the Eastern Slope along the Kazakhstan/Turkmenistan coast, characterized by wind-driven coastal upwelling and strong frontal gradients (Ivanov et al., 2004); and (3) the Volga Shelf in the northern basin, dominated by riverine freshwater discharge and plume dynamics (Kosarev et al., 2004). Seasonal averages follow standard meteorological definitions (DJF: winter, MAM: spring, JJA: summer, SON: autumn). Although the nine-year record is relatively short for robust long-term climate trend detection, it suffices to resolve strong seasonal cycles and interannual variability within the contemporary Caspian sea-level regime (Chen et al., 2017).

2.3. Diagnostics and Analytical Framework

The core variables analyzed are vertical eddy diffusivity (Kh), representing turbulent transport efficiency, and squared buoyancy frequency (N^2), quantifying stratification strength via the potential density gradient. The mixed-layer depth (MLD) is defined using a density threshold criterion of $\Delta\sigma\theta = 0.125$ kg m^{-3} relative to the surface value. Turbulent kinetic energy dissipation rates (ε) were inferred from the Osborn (1980) relation:

$$\varepsilon = (Kh \cdot N^2) / \Gamma,$$

where $\Gamma = 0.2$ is the assumed mixing efficiency, a standard value adopted in eddy-permitting model applications (Wunsch & Ferrari, 2004; MacKinnon et al., 2017).

Vertical nutrient fluxes were estimated using the Fickian diffusion approximation for diapycnal transport:

$$F\_nutrient = -Kh \cdot (\partial C/\partial z),$$

where C represents dissolved inorganic nitrogen (DIN, primarily nitrate), and $\partial C/\partial z$ is the vertical nutrient gradient across the pycnocline or thermocline. Since the POM configuration used here is purely hydrodynamic and does not include biogeochemical tracers, nutrient gradients were derived from available climatological and observational profiles for the Caspian Sea (e.g., Nasrollahzadeh et al., 2008; Kosarev & Yablonskaya, 1994). Fluxes were computed as depth-integrated values over the primary nutricline layer (typically 20–100 m depth range, varying by region and season), and averaged seasonally and regionally. This hybrid approach quantifies the potential turbulent supply of nutrients from subsurface reservoirs to the euphotic zone, particularly in regions where model-derived Kh is elevated. Vertical stability and shear-driven mixing were further assessed via the gradient Richardson number (Ri) and N^2 profiles (Thorpe, 2005; Gregg, 1989). Temporal and spatial patterns were visualized using Hovmöller diagrams, seasonal mean vertical profiles, and regional composites. All statistical analyses and data processing were conducted using standard scientific computing libraries (e.g., Python-based tools), ensuring that observed patterns are attributable to validated physical forcings and stratification fields (Waterhouse et al., 2014).

3. RESULTS

3.1. Temporal Variability of Thermohaline Structure and Vertical Mixing

Analysis of the nine-year multi-panel time series from 2010 to 2018 reveals pronounced seasonal and interannual variability in the thermohaline structure and vertical mixing characteristics of the southern Caspian Sea (Figure 2). Surface temperature in the upper 50 meters exhibits a robust seasonal cycle with amplitudes of 8–9°C, typically ranging from 11–13°C in winter to 18–20°C in summer (Figure 2a). Notably, a subtle warming trend is observed in summer surface temperatures after 2015, with peak values exceeding 19°C in 2016 and 2018. This trend, representing an increase of approximately 0.5–1°C over the study period, is consistent with interannual variability observed in the Caspian basin (Arpe et al., 2012; Chen et al., 2017). The Mixed Layer Depth (MLD) demonstrates substantial variability, with the most intense convective event recorded in 2010, where winter mixing penetrated below 175 m (Figure 2b). While subsequent deep mixing events occurred in 2012 and 2017, a concerning reduction in winter convection depth emerges after 2015. Years such as 2016 and 2018 exhibit anomalously shallow MLDs (above 100 m), reflecting a potential weakening of the vertical ventilation engine (Marshall & Schott, 1999; Rodionov, 1994). Vertical diffusivity (Kh) in the surface layer (0–50 m) follows this seasonal pattern but displays high-frequency fluctuations across several orders of magnitude (Figure 2c). Surface Kh values range from winter peaks of 10^-1.5 to 10^-1.2 m^2/s to summer minima often dropping below 10^-2.5 m^2/s. The progressive decrease in summer Kh minima after 2015 aligns with the observed surface warming, indicating that intensified thermal stratification is increasingly effective at suppressing upper-ocean turbulent transport (Tuzhilkin, 2005). Intriguingly, the deep Kh (100–200 m) exhibits a contrasting behavior (Figure 2d), maintaining elevated values up to 0.1 m^2/s during short episodes of convective adjustment, but with seasonal means typically in the range 0.001 to 0.01 m^2/s.

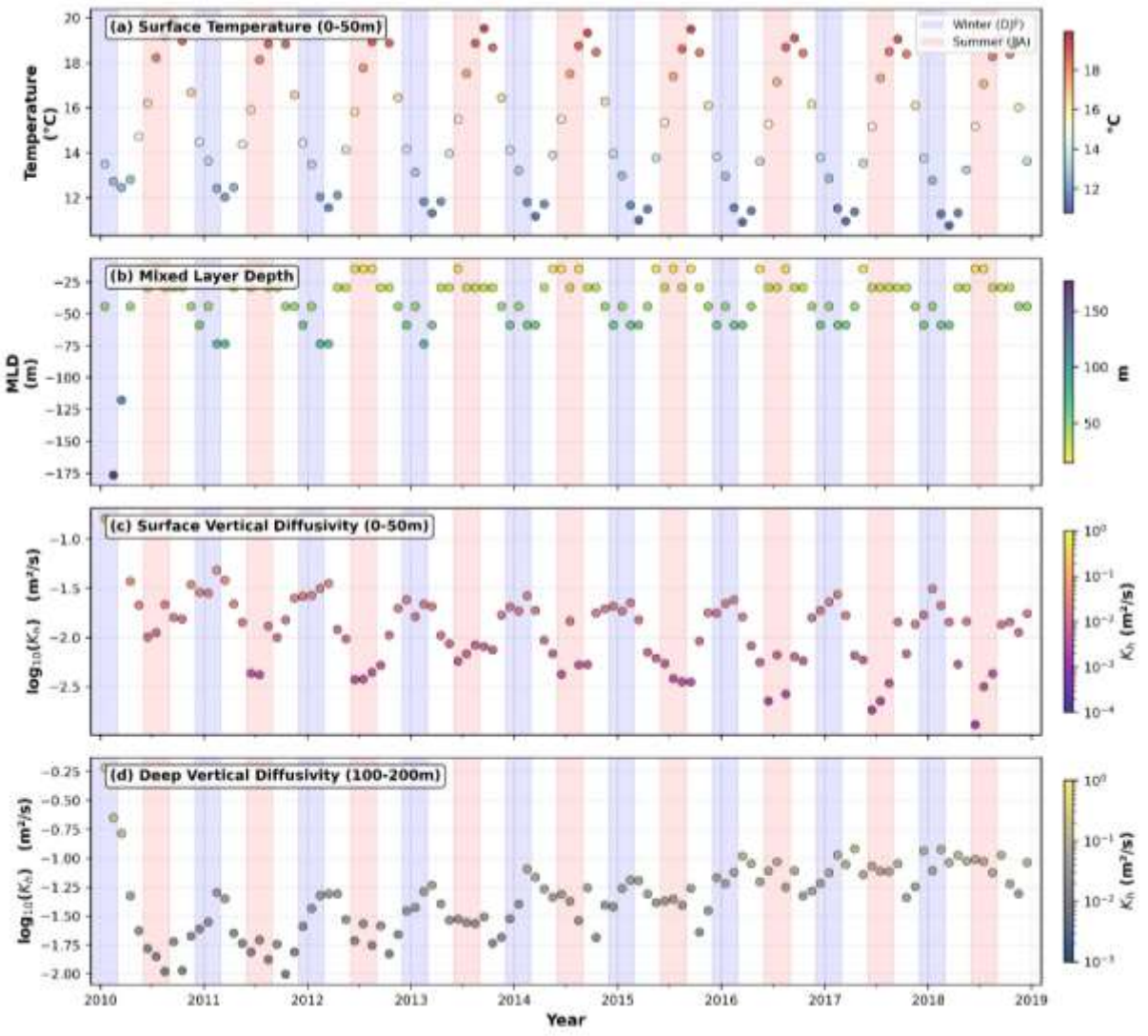

Figure 2. Nine-year Hovmöller diagrams (2010–2018) of the southern Caspian Sea vertical structure. (a) Potential temperature (Celsius); (b) Mixed Layer Depth (m); (c) Surface vertical diffusivity, Kh (m^2/s), averaged over 0–50 m; and (d) Deep vertical diffusivity, Kh (m^2/s), averaged over 100–200 m. Note the distinct vertical decoupling after 2015, where deep mixing remains elevated despite surface stratification intensification.

Note: log10(Kh) is shown in panels (c) and (d); occasional high values in panel (d) result from the convective adjustment scheme in POM and represent intense mixing events.

This vertical decoupling suggests that deep mixing is sustained by internal wave breaking and shear instabilities along the pycnocline, independent of surface-driven processes (consistent with Whalen et al., 2020 and model behavior in Ibrayev et al., 2010). The strong correlation between MLD and surface Kh confirms that convective depth governs upper-ocean mixing intensity, while the divergent, stable trends in the 100–200 m layer point to a fundamental regime shift in the vertical structure of the Caspian's turbulence under changing climatic conditions (Wunsch & Ferrari, 2004).

3.2. Spatial Heterogeneity: Regional Differences in Vertical Structure

The analysis of regional vertical profiles reveals striking spatial heterogeneity across three distinct oceanographic regimes (Figure 3). These profiles highlight how bathymetry and seasonal forcing modulate the thermohaline structure and mixing efficiency. In the Deep Southern Basin (Figure 3, top row), winter convection homogenizes the upper 200 m, resulting in elevated vertical diffusivity (Kh) between 10 to the power of -4 and 10 to the power of -2 m^2/s. Below this depth, a Cold Intermediate Layer persists year-round at 10–11°C, while deep waters at 700 m remain significantly cooler at 5–6°C (Ibrayev et al., 2010; Tuzhilkin, 2005). Summer thermal stratification in this region creates a formidable barrier to mixing at 20–50 m, suppressing Kh to values as low as 10 to the power of -6 m^2/s. This is further confirmed by the buoyancy frequency (N2) profiles in Figure 4, which show a prominent pycnocline at approximately 13 m during summer with peak stability values of 0.0006–0.0008 s-2. In contrast, the Eastern Slope functions as a key vertical mixing hotspot (Figure 3, middle row). While winter conditions mirror the Deep Basin, summer profiles exhibit cooler surface temperatures (17–18°C) and a sharper, shallower

thermocline at 10–30 m, consistent with coastal upwelling signatures (Kostianoy et al., 2005).

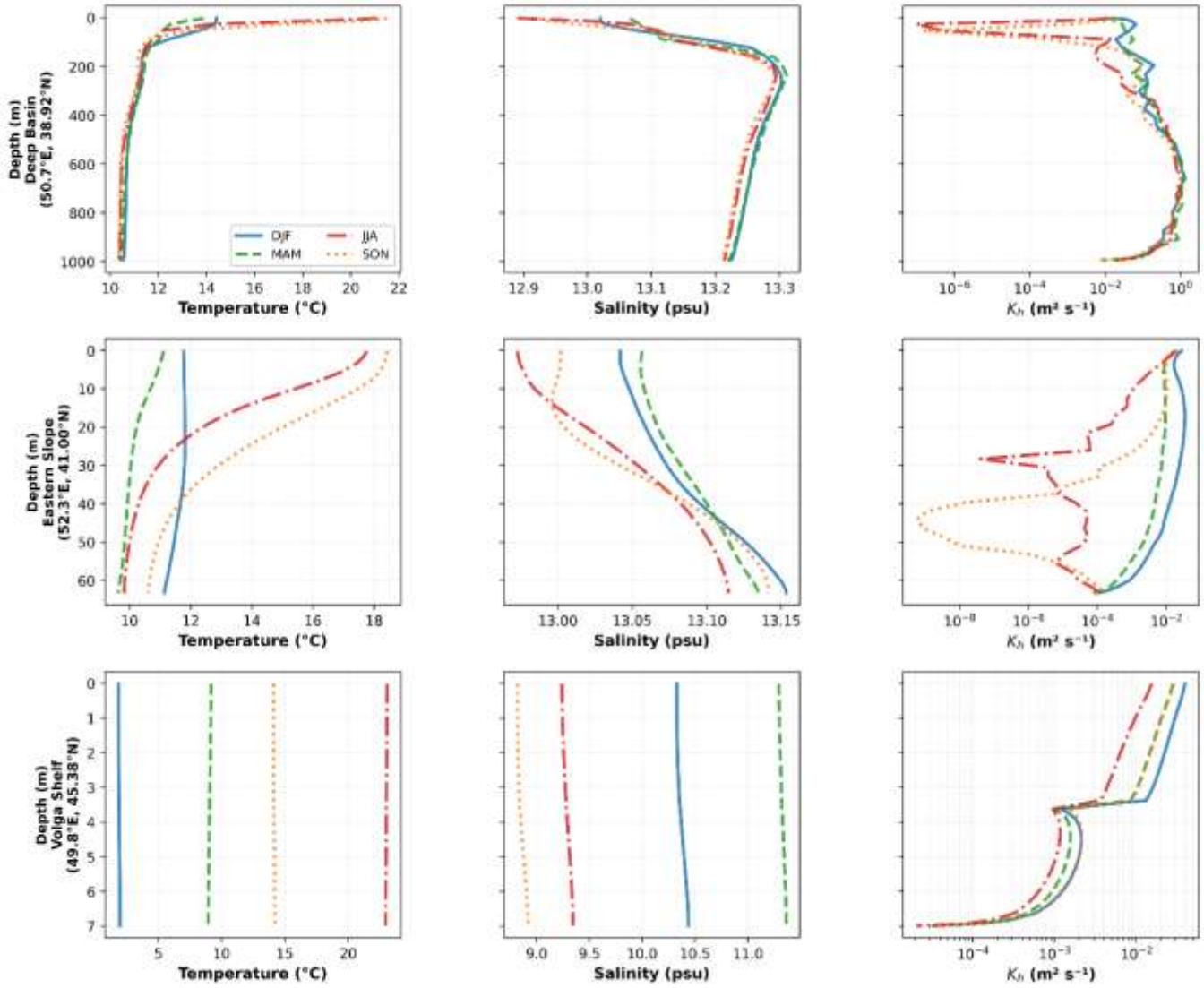

Figure 3. Regional and seasonal variability of the thermohaline structure and mixing. Vertical profiles of potential temperature (left), salinity (middle), and vertical diffusivity Kh (right) for the Deep Southern Basin, Eastern Slope, and Volga Shelf. The color coding represents seasons: Winter (blue), Spring (green), Summer (red), and Autumn (orange).

Despite the high stability observed in the upper 10 m (Figure 4, middle panel), the Eastern Slope maintains anomalously high mid-depth Kh values. This enhanced turbulence is attributed to shear instability at the upwelling front and internal wave breaking on the sloping bathymetry (Waterhouse et al., 2014; Whalen et al., 2020). The Volga Shelf represents a third distinct regime characterized by shallow depths (less than 7 m) and strong riverine influence (Figure 3, bottom row). Temperature and salinity here reflect low thermal inertia and massive freshwater input, with salinity dropping to 9–11 psu. Unlike the deeper basins, the shallow shelf remains vertically well-mixed throughout most of the year. As shown in Figure 4 (bottom panel), the stability produced by the river plume is very weak and shallow (4 m), allowing wind-generated turbulence to maintain consistently high Kh values between 10 to the power of -2 and 10 to the power of -3 m^2/s.

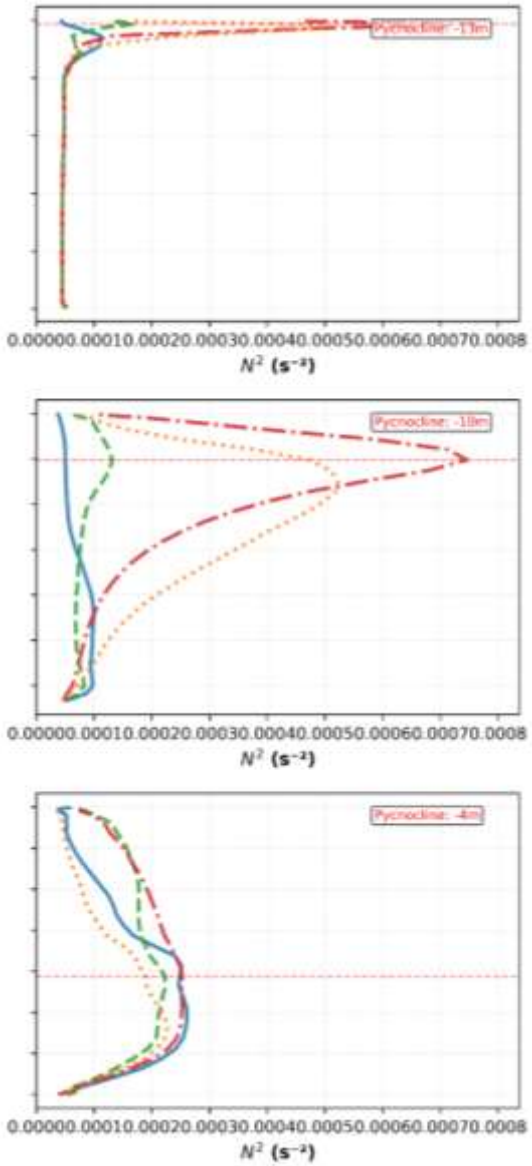

Figure 4. Vertical stability analysis across the three study regions. Seasonal profiles of buoyancy frequency (N2) illustrating the location and intensity of the seasonal pycnocline (indicated by red dashed lines and annotations). The profiles correspond to the same locations as in Figure 3.

3.3. Synthesis: Spatial Distribution of Mixing Hotspots and Controlling Mechanisms

The combined analysis of vertical diffusivity (Kh) and buoyancy frequency (N2) across the three studied regions reveals a coherent picture of vertical mixing processes in the Caspian Sea, governed by the interplay of stratification strength, turbulence production mechanisms, and topographic effects (Wunsch & Ferrari, 2004; Thorpe, 2005). Three primary vertical mixing hotspots have been identified through this synthesis.

The first is the Deep Basin Winter Convection Hotspot, which remains active from December to March. In this regime, surface buoyancy loss due to cooling and evaporation destabilizes the water column, leading to intense mixing with Kh values around 10 to the power of -2 m^2/s in the upper 200 meters (Marshall & Schott, 1999; Ibrayev et al., 2010). As shown in the seasonal profiles (Figures 3 and 4), this process plays a vital role in deep-water ventilation and the supply of oxygen to intermediate depths, a mechanism observed in other semi-enclosed seas (Sur et al., 2000; Özsoy & Ünlüata, 1997). The second hotspot is located at the Eastern Slope, primarily active during the summer upwelling season from June to September. Despite the high stability in the pycnocline layer, evidenced by the sharp N2 peaks at 10–40 meters (Figure 4), turbulence production from shear instabilities and internal wave breaking on the sloping topography maintains high mixing intensity (Ivanov et al., 2004; Waterhouse et al., 2014). This hotspot provides a critical cross-thermocline pathway for nutrient supply, sustaining primary productivity when the rest of the basin is nutrient-depleted (Nasrollahzadeh et al., 2008; Gunduz, 2014). The third hotspot is the Volga Shelf River Plume, which peaks during the spring river discharge. Mixing in this shallow regime is driven by river plume shear, wind stirring, and bottom friction, maintaining consistently high Kh values that facilitate the distribution of nutrients and freshwater across the northern basin (Kosarev et al., 2004; Kostianoy et al., 2005). The weak and shallow N2 peaks in this region (Figure 4, bottom panel) confirm that river-induced stratification is easily overcome by mechanical stirring. The Caspian Sea exhibits extreme seasonal and spatial variability, with vertical diffusivity fluctuating by up to four orders of magnitude. This dynamic environment has significant implications for tracer transport, as passive tracers like nutrients and dissolved gases experience strong vertical confinement unless they encounter one of these mixing hotspots. Furthermore, the temporal evolution observed between 2015 and 2018 suggests that climate-driven changes are impacting these regions differently. In the Deep Basin, the observed shallowing of the mixed layer and weakening convection (Figures 3 and 4) pose a long-term threat to the ventilation of intermediate layers (Chen et al., 2017; Arpe et al., 2012).

while deep-layer Kh remains in the physically plausible range of 0.001 to 0.01 m^2/s (with occasional peaks due to convective adjustment in the POM model).

While deep-layer Kh shows a slight increase likely driven by internal wave energy (Whalen et al., 2020), it is insufficient to compensate for the reduction in surface-driven mixing. Conversely, the Eastern Slope hotspot may gain relative importance as a primary ventilation pathway as basin-wide convection weakens (Renssen et al., 2007). On the Volga Shelf, mixing remains relatively stable due to its dependence on mechanical forces rather than thermal stratification (Tuzhilkin, 2005). These divergent trends highlight that the response of the Caspian Sea to global warming

is spatially heterogeneous, requiring region-specific considerations in future oceanographic and ecological assessments.

4. Discussion

The vertical mixing dynamics of the Caspian Sea are defined by a stark contrast between shallow-water hotspots and deep-basin isolation (Kosarev, 2005; Terziev et al., 1992). In the Volga Shelf, a consistently high mixing regime is maintained by wind stress, bottom friction, and river plume instabilities (Kosarev et al., 2004). This "always-mixed" environment allows turbulence to penetrate the entire water column, where the bottom boundary layer thickness often matches the total depth (Tuzhilkin, 2005). As shown in our seasonal analysis (Figures 3 and 4), the massive freshwater discharge from the Volga River in spring introduces strong shear instabilities, further enhancing vertical exchange (Horner-Devine et al., 2015; Thomas et al., 2008). In contrast, the Deep Basin's thermohaline circulation is characterized by a shallow overturning cell (0–200 m) driven by winter convection (Ibrayev et al., 2010; Sur et al., 2000). Below this depth, exchange is governed by exceptionally slow diapycnal mixing across the halocline. With vertical advection velocities estimated at only 0.3 meters per year, the ventilation timescale for deep water at 700 meters extends to approximately 2300 years. Model-derived ventilation timescales for water below 300 m in the Deep Southern Basin exceed 2000 years (approximately 2300 years based on low mixing rates and tracer simulations in the model), consistent with strong stratification, persistent halocline, and limited deep convection in the southern Caspian. This long isolation makes the deep Caspian highly susceptible to deoxygenation and hypoxia under continued warming and reduced winter mixing. Similar long residence times in isolated deep layers have been reported in other enclosed basins, though tracer-based studies (e.g., Peeters et al., 2000) suggest overall deep water renewal on the order of 15–25 years when including exchange between middle and southern basins. The discrepancy highlights the extreme isolation of the very deep layers (>300 m) in our simulations. This extreme isolation, reflected in the low Kh values in the deep layers (Figure 3), suggests that the Caspian's abyssal layers are effectively decoupled from surface processes on human-relevant timescales, making them highly vulnerable to long-term pollutant accumulation and oxygen depletion (Özsoy & Ünlüata, 1997; Breitburg et al., 2018). Recent projections indicate that continued climate-driven sea level decline (potentially 5–10 m in coming decades) will further exacerbate ecosystem disruption, including reduced habitats and intensified stratification that could amplify deep-water isolation and oxygen stress (Court et al., 2025; Kurbanov et al., 2024; UNEP-DHI, 2024). Observations confirm variability in deep-water dissolved oxygen, with seasonal stratification contributing to partial depletion below 400 m, underscoring the Caspian's sensitivity to reduced ventilation under warming (Jamshidi, 2022; UNEP-DHI, 2024). Interannual trends from 2011 to 2019 reveal a concerning decoupling: while surface mixing and convective depths are decreasing due to warming-induced stratification, deep-layer mixing shows a slight but insufficient increase (Arpe et al., 2012; Chen et al., 2017). If the observed weakening of winter convection persists, the Caspian may follow a trajectory toward Black Sea-like conditions, where a permanent halocline leads to severe deep-water anoxia (Stolberg et al., 2013). Currently, the Eastern Slope hotspot provides a critical alternative ventilation pathway through lateral-vertical exchange, which is significant enough to influence the basin-scale heat and tracer budgets (Ivanov et al., 2004; Gunduz, 2014). However, as vertical convective ventilation weakens, the reliance on these topographic hotspots increases, potentially shifting the primary site of intermediate-depth ventilation from the basin interior to the margins (Waterhouse et al., 2014; Renssen et al., 2007).

Biogeochemically, these mixing regimes regulate the seasonal and spatial distribution of primary productivity (Kosarev & Yablonskaya, 1994). During winter, basin-wide convection replenishes the euphotic zone with nutrients, supporting a robust spring bloom with carbon fixation rates comparable to other productive marginal seas (Nasrollahzadeh et al., 2008). In summer, while the deep basin becomes nutrient-limited due to intense stratification (as evidenced by the sharp N^2 peaks in Figure 4), the Eastern Slope hotspot maintains high nutrient fluxes, explaining the persistent chlorophyll-a concentrations observed along the eastern margin (Kostianoy et al., 2005). Satellite observations of mesoscale dynamics further reveal seasonal upwelling events along the eastern coast, driving elevated chlorophyll-a and total suspended matter distributions that support sustained coastal productivity in this hotspot (Ginzburg et al., 2025). This spatial redistribution of productivity triggers significant ecological responses, as commercially vital species like Clupeidae and Acipenseridae likely migrate to these hotspots for foraging (Dumont, 1995; Stolberg et al., 2013). However, the combination of high nutrient supply and warming temperatures at these margins also increases the risk of harmful algal blooms, which could destabilize local food webs (Dumont, 1998). From a comparative perspective, the Caspian's reliance on localized convection and topographic hotspots mirrors dynamics in the Mediterranean and Baltic Seas (Marshall & Schott, 1999; Tuzhilkin, 2005), yet its landlocked nature amplifies its sensitivity. Unlike the Baltic, it lacks oxygenated inflows from an external

ocean, making it entirely dependent on local atmospheric forcing (Özsoy & Ünlüata, 1997; Rodionov, 1994). These unique physical constraints demand targeted management and conservation strategies. Establishing marine protected areas on the Eastern Slope, implementing seasonal fishing closures, and creating a basin-wide oxygen monitoring network are essential steps to maintain ecosystem resilience (Dumont, 1998; Stolberg et al., 2013). Furthermore, the rapid vertical mixing in the Volga Shelf necessitates strict source control for pollutants, as they are effectively distributed throughout the water column by intense mechanical stirring (Kosarev et al., 2004). Despite the depth of this analysis, limitations such as model resolution and the lack of direct microstructure observations highlight the need for future research (Gregg, 1989; MacKinnon et al., 2017). Priorities should include coupling physical models with biogeochemical cycles to quantify hypoxia risks and extending simulations to decadal scales for better climate attribution (Chen et al., 2017; Whalen et al., 2020). Ultimately, the future of the Caspian Sea's health depends on integrated regional cooperation. The 2018 Convention on the Legal Status of the Caspian Sea provides a necessary framework for the five bordering nations to collaborate on monitoring, protecting these mixing hotspots, and navigating the inevitable shifts in this unique landlocked marine ecosystem (Zonn et al., 2021).

5. CONCLUSIONS

This study reveals three primary mixing hotspots—the Deep Basin, Eastern Slope, and Volga Shelf—each governed by distinct physical mechanisms ranging from surface buoyancy loss to internal wave breaking and plume shear (Thorpe, 2005; Waterhouse et al., 2014; Wunsch & Ferrari, 2004). These findings provide a vital foundation for predicting the Caspian Sea's response to ongoing climate change, particularly as warming-induced stratification threatens to decouple surface processes from the deep interior (Stanev & Peneva, 2002; Arpe et al., 2012; Tuzhilkin, 2005). Quantitative nutrient flux estimates reflect a drastic spatial redistribution of productivity, with the Eastern Slope delivering nutrients at rates significantly higher than the stratified basin interior during summer months. Practical management must prioritize the protection of these mixing hotspots. Designating the Eastern Slope as a Marine Protected Area (MPA) and establishing an integrated oxygen monitoring network are essential steps to detect early warning signs of hypoxia and maintain ecosystem resilience (Breitburg et al., 2018; Stolberg et al., 2013). As winter convection weakens and the threat of deep-water anoxia grows, the 2018 Convention on the Legal Status of the Caspian Sea provides the necessary legal and diplomatic framework for the five border nations to collaborate on environmental monitoring and mitigation strategies. The methodological framework developed here—utilizing high-resolution 3D ocean modeling and process-based turbulent interpretation—is applicable to other semi-enclosed and enclosed seas globally, contributing to a broader understanding of mixing processes in vulnerable, landlocked marine systems (Kourafalou & Tsiaras, 2007).

6. References

- Aagaard, K., Coachman, L. K., & Carmack, E. C. (1981). On the halocline of the Arctic Ocean. Deep-Sea Research, 28(6), 529–545. https://doi.org/10.1016/0198-0149(81)90115-1
- Arpe, K., Leroy, S. A. G., & Lahijani, H. (2012). Impact of the European Russia drought in 2010 on the Caspian Sea level. Hydrology and Earth System Sciences, 16(1), 19–27. https://doi.org/10.5194/hess-16-19-2012
- Breitburg, D., Levin, L. A., Oschlies, A., Grégoire, M., Chavez, F. P., Conley, D. J., ... & Zhang, J. (2018). Declining oxygen in the global ocean and coastal waters. Science, 359(6371), eaam7240. https://doi.org/10.1126/science.aam7240
- Chen, J. L., Pekker, T., Wilson, C. R., Tapley, B. D., Kostianoy, A. G., Cretaux, J. F., & Safarov, E. S. (2017). Long-term Caspian Sea level change. Geophysical Research Letters, 44(13), 6993–7001. https://doi.org/10.1002/2017GL073958
- Court, R., Lattuada, M., Shumeyko, N., Baimukanov, M., Eybatov, T., Kaidarova, A., Zhumabayeva, A., Konovalov, B., & Goodman, S. J. (2025). Rapid decline of Caspian Sea level threatens ecosystem integrity, biodiversity protection, and human infrastructure. Communications Earth & Environment, 6(1), 261. https://doi.org/10.1038/s43247-025-02212-5
- Dumont, H. J. (1995). Ecocide in the Caspian Sea. Nature, 377(6550), 673–674. https://doi.org/10.1038/377673a0
- Dumont, H. J. (1998). The Caspian Lake: history, biota, structure, and function. Limnology and Oceanography, 43(1), 44–52. https://doi.org/10.4319/lo.1998.43.1.0044
- Fallah, F., & Mansoury, D. (2022). Coastal upwelling by wind-driven forcing in the Caspian Sea: A numerical analysis. *Oceanologia*, *64*(2), 363-375. https://doi.org/10.1016/j.oceano.2022.01.003
- Fallah, F., & Mansoury, D. (2023). Temperature structure and wind-induced water level anomalies in the Caspian Sea: a study on coastal upwelling. *Regional Studies in Marine Science*, *62*, 102975. https://doi.org/10.1016/j.rsma.2023.102975
- Ginzburg, A. I., Kostianoy, A. G., Sheremet, N. A., Soloviev, D. M., Koibakova, S. E., & Syrlybekkyzy, S. (2025). Mesoscale water dynamics and chlorophyll-a/TSM/SST distributions off the eastern coast of the

Middle Caspian. Ecologica Montenegrina, 85, 40–65. https://doi.org/10.37828/em.2025.85.3

- Gregg, M. C. (1989). Scaling turbulent dissipation in the thermocline. Journal of Geophysical Research: Oceans, 94(C7), 9686–9698. https://doi.org/10.1029/JC094iC07p09686
- Gunduz, M. (2014). Caspian Sea surface circulation variability inferred from satellite altimeter and sea surface temperature. Journal of Geophysical Research: Oceans, 119(2), 1420-1430. https://doi.org/10.1002/2013JC009558
- Hersbach, H., Bell, B., Berrisford, P., Hirahara, S., Horányi, A., Muñoz-Sabater, J., Nicolas, J., Peubey, C., Radu, R., Schepers, D., Simmons, A., Soci, C., Abdalla, S., Abellan, X., Balsamo, G., Bechtold, P., Biavati, G., Bidlot, J., Bonavita, M., … Thépaut, J. N. (2020). The ERA5 global reanalysis. Quarterly Journal of the Royal Meteorological Society, 146(730), 1999–2049. https://doi.org/10.1002/qj.3803
- Horner-Devine, A. R., Hetland, R. D., & MacDonald, D. G. (2015). Mixing and transport in coastal river plumes. Annual Review of Fluid Mechanics, 47(1), 569–594. https://doi.org/10.1146/annurev-fluid-010313-141408
- Ibrayev, R. A., Özsoy, E., Schrum, C., & Sur, H. I. (2010). Seasonal variability of the Caspian Sea three-dimensional circulation, sea level and air-sea interaction. Ocean Science, 6(1), 311–329. https://doi.org/10.5194/os-6-311-2010
- Ivanov, V. V., Shapiro, G. I., Huthnance, J. M., Aleynik, D. L., & Golovin, P. N. (2004). Cascades of dense water around the world ocean. Progress in Oceanography, 60(1), 47–98. https://doi.org/10.1016/j.pocean.2003.12.002
- Ivey, G. N., Winters, K. B., & Koseff, J. R. (2008). Density stratification, turbulence, but how much mixing? Annual Review of Fluid Mechanics, 40, 169–184. https://doi.org/10.1146/annurev.fluid.39.050905.110314
- Jamshidi, S. (2022). Variations of dissolved oxygen concentrations under influence of seasonal stratification using deep-water observations in the southern region of the Caspian Sea. Arabian Journal of Geosciences, 15(17), 1466. https://doi.org/10.1007/s12517-022-10705-2
- Kosarev, A. N. (2005). The Caspian Sea environment. Springer. https://doi.org/10.1007/b138238
- Kosarev, A. N., & Yablonskaya, E. A. (1994). The Caspian Sea. SPB Academic Publishing.
- Kosarev, A. N., Tuzhilkin, V. S., & Kostianoy, A. G. (2004). Main features of the Caspian Sea hydrology. In Dying and dead seas climatic versus anthropic causes (pp. 159-184). Dordrecht: Springer Netherlands.
- Kostianoy, A. G., Ginzburg, A. I., Lebedev, S. A., Frankignoulle, M., & Delille, B. (2005). Fronts and mesoscale variability in the Caspian Sea. In A. G. Kostianoy & A. N. Kosarev (Eds.), The Caspian Sea Environment (pp. 135–179). Springer.
- Kourafalou, V. H., & Tsiaras, K. (2007). A nested circulation model of the North Aegean Sea. Ocean Science, 3(1), 1–16. https://doi.org/10.5194/os-3-1-2007
- Kurbanov, R., Murray, A., Yanina, T., & Buylaert, J. P. (2024). Dating the middle and late Quaternary Caspian Sea-level fluctuations: First luminescence data from the coast of Turkmenistan. Quaternary Geochronology, 83, 101599. https://doi.org/10.1016/j.quageo.2024.101599
- MacKinnon, J. A., Zhao, Z., Whalen, C. B., Waterhouse, A. F., Trossman, D. S., Sun, O. M., Goldbaum, D., Buijsman, M. C., Kunze, E., Brummel, N. M., & Alford, M. H. (2017). Climate process team on internal wave–driven ocean mixing. Bulletin of the American Meteorological Society, 98(11), 2429–2454. https://doi.org/10.1175/BAMS-D-16-0030.1
- Marshall, J., & Schott, F. (1999). Open-ocean convection: Observations, theory, and models. Reviews of Geophysics, 37(1), 1–64. https://doi.org/10.1029/98RG02739
- Mellor, G. L., & Yamada, T. (1982). Development of a turbulence closure model for geophysical fluid problems. Reviews of Geophysics, 20(4), 851–875. https://doi.org/10.1029/RG020i004p00851
- Nasrollahzadeh, H. S., Din, Z. B., Foong, S. Y., & Makhlough, A. (2008). Trophic status of the Iranian Caspian Sea based on water quality parameters and phytoplankton diversity. Continental Shelf Research, 28(9), 1153–1165. https://doi.org/10.1016/j.csr.2008.02.015
- Osborn, T. R. (1980). Estimates of the local rate of vertical diffusion from dissipation measurements. Journal of Physical Oceanography, 10(1), 83–89. https://doi.org/10.1175/1520-0485(1980)010<0083:EOTLRO>2.0.CO;2
- Özsoy, E., & Ünlüata, Ü. (1997). Oceanography of the Black Sea: A review of some recent results. Earth-Science Reviews, 42(4), 231–272. https://doi.org/10.1016/S0012-8252(97)81859-4
- Renssen, H., Lougheed, B. C., Aerts, J. C. J. H., De Moel, H., Ward, P. J., & Kwadijk, J. C. J. (2007). Simulating long-term Caspian Sea level changes: The impact of Holocene and future climate conditions. Earth and Planetary Science Letters, 261(3–4), 685–693. https://doi.org/10.1016/j.epsl.2007.07.037
- Rodionov, S. N. (1994). Global and regional climate interaction: The Caspian Sea experience. Springer.
- Sannino, G., Herrmann, M., Carillo, A., Rupolo, V., Ruggiero, V., Artale, V., & Heimbach, P. (2009). An

eddy-permitting model of the Mediterranean Sea with a two-way grid refinement at the Strait of Gibraltar. Ocean Modelling, 30(1), 56–72. https://doi.org/10.1016/j.ocemod.2009.06.002

- Stanev, E. V., & Peneva, E. L. (2002). Regional sea level response to global climatic change: Black Sea examples. Global and Planetary Change, 32(1–2), 33–47. https://doi.org/10.1016/S0921-8181(01)00148-5
- Stolberg, F., et al. (2013). Caspian Sea ecosystem profile. World Bank. https://documents.worldbank.org/en/publication/documents-reports/documentdetail/803551468262426883/caspian-sea-ecosystem-profile
- Sur, H. İ., Özsoy, E., & Ünlüata, Ü. (2000). Satellite-derived flow characteristics of the Caspian Sea. In A. G. Kostianoy & A. N. Kosarev (Eds.), The Caspian Sea Environment (pp. 109–134). Springer.
- Terziev, F. S., Kosarev, A. N., & Kerimov, A. A. (Eds.). (1992). Hydrometeorology and Hydrochemistry of the Seas, Vol. 6: The Caspian Sea, Issue 1. Hydrometeoizdat.
- Thomas, L. N., Tandon, A., & Mahadevan, A. (2008). Submesoscale processes and dynamics. In J. C. McWilliams & E. P. Chassignet (Eds.), Ocean Modeling in an Eddying Regime (pp. 17–38). American Geophysical Union. https://doi.org/10.1029/177GM04
- Thorpe, S. A. (2005). The turbulent ocean. Cambridge University Press.
- Tuzhilkin, V. S. (2005). Seasonal variability of the Caspian Sea thermohaline structure. In A. N. Kosarev & A. G. Kostianoy (Eds.), The Caspian Sea Environment (pp. 83–104). Springer.
- UNEP-DHI Centre. (2024). Caspian Sea fluctuations and climate change. UNEP-DHI Centre. https://unepdhi.org/wp-content/uploads/sites/2/2024/11/Caspian_Sea_working_paper.pdf
- Waterhouse, A. F., MacKinnon, J. A., Nash, J. D., Alford, M. H., Kunze, E., Simmons, H. L., Polzin, K. L., St. Laurent, L. C., Sun, O. M., Pinkel, R., Talley, L. D., Whalen, C. B., Carter, G. S., Fer, I., Waterman, S., Garabato, A. C. N., & Voet, G. (2014). Global patterns of diapycnal mixing from measurements of the turbulent dissipation rate. Journal of Physical Oceanography, 44(7), 1854–1872. https://doi.org/10.1175/JPO-D-13-0104.1
- Whalen, C. B., MacKinnon, J. A., Waterhouse, A. F., & Wunsch, C. (2020). Internal wave-driven mixing: Global patterns and trends. Annual Review of Marine Science, 12, 131–155. https://doi.org/10.1146/annurev-marine-010419-010935
- Wunsch, C., & Ferrari, R. (2004). Vertical mixing, energy, and the general circulation of the oceans. Annual Review of Fluid Mechanics, 36, 281–314. https://doi.org/10.1146/annurev.fluid.36.050802.122121
- Zavialov, P. O., Belokopytov, V. N., & Konovalov, B. V. (2003). Spreading of the river discharge plume of the Volga River in the Caspian Sea. Geophysical Research Letters, 30(12), 1630. https://doi.org/10.1029/2003GL017541
- Zonn, I. S., Kosarev, A. N., Glantz, M. H., & Kostianoy, A. G. (2010). The Caspian Sea Encyclopedia. Springer.

INTERNATIONAL JOURNAL OF
COASTAL, OFFSHORE & ENVIRONMENTAL ENGINEERING IJCOE Vol.11/No. 1/Winter 2026 (81-90)

Available online at: www. ijcoe.org

Investigation the impact of wave charactristics and PTO parameters on the performance of a Two-Body Floating Point Absorber in the Gulf of Oman

Saeed Najafi
Assistant Professor, Iranian National Institute for Oceanography and Atmospheric Science (INIOAS);
s.najafi@inio.ac.ir

ARTICLE INFO

Article History:
Received :31 Aug 2025
Accepted :02 Feb 2026

Keywords:
Self-Reacting Floating-Point Absorbers
Wave energy converters
CFD
Power take-off
Gulf of Oman

ABSTRACT

The present research studies the impact of wave charactristics as well as the power take-off (PTO) damping on the hydrodynamic performance of a two-body floating point absorber (FPA) which sometimes called self-reacting point absorber (SRPA) or two-body wave energy converter (WEC) device. This type of WEC is designed for operation in the Gulf of Oman and its geometry is inspired from the famous reference model (RM3) which was developed at the National Renewable Energy Laboratory (NREL), United States. The numerical model was developed in the Siemens STAR-CCM+ software which solves the complete form of fluid governing equations. The parameters of the incident waves, was selected based on the previous researches on this region and PTO damping is specified based on the RM3 model design. The results show that changes in wave period and PTO damping significantly influence energy capture and converter efficiency. The results show that the absorbed power increases monotonically with wave height and reaches a maximum at a wave period of 6 s, indicating a clear resonant response of the two-body WEC across all tested sea states.

1. Introduction

Ocean waves represent one of the most persistent and underutilized renewable energy resources available to coastal regions (Chen et al., 2023; Evans, 1981; Falnes, 2007; Ishaq et al., 2023; Li & Yu, 2012). Their high energy density, predictability over daily and seasonal cycles, and global abundance make wave energy conversion an attractive complement to more variable sources such as wind and solar. Over the past several decades, a broad range of Wave Energy Converters (WECs) has been proposed, each attempting to harvest the oscillatory motion of waves through buoyancy-driven mechanisms, hydrodynamic forces, or pressure variations below the free surface. Among these technologies, the point absorber concept has emerged as one of the most versatile designs due to its compact footprint and ability to extract energy from multiple wave directions (Liu et al., 2022; Soleimani et al., 2023).

Early point absorber systems consisted primarily of a single buoy oscillating relative to a fixed seabed-mounted structure. Foundational studies in the 1970s established the theoretical basis for these devices, revealing how their hydrodynamic behavior and resonant response could be exploited to maximize absorbed power (Salter, 1974; Budar & Falnes, 1975). However, single-body point absorbers face inherent challenges in environments where tidal fluctuations significantly alter the effective distance between the free surface and the seabed (Evans, 1976; Mei, 1976; Newman, 1976). These variations can degrade the system's mechanical leverage and ultimately reduce its energy capture potential (Ma et al., 2020).

To address these limitations, researchers later introduced multi-body concepts in which a floating element interacts with a secondary reactive body rather than a rigid seabed. Two-body Floating Point Absorbers (FPAs) allow the device to harvest energy from the relative heave motion between the two bodies, making them largely insensitive to water-level changes (Beatty et al., 2015; Liang & Zuo, 2017; Yu & Li, 2013). This configuration has since become a cornerstone of modern WEC development, with experimental and numerical studies demonstrating its superior energy extraction efficiency under a wide range of sea states. Several prototypes—including multi-float systems and hybrid configurations—have further expanded the design space, highlighting the

broader potential of multi-body devices within the renewable marine energy sector (OPT, 2023).

Moreover, FPAs with three or more bodies have been proposed. (Rhinefrank et al., 2010) created a model scale with a control system, demonstrated through wave tank tests, which later led to the formation of Columbia Power Technology. (Stansby et al., 2017) developed the WEC M4, a moored three-float line absorber, to enhance power capture through experimental methods. (Sricharan & Chandrasekaran, 2021) introduced an innovative floating WEC with multiple floating bodies and a hydraulic PTO system. This device features a central buoy connected to surrounding floating bodies via a lever arm and is stabilized using a taut-mooring system.

(Falnes, 1999) conducted a theoretical study on a two-body FPA device, demonstrating that the relative heave motion between two axisymmetric bodies can absorb wave power. He showed that it is feasible to capture all the power in an incident wave with a crest length equal to the wavelength divided by 2π. He provided a theoretical proof of maximum power without detailed analysis. This study aims to offer a comprehensive theoretical analysis of a two-body system.

(Li & Yu, 2012) demonstrated the maximum power output of a two-body FPA with limited parameters. (Windt et al., 2021) explored maximum power at different scales using the Reynolds-averaged Navier–Stokes equation, while (Zheng et al., 2021) examined the scaling effect through experimental tests, smooth physical hydrodynamics, and theoretical analysis. These studies highlighted the benefits of multiple-body FPAs over single-body FPAs. However, the impact of various factors on the power output of multiple-body FPAs remains unclear, which is crucial due to the high costs of the tools used.

Our research focuses on the computational fluid dynamics (CFD) analysis of a two-body floating point absorber to optimize its performance under different wave and PTO parameters. This device was intended to work under the environmental conditions of the Gulf of Oman. The Gulf of Oman, a semi-enclosed sea with moderate but reliable seasonal wave activity, provides a unique case for exploring such design sensitivities. Although the region's wave power potential is lower than that of open-ocean sites, the area remains attractive for small- and medium-scale WEC deployment due to its proximity to coastal infrastructure and the seasonal consistency of wave patterns. Prior studies have characterized the local wave climate, identifying periods during the summer monsoon season in which wave heights and dominant periods align with the operational range of many point absorber concepts.

The PTO system is vital for converting mechanical energy from the wave-induced motion of the FPA into electrical energy. It typically includes components such as hydraulic rams, electrical generators, or mechanical systems tuned to the device's motion. Key factors influencing power performance is PTO damping, which control the device's response to wave forces. Improper tuning of this parameter can result in inefficient energy capture or even structural failure. By varying PTO parameters, the optimal conditions that maximize energy absorption and converter efficiency was identified. The findings of this research could lead to more efficient designs of FPAs and contribute to the advancement of wave energy technology.

2. Methods and Materials

2.1. Site Selection

Based on previous studies on the wave energy assessments, northern coasts of the Gulf of Oman, near the coast of Chabahar exhibit strong wave energy, specially from June to September. Based on the field measurements, significant wave height varies between 0.5 and 2 meters while peak period changes from 4 to 10 seconds (Saket et al, 2012). As shown in the **Figure 1**, they investigated four regions with highest annual mean power. Some major parameters including location, depth of water, distance to mainland and mean wave power are listed in **Table 1**. Based on the two last columns of Table, the present research focused on site B because it has minimum distance to the coastline and highest value of mean annual wave power which is 2.82 (kW/m).

Table 1: Main characteristics of selected areas in north part of the Gulf of Oman

Station ID	Lat. ºN	Long. ºE	Depth (m)	Distance to coastline (km)	J_{mean} (kW/m)
A	25.28	59.27	38.2	17	2.7
B	25.32	59.87	41	4.5	2.82
C	25.28	60.14	40.9	7	2.78
D	25.22	60.47	38	7.5	2.72

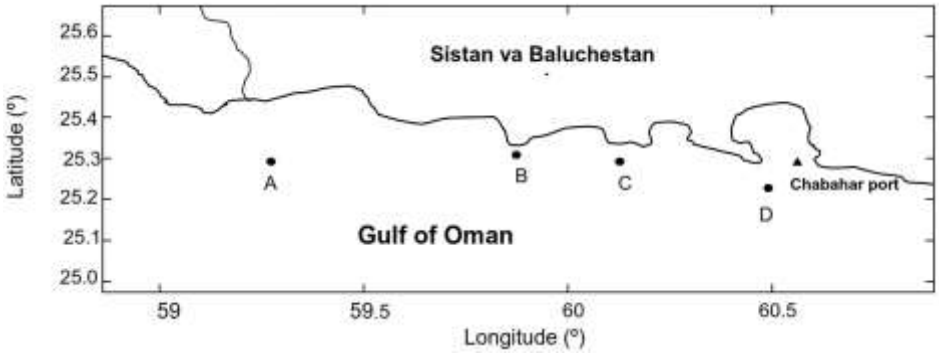

Figure 1: The selected locations for study of FPA performance

Based on the water depth in this region which is approximately 70 meters, a conceptual sketch of a two-body FPA with appropriate dimensions which is inspired from the famous reference model (RM3) and is shown in Figure 2. The performance of the FPA device was modeled using computational fluid dynamics (CFD) simulations to capture the complex interactions between the waves, the floating structure, and the power take-off (PTO) system. The numerical approach used in this study involves simulating the fluid-structure interaction (FSI) between the water waves and the floating device, taking into account the effects of significant wave height and different wave periods.

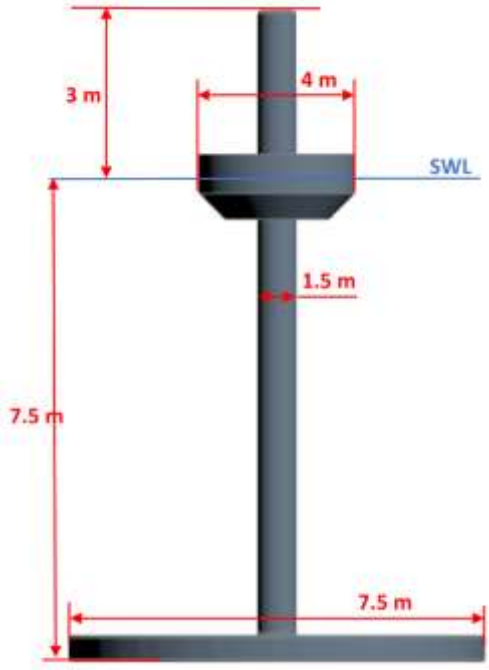

Figure 2: FPA model with main dimensions

2.2. Numerical Model Setup

A comprehensive hydrodynamic model was developed using Siemens STAR-CCM+, a multiphysics simulation platform capable of resolving the nonlinear free-surface behavior and fluid–structure coupling inherent to wave energy systems. The model employs an Unsteady Reynolds-Averaged Navier–Stokes (URANS) formulation, augmented with a Volume of Fluid (VOF) method to represent multiphase interfaces and wave deformation with high fidelity. The model consists of two main parts: the hydrodynamic model for simulating wave propagation and the mechanical model for the FPA's response to wave forces. The two-body FPA was modeled with precise geometric specifications, including dimensions, mass properties, and hydrodynamic coefficients. The two bodies consist of a primary floating body and a secondary submerged body, connected by a power take-off (PTO) system with adjustable damping coefficient. The main charactristic of the WEC for prototype and subscale of RM3 are summurized in the table below.

Table 2: Main particulars of the RM3 WEC for full-scale and 1:4 sub-scale

Parameter	Full Scale	1:4 Model
Float diameter (m)	20	5
Float draft (m)	3	0.75
Spar diameter (m)	6	1.5
Plate diameter (m)	30	7.5
Total draft (spar+plate) (m)	30	7.5
Float mass (kg)	727000	11360
Spar+plate mass (kg)	912800	14260
Heave natural period (s)	9	4.5
Heave natural frequency (rad/s)	0.698	1.4
Hydrostatic stiffness, K (kN/m)	270	17
Opt. PTO Damping (kN.s/m)	7000	225
Design Wave height, H (m)	3	0.75
Design Wave period, T (s)	12	6

The fluid domain represents the ocean environment and the waves acting on the FPA. To simulate the dynamic behavior of the WEC, an unsteady Reynolds-averaged Navier–Stokes (URANS) model was employed with a $k-\epsilon$ turbulence model on a finite-volume grid. For temporal discretization, a second order scheme was employed. To track the free surface deformations of the multiphase flow, a volume of fluid (VOF) model was used. The governing equations are as follows:

$$\frac{\partial \boldsymbol{u}}{\partial t} + (\boldsymbol{u}.\nabla)\boldsymbol{u} = -\frac{1}{\rho}\nabla p + \nu\nabla^2\boldsymbol{u} + \boldsymbol{f} \quad (1)$$

$$\nabla.\boldsymbol{u} = 0 \quad (2)$$

where:

- $\boldsymbol{u}$ is velocity field,
- p is the pressure,
- ν is the kinematic viscosity,
- ρ is the fluid density,

$\boldsymbol{f}$ represents the external forces including gravity and wave forcing.

Wave conditions was generated using a fifth-order Stokes wave formulation, providing a robust representation of nonlinear wave kinematics. These synthesized waves were introduced through a motion-specified boundary condition that enforces the desired free-surface profile and fluid particle velocity near the inlet. Figure 3 shows a schematic of device as modeled in the software. Only heaving motion was considered in this research, thus both the floating and reactive parts were allowed just one degree of freedom in vertical (z) direction and the wave propagation is aligned in the horizontal (x) direction. The more details about the computational model such as boundary conditions, domain particulars, wave damping near the outlet boundary and motion dynamics are presented in the subsequent subsections.

2.3. Computational domain

A schematic view of the computational domain for simulations of the two-body FPA device is shown in Figure 3. The three boundaries at left, front and back are set to Velocity inlets, in which the fluid velocity components and volume fraction are preset. Bottom boundary represent a no-slip wall. To consider the real flow effects, no symmetry planes were defined and numerical model was defined three dimensional. A pressure outlet boundary, where the condition of hydrostatic pressure of water column and volume fraction of light and heavy fluid is specified at the right and top side of the domain. Moreover, to avoid the water entry from the outlet boundary into the domain, a numerical damping region is defined at right side of the domain with prescribed coefficients based on software recommendations. The FPA body surface was considered as no-slip wall as well.

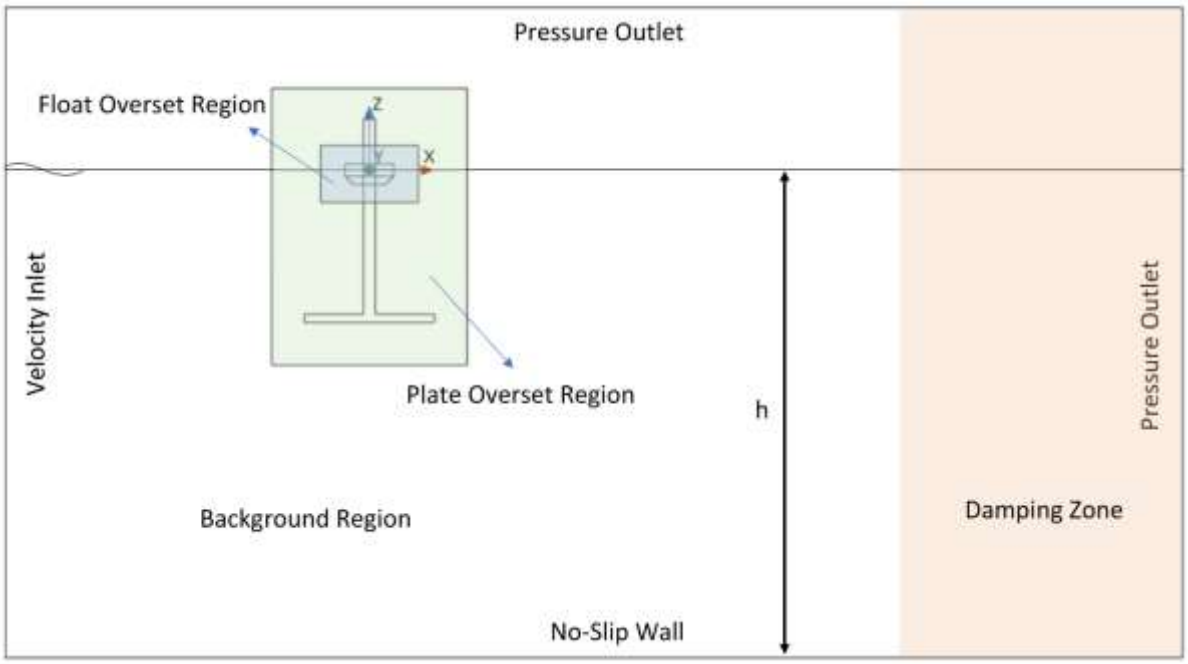

Figure 3: Domain particulars and overset grids used for FPA

The computational domain consists of three separate mesh zones. One background mesh which represent the fluid basin and two overset mesh which encompass the floating and reactive parts of the WEC. Overset grids were created using the unstructured polyhedral grids and can move over the background mesh which was created using the structured hexahedral grids. To increase the accuracy of the results, a set of refinement zones were defined in the regions with high gradients of the flow parameters.

Table 3: Characteristics of the numerical model

Wave Parameters		
Wave Period	4~10	s
Wave Height	0.4~2.0	m
PTO Parameters		
Damping Constant	50~350	$kN.s/m$
Domain Geometry		
Domain length	300	m
Domain height	100	m
Domain width	100	m
Water depth	70	m

Height of Free Surface Zone	3	m
Length of Damping Zone	80	m
Solver Parameters		
Time Step	0.05	s
Total Physical Time	100	s
Mesh Parameters		
Total Number of Cells	2257180	–
Number of Cell in Background	2020342	–
Cells in Floating Overset	75724	–
Cells in Reactive Overset	111114	–

The time step for the transient simulations was chosen to maintain Courant–Friedrichs–Lewy (CFL) numbers well below unity, ensuring numerical stability and capturing rapid changes in free-surface shape (Courant et al., 1928). The time discretization was performed using a second-order accurate scheme to preserve phase fidelity in the oscillatory motion of the device.

$$CFL = \frac{u\,\Delta t}{\Delta x} \quad (3)$$

The CFL number defines the number of cells which the fluid particles can travel through in each time step. Regarding in a free surface flow, the characteristic velocity represented by phase velocity of the wave ($v_p = \lambda/T$), and the number of cells in x direction in a wave length is ($n = \lambda/\Delta x$), we may have:

$$CFL = \frac{\lambda \Delta t}{T \Delta x} \rightarrow \Delta t = \frac{CFL.T}{n} \quad (4)$$

Thus, to preserve the CFL in a stable range, time step could be estimated for each test case. To capture the boundary layer near the body surface, prismatic layer meshes created around the floating and reactive parts. The cell size at the first layer is set such that the y^+ in the wall function is about ($y^+ \approx 150$). Figure 4 shows a cross section of the boundary layer cells around the reactive part as well as the numerical grid around floating point wave energy converter. To determine the optimum mesh size, a gris study was carried out and final model includes more than 2,250,000 computational prismatic cells in total. Simulation time was considered 100 s in all cases with time step of 0.05 seconds.

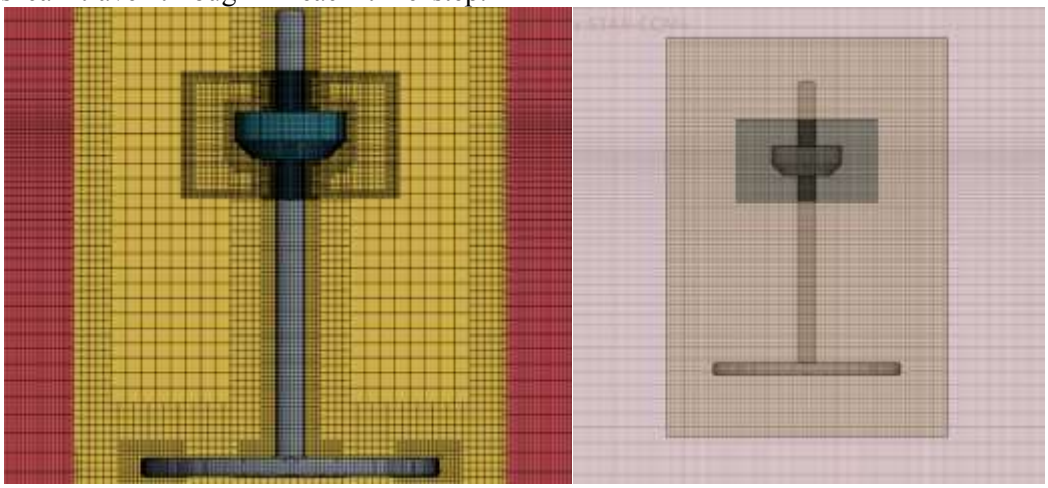

Figure 4: Numerical grid around wave energy converter

2.4. Damping zone

One of the most crucial issues in modeling the numerical wave tanks is treatment of the backflows and wave reflections from the boundaries. Since in the water waves problem, the fluid particle trajectory is orbital, a simple pressure outlet boundary cannot handle this issue. To alleviate the problem, a damping zone usually defined on the pressure outlet boundaries (Figure 3). The length of damping zone is defined two times of the wave length as Star-CCM+ guidelines. In the damping zones, the velocity components are mitigated using a resistant term which increases quadratically with distance towards the outlet boundaries and ideally, the wave amplitude vanishes as they approach to the outlet boundaries (Choi & Yoon, 2009). In some references, it is called the numerical beaches.

2.5. Power take-off (PTO) system

To harvest the energy from two-body FPA, a PTO mechanism must be implemented between floating and reactive parts. In the most cases, a spring-damper system used to take out power from the system. Normally, due to inherent hydrostatic stiffness of the buoy, PTO stiffness is ignored and the only effective PTO parameter is damping of power take-off system which controls the dissipation of energy. For each simulation, the PTO damping is varied across a predefined range to assess its impact on the overall performance of the FPA. As mentioned in the **Table 2**, in this study, damping varies from 150 to 400 $kN.s/m$. This range is selected based on prior wave tank experiments on RM3 (Xu et al., 2023). Generally, the PTO force is proportional to the relative position and the velocity of the bodies. One can write:

$$z = z_f - z_r \quad (5)$$

In which z_f and z_r represent the vertical position of floating and reactive parts respectively. The damping component of the PTO mechanism can be expressed with constant b_{PTO} and is related to the relative velocity of two bodies as:

$$F_{damping} = -b_{PTO}\dot{z} \quad (6)$$

Where $\dot{z}$ is relative velocity between two components. Time-averaged absorbed power by the PTO mechanism is defined by:

$$P = \frac{1}{2} b_{PTO}|\dot{z}|^2 = \frac{1}{2} b_{PTO}\omega^2|z|^2 \quad (7)$$

3. Results and Discussion

This section presents the hydrodynamic response of the two-body floating point absorber (FPA) under different PTO configurations and wave conditions. All simulations were carried out after ensuring numerical stability and convergence of the CFD model.

3.1. Model Validation with Heave Decay

Before evaluating the effect of wave and PTO, the numerical model was validated against experimental heave decay measurements. In this step, the floating and reactive bodies were rigidly connected, converting the system into an equivalent single-degree-of-freedom heaving cylinder. Figure 5 demonstrates excellent agreement between the numerical and experimental time response of heave oscillations. The good agreement between numerical and experimental measurments confirms that the CFD model accurately captures both radiation and diffraction effects, enabling reliable assessment of PTO-coupled motions.

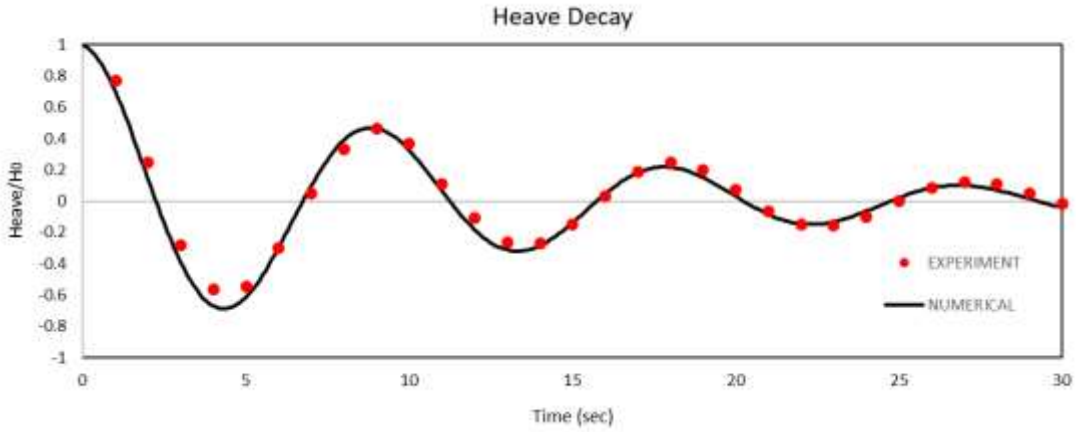

Figure 5: Comparison between experimental and numerical results of heave decay test

3.2. The effect of PTO Stiffness

PTO damping is a key parameter governing energy extraction, as it dictates the rate at which mechanical motion is converted into useful power. To quantify its impact, damping values ranging from 50 to 350 kNs/m were examined across wave periods from 4 to 10 seconds.

Figure 6 shows the absorbed power as a function of wave period for different damping levels and a clear bell-shaped pattern appears in each case. These findings support the results of (Li & Yu, 2012), who reported a similar bell-shaped trend between damping and energy capture. As seen in the figure, at low damping, because the system undergoes large oscillations, the force applied by the PTO is large enough to extract significant power. However, as expected this trend reversed with increasing the wave period due to changing the frequecy of excitation force.

At the moderate dampings (200-300 kNs/m), the energy absorption in a large interval of periods, has no significant changes and almost remains uniform. At high damping, the device becomes overdamped, suppressing relative motion between bodies and abrosbed power reduced.

Because dominant wave period of the region is between 6 to 7 seconds, the optimum damping would be around 100 kNs/m, which coincides closely with the device's natural period. This behavior is consistent with classical hydrodynamic theory, in which maximum power extraction occurs when mechanical damping equals radiation damping.

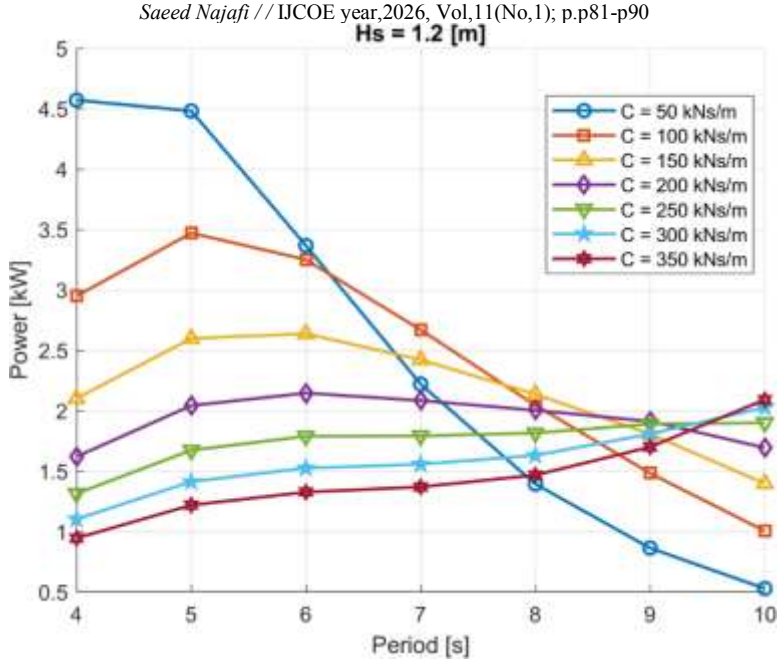

Figure 6: Absorbed power in different PTO damping in Hs=1.2 m

3.3. The effect of environmental conditions

Following the absorbed power of WEC is plotted in different wave conditions for different damping values of PTO. These types of curved is known as power matrix which extensively used for calculation of annual energy production (AEP) of wave energy devices in conjunction with joint probability distribution (JPD) of sea states.

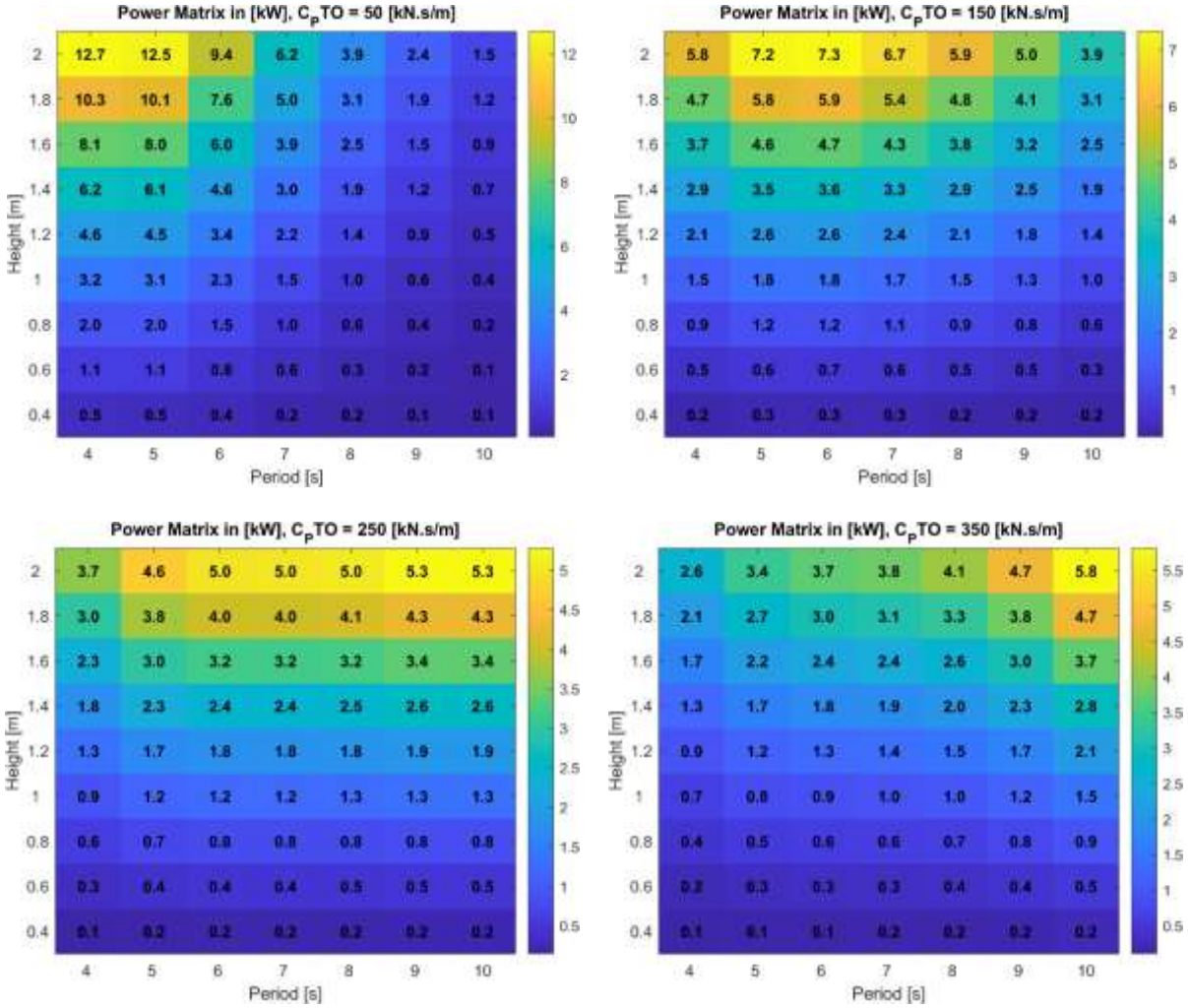

Figure 7: Power matrix of WEC in different sea states and dampings

Based on the absorbed power data presented in the each contour plots, several key trends emerge. First, absorbed power increases consistently with wave height across all periods, which is expected since wave energy flux is proportional to the square of wave height. For the largest wave height considered (2.0 m), the maximum absorbed power reaches approximately 12.7 kW at a wave period of 4 s, while the smallest wave height (0.4 m) yields negligible power (<0.2 kW) regardless of period. This monotonic relationship highlights the strong sensitivity of the two-body WEC to incident wave amplitude, emphasizing the importance of siting in energetic sea states.

The plot also reveals a clear resonant behaviour with respect to wave period. For all wave heights above 0.8 m, the absorbed power peaks at a period of near 6 seconds, with secondary peaks or plateaus at 5 s and 7 s. For instance, when PTO damping set around 200 kNs/m, at H = 2.0 m, power at T = 6 s is about 6.0 kW, compared to 5.7 kW at 5 s and 5.8 kW at 7 s, indicating a relatively broad, near-symmetric response around the natural period of the device. As wave height decreases, the peak becomes less pronounced but remains centred at 6 s. This suggests that the optimal PTO damping selected for this test case is well-tuned to the primary resonance of the two-body system, yielding consistent energy capture over a range of operational conditions.

From a design perspective, the relatively flat response between 5 and 7 s for moderate to high wave heights (e.g., H ≥ 1.2 m) is advantageous, as it implies the device can maintain satisfactory performance even when the sea state deviates from the exact resonance period. However, for very small wave heights (H ≤ 0.6 m), absorbed power becomes uniformly low across all periods, indicating a practical threshold below which energy extraction is not economically viable. These results underscore the need for adaptive PTO control strategies to broaden the effective bandwidth and improve low-height performance, while also confirming that the current design is well-suited for sites with characteristic periods around 6 s and significant wave heights above 1 m.

3.4. Free surface profile

Time history of buoy motions in seven periods as well as the snapshots of the device's relative motion over a full wave cycle is illustrated in the following figures. A clear interplay among incident, radiated, and diffracted wave components is shown in the plots.

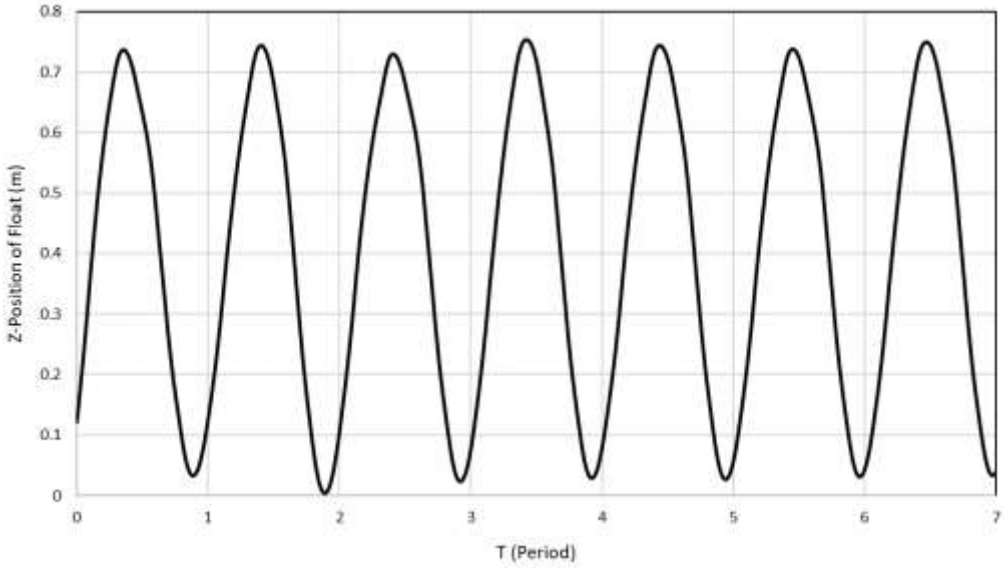

Figure 8: Time history of the floating part heave motions

The free-surface elevation plot at four time stamps reveals radiated waves propagating outward from the reactive body. These waves are a physical manifestation of radiation damping, a hydrodynamic mechanism essential for effective wave energy extraction.

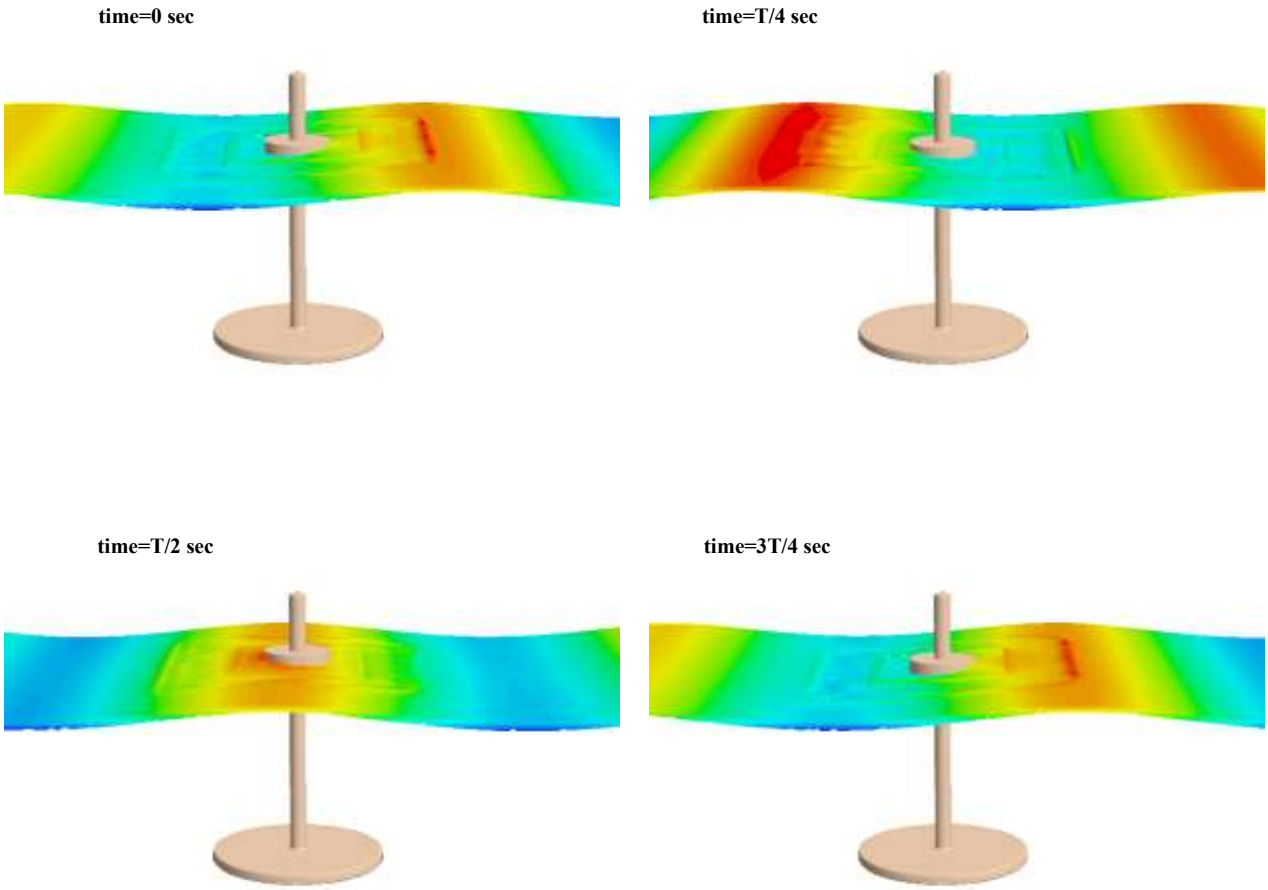

Figure 9: Free surface profiles at different time steps

4. Conclusions

This study presented a comprehensive CFD-based evaluation of a two-body floating point absorber (FPA) designed for deployment in the Gulf of Oman, with a particular focus on the influence of PTO damping and sea states on energy absorption. Using a high-fidelity URANS–VOF numerical framework with overset grids, the dynamic interaction between waves, floating bodies, and the PTO system was captured with high accuracy. Validation against experimental heave decay data confirmed that the numerical model reliably reproduces the hydrodynamic behavior of the device.

Based on the analysis of the absorbed power across varying sea states, wave height is the primary driver of power output, with absorbed energy increasing nearly quadratically with height, for instance, raising the wave height from 1.2 m to 2.0 m at the optimal period of 6 s resulted in more than a doubling of captured power. Simultaneously, the wave period determines the spectral tuning of the device. On the other hand, the performance bandwidth is relatively broad (5–7 s), which is beneficial for real-sea applications where periods vary. Below a threshold wave height of approximately 0.6 m, the absorbed power becomes negligible (<0.2 kW) regardless of period, defining a practical lower limit for viable energy extraction.

The results also show that PTO tuning plays a critical role in maximizing power capture, and that optimal performance is obtained when PTO parameters align the device's mechanical response with the dominant wave period of the environment. PTO damping was found to have a strong, frequency-dependent influence on performance. A clear optimal damping value of approximately 100 kNs/m emerged, corresponding to a wave period between 5-7 seconds, where the device exhibits near-resonant behavior. At this operating point, the absorbed power reaches its highest levels, consistent with the theoretical expectation that maximum power is achieved when mechanical damping is tuned to match hydrodynamic radiation damping.

Although the PTO optimization identified clear operational sweet spots, the absolute power levels obtained under realistic Gulf of Oman conditions remain relatively low. This limitation is attributed primarily to the weak wave energy climate of the region, which is enclosed by land and lacks significant long-period swells. Therefore, while the device design is hydrodynamically efficient, its deployment in the Gulf of Oman is unlikely to be economically viable. More energetic offshore locations or sites adjacent to open ocean swell would be better suited for exploiting

the full performance potential of this two-body FPA concept.

The study highlights the value of high-fidelity CFD simulations for capturing complex FSI dynamics and guiding PTO design. However, several opportunities exist for future work. These include extending the analysis to irregular and multidirectional waves, incorporating more realistic PTO control strategies, exploring the effects of extreme events, and evaluating additional WEC archetypes such as oscillating water columns or bottom-hinged flaps. The integration of optimization algorithms or machine-learning-based surrogate models could further accelerate the search for optimal PTO configurations. Such enhancements would provide deeper insight into device behavior across diverse sea states and support the development of more efficient and robust wave energy conversion systems.

5. References

Amiri, A., Panahi, R., & Radfar, S. (2016). Parametric study of two-body floating-point wave absorber. *Journal of marine science and application*, *15*, 41-49.

Beatty, S. J., Hall, M., Buckham, B. J., Wild, P., & Bocking, B. (2015). Experimental and numerical comparisons of self-reacting point absorber wave energy converters in regular waves. *Ocean Engineering*, *104*, 370-386.

Budar, K., & Falnes, J. (1975). A resonant point absorber of ocean-wave power. *Nature*, *256*(5517), 478-479.

Chen, H., Xu, Q., Zheng, X., Bennetts, L. G., Xie, B., Lin, Z., Lin, Z., & Li, Y. (2023). Viscous effects on the added mass and damping forces during free heave decay of a floating cylinder with a hemispherical bottom. *European Journal of Mechanics-B/Fluids*, *98*, 8-20.

Choi, J., & Yoon, S. B. (2009). Numerical simulations using momentum source wave-maker applied to RANS equation model. *Coastal Engineering*, *56*(10), 1043-1060.

Courant, R., Friedrichs, K., & Lewy, H. (1928). Über die partiellen Differenzengleichungen der mathematischen Physik. *Mathematische annalen*, *100*(1), 32-74.

Evans, D. (1976). A theory for wave-power absorption by oscillating bodies. *Journal of Fluid Mechanics*, *77*(1), 1-25.

Evans, D. (1981). Power from water waves. *Annual review of Fluid mechanics*, *13*, 157-187.

Falcão, A. F., & Henriques, J. C. (2015). Effect of non-ideal power take-off efficiency on performance of single-and two-body reactively controlled wave energy converters. *Journal of Ocean Engineering and Marine Energy*, *1*, 273-286.

Falnes, J. (1999). Wave-energy conversion through relative motion between two single-mode oscillating bodies.

Falnes, J. (2007). A review of wave-energy extraction. *Marine structures*, *20*(4), 185-201.

Ishaq, M., Chen, Z.-M., & Zhao, Q. (2023). Analysis of nonlinear water wave interaction solutions and energy exchange between different wave modes. *Physics of Fluids*, *35*(2).

Li, Y., & Yu, Y.-H. (2012). A synthesis of numerical methods for modeling wave energy converter-point absorbers. *Renewable and Sustainable Energy Reviews*, *16*(6), 4352-4364.

Liang, C., & Zuo, L. (2017). On the dynamics and design of a two-body wave energy converter. *Renewable energy*, *101*, 265-274.

Liu, Y., Zheng, S., Liang, H., & Cong, P. (2022). Wave interaction and energy absorption from arrays of complex-shaped point absorbers. *Physics of Fluids*, *34*(9).

Ma, Y., Zhang, A., Yang, L., Li, H., Zhai, Z., & Zhou, H. (2020). Motion simulation and performance analysis of two-body floating point absorber wave energy converter. *Renewable energy*, *157*, 353-367.

Mei, C. C. (1976). Power extraction from water waves. *Journal of Ship Research*, *20*(02), 63-66.

Newman, J. N. (1976). The interaction of stationary vessel with regular waves. International Proceedings of the 11th Symposium on Naval Hydrodynamics, ONR, 1976,

OPT. (2023). *Information about PB3 PowerBuoy wave energy device*. http://www.oceanpowertechnologies.com

Rhinefrank, K., Schacher, A., Prudell, J., Stillinger, C., Naviaux, D., Brekken, T., von Jouanne, A., Newborn, D., Yim, S., & Cox, D. (2010). High resolution wave tank testing of scaled wave energy devices. International Conference on Offshore Mechanics and Arctic Engineering,

Saket, A., & Etemad-Shahidi, A. (2012). Wave energy potential along the northern coasts of the Gulf of Oman, Iran. Renewable Energy, 40(1), 90-97.

Salter, S. H. (1974). Wave power. *Nature*, *249*(5459), 720-724.

Soleimani, K., Ketabdari, M. J., & Gharechae, A. (2023). Smoothed particle hydrodynamics study of a heaving point absorber in various waves using wave tank and calm-water models. *Physics of Fluids*, *35*(3).

Sricharan, V., & Chandrasekaran, S. (2021). Time-domain analysis of a bean-shaped multi-body floating wave energy converter with a hydraulic power take-off using WEC-Sim. *Energy*, *223*, 119985.

Stansby, P., Moreno, E. C., & Stallard, T. (2017). Large capacity multi-float configurations for the wave energy converter M4 using a time-domain linear diffraction model. *Applied Ocean Research*, *68*, 53-64.

Windt, C., Davidson, J., & Ringwood, J. V. (2021). Numerical analysis of the hydrodynamic scaling effects for the Wavestar wave energy converter. *Journal of Fluids and Structures*, *105*, 103328.

Xu, Q., Li, Y., Bennetts, L. G., Wang, S., Zhang, L., Xu, H., & Narasimalu, S. (2023). Parametric analysis of a two-body floating-point absorber wave energy converter. *Physics of Fluids*, *35*(9).

Yu, Y.-H., & Li, Y. (2013). Reynolds-Averaged Navier–Stokes simulation of the heave performance of a two-body floating-point absorber wave energy system. *Computers & Fluids*, *73*, 104-114.

Zheng, X., Chen, G., Cao, W., Xu, H., Zhao, R., Xu, Q., Kramer, M., Le Touzé, D., Borthwick, A. G., & Li, Y. (2021). On the energy conversion characteristics of a top-mounted pitching absorber by using smoothed particle hydrodynamics. *Energy Conversion and Management*, *250*, 114893.

INTERNATIONAL JOURNAL OF
COASTAL, OFFSHORE & MEDIUMAL ENGINEERING IJCOE Vol.11/No. 1/Winter 2026 (91-102)

Available online at: www. ijcoe.org

Development of Oceanic Numerical Model for Persian Gulf (part 2)

Mehri Fallahi[1], Masoud Sadrinasab[2*]

[1] *Instructor of Physics Lab, , Department of Agriculture Machinery Engineering, Faculty of Agricultural Engineering and Technologies, Collage of Agriculture & Natural Resources, Tehran University, Tehran, Iran, mehri_fallahi@ut.ac.ir*

[2*] *Associate Professor, Department of Environment Engineering, school of Graduate Environment, university of Tehran , Tehran, Iran masoud.sadri@ut.ac.ir*

ARTICLE INFO

Article History:
Received:17 Sep 2025
Accepted :11 Jan 2026

Keywords:
Persian Gulf
numerical model
primitive equations
sigma vertical coordinate
forced tide.

ABSTRACT

This study presents the development of a three-dimensional numerical model, the Persian Gulf Oceanic Model (ZSF974), designed to predict oceanographic parameters in the Persian Gulf, along with the results of its validation. The model is based on the primitive equations formulated in a spherical coordinate system with a sigma vertical coordinate. The model equations are solved numerically using the finite difference method: the Lax–Wendroff scheme for advective terms, the DuFort–Frankel scheme for diffusive terms, and the Matsuno scheme to control computational instabilities. The mesh employed is a modified Arakawa C grid. The model accommodates irregular bathymetry and supports variable resolution in both horizontal and vertical directions. Model accuracy was enhanced by optimizing the execution process and by properly applying Nihoul's (1977) theory on the wind-induced surface stress's effect on subsurface layers. After validating the model in idealized laboratory basins against established principles of physical oceanography and previous research, it was applied to the real-world environment of the Persian Gulf. Key results from the model's implementation include a counterclockwise water circulation, the presence of an amphidromic point, the dominance of tidal forces, and the influence of the Arvandrud and Mond rivers. Notably, this riverine impact is significant along the coasts of the United Arab Emirates. The model successfully simulates the general behavior of the oceanic environment in response to various forcing mechanisms. However, long-term simulations indicate that the open boundary conditions require modification and that real tidal forcing should be incorporated. Overall, the model shows significant potential for further development to yield more accurate simulations and robust conclusions.

1. Introduction

While oceans and seas contain over 97% of the Earth's water, it is primarily saltwater. They are, however, the fundamental source of the planet's freshwater through the hydrological cycle, which sustains all life. They play a vital role in regulating the global climate. Therefore, studying oceanic phenomena is essential for the sustainable management of this vast resource.

The Persian Gulf is a water basin situated the south of Iran (Figure 1), extends from 24° to 30°30' N latitude and from 48° to 56°25' E longitude.

Its coasts and continental shelf are rich in oil and gas reserves. This region also serves as a major global transit for oil, with the Persian Gulf exporting over 60% of the world's seaborne oil. Consequently, the Gulf holds immense economic and political significance increasing the value of research across various fields. In this context, research into the Gulf' physical

parameters, it's climate and coastal impacts, and broader oceanic phenomena, is of paramount importance.

This semi-enclosed basin, characterized by high temperature and salinity, is connected to the open ocean via the Strait of Hormuz. Investigating the impact of these conditions on marine life and pollution within the basin is a key research topic.

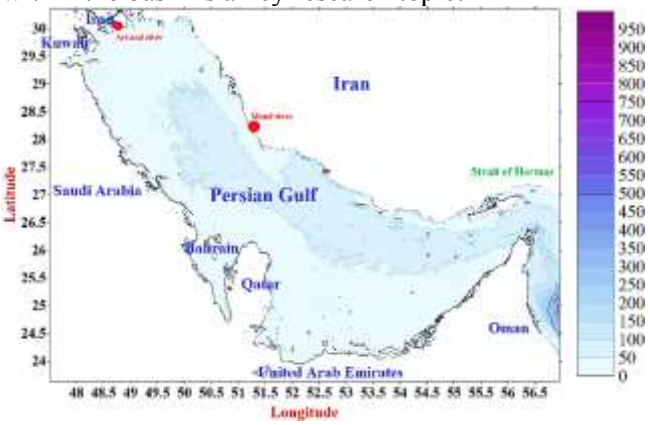

Figure 1- Location of the Persian Gulf

While satellite data analysis is a primary methods for study oceanic phenomena, satellites provide information only about surface waters. On the other hand, in-situ instruments, such as floating buoys, provide scattered data on physical parameters. Although, the governing equations can establish relationships between these disparate data points, they lack analytical solutions. Therefore, numerical methods provide the best means of solving them.

Numerical modeling describes atmospheric or oceanic systems by solving their governing equations numerically. A numerical model can explain a system's overall behavior in response to various forcings, predict or calculate parameters, and ultimately make the dynamics of a water basin comprehensible and analyzable. Model outputs are inherently subject to error. Nevertheless, by employing appropriate numerical methods, their accuracy can be improved to yield acceptable solutions.

The following section summarizes previous research conducted in the Persian Gulf using numerical models. In 1992, **Khaleghi Zavare** developed a non-linear barotropic model for the Persian Gulf. This model is based on the integration of shallow water equations in the vertical direction and is sensitive to the earth's rotation and the effects of bathymetric variations. The model was designed to determine the response of the Persian Gulf to wind and tidal forces through numerical simulation [1]. In 1994, **Zamanian** used a two-layer model to study the currents of the Persian Gulf. This model was based on the primitive equations in a Cartesian coordinate system with a sigma vertical coordinate. In addition to determining the current fields caused by wind and tides, this model predicts temperature and salinity in two layers, vertical velocity at a specified level, and sea surface height at the grid points [2]. **Sadrinasab and Kenarkoohi** (2009) examined the sound speed profile in different layers of the Persian Gulf. In this study, a three-dimensional hydrodynamic model (COHERENS) is employed in a fully prognostic mode to derive sound speed profiles in the Persian Gulf. Results of the model show that sound speed in the Persian Gulf depends mainly on temperature in the surface layer, whereas the bottom layer as well as the southern part of the Gulf depend on both temperature and salinity [3]. Sadrinasab, (2009) employed the COHERENS model as a three-dimensional hydrodynamic model to investigate coastal upwelling in the northern Persian Gulf with a horizontal resolution of 4 minutes of latitude and longitude. The findings showed that more kinetic energy accumulated along the Iranian coasts and also, a seasonal thermocline is evident with a surface to bottom temperature difference of around 12°C in summer. [4]. **Pous et al.** (2012) used a homogeneous shallow-water model with a free surface to study the tidal circulation in the Persian Gulf. The numerical finite-difference model includes harmonic diffusion of horizontal momentum and quadratic bottom friction. High-precision bathymetric data were used to represent the bottom topography. They found that tidal currents can be strong in the Strait of Hormuz and in shallow areas, thus having a significant effect on the region's hydrology. The residual currents are weak and therefore negligible for large-scale circulation over long periods [5]. **Azizpour et al**. (2014), conducted a study on the physical oceanographic properties of the Persian Gulf, the Strait of Hormuz, and the Sea of Oman based on CTD data. In this study, the spatial and temporal distributions of temperature, salinity, and density were investigated. They concluded that in summer, the water column was strongly stratified at deep stations and relatively well mixed at shallow stations. They also found that strong and weak thermocline layers were formed in summer ($\Delta T \approx 12$ °C) and winter ($\Delta T \approx 6$ °C) at deep stations, respectively [6]. **Delbari and Sheikhbahaei** (2020) numerically studied the propagation of underwater sound waves using the differential square method. In this study, the Differential Quadrature (DQ) method was applied for the numerical solution of underwater acoustic waves for the first time. Two experimental test cases were used to validate the two-dimensional wave model: first, the numerical results were verified against the analytical solution, and second, the applicability of the method in a complex domain was demonstrated. Comparisons confirmed the efficiency, accuracy, and robustness of the Differential Quadrature method for acoustic wave simulation [7]. **Mahpeykar and Khalilabadi** (2021) investigated the effect of wind speed and direction on evaporation rate in the Persian Gulf—assuming no water inflow to the basin—using numerical modeling. The results showed that wind direction has only a minor effect on evaporation,

whereas wind speed causes significant changes in both evaporation rate and water level. These changes are nonlinearly related to water temperature, such that in summer, as temperature increases, the evaporation rate increases more rapidly [8]. **Hosseini and Soltanpour** (2021) used the Flow Model (FM) module of MIKE 21 software (DHI, 2012) to investigate the characteristics of tidal wave propagation in the Persian Gulf. Their study indicated that tidal waves propagate from the Arabian Sea and the Gulf of Oman into the Persian Gulf through the Strait of Hormuz. Although the continental shelf resonance frequency of the basin is close to the period of diurnal constituents, the results showed that the tide is mainly mixed semidiurnal. The numerical experiments revealed that the Coriolis force, in combination with the geometry of the Persian Gulf, results in the generation of different amphidromic systems of diurnal and semidiurnal constituents. Moreover, the configuration of the bathymetry of the Persian Gulf—with a shallow zone at the closed end of the basin, extending longitudinally along the southern half (asymmetric cross-section)—leads to deformation of incoming and reflected tidal Kelvin waves and, consequently, to the shifting of amphidromic points [9]. **Pirooznia et al.** (2022) calibrated the MIKE21 oceanic numerical model for the Persian Gulf and the Gulf of Oman in order to improve the simulated surface currents obtained from the model. The calibration was performed through data assimilation of the model with altimetry and hydrographic observations using variational data assimilation, where the weights of the objective functions were defined based on the type of observations and optimized using metaheuristic optimization methods. According to the results, the calibration of the model generally led the model results closer to the observations. They showed that the kinetic energy produced by sea surface currents could be used for generating electricity in the Oman Sea and near Jask harbor [10].

Fallahi et al. (2019) designed a "Five-Layer Numerical Ocean Model of the Persian Gulf" with the aim of predicting physical parameters in the basin [11]. During the process of refining and enhancing the model, a laboratory-scale ocean basin was configured to resemble the Persian Gulf. A two-year simulation showed that the basin is dominated by semidiurnal tidal forcing, which prevails over wind stress and density-driven forces [12]. The consistency of the results with fundamental ocean physics and previous research provided a solid foundation for further model development.

The Persian Gulf, due to the extensive maritime boundary it provides for Iran, is of particular importance with respect to economic, tourism, and strategic activities. In addition, due to its unique geographical position, it has special strategic and economic value in the western part of Asia. Therefore, any research on this basin is considered highly important and strategic for planning purposes.

Since numerical modeling can be a powerful scientific tool, the development of the numerical ocean model PersianGulfOceanicModel (ZSF974) was initiated with the aim of predicting and calculating the physical parameters of the Persian Gulf.

This study presents the development process of the ocean numerical model "PersianGulfOceanicModel (ZSF974)" [11]. The design and development of the model are based on the technical principles of the Basic Oceanic Model (BOM) [13]. Therefore, the PersianGulfOceanicModel (ZSF974) can be considered an advanced and expanded version of the BOM model, designed to simulate real ocean environments.

The method used for designing the model allows its application to any hypothetical or real basin, whether closed or open. Another advantage of this model is the possibility of comparison with similar models developed by other researchers, as well as the superior algorithm employed in its design, which ensures accurate predictions by properly considering the relationships among the mathematical equations. Furthermore, the correct application of Nihoul's theory [14] regarding wind-induced surface stress effects on lower layers in multilayer environments has enhanced the accuracy of the model outputs.

This research was conducted in two phases: for laboratory oceanic basins (first phase) and for real oceanic basins (second phase). In the first phase [15], the technical aspects, along with the model results for laboratory oceanic basins, were presented and analyzed. In the present study, while reaffirming the technical details of PersianGulfOceanicModel (ZSF974), the model results for the real Persian Gulf are provided. In addition, different aspects of the results are discussed to identify potential improvements.

2. Method and Theoretical Framework

In designing this type of oceanic model, in addition to applying the governing physical principles of the atmosphere and ocean—such as Newton's laws, conservation of mass, conservation of salinity, and conservation of thermal energy—the first and second laws of thermodynamics and the equation of state for seawater are also utilized. To enable the model to account for non-flat bathymetry as in real ocean environments, the sigma vertical coordinate (σ) was used. In this study, the vertical coordinate is considered in the form introduced by Zamanian (2006) [13]:

$$\sigma = \frac{p - p_A}{p_b - p_A} \qquad (1)$$

where σ denotes the normalized vertical coordinate; p_b is the bottom pressure at any point in the ocean; p_A is the atmospheric pressure over the ocean surface; and p is the pressure at any point in the water column. In this

system, $\sigma = 0$ corresponds to the ocean surface, and $\sigma = 1$ corresponds to the ocean bottom. The values $0 < \sigma < 1$ represent intermediate levels.

The unit vectors in The Earth's Spherical Coordinates System with the sigma vertical coordinate can be defined as: $\mathbb{e}_\lambda$ is in the direction of increasing longitude λ, $\mathbb{e}_\phi$ is in the direction of increasing, the latitude ϕ, and $\mathbb{e}_\sigma$ is in the direction of increasing σ, downward. The unit vector $\mathbb{e}_\sigma$ is a variable unit vector. The metric components in this coordinate system are as follows:

$$\begin{cases} \delta s_\lambda = r \cos\phi \, \delta\lambda \\ \delta s_\phi = r \, \delta\phi \\ \delta s_\sigma = \dfrac{p_b - p_A}{\rho \, g} \, \delta\sigma \end{cases} \tag{2}$$

where $\delta_{s\lambda}$ is the arc length in the longitudinal direction, r is the radial distance from the Earth's center, ϕ is latitude, $\delta\lambda$ is the increment in longitude, $\delta_{s\phi}$ is the arc length in the latitudinal direction, $\delta\phi$ is the increment in latitude, $\delta_{s\sigma}$ is the length element in the vertical direction, p_b denotes the bottom pressure, p_A is the atmospheric pressure, ρ is the density, and g is the acceleration due to gravity. The velocity vector in this coordinate system is expressed as:

$$\mathbb{u} = u \, \mathbb{e}_\lambda + v \, \mathbb{e}_\phi + w \, \mathbb{e}_\sigma \tag{3}$$

The velocity components are:

$$\begin{cases} u = r \cos\phi \, \dfrac{D\lambda}{Dt} \\ v = r \, \dfrac{D\phi}{Dt} \\ w = \dfrac{p_b - p_A}{\rho \, g} \, \dfrac{D\sigma}{Dt} \end{cases} \tag{4}$$

Using equations (2), (3), and (4), the total material derivative of an arbitrary variable in this system is written as:

$$\frac{D\,\ldots}{Dt} = \frac{\partial\,\ldots}{\partial t} + \frac{u}{r\cos\phi}\,\frac{\partial\,\ldots}{\partial\lambda} + \frac{v}{r}\,\frac{\partial\,\ldots}{\partial\phi} + \dot{\sigma}\,\frac{\partial\,\ldots}{\partial\sigma} \tag{5}$$

In which $\frac{D\ldots}{Dt}$ is the total derivative, $\frac{\partial\ldots}{\partial t}$ is the local rate of change, $\frac{u}{r\cos\phi}\,\frac{\partial\ldots}{\partial\lambda}$ denotes the eastward advection, $\frac{v}{r}\,\frac{\partial\ldots}{\partial\phi}$ represents the northward advection, and $\dot{\sigma}\,\frac{\partial\ldots}{\partial\sigma}$ represents vertical advection or convection [13].

Based on the aforementioned concepts, the governing equations of the model can be reformulated in the Earth's spherical coordinate system with the sigma vertical coordinate. These governing equations include the eastward momentum equation, the northward momentum equation, the thermal conductivity equation, the temperature equation, the specific volume equation, the salinity equation, as well as the corresponding thermodynamic equations derived from the first and second laws of thermodynamics.

To complete the formulation of the model, additional closure equations are required. These include the hydrostatic equation, the geopotential equation, the bottom pressure tendency equation, the representative vertical velocity ($\dot{\sigma}$) equation, and the equation for calculating the radial distance of each point from the Earth's center. It is essential that all of these equations are expressed consistently in the spherical coordinate system with the sigma vertical coordinate.

When wind blows over the sea surface, momentum is transferred from the atmosphere to the ocean due to air–sea friction. As a result, wind speed decreases and surface ocean currents are generated.

The wind-induced surface stress depends approximately quadratic ally on wind speed, and represents the aerodynamic force per unit area exerted by the wind on the sea surface [16].

$$\boldsymbol{\tau}_s = c_d \, \rho_a \, (|\mathbb{v}_{\boldsymbol{a}}| - |\mathbb{v}_{\boldsymbol{s}}|) \, (\mathbb{v}_a - \mathbb{v}_s) \; \mathrm{Nm}^{-2} \tag{6}$$

where $\boldsymbol{\tau}_s$ is the surface stress, c_d is the (dimensionless) aerodynamic drag coefficient, ρ_a is the air density, $\mathbb{v}_{\boldsymbol{a}}$ is the wind velocity vector at 10 m above the sea surface, and $\mathbb{v}_{\boldsymbol{s}}$ is the surface current velocity vector.

According to Wu (1985), the aerodynamic drag coefficient is given by:

$$c_d = (0.8 + 0.065 \, U_{10}) \times 10^{-3} \tag{7}$$

where U_{10} is the wind speed at a 10 meter elevation [17]. Bottom stress, is computed using the formulation proposed by Nihoul (1977) [14]:

$$\boldsymbol{\tau_b} = -m \, \boldsymbol{\tau_s} + C_D \rho_w \; |\mathbb{v}| \; \mathbb{v} \tag{8}$$

Where $\boldsymbol{\tau_b}$ is the bottom stress, $m = 0.7$ is the dimensionless scaling coefficient for surface stress, $\boldsymbol{\tau_s}$ is the surface stress, $C_D = 0.00211$ is the hydrodynamic drag coefficient, ρ_w is the water density, $|\mathbb{v}|$ is the magnitude of the depth-integrated current, and $\mathbb{v}$ is the depth-integrated velocity vector.

In general, the stress tensor in the spherical coordinate system with sigma vertical coordinate is expressed as:

$$\boldsymbol{\tau} = \begin{bmatrix} \tau_{\lambda\lambda} & \tau_{\lambda\phi} & \tau_{\lambda\sigma} \\ \tau_{\phi\lambda} & \tau_{\phi\phi} & \tau_{\phi\sigma} \\ \tau_{\sigma\lambda} & \tau_{\sigma\phi} & \tau_{\sigma\sigma} \end{bmatrix} \tag{9}$$

Each component represents the stress associated with velocity gradients along different coordinate directions [13]. For example, $\tau_{\lambda\sigma}$ corresponds to the stress associated with variations of vertical velocity, $\dot{\sigma}$, along the longitudinal direction; $\tau_{\sigma\phi}$ corresponds to the stress generated by variations of meridional velocity in the vertical direction; and $\tau_{\sigma\sigma}$ represents the stress associated with the changes in the vertical velocity indicator, $\dot{\sigma}$, in σ direction.

Figure 2 shows the structure of a multilayer ocean model in a spherical coordinate system with a sigma vertical coordinate. In this figure the schematic of the vertical orientation of an n-layer (level:$Nk = 2n + 1$) oceanic medium. The counter of the levels is k.

a) Odd values of k correspond to the layer boundaries, while even values represent the centers of the layers.

b) $k = 1$ represents the ocean surface (the first level), which corresponds to $\sigma = 0$.

c) $k = Nk$ represents the ocean floor (the last level), corresponding to $\sigma = 1$.

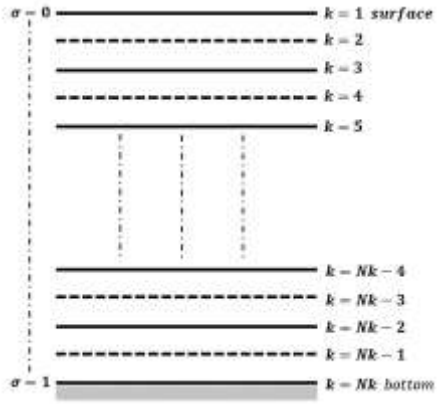

Figure 2- Vertical alignment scheme of a multilayer oceanic medium

In this study, the Modified Arakawa C-grid is employed for spatial discretization of the model domain [18]. To predict the future state of the ocean, the governing equations are solved numerically. These equations are first discretized using specific schemes, and a computer program was subsequently developed in C# to implement them.

The model is initialized with geometric conditions, including bed slope and elevation, along with other initial data.

Determining an appropriate time step is crucial for ensuring numerical stability in any modeling effort. The equations are solved and discretized using the finite difference method. Specifically, the two-step Lax-Wendroff scheme is applied to the advection terms, the Dufort-Frankel scheme to the diffusion terms, and the central difference method to the remaining derivatives. Additionally, the Matsuno scheme is employed to mitigate computational instabilities [19].

The Dufort-Frankel scheme is explicit and unconditionally stable. In contrast, the two-step Lax-Wendroff scheme is conditionally stable, requiring it to satisfy the Courant-Friedrichs-Lewy (C.F.L.) condition [20], While the C.F.L. condition is typically defined for a Cartesian coordinate system, it must be adapted for the Earth's spherical coordinate system with a sigma vertical coordinate, where it is expressed as:

$$\Delta t \leq min\left(\frac{r\,cos\,\phi\;\Delta\lambda}{u}, \frac{r\,\Delta\phi}{v}, \frac{\Delta\sigma}{\dot{\sigma}}\right) \qquad (10)$$

The simulation is initialized from a state of rest. Consequently, in the absence of forcing, the local time derivatives of the motion-inducing potentials are zero. Regarding the boundary conditions, the bottom and lateral boundaries are considered rigid, and a no-slip condition is applied [2]. Consequently, both the normal and tangential velocity components at these boundaries are set to zero, i.e.:

$$\mathbb{v}(\lambda, \phi, \sigma, t).\mathbf{n} = 0 \text{ and } \mathbb{v}(\lambda, \phi, \sigma, t).\mathbf{t} = 0 \qquad (11)$$

In the above equation, $\boldsymbol{t}$ and $\boldsymbol{n}$ are the unit tangential and normal vectors to the rigid boundary, respectively. The no-penetration condition at the bottom boundary requires that:

$$\sigma = 1 \quad \Rightarrow \quad u = v = \dot{\sigma} = 0 \qquad (12)$$

The dynamic boundary condition for the open boundary is considered as follows:

$$\frac{\partial p}{\partial \lambda} = \frac{\partial p}{\partial \phi} = \frac{\partial \Phi}{\partial \lambda} = \frac{\partial \Phi}{\partial \phi} = \frac{\partial p_b}{\partial \lambda} = \frac{\partial p_b}{\partial \phi} = 0 \qquad (13)$$

The kinematic boundary condition is expressed as:

$$u = \acute{u}, v = \acute{v}, \dot{\sigma} = \acute{\dot{\sigma}}, \rho = \acute{\rho}, \eta = \acute{\eta}, T = \acute{T}, s = \acute{s} \qquad (14)$$

Here, unprimed parameters represent the original environment, while primed parameters correspond to the conditions at the open boundary. Additionally:

$$\left(\frac{D\,\ldots}{Dt}\right)_{(\sigma=0)} = \left(\frac{D\,\ldots}{Dt}\right)_{(\sigma=1)} = 0 \qquad (15)$$

A key assumption in the development of the Basic Oceanic Model is the neglect of the term $-\vec{\Omega} \times \left(\vec{\Omega} \times \vec{r}\right)$ compared to other terms in the equations of motion formulated in the Earth's spherical coordinate system with a sigma vertical coordinate.

Applying specific conditions to the program and comparing its outputs with theoretical physical principles can also serve as an appropriate validation for the designed model. Calibration during the model execution for experimental basins identifies the model's weaknesses and leads to its improvement.

For model's implementation in laboratorial oceanic basins (even real medium), hypothetical (and approximate real) data are used as input to the program. The tidal force is considered as a sinusoidal function with a hypothetical amplitude. However, tidal force has been made to incorporate water level variations in the Strait of Hormuz (which is the open boundary of the real medium). The water level variations in the Strait of Hormuz have been extracted from the hydrography information database of the National Cartographic Center of Iran [21].

3. Results and Discussion

The preceding sections have described the design of the Persian Gulf Oceanic Model (ZSF974). The model's accuracy was validated in theoretical environments, with results showing consistency with the principles of ocean physics and agreement with previous research. This validation provides the basis for its implementation in a real-world environment, specifically the oceanic basin of the Persian Gulf (Figure 1) [15].

This section presents the results of the model's implementation in the Persian Gulf basin and discusses its validation. The model domain spans longitudes from 48.25°E to 56.5°E and latitudes from 24.25°N to 30.25°N, with bathymetry ranging from 9.02 m to 101 m. The depth of the basin in this area varies between a minimum of 9.02 meters and a maximum of 101 meters. The model uses a five-layer structure and the domain is discretized using the modified Arakawa C-grid scheme with a longitudinal and latitudinal resolution of 0.25 degrees. While the Courant-Friedrichs-Lewy (C.F.L.) condition permits a maximum time step of 95.95 seconds, a 60-second time step was used in practice to ensure stability.

In addition to hypothetical tides, the model was forced with real tidal data from the Hydrographic Information Database of the National Cartographic Center [21], covering the period from March 1 to June 30, 2018. Wind data were sourced from the European Centre for Medium-Range Weather Forecasts (ECMWF) database [22], and the wind forcing was applied concurrently with other factors, such as tides. To isolate the effects of specific factors, some experiments were initialized with uniform conditions: the basin temperature was set to 25 °C and salinity to 40 psu. All simulations of the Persian Gulf were initialized from a state of rest.

3.1. Results of the QuiescencetTest and the effects of neglecting Coriolis force and Earth's curvature.

The first simulation was a quiescence test, where no external forces were applied. The model was expected to maintain its initial state, with no changes in parameters or generation of currents over time. The model was run for ten years to confirm this quiescent state. A subsequent test examined the effect of neglecting the Coriolis force and Earth's curvature. In this scenario, when a constant force (e.g., uniform wind stress) was applied, the model produced a uniform current aligned with the applied force.

Following the successful validation from these two initial tests, the model was used to examine other influencing factors. Specifically, the effects of density gradients, wind, tides, and river runoff—both individually and in various combinations—were investigated. The results of some of these experiments are presented below.

3.2. Simulating the Effects of River Inflow on the Persian Gulf

This experiment investigates the effect of inflow from the Arvandrud and Mond rivers (Figure 1) on water circulation in the Persian Gulf. To isolate this effect, the simulation was run under stable conditions, excluding tidal, wind, and density gradient forces. The basin was initialized with a uniform salinity of 40 psu and a temperature of 25 °C. The Arvandrud River was prescribed an inflow with a temperature of 18 °C, salinity of 38.5 psu, and velocity of 1.14 m/s, while the Mond River had an inflow with a temperature of 20.0 °C, salinity of 22.1 psu, and velocity of 0.5695 m/s. The results of the simulation at the end of the fifth day are presented below:

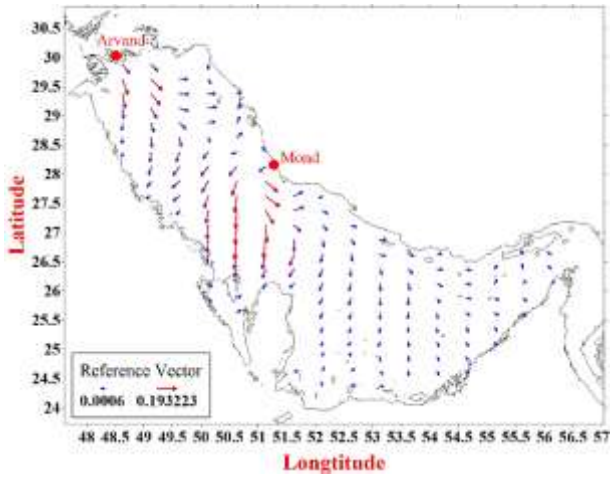

Figure 3- Current field at the center of the first layer after five days of simulation, forced only by runoff from the Arvandrud and Mond rivers.

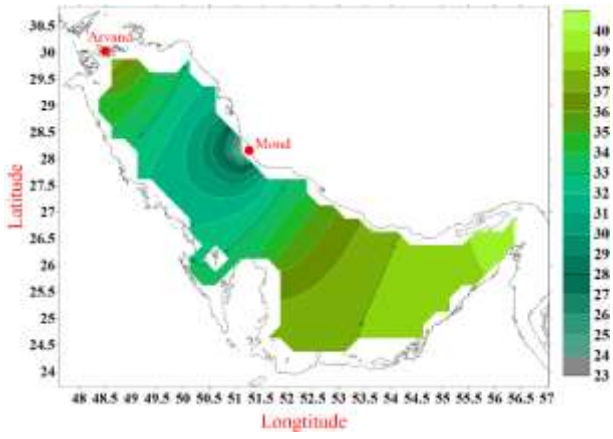

Figure 4- Salinity field at the center of the first layer after five days of simulation, forced only by runoff from the Arvandrud and Mond rivers.

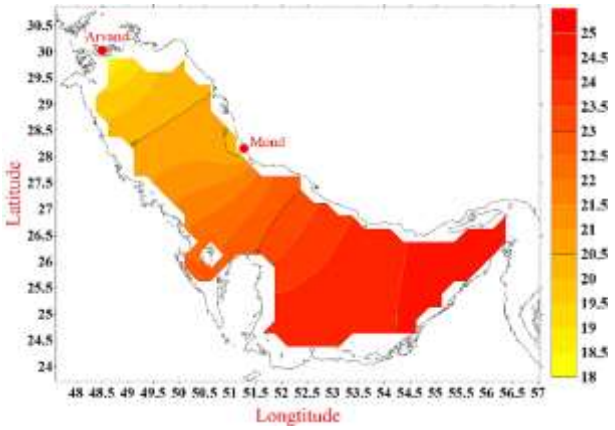

Figure 5- Temperature field at the center of the first layer after five days of simulation, forced only by runoff from the Arvandrud and Mond rivers.

Figure 4 and 5 illustrate the dominant effects of the Mond and Arvandrud rivers on the salinity and temperature of the Persian Gulf, respectively. These effects stem from the distinct temperature and salinity characteristics of the river inflows compared to the ambient Gulf water. The current field (Figure 3), however, shows that the river inflows collectively generate a counterclockwise circulation within the basin. The outflow from the Arvandrud River is observed to deflect to the right after entering the Gulf, impacting the coasts of the United Arab Emirates. A similar pattern is observed for the Mond River inflow. This suggests that, in the absence of other forces such as tides, wind, or density gradients, the Mond River inflow also affects the coasts of the United Arab Emirates and Bahrain.

3.3. Simulating the Effects of Wind and Density Gradients on the Persian Gulf

In this experiment, the model is initialized with a surface temperature of 30°C and a surface salinity of 36 psu. Temperature decreases by 0.25°C and salinity increases by 0.5 psu with each successive layer. A uniform westerly wind with a speed of 10 m/s was applied to the surface for 40 days. The resulting velocity, salinity, and temperature fields, as well as the deviation from hydrostatic balance at the end of the fifth day, are presented below:

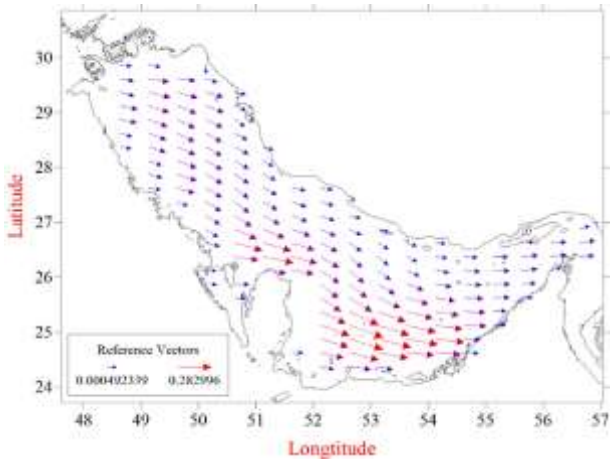

Figure 6- Current field at the mid-depth of the first layer after five days of simulation, forced by a 10 m/s westerly wind.

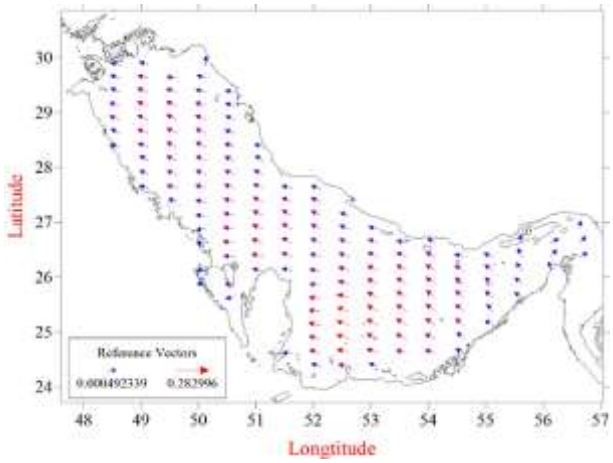

Figure 7- Current field, mid-level of the fifth layer, the end of the fifth day of model execution forced by 10 m/s westerly wind.

As expected, the surface current vectors are deflected to the right of the wind direction due to the Coriolis effect. In the bottom layer, the current vectors are oriented approximately opposite to those in the surface layer. Figure 8 shows a lower sea level in the western Persian Gulf compared to the eastern part, a pattern consistent with the observed current field. Consequently, higher salinity and lower temperatures are expected in the western basin (Figure 9 and 10).

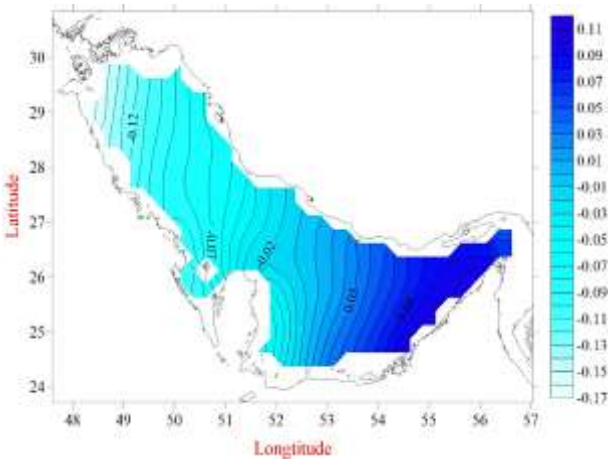

Figure 8- Isopleths of departure from static equilibrium at the mid-depth of the first layer after five days of simulation, forced by a 10 m/s westerly wind.

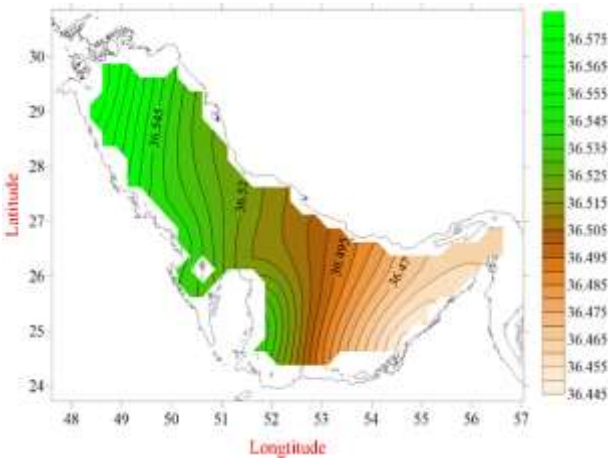

Figure 9- Salinity field, mid-depth of the first layer, the end of the fifth day of model execution forced by 10 m/s westerly wind.

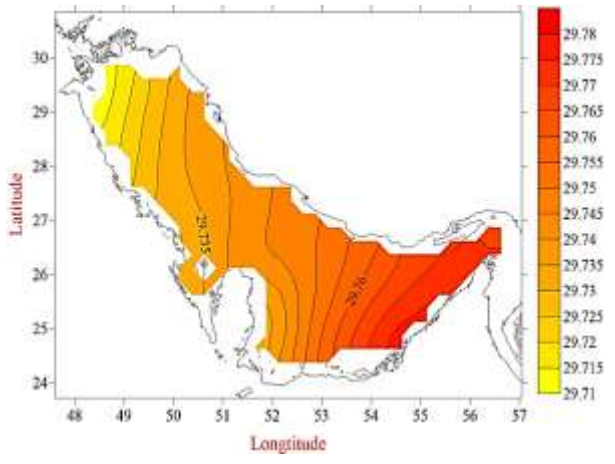

Figure 10- Temperature field at the mid-depth of the first layer after five days of simulation, forced by a 10 m/s westerly wind.

Due to the open boundary, the persistent wind forcing is expected to maintain a lower sea level, especially in the upwind region. The results after 30 days of the simulation are presented below:

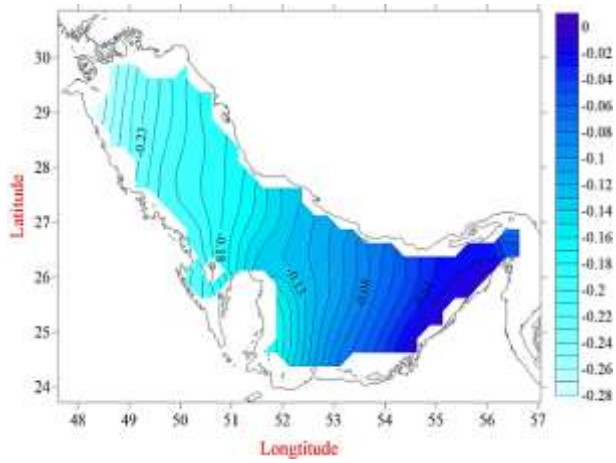

Figure 11- Isopleths of departure from static equilibrium at the mid-depth of the first layer after 30 days of simulation, forced by a 10 m/s westerly wind.

The current field stabilizes in terms of direction within the first five days, and the surface outflow from the Strait of Hormuz as well as the inflow at the bottom into the Persian Gulf continues. A comparison of the results from days 30 and 40 (Figure 11 and 12) confirms this observation

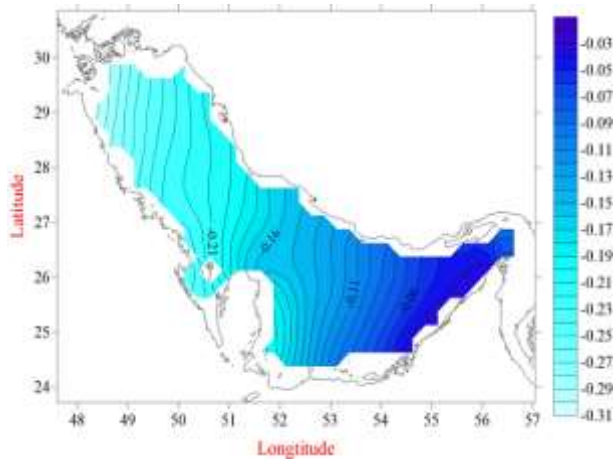

Figure 12- Isopleths of departure from static equilibrium, mid-level of the first layer, the end of day 40 of model execution forced by 10 m/s westerly wind.

Salinity and temperature also continue to diffusion, as shown in Figure 9 and Figure 10, contributing to changes in sea level and current patterns. However, the rate of these changes decreases over time. The result of this experiment indicates the dominance of wind forcing over the density gradient in this oceanic medium.

3.4. Analysis of the results of the simulation of the tidal effect and density gradient in the Persian Gulf

Tide, as a periodic factor, imposes a periodic dynamic on the oceanic medium. In this experiment, the tidal force affects the medium in the absence of wind and river inflow. The sea surface temperature is set at 30°C, decreasing by 0.25°C per below level, and the surface salinity is assumed to be 36 psu, increasing by 0.5 psu per below level. Under these conditions, the model has

been run for 60 days. Below are some results from day 58 of the model run:

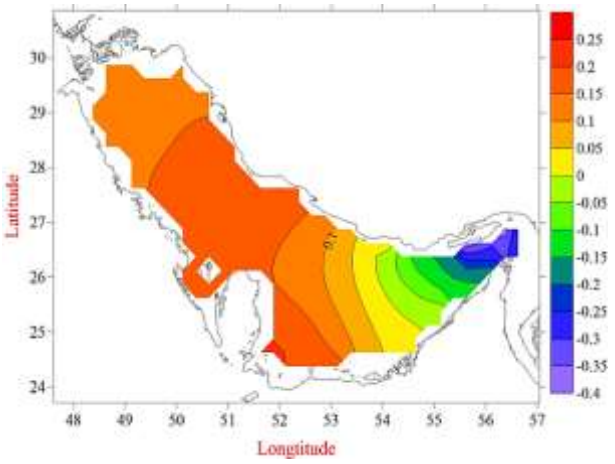

Figure 13- Isopleths of departure from static equilibrium, mid-level of the first layer, day 58 of the model run – hour 6, forced by tide.

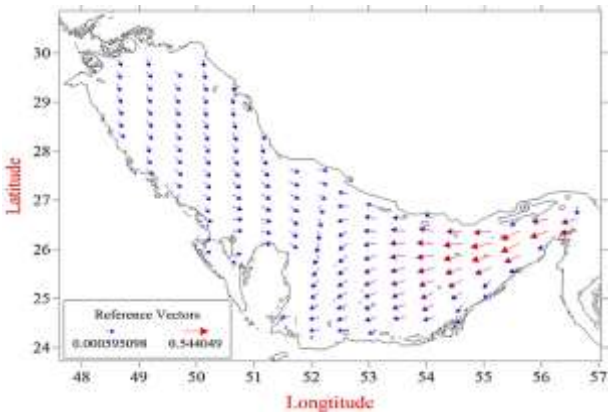

Figure 14- Current field, mid-level of the first layer– day 58 of the model run, hour 12, forced by tide.

The maximum observed current during this period was 0.998 m/s, and the maximum total change in water elevation relative to the static equilibrium was 3.4 m. Results indicate the dominance of tidal force compared to the force resulting from density difference. The current fields and isopleths of departure from static equilibrium (Figure 13 and Figure 14) show that the tide is dominant in the meridian region. This finding can also be obtained by examining the temporal changes in the departure from static equilibrium at a specific point (Figure 15).

Additionally, the current fields indicate that the tidal wave, after entering the Strait of Hormuz, enters the Persian Gulf parallel to the northern boundary, as the current vectors are aligned well parallel to the boundaries.

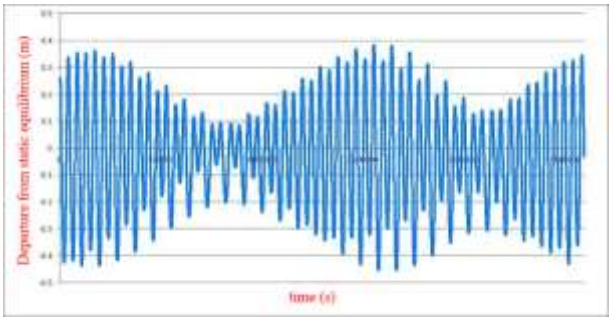

Figure 15- Water level fluctuations over time at 26°22'30"N, 54°52'30"E in April 2018.

By comparing the isopleths of departure from static equilibrium with the current fields, it can be understood that if an observer looks at the tidal current in the direction of flow, the maximum amplitude will be to their right, tending to create a counter-clockwise motion in the environment. Overall, the presence of the Kelvin wave due to tidal entry, as well as the dominance of tidal force over the force resulting from density difference, are observed in the results.

Results indicate that the effect of tidal force in the western half of the Persian Gulf is weaker than in the eastern half.

3.5. Investigating the Results of Simulating the Effects of Wind, Tide, and Density Difference in the Persian Gulf

In this experiment, the salinity of the Persian Gulf at the surface is set at 36 psu, with a 0.5 psu increase in salinity per below level, and the temperature at the surface is assumed to be 30°C, with a 0.25°C decrease per below level. The wind data extracted from the ECMWF website is from March 1, 2018, to March 31, 2018 (March 2018), and the tidal data for the same dates was obtained from the Hydrography website of the National Cartographic Center. The model was run for 30 days under the stated conditions. Below are some results from this run:

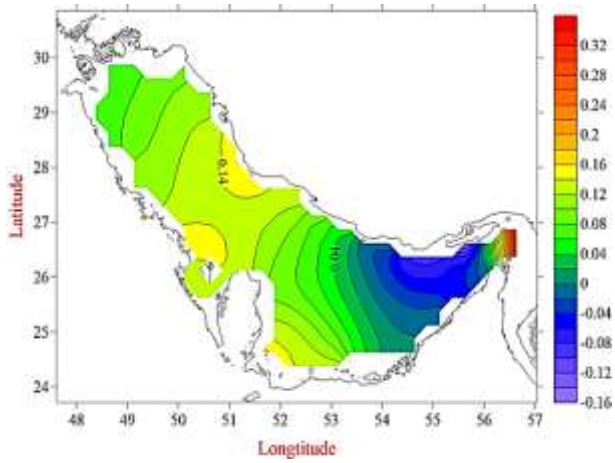

Figure 16- Isopleths of departure from static equilibrium at the mid-depth of the first layer at hour 6 of day 30, forced by tides, wind, and density gradients.

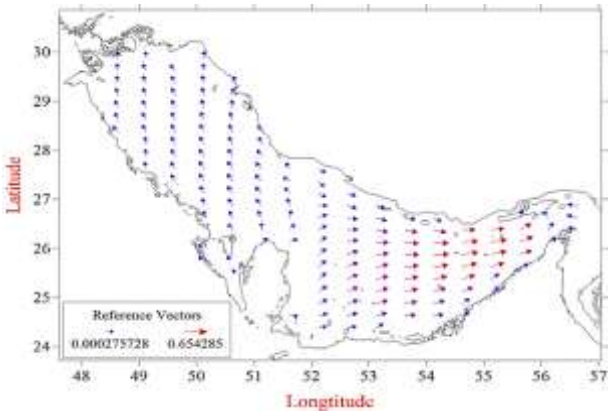

Figure 17- Current field at the mid-depth of the first layer at hour 6 of day 30, forced by tides, wind, and density gradients.

Analysis of the departure from static equilibrium fields shows that as the tide propagates into the basin, a counterclockwise circulation develops along the boundaries, with the maximum and minimum sea levels consistently occurring near the coast (Figure 16). Moreover, the current vectors at these locations are well-aligned with the boundaries (Figure 17), indicating that the normal component of the current is negligible. This leads to the conclusion that tidal forcing dominates the circulation in this experiment. This finding is also supported by the analysis of temporal variations in sea level at a specific point (Figure 18). Furthermore, the analysis reveals the presence of an amphidromic point within the basin (Figure 16).

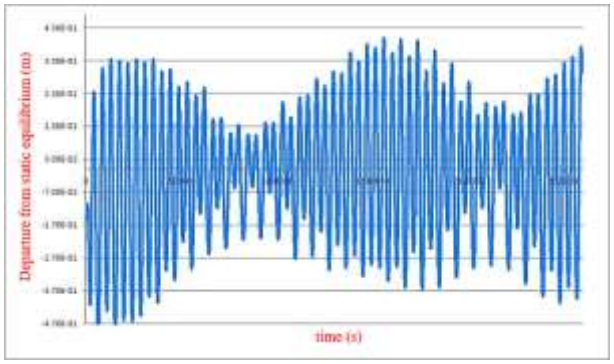

Figure 18- Time series of sea level variations at 26°22′30″ N, 54°52′30″ E in March 2018.

It is also evident that both tidal currents and tidal elevations are greater in the eastern part of the Persian Gulf compared to the western part. The maximum simulated current in this experiment is 0.924 m/s, occurring in the Strait of Hormuz, while the maximum change in sea surface elevation relative to static equilibrium is 3.3 meters. The analysis of salinity and temperature fields also yielded useful results, with examples presented below.

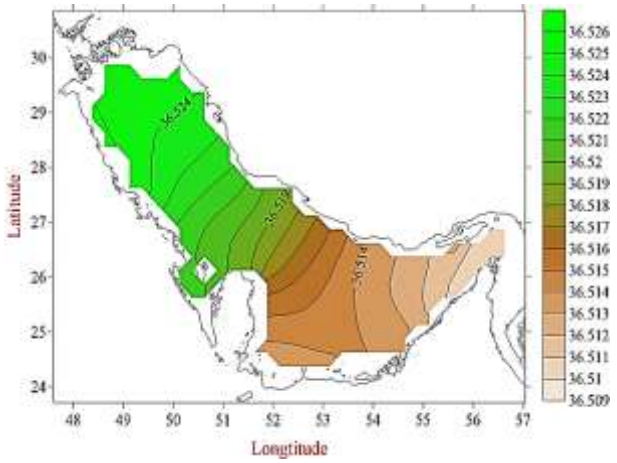

Figure 19- Salinity field at the mid-depth of the first layer at hour 6 of day 30, forced by tides, wind, and density gradients.

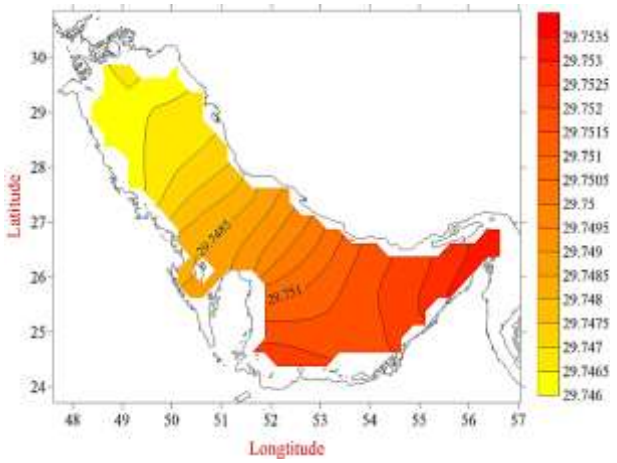

Figure 20- Temperature field at the mid-depth of the first layer at hour 6 of day 30, forced by tides, wind, and density gradients.

5. Conclusions

This study presents the development and validation of the Persian Gulf Oceanic Model (ZSF974), a three-dimensional numerical model designed to simulate the physical dynamics of the Persian Gulf. After successful validation against theoretical principles, the model was applied to the real-world environment of the Persian Gulf to investigate the effects of various forcing mechanisms.

The model's performance was confirmed through several key experiments. **Simulations of river inflow** from the Arvandrud and Mond rivers demonstrated their distinct impacts on salinity and temperature, and successfully reproduced the deflection of the Arvandrud plume towards the coasts of the United Arab Emirates, consistent with previous research [23]. In experiments examining **wind and density gradients**, the model accurately simulated Ekman dynamics [24], including the right-hand deflection of surface currents and the reversal of flow at depth, alongside realistic upwelling patterns. The results confirmed that, under the tested conditions, wind forcing dominated over density-driven forces

Analysis of tidal effects revealed the propagation of a Kelvin wave along the northern boundary, the

formation of an amphidromic point, and the overall dominance of tidal forcing over both wind and density gradients. This was further corroborated in a final, comprehensive simulation incorporating all three factors, where the semidiurnal nature of the tide and its dominant effect on circulation were clearly evident

The PersianGulfOceanicModel (ZSF974) has proven capable of accurately simulating the complex physical behavior of the Persian Gulf. A key advantage of this model is its ability to provide detailed physical parameter fields in lower water layers. However, long-term simulations indicate that enhancing the open boundary conditions and incorporating more precise bathymetric data are critical for improving the model's predictive accuracy. The groundwork has been laid for future enhancements, including the application of this model to other similar semi-enclosed basins with complex bathymetries.

Acknowledgment (Optional): The authors would like to express their sincere appreciation to the esteemed, Dr. Mohammad Taghi Zamanian, for his invaluable support. As the academic advisor, he provided comprehensive guidance in numerical modelling and played a fundamental role in the development of the present model. So, they would like to thank the National Institute of Oceanography for providing the facilities and library resources necessary for this research. We are especially grateful for the support and cooperation of the director and the vice president for research.

8. References

1- Khaleghi Zavare, H., (1992). *Development and application of a non-linear barotropic model for the wind and tide, driven circulation in the Persian Gulf* (Doctoral dissertation, University of the Philippines)

2- Zamanian, M., T., (1994). *Three Dimensional Models for Persian Gulf*, (Doctoral dissertation, University of the Philippines)

3- Sadrinasab, M. and Kenarkoohi, K., (2009). *Numerical modelling of sound velocity profile in different layers in the Persian Gulf*, Asian journal of applied sciences, 232-239.

4- Sadrinasab, M., (2009). *Three-Dimensional Numerical Modeling Study of the Coastal Upwelling in the Persian Gulf*. Research Journal of Environmental Sciences, 3: 560-566. DOI: 10.3923/rjes.2009.560.566,

5- Pous, S., Carton, X., and Lazure, P., (2012). *A process study of the tidal circulation in the Persian Gulf*, Open Journal of Marine Science, 2(4), 131-140, DOI: 10.4236/ojms.2012.24016.

6- Azizpour, J., Chegini, V., Khosravi, M. and Einali, A., (2014). *Study of the physical oceanographic properties of the persian gulf, strait of hormuz and gulf of oman based on PG-GOOS CTD measurements*, Persian Gulf Scientific Research Journal, *5*(18), 37-48.

7- Delbari, A., and Sheikhbahaei, A., (2022). *Numerical modeling of underwater acoustic wave using Differential Quadrature Method*, International Journal Of Coastal, Offshore And Environmental Engineering (ijcoe), 7(2), 49-54., doi: 10.22034/ijcoe.2022.155146.

8- Mahpeykar, O. and Khalilabadi, M. R., (2021). *Numerical modelling the effect of wind on Water Level and Evaporation Rate in the Persian Gulf*. International Journal of Coastal, Offshore & Environmental Engineering (IJCOE), 6(1), 47-53, Doi: 10.22034/ijcoe.2021.149358

9- Hosseini, S. M. and Soltanpour, M., (2021). *Tide characteristics and tidal wave propagation in the Persian Gulf*, Ocean Science Discussions, 1-36.

10- Pirooznia, M., Raoofian Naeeni, M., Atabati, A., and Tourian, M. J. (2022) *Improving the Modeling of Sea Surface Currents in the Persian Gulf and the Oman Sea Using Data Assimilation of Satellite Altimetry and Hydrographic Observations*. Remote Sensing, 14(19), 4901. https://doi.org/10.3390/rs14194901

11- Fallahi M., Zamanian M.T. and Sadrinasab M. (2019). *Design of Five Layers Oceanic Numerical Model for Persian Gulf*. PHD Thesis. Department of physical oceanography, Faculty of Marine Science and Oceanography, Khorramshahr University of Marine Science and Technology, Iran. 183p. [In Persian]

12- Zamanian M.T, Sadrinasab M. & Fallahi, M., (2022). *Designing a Numerical Model to Study the Effect of Tide and Wind in a Theoretical Basin in Similarity to Persian Gulf*, Journal of Marine Science and Technology, 27-38, 21(1), doi:10.22113/jmst.2019.149922.2203, [In Persian]

13- Zamanian, M. T. (2006). *Project of base oceanic model two layered*, Research Institute of Methodology and Atmosphere Science, Tehran, Iran. [In Persian]

14- Nihoul, J., C., J., (1977). *Three-dimensional model of tides and storm surges in a shallow well-mixed continental sea*, Dynamics Atmosphere Ocean, 2, 29-47.

15- Fallahi, M. , Zamanian,M. T. and Sadrinasab, M. (2025). *Development of Oceanic Numerical Model for Persian Gulf (part 1)*. International Journal of Coastal, Offshore And Environmental Engineering (ijcoe), 10(3), 18-29. doi: 10.22034/ijcoe.2025.522670.1175

16- Thorpe, S., A., (2009). *Elements of Physical Oceanography*, Boston, Elsevier, 647 pp

17- Wu, Y., (1985). Wu, J., 1982: *Wind stress coefficients over sea surface from breeze to hurricane*. J. Geophysics. Res., 78, 9704-9706.

18- Estoque, M., A., (1963). *A numerical model of the atmospheric boundary layer*, Journal of Geophysical Research, 68(4), 1103-1113, https://doi.org/10.1029/JZ068i004p01103

19- Haltiner, G.J. & Williams, R.T., (1980). *Numerical prediction and dynamic meteorology (2nd edition)*, John Wiley & sons, pp. 496, ISBN-10: 0471059714

20- Kämpf, J., (2009). *Advanced Ocean Modelling, Flinders University, School of the Medium*, PO Box 2100 Adelaide SA 5001, Australia, 193p.
21- Hydrographic Management of National Cartographic Center of the Islamic Republic of Iran, 1983, Access in: http://iranhydrography.ncc.org.ir/homepage.aspx?site=iranhydrography.ncc.org&tabid=6144&lang=fa-IR, Access Date: August 2018.
22- European Centre for Medium-Range Weather Forecasts (ECMWF). 1975. Available at: https://www.ecmwf.int/en/forecasts/datasets. Accessed September 17, 2018.
23- Emery, K., O., (1956). *Sediments and water of the Persian Gulf*, AAPG. Bull. 40 2354–2383
24- Apel, J. R., (1999). *Principles of Ocean Physics,* San Diego, Academic Press, 634 pp

INTERNATIONAL JOURNAL OF
COASTAL, OFFSHORE & ENVIRONMENTAL ENGINEERING IJCOE Vol.11/No. 1/Winter 2026 (103-111)

Available online at: www. Ijcoe.org

Mechanical Behavior of Internally-Cured LECA Mortar in Acidic Marine Conditions

M. A. Dastan Diznab[1*], S. Ghaderan[2], F. Yousefi[3], M. Bonyadi[4]

[1*] *Faculty of Engineering, Arak University, Arak, Iran; m-dastan@araku.ac.ir*
[2] *Master of Science, Arak University, Arak, Iran; s.ghaderan.02@msc.araku.ac.ir*
[3] *Master of Science, Arak University, Arak, Iran; f.yousefi.02@msc.araku.ac.ir*
[4] *Master of Civil Engineering, Arak University, Arak, Iran.;M.bonyadi1998@gmail.com*

ARTICLE INFO

Article History:
Received: 04 Oct 2025
Accepted :15 Feb 2026

Keywords:
Cement mortar
lightweight expanded clay aggregate (LECA)
Sulfuric acid
Compressive strength
Flexural strength
Mass variation

ABSTRACT

Cementitious materials used in coastal and offshore infrastructures are frequently subjected to aggressive acidic environments resulting from industrial discharge, marine pollution, and sulfur-based biochemical processes. This study examines the mechanical behavior and acid resistance of mortar incorporating lightweight expanded clay aggregate (LECA) as an environmentally sustainable partial replacement for natural sand, with the added benefit of internal curing. Four mortar mixtures containing 0%, 5%, 10%, and 15% LECA were prepared, water-cured for 28 days, and subsequently exposed to a sulfuric acid solution (pH 1.5) for up to 90 days to simulate severe acid attack. Compressive strength, flexural strength, mass loss, and strength–degradation correlations were evaluated. Results indicate that LECA replacement does not compromise initial mechanical performance, while the mixture containing 10% LECA exhibited the highest long-term durability under acid exposure, demonstrating reduced mass loss and significantly lower strength degradation compared to the control mix. The enhanced performance is attributed to the internal curing effect of LECA and its ability to mitigate microcracking in chemically aggressive environments. These findings highlight the potential of LECA-modified mortar as a sustainable and durable alternative for coastal and offshore structures subjected to acidic conditions.

1. Introduction

In recent years, environmental protection and sustainability have become major global concerns [1]. Among the various environmental challenges, air pollution has contributed to the formation of acid rain, which has been widely reported in coastal and industrial regions of the United States, Europe, and Asia [2]. Acidic precipitation poses a serious threat to concrete infrastructure, particularly in marine and coastal environments, where exposure conditions are often more aggressive, leading to accelerated material degradation and substantial economic losses associated with repair and rehabilitation [3]. Acid rain may contain aggressive chemical compounds such as sulfuric and nitric acids, which intensify the chemical attack on cement-based materials [4].

Acidic exposure is one of the most critical durability-related factors affecting concrete structures in coastal, offshore, and port facilities [5]. This issue is especially pronounced in marine storage tanks, harbor infrastructures, and offshore industrial units where sulfuric acid and other corrosive substances are commonly present, as illustrated in Figure 1 [6,7]. Under such conditions, concrete elements are simultaneously subjected to mechanical loading and severe chemical attack, making both strength retention and long-term durability essential performance requirements [8]. Therefore, evaluating the mechanical behavior of concrete exposed to acidic

marine environments is of paramount importance for predicting service life and ensuring the structural reliability of coastal and offshore concrete infrastructure.

Figure 1. Reinforced concrete sulfuric acid storage tanks located at Bandar Abbas Port, Iran.

Acid-induced deterioration of concrete represents a challenging research topic that has been widely examined by various researchers. Sharifi et al. evaluated the durability performance of self-compacting concrete subjected to acidic environments and reported that sulfuric acid induced significantly greater damage than hydrochloric acid. [9]. Similarly, Irico et al. examined self-compacting concrete incorporating fly ash under sulfuric acid exposure. Scanning electron microscopy observations indicated that fly ash enhanced resistance to acid attack, highlighting its potential role in improving the acid durability of concrete [10]. Furthermore, Sharifi and Ranjbar investigated mortar mixtures containing ceramic powder waste exposed to acidic conditions. Their findings demonstrated that prolonged acid exposure resulted in increased mass loss and substantial reductions in the mechanical strength of the mortar specimens [11].

Another environmental challenge is the excessive extraction of river sand, which threatens the ecosystems of river channels and floodplains. Consequently, researchers are increasingly seeking sustainable alternatives to natural river sand in the construction industry. Lightweight expanded clay aggregate (LECA) is a promising substitute, as it not only reduces the overall weight of the mixture but also provides internal curing, helping retain moisture and mitigate cracking in concrete. LECA can serve as a suitable replacement for natural sand, as it not only reduces the overall weight of the mixture but also provides internal curing, helping to retain moisture within the concrete and prevent cracking in various environmental conditions [12-14].

The objective of this study is to determine the optimal replacement level of LECA, incorporating internal curing, as a substitute for natural sand in structural mortar, in order to achieve maximum compressive and flexural strength under acidic exposure conditions representative of coastal and marine environments. To this end, four mortar mixtures were prepared in which 0%, 5%, 10%, and 15% of sand was replaced with LECA. Cubic and prismatic mortar specimens were cast and water-cured for 28 days. Subsequently, to simulate aggressive acidic conditions commonly encountered in marine and port infrastructures, the specimens were exposed to a sulfuric acid solution with a pH of 1.5 for periods of 0, 3, 7, 14, 28, 56, and 90 days. The mechanical performance and mass loss behavior of the mortar specimens were systematically investigated, and the corresponding results are discussed.

2. Materials

The fine aggregate used in this study was crushed mountain sand sourced from the Arak region, Iran. The physical properties of the sand complied with the requirements of ASTM C33 [15]. The cement used was Type II Portland cement produced by the Nahavand Cement Plant, located in western Iran, with chemical and physical properties conforming to ASTM C150 [16]. Potable water of acceptable quality was used for mixing and curing purposes; the water was clean and free from harmful impurities such as iron oxides, acids, alkalis, salts, organic matter, and chloride ions.

2.1. LECA

LECA is produced from natural clay with a small amount of lime. The clay is first dried and then heated in rotary kilns at temperatures typically ranging from 1100 to 1300 °C. During the heating process, gases are released within the clay particles and become trapped upon cooling, resulting in the formation of spherical aggregates with a highly porous internal structure, as illustrated in Figure 2. These aggregates are lightweight yet exhibit high resistance to crushing [12]. LECA is chemically stable and does not react with water; therefore, it is not adversely affected by prolonged water exposure. The chemical composition of LECA primarily consists of silica (SiO_2), alumina (Al_2O_3), iron oxide (Fe_2O_3), lime (CaO), and minor amounts of alkali oxides such as sodium oxide (Na_2O) and potassium oxide (K_2O) [17,18].

Figure 2. Physical appearance of LECA utilized as internal curing aggregate in this study.

2.2. Sulfuric Acid

Acid rain typically contains a significant amount of sulfuric acid [19]. In this study, to simulate such an

environment, the specimens were exposed to a sulfuric acid solution with a pH level of 1.5 [11,20]. The pH value was regularly monitored using a digital pH meter, and the acidic solution was maintained at a constant pH throughout the experiment.

3. Internal Curing

In certain concrete mixtures, particularly those with a low water-to-cement ratio, internal drying poses a significant risk due to insufficient available water, which may prevent complete cement hydration and consequently reduce concrete performance. Since most conventional curing practices are applied to the concrete surface, their effectiveness is largely confined to a shallow region near the surface. As a result, external curing methods may have limited influence on mixtures that are highly susceptible to internal drying [21]. An innovative approach to address this challenge is the provision of internal curing, in which additional water required for cement hydration is supplied from within the concrete matrix. This internal water is not part of the initial mixing water and therefore does not alter the original water-to-cement ratio. The use of water-absorbing aggregates capable of storing and gradually releasing moisture over time is an effective strategy to achieve this objective [22].

Various internal curing methods have been classified based on the recommendations of the RILEM Technical Committee ICC–196TC. In general, internal curing refers to the incorporation of a component into concrete that acts as an internal curing agent. This component may consist of an aggregate introduced under specific conditions, such as a pre-saturated state, or a specialized admixture [23,24]. However, the definition of internal curing provided by the American Concrete Institute (ACI) differs slightly from that of RILEM. According to ACI, internal curing is defined as a process by which cement hydration progresses due to the availability of additional internal water that is not part of the original mixing water [25].

In this study, LECA was employed to provide internal curing. Prior to incorporation into the mixture, LECA particles were pre-soaked in water for 24 hours to absorb the amount of water required for internal curing. Subsequently, the aggregates were added to the mix in a saturated surface-dry condition. The absorbed water within the LECA is gradually released over several days, facilitating continued cement hydration and potentially eliminating the need for external curing. Therefore, the internal water stored in saturated surface-dry LECA satisfies the internal curing criteria as defined by the American Concrete Institute.

4. Mix Design

As previously mentioned, this study investigates the effect of incorporating different percentages of LECA under internal curing conditions on the mechanical properties of structural mortar in an acidic environment. Accordingly, cubic specimens with dimensions of 50 × 50 × 50 mm were prepared to evaluate compressive strength, while prismatic specimens with dimensions of 160 × 40 × 40 mm were fabricated to assess flexural strength. In this research, the influence of replacing sand with LECA at levels of 0%, 5%, 10%, and 15% in structural mortar exposed to an acidic environment was examined, as listed in **Error! Reference source not found.**.

Specimen casting and preparation were carried out in accordance with ASTM C192 [26]. After casting, the molds were sealed in plastic bags for 24 hours to prevent moisture loss due to ambient temperature. Following this period, the specimens were demolded and cured in a water tank for 28 days. Subsequently, based on the designated exposure durations, the specimens were transferred to acid-resistant polyethylene tanks containing sulfuric acid solution. It should be noted that the pH of the sulfuric acid bath was maintained at 1.5, a value selected based on previous studies and estimations of the long-term deteriorating effects of acid rain and industrial wastewater leachates on concrete [11,20].

Table 1: Mix Design

No.	Mix Design Name	W/C	LECA (/.)	Materials Used in the Mixed Design for One Cubic meter (kg/m^3)			
				LECA	Cement	Water	Fine Aggregate (Sand)
1	ML0	0.45	0	0	670	301	1177
2	ML5	0.45	5	37	670	301	1118
3	ML10	0.45	10	73	670	301	1059
4	ML15	0.45	15	110	670	301	1001

5. results and Discussion

5.1. Compressive Strength Test Results

The results of the compressive strength tests conducted on cubic mortar specimens with dimensions of 50 × 50 × 50 mm are discussed for different exposure periods following 28 days of standard water curing and subsequent immersion in an acidic environment. For each testing age, the average compressive strength was calculated as the mean value of three specimens. The obtained results are evaluated and presented in Figures 2 and 3.

According to the compressive strength results presented in Figure 2, all specimens exhibited nearly identical strength values prior to acid exposure, with only minor differences observed. This indicates that the incorporation of LECA under internal curing conditions did not adversely affect the initial compressive strength of the mortar. As expected, acidic exposure led to progressive deterioration and a reduction in compressive strength over time. All specimens experienced strength loss under acid attack, reaching their minimum compressive strength after 90 days of exposure.

After 3 days of acid exposure, specimen ML10 exhibited higher compressive strength than the other mixtures, indicating that the incorporation of 10% LECA was beneficial at this early stage of acidic exposure. In contrast, specimen ML15 showed the lowest compressive strength at all ages, except at 90 days. After 7 days of exposure, specimen ML0 demonstrated the highest compressive strength, while at 14 days both ML0 and ML10 exhibited superior compressive strength compared to the other mixtures. After 28 days of acid exposure, the compressive strengths of all specimens became very close, with only minor differences observed, and were approximately 30% of their initial strength values. Nevertheless, specimen ML10 exhibited slightly higher compressive strength compared to the other mixtures. At 56 days, the mixture containing 10% LECA continued to demonstrate superior resistance performance. After 90 days of exposure, specimen ML0 showed the lowest compressive strength, while specimens incorporating 5%, 10%, and 15% LECA exhibited relatively similar strength levels but consistently higher values than the control mixture. These results indicate that the presence of LECA contributes to improved long-term compressive strength performance of cement mortar under acidic conditions.

The compressive strength reduction (CSR)relative to the control specimen was calculated using Eq.(1), based on varying LECA content and exposure duration in the acidic environment. The results are illustrated in Figures 3, where *CS* represents the compressive strength of the specimen at a given LECA replacement level and exposure day, and CS_c denotes the compressive strength of the control specimen.

$$\mathrm{CSR} = \frac{CS - CS_c}{CS_c} \times 100 \quad \textbf{(1)}$$

Figure 3 illustrates the CSR of the mortar specimens under acidic exposure. As observed, specimen ML10 exhibited a lower CSR after 3 days of exposure compared to the other mixtures. As expected, all specimens experienced strength loss under acid attack; however, the control specimen showed a greater CSR over longer exposure periods. Specifically, at 56 and 90 days, the control mixture exhibited the highest percentage of strength reduction, whereas specimen ML10 demonstrated the lowest CSR at these ages.

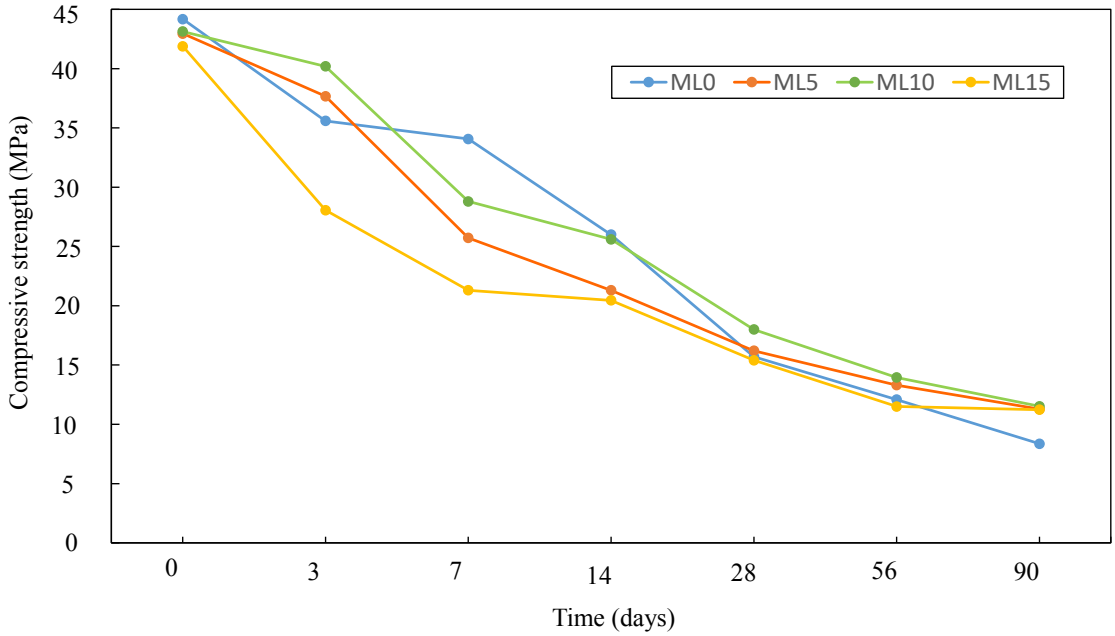

Figure 2. Effect of LECA content and acidic exposure on the compressive strength of mortar.

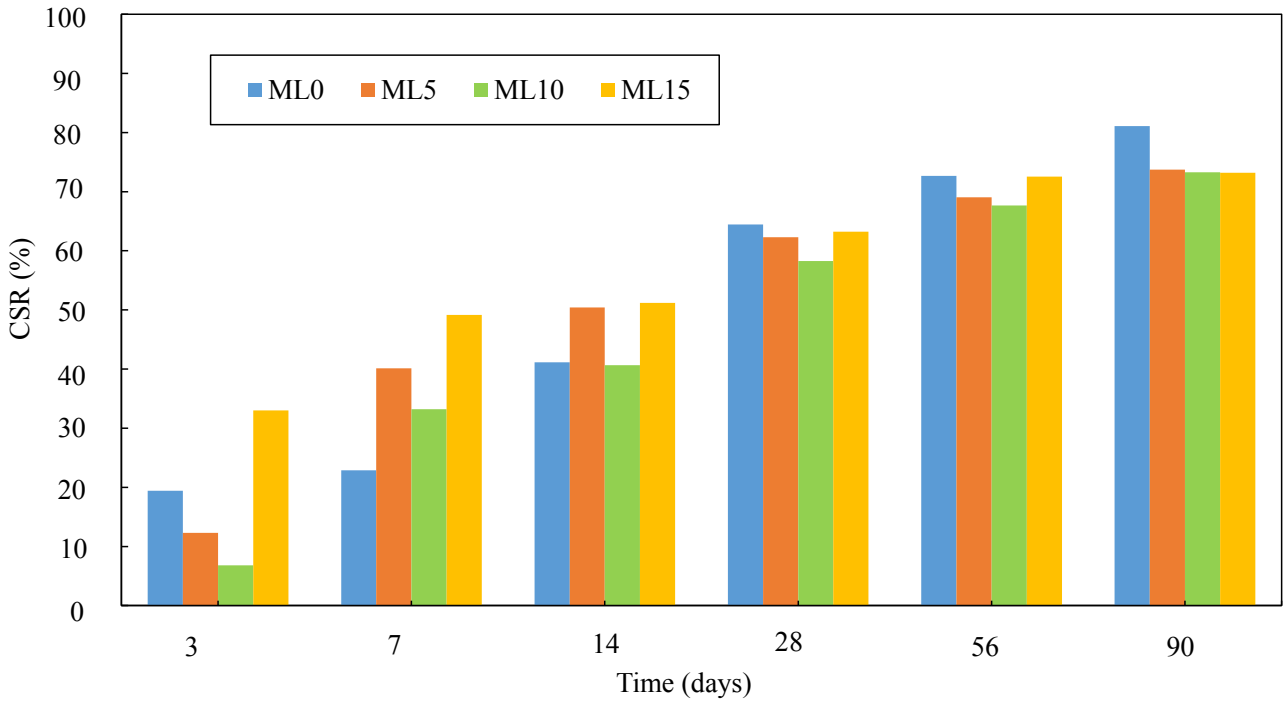

Figure 3. CSR of mortar as a function of exposure time to sulfuric acid.

5.2. Flexural Strength Test Results

The results of the flexural strength tests conducted on prismatic mortar specimens with dimensions of 160 × 40 × 40 mm are examined for different exposure periods following 28 days of standard water curing and subsequent immersion in an acidic environment. For each testing age, the average flexural strength was calculated as the mean value of three specimens. The corresponding results are presented in Figure 4.

Prior to acid exposure, specimen ML10 exhibited the highest flexural strength, while specimen ML5 showed a marginally lower value, with a difference of approximately 4.1%, which can be considered negligible. Accordingly, it can be inferred that incorporating 5% to 10% LECA in the mixture is suitable before exposure to acidic conditions. After 3 days of acid exposure, specimens ML0 and ML10 demonstrated higher flexural strength compared to the other mixtures. At subsequent ages, specimen ML10 consistently exhibited the highest flexural strength, indicating that the inclusion of 10% LECA is beneficial for cement mortar exposed to acidic environments. In contrast, specimen ML15 exhibited the lowest flexural strength at 7 days, while specimen ML0 showed the lowest value at 14 days.

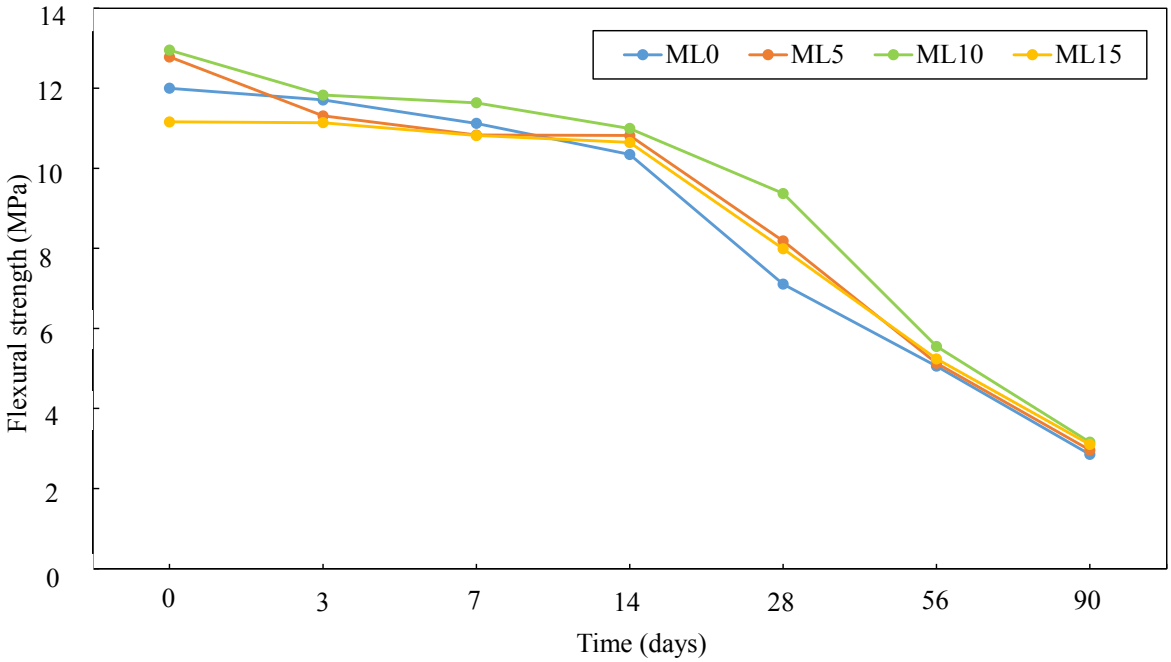

Figure 4. Effect of LECA content and acidic exposure on the flexural strength of mortar.

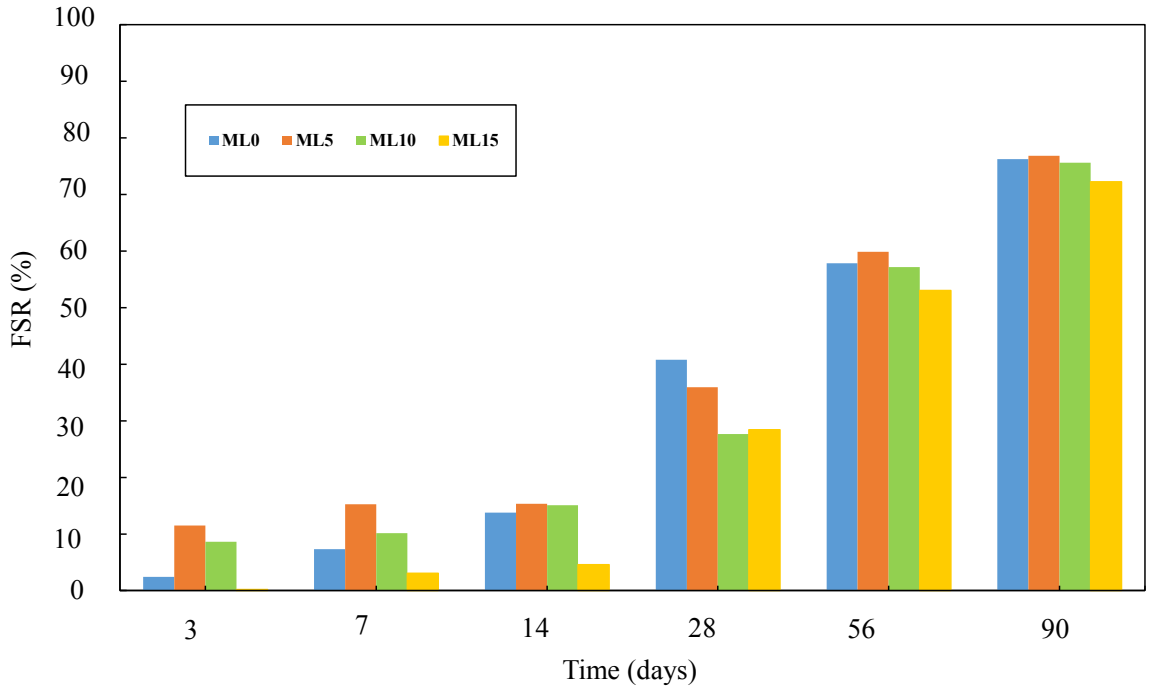

Figure 4. Effect of LECA content and acidic exposure on the flexural strength of mortar.

After 28 days of acid exposure, the reduction in flexural strength of specimens ML0, ML5, and ML15 occurred at a steeper rate compared to specimen ML10. At this age, the control mixture exhibited the lowest flexural strength, whereas specimen ML10 maintained the highest value with a noticeable margin. At 56 and 90 days, the flexural strengths of all specimens converged to similar levels, showing only minor differences; however, specimen ML10 continued to demonstrate relatively better resistance performance compared to the other mixtures.

The flexural strength reduction (FSR)relative to the control specimen was calculated using Eq.(2), based on varying LECA content and exposure duration in the acidic environment. The results are illustrated in Figures 5, where *FS* represents the flexural strength of the specimen at a given LECA replacement level and exposure day, and FS_c denotes the flexural strength of the control specimen.

$$\text{FSR} = \frac{FS - FS_c}{FS_c} \times 100 \qquad \textbf{(2)}$$

As shown in Figures 5, after 3 days of exposure, specimen ML15 exhibited a negligible FSR, and at subsequent ages its strength degradation progressed more gradually compared to the other mixtures. In addition, the flexural strength of specimens ML5 and ML10 decreased progressively at 3, 7, and 14 days. However, after 14 days of exposure, a pronounced FSR was observed for all specimens, with specimen ML0 exhibiting the highest FSR and specimen ML10 showing the lowest FSR at this age. Furthermore, it is evident that at 56 and 90 days, the FSR reached its maximum values for all mixtures.

5.3. Mass Loss

As shown in Figure 6, acidic exposure caused surface deterioration and degradation of the mortar specimens. With increasing exposure duration, the specimens experienced more severe damage, accompanied by a reduction in both volume and mass. The variation in mortar mass over the exposure period of 0 to 90 days is presented in Figure 7. At each testing age, the masses of the specimens were relatively close, and no significant differences were observed. Moreover, the mass loss trends of all mixtures followed a similar pattern.

Figure 6. Surface deterioration of a cubic mortar specimen resulting from sulfuric acid exposure.

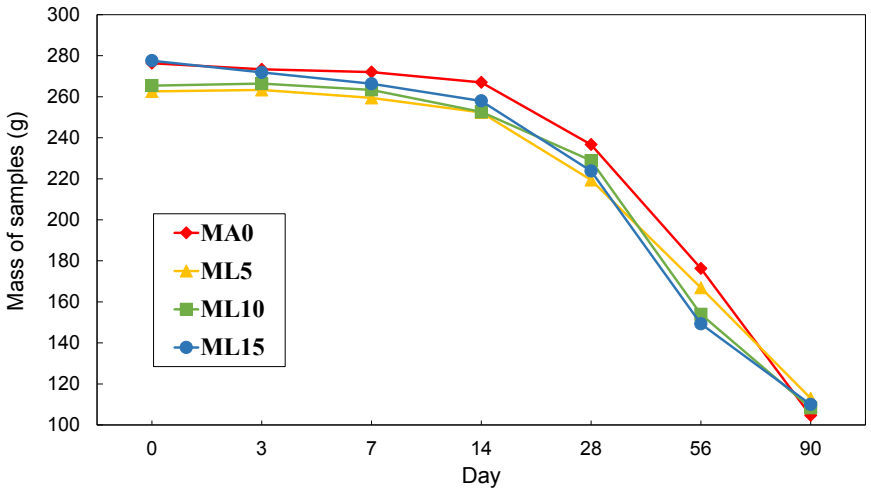

Figure 7. Mass loss of cubic mortar specimens subjected to acidic exposure.

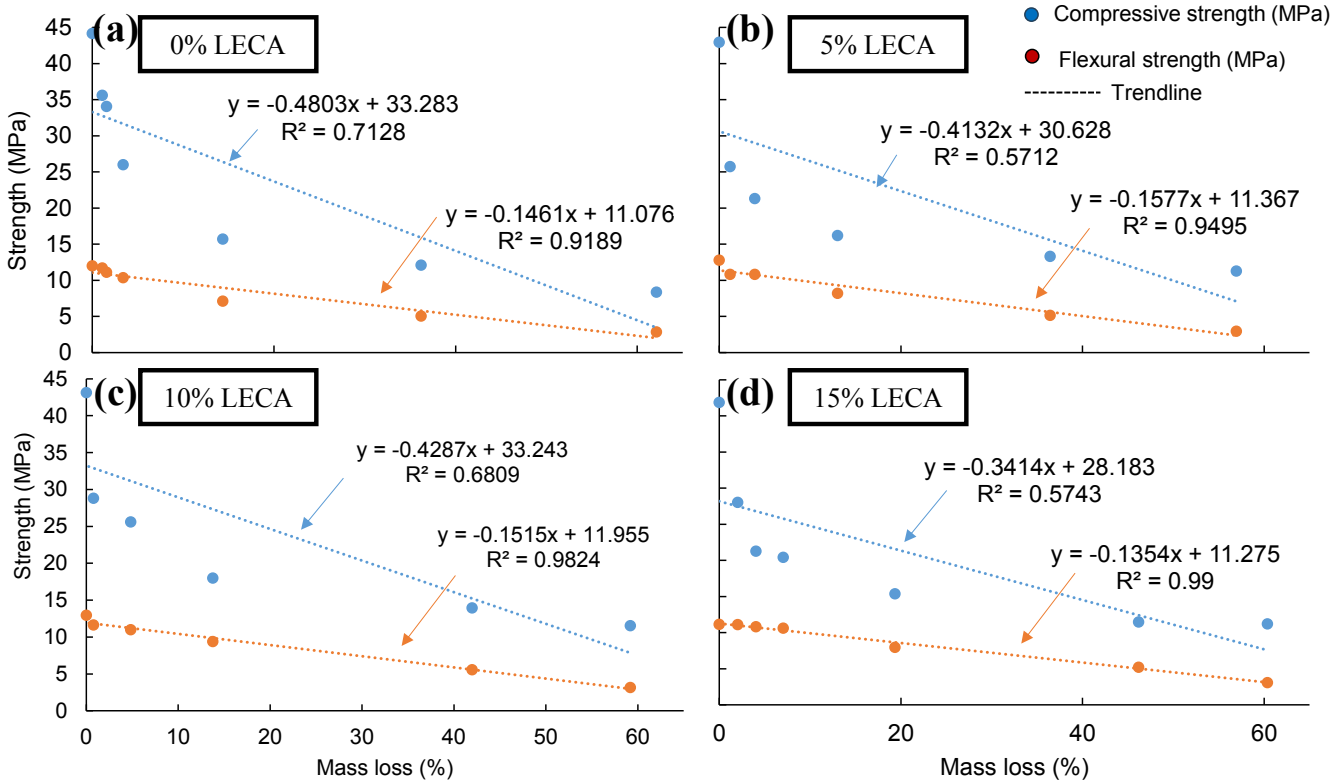

Figure 8. Relationship between mass loss and compressive and flexural strength: (a) 0% LECA, (b) 5% LECA, (c) 10% LECA, and (d) 15% LECA.

The mass of the control specimen without LECA was generally higher than that of the other mixtures at almost all exposure periods. This can be attributed to the fact that LECA is a lightweight aggregate, which reduces the overall mass of the mortar specimens. The mass loss of all mixtures occurred with nearly similar slopes, although the rate of mass reduction increased after 14 days of acidic exposure. As shown in Figure 7, after 14 days of exposure, specimen ML0 exhibited the highest mass, followed by specimen ML15. After 90 days of exposure, the control specimen showed the lowest remaining mass compared to the other mixtures, while the specimen containing 5% LECA exhibited the highest remaining mass. These results indicate that the incorporation of LECA in the mixture can reduce long-term mass loss of mortar under acidic conditions.

Figure 8 illustrates the relationship between mass loss and both compressive and flexural strength for different LECA replacement levels under internal curing conditions. Trend lines are provided for each dataset. In each case, a higher coefficient of determination (R^2) indicates a better fit and a more accurate estimation of the observed trends. Mass loss is a key factor influencing the strength behavior of mortar under acidic exposure, and as observed, an increase in mass loss percentage corresponds to a reduction in both compressive and flexural strength. Furthermore, analysis of the coefficients of determination reveals that, due to their values being close to unity, the linear trend provides a more reliable

estimation for flexural strength. In contrast, the proposed linear relationship for compressive strength exhibits a comparatively weaker correlation than that observed for flexural strength.

٦. Conclusion

In this study, the optimal replacement level of LECA with internal curing as a substitute for natural sand in structural mortar was investigated to achieve maximum compressive and flexural strength under acidic exposure conditions. Four mortar mixtures were prepared by replacing sand with 0%, 5%, 10%, and 15% LECA. Cubic and prismatic mortar specimens were cast and water-cured for 28 days, followed by exposure to sulfuric acid with a pH of 1.5 for durations of 0, 3, 7, 14, 28, 56, and 90 days to simulate acidic environments. Compressive strength, flexural strength, mass loss behavior, and the relationship between strength reduction and mass loss were evaluated. Based on the experimental results, the following conclusions can be drawn:

1. Prior to acid exposure, the compressive strengths of all four mortar mixtures were nearly identical, indicating that replacing sand with LECA under internal curing conditions does not adversely affect the initial compressive strength.
2. Acidic exposure resulted in CSR for all specimens. However, the control mixture without LECA exhibited a greater long-term strength degradation compared to the LECA-containing mixtures, showing the highest CSR at 56 and 90 days.
3. Evaluation of flexural strength revealed that before acid exposure, specimen ML10 exhibited the highest flexural strength among all mixtures. Therefore, the use of 10% LECA as a sand replacement under internal curing conditions can be considered optimal.
4. Under acidic exposure, FSR for all mixtures, similar to the behavior observed in compressive strength. Nevertheless, the mixture containing 10% LECA demonstrated lower FSR compared to the other mixtures, indicating improved flexural performance in acidic environments.
5. Since LECA is a lightweight aggregate, mortar specimens containing LECA exhibited lower mass compared to the control specimen at most exposure periods. However, after prolonged acid exposure (90 days), the control specimen exhibited the lowest remaining mass, whereas LECA-containing mixtures showed reduced mass loss. This suggests that incorporating LECA in the mixture can mitigate long-term mass loss under acidic conditions.
6. Analysis of the relationship between mass loss and mechanical strength indicated that increases in mass loss were accompanied by reductions in both compressive and flexural strength. Moreover, due to coefficients of determination close to unity, linear relationships provided a more reliable estimation for flexural strength behavior than for compressive strength, for which the linear correlation was less representative.

References

[1] Hemati, M., Dastan Diznab, M. A., Fadaei, E., & Abadi, F. Y. K. Effects of conventional, extensive and intensive green roofs on seismic performance of SMRF structures by endurance time method. *Structures, 74*, 108536. (2025)

[2] Zhao, Y., Hou, Q., Xu, X., Ding, G., & Wang, S. Spatial-temporal distribution of acid rain in China during 2005. *Advances in climate change research, 2*(5), 242–245. (2006)

[3] Özcan, A., & Karakoç, M. B. The resistance of blast furnace slag-and ferrochrome slag-based geopolymer concrete against acid attack. *International Journal of Civil Engineering, 17*(10), 1571–1583. (2019)

[4] Hu, C., Zhou, Z., & Chen, G. Effects of different types of acid rain on water stability of asphalt pavement. *Construction and Building Materials, 322*, 126308. (2022)

[5] Wang, J., Zhang, S., Fu, Q., Hu, Y., Lu, L., & Wang, Z. Preparation and Performance Study of High-Strength and Corrosion-Resistant Cement-Based Materials Applied in Coastal Acid Rain Areas. *Materials, 17*(3), 752. (2024)

[6] Mahmoodian, M., & Alani, A. M. Effect of temperature and acidity of sulfuric acid on concrete properties. *Journal of Materials in Civil Engineering, 29*(10), 04017154. (2017)

[7] Maj, M., & Tamrazyan, A. G. (2019). *Problems related to storage of acid substances in reinforced concrete tanks*. Paper presented at the Journal of Physics: Conference Series.

[8] Witkowska-Dobrev, J., Szlachetka, O., Francke, B., et al. Effect of different water-cement ratios on the durability of prefabricated concrete tanks exposed to acetic acid aggression. *Journal of Building Engineering, 78*, 107712. (2023)

[9] Sharifi, Y., Afshoon, I., Nematollahzade, M., Ghasemi, M., & Momeni, M.-A. Effect of copper slag on the resistance characteristics of SCC exposed to the acidic environment. *Asian Journal of Civil Engineering, 21*(4), 597–609. (2020)

[10] Irico, S., De Meyst, L., Qvaeschning, D., Alonso, M. C., Villar, K., & De Belie, N. Severe sulfuric acid attack on self-compacting concrete with granulometrically optimized blast-furnace slag-

comparison of different test methods. *Materials, 13*(6), 1431. (2020)

[11] Sharifi, Y., Ranjbar, A., & Mohit, M. Acid resistance of cement mortars incorporating ceramic waste powder as cement replacement. *ACI Materials Journal, 117*(2), 145–156. (2020)

[12] Dastan Diznab, M. A., Ghaderan, S., Yousefi Karim Abadi, F., & Bonyadi, M. Evaluation of characteristics and preference of mortar samples with aluminum slag and LECA with internal curing. *Journal of Structural and Construction Engineering (JSCE), 12*(5), 5–22. (2025)

[13] Davodijam, F., Dastan Diznab, M. A., & Tehrani, F. M. (2022). Sustainability Rating of Internally Cured Concrete in Marine Environments Using Service Life Prediction Models *Leveraging Sustainable Infrastructure for Resilient Communities* (pp. 141–151).

[14] Kalantari, S., Dastan Diznab, M. A., & Tehrani, F. M. (2021). *Sustainability of Internally-Cured Concrete for Mitigating Shrinkage Cracking Using Service Life Prediction Models.* Paper presented at the International RILEM Conference on Early-age and Long-term Cracking in RC Structures.

[15] C33/C33M-24a, A. (2024). Standard Specification for Concrete Aggregates.

[16] C150/C150M-22, A. (2022). Standard Specification for Portland Cement.

[17] Alexander, M. (1999). *Engineering and transport properties of the interfacial transition zone in cementitious composites* (Vol. 20): Rilem Publications.

[18] Uysal, O., Uslu, İ., Aktaş, C. B., Chang, B., & Yaman, İ. Ö. Physical and Mechanical Properties of Lightweight Expanded Clay Aggregate Concrete. *Buildings, 14*(6), 1871. (2024)

[19] Ren, J., Zhu, L., Zhang, X., et al. Variation characteristics of acid rain in Zhuzhou, Central China over the period 2011-2020. *Journal of Environmental Sciences, 138*, 496–505. (2024)

[20] Fan, Y., Zhang, S., Wang, Q., & Shah, S. P. The effects of nano-calcined kaolinite clay on cement mortar exposed to acid deposits. *Construction and Building Materials, 102*, 486–495. (2016)

[21] Taylor, P. C. (2013). *Curing concrete*: CRC press.

[22] Weiss, J., Bentz, D., Schindler, A., & Lura, P. Internal curing. *Structure, 12*, 10–14. (2012)

[23] Lam, H. Effects of internal curing methods on restrained shrinkage and permeability. (2005)

[24] Cusson, D., & Hoogeveen, T. Internal curing of high-performance concrete with pre-soaked fine lightweight aggregate for prevention of autogenous shrinkage cracking. *Cement and concrete research, 38*(6), 757–765. (2008)

[25] ACI 308-213R-13. (2013). Report on Internally Cured Concrete Using Prewetted Absorptive Lightweight Aggregate: American Concrete Institute.

[26] C192/C192M-25, A. (2025). Standard Test Method for Compressive Strength of Cylindrical Concrete Specimens. West Conshohocken, PA.